UNIVERSITY OF SOUTHAMPTON
Department of Physics and Astronomy

Double Photoionization of Alkaline Earth Atoms and Photoelectron Spectroscopy of Reactive Intermediates

by

Alberto De Fanis

A thesis submitted for the degree of
Doctor of Philosophy

July 2000

UNIVERSITY OF SOUTHAMPTON

Abstract

FACULTY OF SCIENCE

DEPARTMENT OF PHYSICS

Doctor of Philosophy

Double Photoionization of Alkaline Earth Atoms and Photoelectron Spectroscopy of Reactive Intermediates

by Alberto De Fanis

Double photoionization (DPI) of the outermost s^2 electrons of Ca and Sr atoms in the vapour phase has been studied by measurements of the angular correlation between the directions of emission of the two electrons. This process has been studied using monochromatic radiation produced by the second generation Daresbury synchrotron radiation source (SRS). The extremely low cross sections of the DPI processes were enhanced by using incident radiation at wavelengths corresponding to autoionizing resonances of the neutral species. Measurements of DPI for Ca atoms have also been collected at a non resonant photon energy using the third generation Elettra SRS in Trieste. Discrepancies between the present experimental results and the limited existing theory are found for the non resonant process.

Two-step double photoionization via intermediate excited ionic states has been studied in both Ca and Sr atoms. Measurements of angular distributions and angular correlations between the directions of emission of inner shell photoelectrons and the associated Auger electrons allowed detailed characterizations of the photoionization processes.

Valence photoelectron spectroscopy of the short-lived reactive intermediates $O_2(a^1\Delta_g)$, OH and OD has been performed using the Daresbury SRS. Autoionizing resonances have been assigned to members of series of Rydberg states converging towards higher ionic limits. Measurements of angular distributions of photoelectrons allowed further insight into the photoionization processes to be obtained.

Suggestions are presented for further experimental investigations.

Memorandum

This thesis is an account of original research performed by the author in the Department of Physics and Astronomy, and in the Department of Chemistry of the University of Southampton, between October 1997 and July 2000. Where findings of other work have been used, due reference has been given.

Acknowledgments

I would like to express my profound gratitude to my supervisors, Prof. John M. Dyke and Dr. Kevin J. Ross for having always provided guidance, strong support and injection of enthusiasm during the work of this thesis.

Dr. John B. West from Daresbury is thanked for endless patience, invaluable support and constant useful discussions.

Dr. Alan Morris is gratefully acknowledged for having provided important technical help during the physical chemistry part of the project.

Thanks to Dr. Jurgen-Hans Beyer from Stirling for his important assistance during the work on metal vapours.

Many thanks to Prof. Kiyosci Ueda from Sendai for his help on the analysis of two-step double photoionization of Ca.

I am grateful to Prof. Nikolai M. Kabachnik from Moscow for having introduced me to the beauty and power of the statistical tensor.

Thanks to Dr. Stefano Stranges from Rome for his help during the work on reactive intermediates.

Dr. Stuart G. Gamblin and all the other members of the Southampton PES group are acknowledged for having provided help and support: Mr. Jonathan D. Barr, Mr. Levi Beeching, Miss Nicole Hooper, Dr. Ed P.F. Lee, Dr. Paul Mack, Dr. Pavel Soldan, Dr. Oliver W. Warschkow, Dr. Andrew E. Wright and Dr. Timothy G. Wright.

The greatest thank goes to my family, without whom I could have never achieved this level of education.

Contents

Chapter 1

Introduction

1.1 Photoelectron spectroscopy

The photoelectric effect, the emission of an electron from a system following the absorption of a photon, was observed for the first time by Hertz in 1887 [1], and was put on a theoretical footing by Einstein in 1905 [2]. However, only in the last half century this effect has been used systematically to investigate the electronic structure of atoms and molecules [3].

Photoelectron spectroscopy (PES) is the technique that uses the photoelectric effect to measure energies and cross sections of specific photoionization processes. A photoelectron spectrum is a measure of the yield of electrons emitted in a specific direction as a function of their kinetic energies, for a selected energy $h\nu$ of the incident photons. The energy of each photoelectron (PE) is determined by the radiation energy, by the initial state of the system, and by the state in which the ion is left. The basic atomic photoionization process can be written as

$$A^+ + e^- \leftarrow A + h\nu, \tag{1.1}$$

and conservation of energy applied to the process (1.1) gives

$$E(e^-) = h\nu - E(A^+) + E(A), \tag{1.2}$$

where A is the neutral species, normally in its ground state, A^+ is the singly charged positive ion, and $E(e^-)$ is the kinetic energy of the photoelectron.

Both so-called main and satellite photolines can appear in PE spectra. The former correspond to photoionization from a single orbital with the other orbitals left virtually unchanged, whereas the latter result from the photoionization process being accompanied

by excitation of one or more electrons to a former unoccupied orbital (shake-up).

In principle, PES is a simple technique. It requires a source of monochromatic and sufficiently energetic radiation, a sample, an electron kinetic energy analyser and an electron detector.

Radiation of tens of eV of energy, in the region called vacuum ultraviolet (VUV), is sufficiently energetic to ionize electrons from valence orbitals. With radiation in the region called extreme ultraviolet (XUV), whose energy is between tens and hundreds of eV, electrons from more closely bound orbitals can also be ionized, and the ion is left in excited states with an inner shell vacancy. Interaction between the vacancy and the remaining electrons can lead to the Auger process [4], the process where an electron from a less bound orbital fills the vacancy in the singly charged ion and a second electron is emitted. This process can be schematically written as

$$A^+ + e_e^- \leftarrow A + h\nu \tag{1.3}$$

$$A^+ + e_e^- \rightarrow A^{++} + e_e^- + e_{Auger}^- \tag{1.4}$$

and conservation of energy applied to the processes (1.3) and (1.4) gives

$$E(e_{Auger}^-) = E(A^{++}) - E(A^+). \tag{1.5}$$

Photoelectron spectroscopy has been changing consistently during the last twenty five years, when synchrotron radiation (SR) has been used systematically [5]. Synchrotron radiation is emitted by electrons at relativistic energies (GeV) experiencing radial acceleration in magnetic fields, tangentially to the electron flight path. SR can be monochromatized and tuned continuously in the range of energy from the far infrared to the hard X-rays region, in contrast to radiation at fixed wavelengths emitted by most rare-gases discharge lamps. SR is also naturally linearly polarized, and angle-resolved experiments are therefore feasible. Chapter 2 in this thesis outlines the fundamental properties of synchrotron radiation.

In addition to photoelectron spectra, constant ionic state (CIS) spectra can also be recorded with a synchrotron radiation source (SRS). A CIS spectrum is the measurements of the cross section for photoionization to a specific ionic state as a function of the photon energy. Resonances in CIS spectra can occur when the energy of the incident radiation matches the excitation energy of neutral states above the ionization limit, to

produce excited states that autoionize and modify the process (1.1) to the following:

$$A^* \leftarrow A + h\nu \tag{1.6}$$

$$A^* \rightarrow A^+ + e^-. \tag{1.7}$$

The presence of an autoionizing resonance normally enhances the photoionization cross sections, in some cases even up to several orders of magnitude; this is a fact of major importance in the following of this thesis.

1.2 Double photoionization

Electronic states of atoms are often described by a single electronic configuration, which is an antisymmetric combination of a single set of functions, called orbitals, each depending on the coordinates of only one electron.

The presence of electron-electron interaction makes the single electronic configuration only an approximation. Nevertheless, this is a good approximation in most cases. In fact, most of the processes that within the single electronic configuration picture and the dipole approximation are forbidden, such as transitions between states whose configurations differ by more than one orbital, normally have very low cross sections.

Several theoretical methods exist that can accurately describe interelectron correlation in bound states. However, much less is known about electron correlation in continua, where the electrons are not bound to a nucleus. The lack of knowledge on interelectron correlation in the continua has stimulated studies of double photoionization (DPI), the process where the absorption of one photon leads to the emission of two electrons. This is a process that happens only due to the interelectron correlation, and is particularly dependent on the electron correlation in the continuum. The DPI process can be schematically represented as

$$A^{++} + e_1^- + e_2^- \leftarrow A + h\nu, \tag{1.8}$$

and conservation of energy applied to the process (1.8) gives

$$E_1 + E_2 = h\nu - E(A^{++}) + E(A). \tag{1.9}$$

In atoms other than He DPI can occur in two limits. In the first limit, called direct DPI in the following of this thesis, the two electrons are emitted simultaneously, as in equation

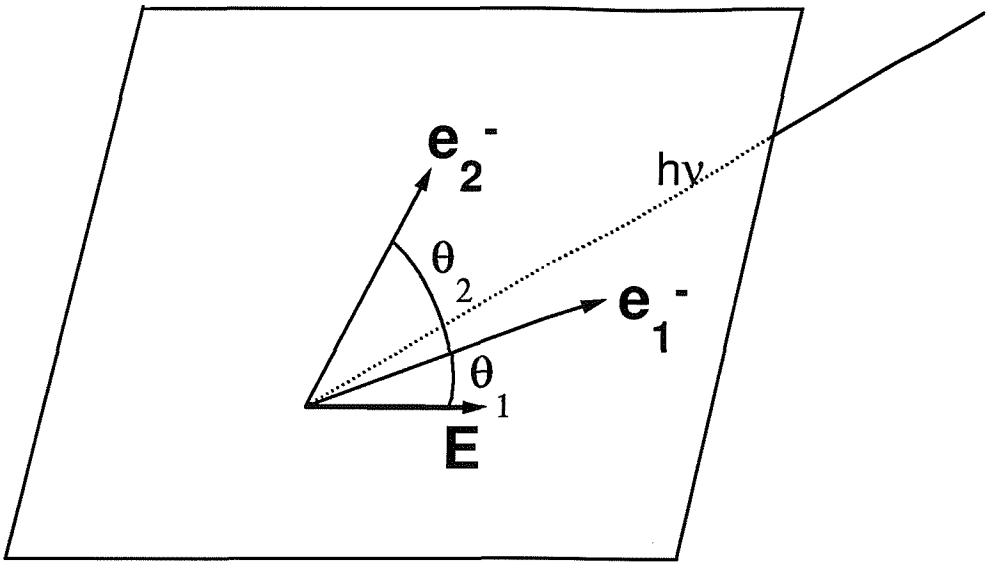

Figure 1.1: Scheme of DPI in the plane perpendicular to the incoming radiation.

(1.8). Resonant DPI is a special case of direct DPI in which the process (1.8) proceeds via a resonant state of the neutral atom, which then autoionizes into the continuum:

$$A^* \leftarrow A + h\nu, \tag{1.10}$$

$$A^* \rightarrow A^{++} + e_1^- + e_2^- \tag{1.11}$$

The second limit of the DPI process is called in this work two-step DPI. In this case the process proceeds through an intermediate excited state of the singly charged ion which decays by emitting an Auger electron, as in equations (1.3)-(1.4). In this case the two electrons are a photoelectron and an Auger electron for the first and second step respectively, and their energies are given by equation (1.2) and (1.5) respectively.

DPI of He, where only the direct process is possible, received considerable attention in the last decade [6]. The interest in double photoionization of He is enhanced by the fact that the final state has three unbound particles, a nucleus and two electrons, in mutual interactions which are inversely proportional to their separations, a fundamental problem that has attracted the attention of physicists since the time of Newton.

The cross sections of processes such as (1.8) and (1.10)-(1.11), which are differential with respect to the energies of the electrons and their directions of emission, are called triple

differential cross sections (TDCS) and are indicated as

$$TDCS = \frac{d\sigma}{dE_1 d\mathbf{\Omega}_1 d\mathbf{\Omega}_2}. \tag{1.12}$$

Only one energy enters in equation (1.12), the other being constrained by the energy conservation rule (1.9).

In experimental studies of TDCS, the angular correlation between the directions of emission of the two electrons is measured. Quantities that can be varied are the excess energy of the electron pair, the individual electron energies and their directions of emission, and the polarization of the incident radiation.

Theoretically, TDCS are calculated starting from the Fermi's golden rule [7]:

$$TDCS = 4\pi^2 \alpha \frac{p_1 p_2}{h\nu} \left| \langle A^{++}, \mathbf{p}_1, \mathbf{p}_2 | \hat{\epsilon} \cdot (\nabla_1 + \nabla_2) | A \rangle \right|^2, \tag{1.13}$$

written in atomic units with the length form of the dipole approximation; α is the fine structure constant, $\mathbf{p}_1$ and $\mathbf{p}_2$ are the linear momenta of the electrons, $h\nu$ is the energy of the incident photon and $\hat{\epsilon}$ represents its state of polarization. The main challenge of any theoretical treatment is to represent correctly the wavefunction of the two-electron continuum, apart from providing a description of the initial atomic and final ionic states.

If the two electrons are emitted in the plane perpendicular to the incoming radiation, the two angles of emission are denoted θ_1 and θ_2, and are normally measured relative to the major axis of linear polarization, as is shown in figure 1.1.

The theory necessary to extract physical information on direct DPI processes from measurements of TDCS is presented in chapter 3. Chapter 4 reviews other studies of DPI that are relevant for the work of this thesis.

In the work of this thesis both resonant and non-resonant direct DPI of the outermost s^2 electrons in Ca and Sr have been studied by measurements of TDCS for different conditions of energy sharing; the original results of these studies are presented in chapter 7.

1.3 Complete photoionization experiments

In the last twenty years intensive efforts have been made to perform "complete" photoionization experiments [8]. In conventional PES only energies and cross sections of photoionization processes are measured; other quantities that also control the dynamics of such

processes cannot be obtained. For example, photoionization from an np shell of a closed shell atom results in an ion with a ^2P symmetry and a photoelectron in a superposition of degenerate waves with s and d orbital angular momenta. In the independent electron picture the cross section for such a process is proportional to the sum of the squared amplitudes of the reduced matrix elements of the dipole operator between the radial part of the initial bound orbital, R_{np}, and of the two degenerate waves, $R_{\epsilon l}$:

$$\sigma_p \propto |D_s|^2 + |D_d|^2 \tag{1.14}$$

$$D_l \equiv \int_0^{+\infty} R_{np}(r) r R_{\epsilon l}(r) r^2 dr. \tag{1.15}$$

Measurements of such cross sections do not reveal information on the individual complex values of D_s and D_d. The objective of complete experiments is to extract all the quantities that characterize a specific ionization process, in this example the individual amplitudes and the relative phase of the D_l elements.

In the work of this thesis complete experiments have been performed for the $3p$ and $4p$ photoionizations of Ca and Sr respectively. These have been made by measurements of angular distributions of photoelectrons and of the associated Auger electrons, as well as measurements of the angular correlations between their directions of emission, by detecting the two electrons in coincidence. These complete experiments are particularly relevant to the work of this thesis because they are based on two-step DPI processes.

The theory necessary to extract the D_l parameters from the measurements of angular distributions and angular correlations is presented in chapter 3, and the results of complete photoionization experiments on Ca and Sr are presented in chapter 8.

1.4 Alkaline earth atoms

Alkaline earth atoms are the subject of the DPI studies described in this thesis. They have electronic configurations with an s^2 electron pair around a closed ionic core. Studies of DPI from these valence orbitals are very interesting for comparison with those obtained for He. Differences between DPI of He and other s^2 systems can be introduced by the electronic structure in the initial atomic and final ionic states, as well as by the different radial distributions of the s orbitals and by the interaction between the ion and the electrons during the preliminary stage of the electron escape.

Experimentally, studies of DPI of metal atoms are challenging because the target is obtained by high temperature vaporization of a solid sample, producing lower atom density

than is available in equivalent studies of samples which are gaseous at room temperature.

Theoretically, studies of DPI of metal atoms are complicated by higher atomic numbers compared with He, the electrons acting as an additional source of correlation both in the neutral and in the doubly charged ion.

1.5 Molecular photoelectron spectroscopy

Most of the chemical properties of molecules are principally determined by their electronic structure, and in particular by the character of their valence electrons.

To understand characteristics of molecules, such as absorption and emission of radiation, formation of chemical bonds, dissociation, ionization, chemical reactivity, it is of vital importance to obtain detailed information on their electronic structures.

A great variety of spectroscopic methods has been developed during the last century; among these, only few techniques are dedicated to ions. Photoelectron spectroscopy is particularly suited to study electronic states of singly charged molecular ions, photoionization and autoionization processes. Since its beginning, photoelectron spectroscopy has focused on molecules at least as intensively as on atoms [9].

1.5.1 Vibrational structure

The resolution normally achievable in VUV photoelectron spectroscopy allows vibrational structure to be resolved in most light molecules. In contrast, resolution of rotational structure, is far beyond the capabilities of conventional PES, with the exception of an extremely small number of cases.

In direct photoionization of molecules, schematically written as

$$M^+(v^+) + e^- \leftarrow M(v'') + h\nu, \tag{1.16}$$

the distribution of intensity within the v^+ vibrational components of a photoelectron band can often be approximated to the Franck-Condon factors (FCFs), the square of the overlap integral between the vibrational wavefunctions of the initial (neutral) and final (ionic) states:

$$I_{v^+ \leftarrow v''} \propto \left| \int_0^{+\infty} \Psi_{M^+,v^+}(R) \Psi_{M,v''}(R) dR \right|^2 . \tag{1.17}$$

In the case of resonant photoionization, written here as

$$M^*(v') \leftarrow M(v'') + h\nu \tag{1.18}$$

$$M^*(v') \rightarrow M^+(v^+) + e^- \tag{1.19}$$

this principle is extended by transforming equation (1.17) to the following:

$$I_{v^+ \leftarrow v' \leftarrow v''} \propto \left| \int_0^{+\infty} \Psi_{M^+,v^+}(R)\Psi_{M^*,v'}(R)dR \right|^2 \times \left| \int_0^{+\infty} \Psi_{M^*,v'}(R)\Psi_{M,v''}(R)dR \right|^2 . \tag{1.20}$$

It is normally the case that vibrational profiles of photoelectron bands change, sometimes dramatically, when the energy of the incident radiation matches the excitation energy of an autoionizing state. In most cases the vibrational profile of a PE band is extended over more ionic components. This is a key principle in the analysis of vibrational structure in photoelectron bands of small light molecules. Analysis of vibrational structures is of particular help to physical chemists as it can allow information on the equilibrium bond lengths of the ions, dissociation energies, vibrational frequencies and anharmonicities, as well as the bonding character of the orbital from which ionization occurred.

1.6 Rydberg states

As in the case of atoms, most of the autoionizing states of molecules in the VUV region have Rydberg character. Rydberg states can be described by electronic configurations where one orbital has a principal quantum number greater than those of the other occupied orbitals. The electronic configuration of the passive electrons corresponds to a state of the positively charged ion, and for this reason it is conventionally called ionic core.

Similar to the Rydberg states of one-electron atoms, Rydberg states in multielectron systems are grouped into series converging to ionic limits. Their excitation energies $E_{n,l}$ can be approximated with the following expression

$$E_{n,l} = Ie - \frac{R}{(n-\delta)^2}, \tag{1.21}$$

where Ie is the ionization energy to their ionic limit, R is the Rydberg constant ($13.61\ eV$), n is the principal quantum number and δ is called the quantum defect. In fact, the most precise values of ionization energies are obtained by extrapolations of transitions energies to Rydberg states using equations such as (1.21). The magnitude of the quantum defect δ reflects the penetration of the Rydberg orbital into the ionic core; therefore it is principally

related to the radial distribution of the excited orbital and, as a consequence, on its angular momentum composition. In fact, the angular momentum of a Rydberg orbital is extracted by analysis of its quantum defect; orbitals with the same angular momentum tend to have very close values of δ: 1.0, 0.5 and 0.1 are typical values for s, p and d Rydberg orbitals.

Every ionic state of a molecule has one or more series of Rydberg states converging to that limit. The potential energy curves of molecular Rydberg states approach rapidly those of their ionic limit; this is a further key factor in the analysis of vibrational structure in molecular photoelectron bands and in resonant bands in CIS spectra.

In PES it is common to assume that vibrational properties of Rydberg states such as the vibrational frequencies and FCFs are identical to those of their ionic core. As it is normally the case in CIS spectra, most of the resonances observed in CIS spectra in the present work are assigned to excitation to Rydberg states belonging to series converging to nearby ionic limits.

1.7 Reactive intermediates

In contrast to most light stable molecules, reactive intermediates are the subject of limited spectroscopic investigations. Despite this fact, knowledge of the electronic structure of these molecules is of extreme importance as they play key roles in the chemistry of terrestrial and extraterrestrial atmospheres, combustion processes and interstellar media [10].

Studies of these species present challenging experimental difficulties, mainly connected to their high reactivity and short lifetimes.

The Southampton PES group has always had the study of photoelectron spectroscopy of reactive intermediates [11] as its main theme. This has been recently extended to photoelectron spectroscopy of reactive intermediates with synchrotron radiation [12].

Two studies of photoelectron spectroscopy of reactive intermediates with synchrotron radiation are presented in this thesis: on $O_2(a^1\Delta_g)$, and on OH and OD. In chapter 9, the apparatus used for these studies is described, the results of these investigations on $O_2(a^1\Delta_g)$, and on OH and OD are described in chapters 10 and 11 respectively.

1.8 Aims of this work

The aims of this work are grouped in two areas of photoelectron spectroscopy with synchrotron radiation: DPI of metal vapours and PES of reactive intermediates.

For the studies of DPI of metal vapours the objectives were to record measurements of TDCS for DPI of the outermost s^2 electrons in Ca and Sr in the vapour phase using an existing apparatus. The aim was to collect measurements of TDCS for different conditions of energy sharing, angles of emission, and with resonant and non-resonant wavelengths. Studies of both direct and two-step DPI were planned, the latter with the aim of performing complete photoionization experiments.

For the studies of PES of reactive intermediates it was proposed to extend previous investigations of HeI PES to PES with synchrotron radiation. One of the goals to be achieved in this part of the thesis was also to measure angular distributions of photoelectrons from these molecules. A modification of the experimental apparatus by up-grading the detection method, was also proposed.

All the measurements were planned to be collected at the Daresbury SRS in Cheshire, England, or at the Elettra SRS in Trieste, Italy.

1.9 Outline of the thesis

This thesis is organized as follows. Chapter 2 gives a brief introduction of the characteristics of synchrotron radiation. Chapter 3 outlines the theory necessary to extract physical information on DPI from measurements of TDCS, and is also needed to analyse the two-step DPI in terms of complete experiments. Previous studies of DPI that are relevant for the present work are reviewed in chapter 4, while previous investigations of Ca and Sr with electron spectroscopy are presented in chapter 5. Chapter 6 describes the experimental apparatus used for the study of DPI of metal vapours. The results of the original studies on DPI and complete photoionization experiments on Ca and Sr are presented in chapters 7 and 8 respectively. Chapter 9 describes the experimental apparatus used for the study of PES of reactive intermediates. The results of original studies on $O_2(a^1\Delta_g)$, and on OH and OD, are presented in chapters 10 and 11 respectively. Finally, chapter 12 summarizes the results of this work and suggests possible extensions of these investigations.

Bibliography

[1] H Hertz, *Annalen der Physik*, **31** 983 (1887).

[2] A Einstein, *Annalen der Physik*, **17** 132 (1905).

[3] Photoelectron Spectroscopy.
JHD Eland, Butterworths, London (1974).

[4] P Auger, *Annal de Physique*, **6** 183 (1926).

[5] Electron Spectrometry of Atoms using Synchrotron Radiation.
V Schmidt, Cambridge University Press, Cambridge (1997).

[6] JS Briggs and V Schmidt, *Journal of Physics B: Atomic, Molecular and Optical Physics*, **33** R1-R48 (2000).

[7] H Le Rouzo and C Dal Cappello, *Physical Review A*, **43** 318-329 (1991).

[8] U Becker and B Langer, *Physica Scripta*, **T78** 13-18 (1998).
U Becker, *Journal of Electron Spectroscopy and Related Phenomena*, **96** 105-115 (1998).

[9] Molecular Photoelectron Spectroscopy.
DW Turner, Wiley - Interscience, London (1970).

[10] Chemistry of Atmosphere.
RP Wayne, Clarendon Press, Oxford (1969).

[11] Photoelectron Spectroscopy of Short-Lived Molecules.
MCR Cockett, JM Dyke and H Zamanpour, in *Vacuum Ultraviolet Photoionization and Photodissociation of Molecules and Clusters*, edited by CY Ng, World Scientific, London (1991).

[12] JM Dyke, D Haggerston, A Morris, S Stranges, JB West, TG Wright and AE Wright, *Journal of Electron Spectroscopy and Related Phenomena*, **76** 165-170 (1995).
JM Dyke, SD Gamblin, D Haggerston, A Morris, S Stranges, JB West, TG Wright and AE Wright, *Journal of Chemical Physics*, **108** 6258-6255 (1998).
JD Barr, A De Fanis, JM Dyke, SD Gamblin, A Morris, S Stranges, JB West, TG Wright and AE Wright, *Journal of Chemical Physics*, **109** 2737-2747 (1998).
JD Barr, A De Fanis, JM Dyke, SD Gamblin, N Hooper, A Morris, S Stranges, JB West and TG Wright, *Journal of Chemical Physics*, **110** 345-354 (1998).
L Beeching, A De Fanis, JM Dyke, SD Gamblin, N Hooper, A Morris and JB West, *Journal of Chemical Physics*, **112** 1707-1712 (2000).

Chapter 2

Synchrotron Radiation

2.1 Introduction

Synchrotron radiation (SR) is light generated when electrons are accelerated at high energy accelerators, synchrotrons, or storage rings. Due to the large difference in electron and proton masses, SR is significant only for electron accelerators. It was Lienard in 1898 [1] who pointed out that electrons following circular trajectories should radiate energy. In storage rings the electrons travel at about the speed of light; as they are accelerated around the circle by bending magnets, they radiate at frequencies ranging from the far infrared to the X-rays regions of the spectrum. Full quantum and relativistic treatments of the radiation process, particularly by Schwinger in 1949 [2], showed that quantum effects were negligible, but that relativistic corrections at high energies substantially changed the spectrum and the angular distribution of the radiation. Synchrotron radiation was first observed in the $70\,MeV$ electron synchrotron at the General Electric research laboratory at New York in 1947 [3], but it was not until 1963 that the first workers, Madden and Codling [4], used the radiation for atomic spectroscopy. As the value of synchrotron radiation became recognised, dedicated sources were built and more being constructed for use by atomic and molecular physicists, biologists, crystallographers, material scientists and others.

2.2 Characteristics of synchrotron radiation

Synchrotron radiation provides intense continuum radiation between approximately $150\,keV$ and $0.1\,eV$, (0.1 and 10^5 $\AA$), and therefore covers the large range between infrared and X-rays as well as being an unique tunable X-rays source. Conventional lasers in the vacuum ultraviolet region (VUV) have been constructed, but tuning is possible only over a very

small range.

SR has many unique properties which make it a highly desirable research tool:
It is very intense, being orders of magnitude brighter than conventional sources, and it is predominantly linearly polarized with the electric field vector **E** horizontal, parallel to the plane of electron orbit. This is not surprising as an observer looking towards the storage ring on its plane sees substantially an oscillating dipole. The state of polarization varies with azimuthal (out-of-plane) angle. With increasing azimuthal angle, the polarization changes from linear to elliptical and approaches circular at large angles where the intensity of the two components tends asymptotically to zero. The degree of linear polarization remains high ($\geq$ 0.75) even when radiation is collected over the full aperture.
SR is well collimated, with a divergence smaller than most laser beams.
It has a smooth, continuous spectrum stretching from infrared to X-rays.
SR makes nanosecond time-resolved spectroscopy possible due to its precise time structure with the advantage that different pulses have the same intensity, unlike lasers.
The geometry, intensity and wavelength distribution of the beam are stable over many hours.
SR is emitted under ultra high vacuum (UHV), and this provides a clean environment.
Properties of SR can be calculated accurately.

Synchrotron radiation sources have also some disadvantages: for example, they have very high costs and large dimensions. Also, radiation is dissipated in the range outside the desired spectral band. This problem is particularly acute for VUV beam-lines, where a large flux of X-rays must be safely absorbed; this has led to problems when large thermal loading has damaged mirrors. The X-rays also crack any organic contaminants which exist in the mirror environment, leaving a surface layer of carbon which reduces the reflectivity of the mirrors.

Another problem arises from the wavelength distribution of the radiation generated. For all but hard X-rays, the intensity of the radiation increases with increasing energy. Consequently, the intensity of second order radiation may be an appreciable fraction of the intensity of first order and therefore difficult to suppress.

2.3 Theory of synchrotron radiation from bending magnets

The theory of SR has been developed over many years, the first extensive theoretical treatment of radiation from relativistic accelerated electrons was carried out by Shwinger in 1949 [2]; reviews and also books on the subject exist [5]. Only details of interest for practical calculations are illustrated here.

The instantaneous power radiated by a particle of kinetic energy E travelling in a circular motion is

$$I = \frac{2e^2c}{3R^2}\left(\frac{E}{mc^2}\right)^2, \tag{2.1}$$

or numerically

$$I[erg\,s^{-1}] \simeq \frac{7(E[GeV])^4}{(R[m])^2}. \tag{2.2}$$

In equation (2.1) e and m are the charge and rest mass of the particle, c is the speed of light and R the radius of the orbit. Equation (2.1) shows why protons would radiate much less power than electrons with the same energy. It also shows the importance of the energy E and of the radius R. It is clear that the loss of energy in the production of SR is a problem which increases dramatically with higher electron energy and lower radius. The losses due to synchrotron radiation are made up by injecting radio frequency (RF) power into the ring.

2.3.1 Spectral and angular distribution

The wavelength distribution of the total instantaneous power was given by Tomboulian and Hartman in 1956 [6]:

$$\frac{dI}{d\lambda} = \frac{3^{5/2}}{16\pi^2}\frac{ce^2}{R^3}\left(\frac{E}{mc^2}\right)^7 G(Y), \tag{2.3}$$

with

$$G(Y) \equiv Y^3 \int_Y^\infty K_{5/3}(\eta)d\eta, \tag{2.4}$$

where $K_{5/3}(\eta)$ is a modified Bessel function of the second kind, and

$$Y \equiv \frac{4\pi R}{3\lambda}\left(\frac{mc^2}{E}\right)^3 \equiv \frac{\lambda_c}{\lambda}. \tag{2.5}$$

Therefore, the wavelength distribution of the radiation emitted by synchrotrons is a universal function of the ratio λ/λ_c. Equation (2.3) can be written numerically as

$$\frac{dI}{d\lambda}[erg\,s^{-1}\,\mathring{A}^{-1}] \simeq \frac{0.9(E[GeV])^7}{(R[m])^3} G(Y). \tag{2.6}$$

The quantity λ_c is a useful parameter since is the midpoint of the spectrum energy. The maximum of $dI/d\lambda$ is at

$$\lambda_p \simeq 0.4\,\lambda_c, \tag{2.7}$$

numerically this gives

$$\lambda_p[\mathring{A}] \simeq \frac{2.5\,R[m]}{(E[GeV])^3}, \tag{2.8}$$

and in the case of the $2\,GeV$ Daresbury SRS, $\lambda_p = 1.63\,\mathring{A}$. The intensity maximum shifts to shorter wavelengths as the electron energy is increased. For $\lambda \gg \lambda_c$ the power radiated becomes independent of electron energy; thus the main effect of increasing the electron energy is to move the spectral distribution towards shorter wavelengths. A storage ring of at least $100\,MeV$ is needed if extreme ultraviolet (XUV) radiation is required.

The familiar sine-squared angular distribution of radiation from an oscillating dipole is completely altered at relativistic energy, so that the radiation pattern is confined to the forward direction of the electron motion. Here the zeros in the radiation pattern are thrown forward to an angle $\theta = mc^2/E$. The distribution in the direction perpendicular to the orbital plane is confined and described by $\psi_{1/2} = 2mc^2/E$, with $\psi_{1/2}$ the full width at half maximum (FWHM) of the angular distribution. These formulae indicate the small divergence of SR at high storage energies ($0.1\,mrad$ at $4\,GeV$). Because of the confined nature of SR in the orbital plane (θ), the observer looking along the tangent receives a pulse of radiation every time the electron passes by. The emitted power spectrum is therefore comprised of the Fourier components of this pulse, which repeats at the orbital frequency of the electrons, typically in the MHz region. However, due to the Doppler effect, with the electrons moving towards the observer at almost the speed of light, the radiated power shifts to shorter wavelengths, indeed lower than the XUV region. Also, since the electrons do not have constant orbital velocity due to synchrotron oscillations, the spectrum results in a continuum.

According to Tomboulian and Hartman [6], the instantaneous power radiated by an electron in circular motion, expressed as energy per unit time per unit angle per unit wave-

length is

$$\frac{dI}{d\psi d\lambda} = \frac{8\pi^2 e^2 cR}{3\lambda^4}\left(\frac{mc^2}{E}\right)^4 (1+\zeta^2)^2 \left[K_{1/3}^2(\zeta) + \frac{\zeta^2}{1+\zeta^2}K_{2/3}^2(\zeta)\right], \tag{2.9}$$

with

$$\zeta \equiv \frac{2\pi R}{3\lambda}\left(\frac{mc^2}{E}\right)\left[1+\left(\frac{E}{mc^2}\right)^2\psi^2\right]^{3/2}. \tag{2.10}$$

Here ψ is the angle between the direction of observation and its projection on the orbital plane. $K_{1/3}$ and $K_{2/3}$ are modified Bessel functions of the second kind.

2.4 The Daresbury synchrotron radiation source

Synchrotron radiation research began in Daresbury in 1968 with parassitic use of the SR produced by the $5\,GeV$ NINA synchrotron, used mainly by high energy physics experiments. The $2\,GeV$ SRS was proposed in 1974 and inaugurated in 1980, when it was the first dedicated SRS in the world.

At the Daresbury SRS electrons are emitted by a hot cathode, accelerated to $100\,keV$ by a dc potential and then to an energy of $12\,MeV$ in a linear accelerator (LINAC). The LINAC injects the electrons into a small booster synchrotron, which accelerates them further to $700\,MeV$, and feeds them in *bunches* into the main storage ring. They are then accelerated to $2\,GeV$ by raising the magnetic field, radiation losses being compensate by injecting RF power into the ring at a frequency of $500\,MHz$. The electron beam is constrained in a closed orbit by 16 dipole bending magnets and 16 quadrupole magnets, which also focus the electron orbit within the vacuum chamber. The electron orbit is approximately circular with a radius of $15\,m$; 16 multipole magnets are used to trim the orbit for fine alignment of the synchrotron radiation beam.

The stored current, and hence the flux, gradually decline as electrons are lost, mostly by collision with background gas in the ring (the typical pressure in the storage ring is of the order of $10^{-12} - 10^{-13}\,mbar$). In normal operating condition the storage ring is refilled every 24 hours.

At each bending magnet on the storage ring, SR is extracted through port holes into straight tubes (*lines*). Eventually these lines split into branches (*beam-lines*), each leading to a different experimental station.

2.4.1 Line VUV-XUV 3

Beam-lines are connected to bending magnets in storage rings to transport, monochromatize and focus the radiation onto the experimental sample.

A beam-line is normally composed of a set of pre-focusing mirrors that direct and focus the light beam on the entrance slits of the monochromator, followed by the monochromator itself and the exit slits, and eventually a set of mirrors that refocus the light into the interaction region of the experiment. In a beam-line the number of mirrors are normally kept at a minimum. This is particularly important for VUV-XUV because, apart from making alignment more critical, they also absorb a part of the radiation.

The monochromators for the VUV-XUV range contain diffraction gratings which also have focusing properties. The wavelength is scanned by changing the position of the grating under computer control. The wavelength bandwidth depends on the width of entrance and exit slits: narrower slits give higher resolution, but at the expense of the photon flux, and a compromise between intensity and resolution must always be found.

The beam-line is normally maintained under ultra high vacuum (UHV), $P < 10^{-8}\,mbar$, to protect the delicate optical elements from contamination. Differential pumping is also needed because the experimental chamber is commonly under high vacuum, $P < 10^{-5}\,mbar$, and in the case of VUV-XUV is attached to the end of the beam-line by a windowless connection, since no material suitable for windows exist for this spectral range.

During the course of this work the VUV-XUV line 3 at the Daresbury SRS [7] has been extensively used.

Line 3 accepts radiation from a tangent point in the magnet number 3 of the SRS, in a solid angle approximately $28\,mrad \times 5\,mrad$ (FWHM) in the horizontal and vertical planes. The radiation source is the bending magnet itself. Three mirrors are used to split the beam into four components. The undeviated portion goes to a beam-line for the soft X-rays (beam-line 3.4), while the other three branches go respectively to beam-line 3.1 (Seya-Namioka monochromator), beam-line 3.2, and beam-line 3.3. During the course of this thesis experiments have been undertaken on beam-lines 3.2 and 3.3.

2.4.2 Beam-line 3.2

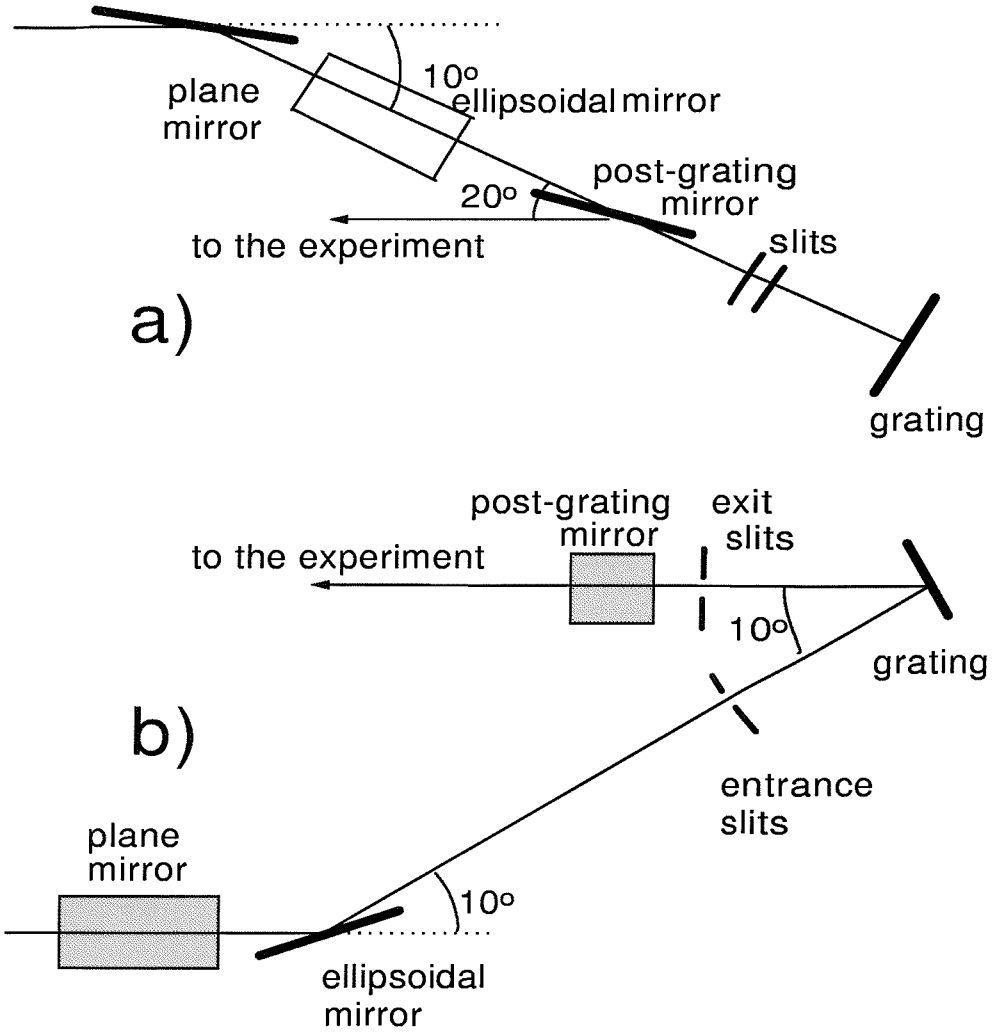

Figure 2.1: Horizontal (a) and vertical (b) optical layout of the McPherson NIM beam-line 3.2. The drawing is not to scale.

Figure 2.1 shows an optical layout of beam-line 3.2 [8]. Two mirrors are present before the monochromator. A plane mirror at $10.5\,m$ from the tangent point deviates the light beam horizontally by 10^o, this mirror accepts a $5\,mrad \times 5\,mrad$ portion of the entire light of line 3. The first mirror is followed by an ellipsoidal mirror that deflects the light vertically by 10^o, the second mirror focuses the light onto the monochromator entrance slits. These mirrors are of importance for aligning the beam after each refill of the ring, they can be adjusted by using micrometers on the sides of the mirror boxes.

The monochromator is a $5\,m$ normal incidence (NIM) McPherson model that disperses the radiation in the vertical plane. It has two gratings interchangable under vacuum to

cover the photon energy range $10 - 40\,eV$ ($300 - 1200\,\mathring{A}$). Slit assemblies at the entrance and exit allow a compromise between intensity and resolution; typical settings give a resolution of $0.4 - 1.0\,\mathring{A}$, which at $21.22\,eV$ makes $15 - 35\,meV$. The wavelength of the output light is controlled by a drive mechanism that simultaneously rotates and translates the gratings. The gratings sit on the end of a tilt arm which is driven around a cam by a leadscrew geared to a stepper motor. The cam mechanism ensures that the gratings are translated as well as rotated so as to remain in focus at all times. The drive mechanism was originally calibrated by observing known absorption lines of rare gases [8]; but in part of this work it was found necessary to calibrate it again with CIS spectra of atomic oxygen $O(^3P)$.

A post-monochromator mirror box present after the NIM contains a focusing mirror that directs the beam into the spectrometer and protects the monochromator from contamination. The mirror also acts as a further stage of differential pumping between the spectrometer and the monochromator. By deflecting the light through a narrow angle it also removes any direct line-of-sight between the sample under study, possibly aggressive, and the NIM grating. A glass capillary, normally $2\,mm$ bore, channels the light from the mirror box to the interaction region of the spectrometer.

2.4.3 Beam-line 3.3

Beam-line 3.3 [9], provides radiation over the photon energy range $10 - 120\,eV$ ($100 - 1200\,\mathring{A}$). Optical layouts of the beam-line are shown in figure 2.2. Two cylindrical mirrors with radii 8 and $6.5\,m$, and distant 6.5 and $8.3\,m$ from the source, focus the light beam horizontally and vertically on the entrance slits of the monochromator.

The positions of these mirrors can be manually adjusted to maximise the photon flux, measured by a 95% transmitting metallic mesh before the chamber and also by a photodiode at the end of the vacuum chamber.

On beam-line 3.3 the entrance slits are positioned $2.04\,m$ before the grating; they are normally $50\,\mu m$ wide, which is also the vertical dimension of the light beam at this point. The monochromator consists of two interchangeable gratings ruled with 710 and 2400 lines/mm for the photon energy ranges $10 - 60$ and $60 - 120\,eV$ respectively. It has the shape of a section of torus with meridional and sagittal radii of curvature $15\,m$ and $60\,cm$, and for this reason is called *toroidal grating monochromator* (TGM). To scan the wavelength the grating is rotated around the axis passing through its pole, perpendicular to the entrance and exit arms, at their intersection. The entrance and exit arms are fixed at an angle of 155^o. Different wavelengths are dispersed according to the following

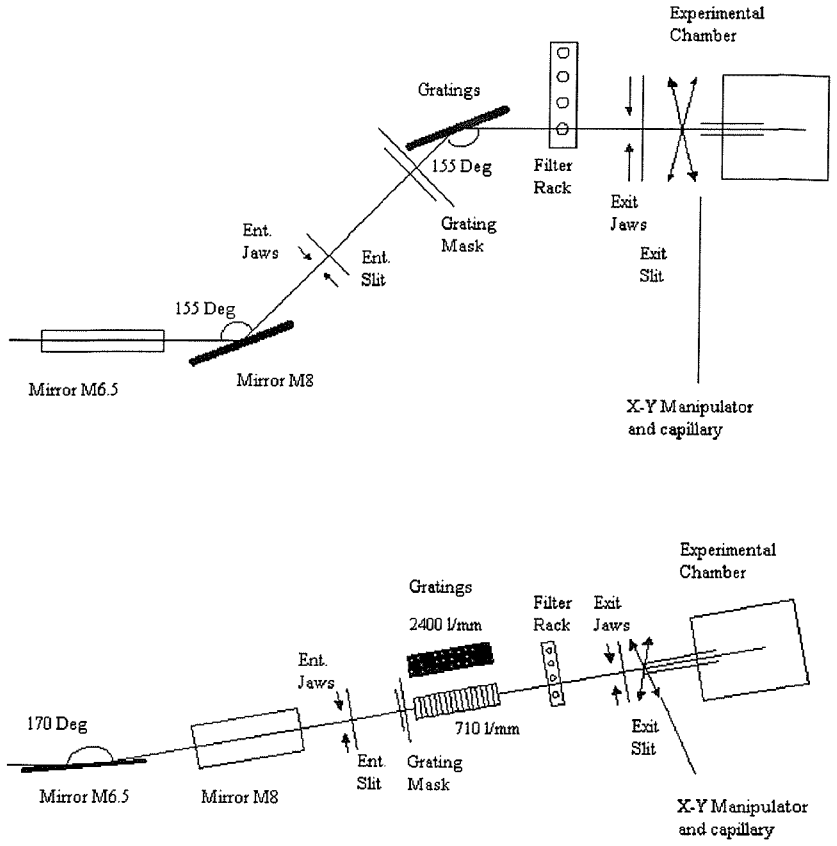

Figure 2.2: Vertical and horizontal layouts of the TGM beam-line 3.3. The drawing is not to scale.

equation [10]

$$nN\lambda = \sin\alpha + \sin\beta, \tag{2.11}$$

where n is the order of diffraction, N is the number of grooves per unit length in the grating, λ is the wavelength diffracted at the angle β, and α and β are the angles of incidence and of diffraction, that are related by the constraint

$$\alpha - \beta = 155^{o}. \tag{2.12}$$

The TGM focuses the light at the exit slits, $4.56\,m$ from the grating itself. Different wavelengths are focused at slightly different positions. The exit slits are mounted on a translatable trolley connected by bellows to the exit arm. To reduce the defocus contribution to the light band-width, the trolley can be moved along the exit arm ($\pm 20\,cm$).

No mirrors are present after the TGM, and the light beam is channelled into the interaction region from the exit slit by a quartz capillary $50\,cm$ long and $4\,mm$ bore, attached to the exit slits. Quartz rather than glass is required for metal vapours high temperature experiments. In addition to acting as a light guide, the capillary also has a low conductance,

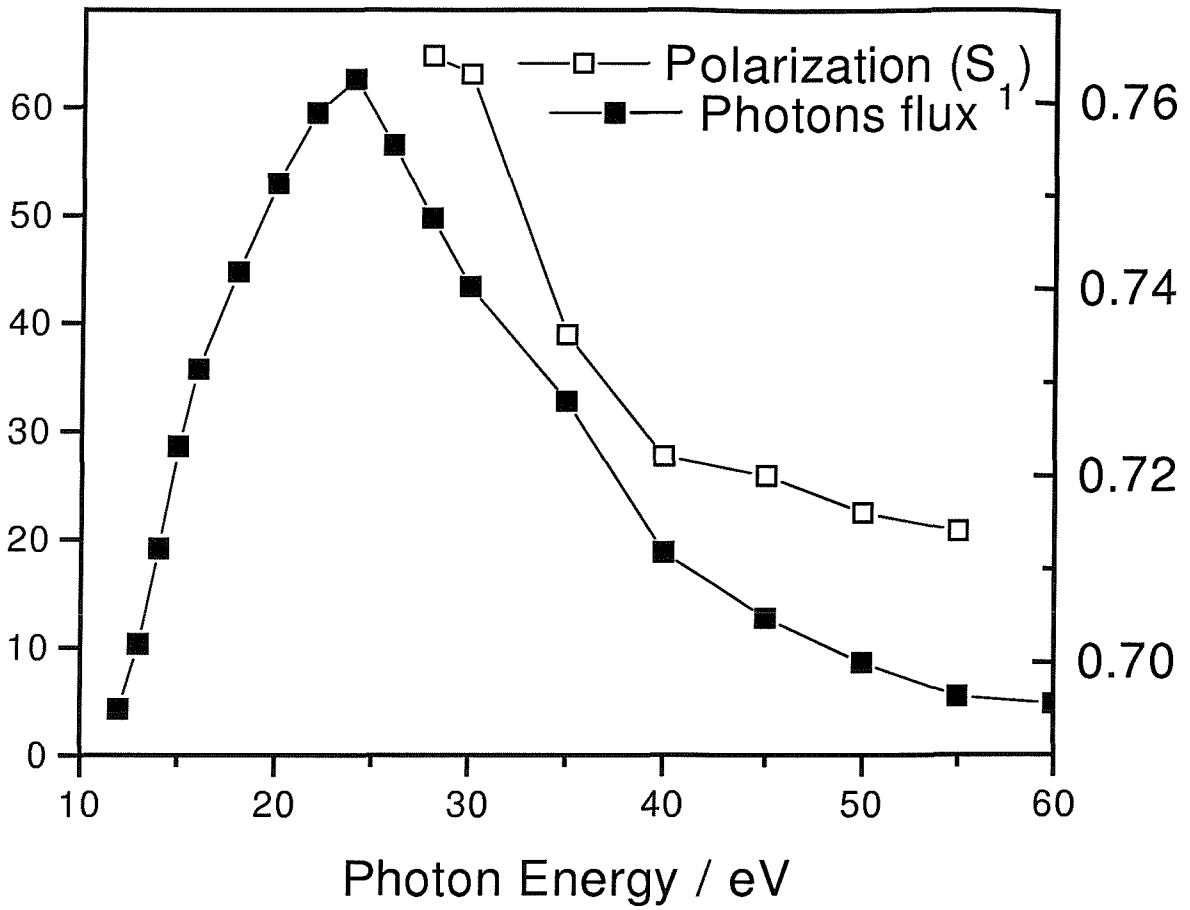

Figure 2.3: Output of the low energy grating for different photon energies, at $50\,meV$ bandwidth. Scale on the right for the polarization, on the left for the photon flux. Units for the photon flux scale are 10^{10} photon/sec per $100\,mA$ of ring current.

which assists to preserve differential pumping between the experimental chamber and the beam-line. However, it has the disadvantage of producing background photoelectrons; to reduce this effect the front end of the capillary is coated with graphite and is electrically earthed. Adjustment of the position of the light guide is provided by a 2 dimensional $X-Y$ micromanipulator.

In order to protect the vacuum in the beam-line and in the storage ring a series of valves are present along the beam-line, which automatically shut when the pressure rises higher than pre-set limits. The last valve towards the experiment is a *window valve* and is transparent to visible light. The oven and the analysers are aligned with the beam-line using the visible components of the zeroth order from the TGM passing through the window valve.

Figure 2.3 shows the photon intensity and degree of linear polarization (S_1) for the low energy grating, measured with $50\,meV$ bandwidth and a glass capillary $54\,cm$ long and

$2\,mm$ bore.

2.5 Insertion devices

Although insertion devices have been minimally used during the course of this work, they deserve a brief mention here due to their importance to the community of synchrotron radiation.

2.5.1 Wigglers and undulators

In contrast to the smooth spectral distribution of radiation from a bending magnet, radiation from an undulator, and to a certain extent also from a wiggler, shows characteristic maxima. These maxima are due to the periodic magnetic structure of insertion devices: a transverse magnetic field with N periods of length λ_u produces an oscillatory (wiggling, or undulating) path for the electrons which is similar to the response generated by 2N bending magnets. A characteristic parameter for these devices relates the maximum deflection angle α of the electron path to the natural opening angle of the radiation cone γ, and is given by

$$K \equiv \alpha\gamma = \frac{eB_0\lambda_u}{2\pi mc} \simeq 100 B_0[T]\lambda_u[m], \tag{2.13}$$

where B_0 is the peak field. Depending on the K-value, the radiation cones from individual wiggles can contribute separately. This happens if $K \gg 1$ and the device is then called a wiggler; alternatively they can act coherently, which happens if $K \leq 1$ and the device is then called an undulator.

The interference between electromagnetic waves emitted by the same electron at different wiggles yields a redistribution of the spatial and spectral intensity. The condition for constructive interference follows from the proper timing for the movement of the electron and its emission of light with wavelength λ. The time taken by the electron to travel through one undulator period λ_u minus the time taken by the light to travel this distance must equal $n\lambda/c$, where n is an integer number. For light emitted at angles Θ and Ψ with respect to the undulator axis one gets [11]

$$\lambda_n = \frac{\lambda_u}{2n}\left(\frac{mc^2}{E}\right)^2\left[1 + \frac{K^2}{2} + \gamma^2(\Theta^2 + \Psi^2)\right], \tag{2.14}$$

where λ_n indicates the wavelength of the nth harmonic. The harmonics are characteristic of the spectrum of undulator radiation. Hence it is advantageous to work at the energy

of such harmonics and to tune the value of λ_n for a given undulator to the experimental needs. This is usually done by changing the gap between the permanent magnets of the insertion devices, which, in turn, changes the field strength B_0, the parameter K, and thus λ_n.

The quantity that best describes the quality of a radiation source is called *brightness* [12]. This takes into account both the spatial distribution of the electrons circulating in the ring and the spatial distribution of the light emission, and is defined as

$$B \equiv \frac{spectral\ flux\ into\ 0.1\%\ bandpass\ per\ 100\,mA\ ring\ current\ [photons/s]}{source\ area\ [mm^2]\ \times\ solid\ angle\ [mrad^2]}. \quad (2.15)$$

Synchrotron radiation from undulators can have *brightness* three orders of magnitude higher than that from bending magnets. Undulator light is also much more collimated and has a higher degree of linear polarization (≥ 0.95). With appropriate geometry of the magnets, undulators can also produce light nearly completely circularly polarized.

The intensity of the radiation emitted from a wiggler is proportional to the number of magnets and to the ring current; in the case of an undulator there is a gain in brightness proportional to the squares of these values. The band-width and the opening angles are inversely proportional to the number of magnets for a wiggler and to its square for an undulator.

2.5.2 Free electron laser (FEL)

FELs have not been used in the course of this work, but they deserve a brief note due to their importance in the field of SR.

A FEL in a storage ring combines the principle of an optical resonant cavity and stimulated emission through a gain medium, with that of undulator light [13]. The active medium in a FEL is the electron beam itself travelling along the undulator axis. The optical beam is obtained by taking a portion of the output undulator light and returning it backward to the input end of the FEL. This can be done by using a partially reflecting mirror that splits the light coming out from the undulator and returning it back through the undulator. Together with a highly reflecting second mirror they form the optical laser cavity where the interaction of the emitted radiation with the electron beam can lead to light amplification. For the VUV-XUV region most of the experimental challenge consists in the development of suitable reflecting mirrors.

In the VUV-XUV spectral range, the brightness available from a FEL is expected to be

up to 3 to 4 order of magnitude higher than that available from the brightest undulators. FEL in LINACs and in storage rings are now being used in the IR and visible range [14], and are under investigation for the VUV-XUV spectral region [15].

2.6 The gas-phase photoemission beam-line at Elettra

Although most of the results included in this thesis have been obtained at the SRS, one beam-time period was also used at the Elettra SRS in Trieste. Elettra is a third generation synchrotron dedicated to the production of X-rays. The term third generation means that it has been specifically designed with the idea to include insertion devices into straight lines of the storage ring. The storage ring operates at either 1 or $2\,GeV$, and it includes 16 ports for beam-lines.

The gas phase photoemission beam-line at Elettra, provides radiation in the photon energy range $20 - 900\,eV$ ($15 - 600\,\mathring{A}$) [16]. A drawing of the beam-line is shown in figure 2.4. The light source is an undulator with $12.5\,cm$ period, $4.5\,m$ length and tunable gap. The undulator has been used in 1st harmonic, where its output is most intense and the half-width is approximately 4% of the photon energy.

A first mirror focuses the light onto the entrance slits of the monochromator. The monochromator consists of a plane mirror and a set of five interchangeable spherical gratings. The grating that was used is ruled with 400 lines/mm and covers the photon energy range $20 - 50\,eV$. Entrance and exit slits are in fixed positions at 4 and $1.6\,m$ from the grating pole. After the exit slits two mirrors refocus the light in the horizontal and vertical plane at the position of the experimental chamber, chamber A in the drawing. Although in the present work it was not used, an additional mirror can be positioned between the exit slits and the first refocus mirror; it would deviate the light into a different experimental chamber, chamber B. This can be advantageous during mounting and dismounting time at the beginning and at the end of beam-times.

No capillary was used to channel the light into the spectrometer, as the beam is well collimated and has a small spot size ($< 1\,mm$).

In the present work high photon flux rather than a high resolution was needed and entrance and exit slits apertures were widened to 50 and $300\,\mu m$. In these conditions the wavelength band-width is still less than $50\,meV$, negligible compared to the electron spectrometer resolution. The photon flux at the photon energy used, $43.03\,eV$, was estimated from

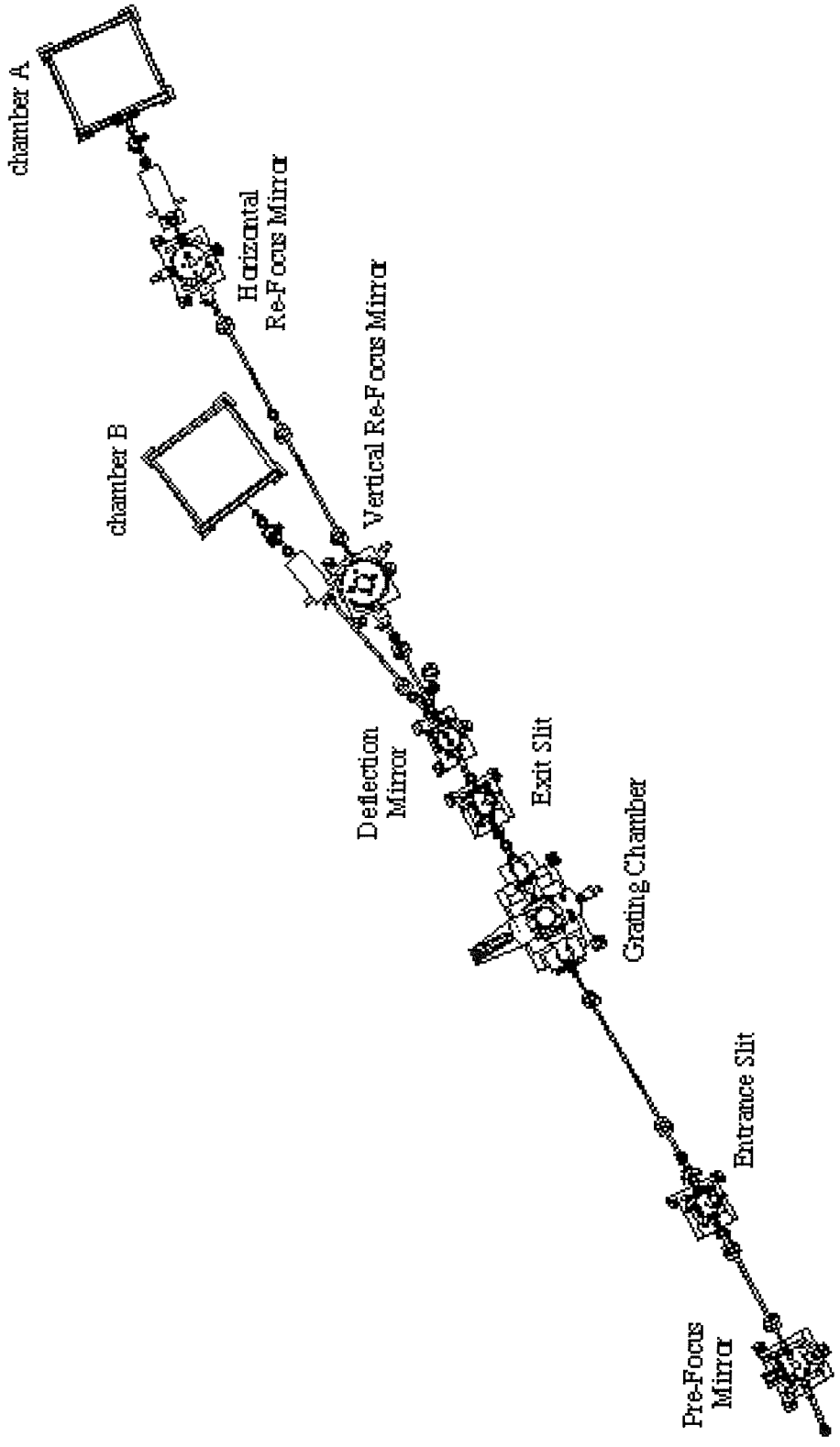

Figure 2.4: Scheme of the gas-phase photoemission beam-line at Elettra.

a reading on a photodiode mounted on the back of the chamber and it resulted in an intensity of the order of 10^{13} photons/s per $100\,mA$ of ring current.

Because the undulator does not produce visible light, the experimental chamber with the oven and the analysers was aligned with the visible light produced by the bending magnet present after the undulator. This operation assumes that the undulator light is on the same line of the much weaker light beam from the bending magnet, and this has been previously established to be the case for this beam-line.

Bibliography

[1] A Lienard, *L'eclairage elect.*, **16** 5-14 (1898).

[2] J Schwinger, *Physical Review*, **75** 1912-1925 (1949).

[3] FR Elderer, AM Gurewitsch, RV Langmuir and HC Pollock, *Physical Review*, **71** 829-837 (1947).

[4] RP Madden and K Codling, *Physical Review Letters*, **10** 526-528 (1963).

[5] Classical Electrodynamics.
JD Jackson, John Wiley, New York (1962).
Classical Electricity and Magnetism.
WKH Panovsky and M Phillips, Addison Wesley, London (1962).

[6] DH Tomboulian and PL Hartman, *Physical Review*, **102** 1423-1426 (1956).

[7] http://srs.dl.ac.uk/XUV-VUV/.

[8] DMP Holland, JB West, AA MacDowell, IH Munro and AG Beckett, *Nuclear Instruments and Methods in Physics Research*, **B44** 233-241 (1989).

[9] Optical Engineering.
JB West and HA Padmore, in *Handbook on Synchrotron Radiation*, edited by GV Marr, North Holland, Amsterdam (1987).

[10] HG Beutler, *Journal of the Optical Society of America*, **35** 111-121 (1945).

[11] Electron Spectrometry of Atoms using Synchrotron Radiation.
V Schmidt, Cambridge University Press, Cambridge (1997).

[12] Synchrotron Radiation - a Power Tool in Science.
EE Koch, DE Eastman and Y Frage, edited by EE Koch, North Holland, Amsterdam (1983).

[13] Free Electron Lasers.
CA Brau, in *Advances in Electronics and Electron Physics*, (1990).

[14] JM Ortega, *Synchrotron Radiation News*, **9** 20-33 (1996).

[15] A VUV Free Electron Laser at the TESLA Test Facility at DESY.
DESY Print (1995).

[16] RR Blyth, R Delaunay, M Zitnik, J Krempansky, R Krempaska, J Slezak, KC Prince, R Richter, M Vondracek, R Camilloni, L Avaldi, M Coreno, G Stefani, C Furlani, M De Simone, S Stranges and M-Y Adam, *Journal of Electron Spectroscopy and Related Phenomena*, **101** 959-964 (1999).
P Melpignano, S Di Fonzo, A Bianco and W Jark, *Review of Scientific Instruments*, **66** 2125-2128 (1995).
KC Prince, R R Blyth, R Delaunay, M Zitnik, J Krempasky, J Slezak, R Camilloni, L Avaldi, M Coreno, G Stefani, C Furlani, M De Simone and S Stranges, *Journal of Synchrotron Radiation*, **5** 565-568 (1998).
http://www.elettra.trieste.it.

Chapter 3

Theoretical section

3.1 Introduction

In this chapter the single and double photoionization processes of closed shell atoms are considered from a theoretical point of view. Both direct and two-step DPI are emphasised. The quantum mechanical descriptions of these two processes are discussed together with the different physical information that can be extracted from experimental studies of these two phenomena.

This chapter is organized as follows. In sections 3.2 and 3.3 the equations for the angular distribution of photoelectrons and Auger electrons are derived. Section 3.4 introduces the lsj approximation that will be used in the following. Section 3.5 presents a parameterization of the two-step DPI for the analysis of the measurements where the photoelectron and the associated Auger electron are detected in coincidence. Section 3.6 introduces the idea of complete experiments. Section 3.7 describes the random phase approximation with exchange (RPAE) calculations that have been used to study the $3p$ photoionization of Ca. Parameterizations of the direct DPI in terms of 1) the continuum electron configuration and 2) an angular and a correlation factor are given in section 3.8.

3.2 Angular distribution of photoelectrons

The cross section for emission of a photoelectron with linear momentum $\mathbf{p}$ can be expressed in terms of the diagonal elements of the density matrix of the final state of the ionization process:

$$\frac{d\sigma}{d\Omega_e} = \sum_{m_s M_c} \langle J_c M_c s m_s \mathbf{p} | \rho^f | J_c M_c s m_s \mathbf{p} \rangle. \tag{3.1}$$

The sum is performed over the unobserved quantum numbers: the projection of the angular momenta of the ion J_c: M_c, and the spin polarization of the photoelectron: m_s; $\mathbf{\Omega}_e$ is the angle of emission.

Due to the spherical symmetry of the problem, it is convenient to express the states in equation (3.1) as a superposition of partial waves with defined angular momenta:

$$|J_c M_c s m_s \mathbf{p}\rangle = \sum_{lmjm_jJM} \langle J_c M_c j m_j | JM\rangle \langle lms m_s | jm_j\rangle Y^*_{lm}(\mathbf{\Omega}_e) |J_c (ls) j : JM\mathbf{p}\rangle, \qquad (3.2)$$

where standard notations for angular momenta have been used. In this expansion the first two factors are Clebsch-Gordan coefficients, the angular dependence is included in the spherical harmonics $Y^*_{lm}(\mathbf{\Omega}_e)$, and the radial and energy dependence are included in the final factor, which is the projection of the final state over a component with defined angular momenta.

Using the partial wave expansion (3.2), together with the relation between density matrices for initial and final states through the time evolution operator: $\rho^f = U^\dagger \rho^i U$, it is possible to expand the cross section (3.1) as a weighted sum of elements such as

$$\begin{aligned} & \sum_{J''M''J'''M'''} \langle J_c M_c j' m'_j : J'M' | U | J''M''\rangle \\ \times \quad & \langle J_c M_c j m_j : JM | U | J'''M'''\rangle^* \langle J''M'' | \rho^i | J'''M'''\rangle. \end{aligned} \qquad (3.3)$$

In the case of VUV photoionization the matrix elements of the time evolution operator in the above equation can be simplified by assuming the dipole approximation. The great strength of this approximation is that the dipole operator reduces the infinite expansion (3.2) to a limited number of components. In addition, the dependence of the dipole elements on the magnetic quantum numbers are factorized using the Wigner-Eckart theorem, that introduces the "reduced" matrix elements:

$$D_{lj} \equiv \langle J_c (ls) j : J \| \mathbf{D} \| J\rangle, \qquad (3.4)$$

where the dipole operator is

$$\mathbf{D} \equiv \sum_n \mathbf{r}_n. \qquad (3.5)$$

It will be of advantage in the following to replace the density matrix in (3.1) with the statistical tensor ρ_{Kq}, that according to references [1], [2], is defined as:

$$\rho_{Kq}(J, J') \equiv \sum_{MM'} (-1)^{J'-M'} \langle JMJ' - M' | Kq\rangle \langle JM | \rho | J'M'\rangle. \qquad (3.6)$$

The reason for this substitution is that because of its tensorial nature, ρ_{Kq} fully exploits the spherical symmetry of the problem and makes further calculation easier.

The statistical tensor of the ground state of a closed shell atom and an incident photon corresponds to the statistical tensor of the photon; with the quantization axis along the radiation beam the statistical tensor of the photon has the following explicit form [2]:

$$\begin{array}{lll} \rho^{\gamma}_{00} = 1/\sqrt{3} & \rho^{\gamma}_{10} = 0 & \rho^{\gamma}_{1\pm1} = \mp S_3/\sqrt{2} \\ \rho^{\gamma}_{22} = iS_2/2 & \rho^{\gamma}_{2\pm2} = (1 - S_1)/4 & \rho^{\gamma}_{20} = -(1 + S_1)/2\sqrt{6}, \end{array} \tag{3.7}$$

where S_1 and S_2 are the degrees of linear polarization along the x and y axis, and S_3 is the degree of circular polarization.

At this point the solution of the photoionization problem is a straightforward application of the above equations and of the Wigner-Eckart theorem, together with standard Clebsh-Gordan and nj term algebra. The angular distribution of photoelectron with arbitrarily polarized light is expressed as follows [3]-[5]:

$$\begin{aligned} \frac{d\sigma}{d\mathbf{\Omega}_e} = \quad & \sum i^{l-l'} \hat{l}\hat{l}'\hat{j}\hat{j}'(-1)^{2j+j'+1-K+l'-J_c} D_{lj} D^*_{l'j'} \rho^i_{2q'} Y_{LM}(\mathbf{\Omega}_e) \\ & \times \langle l0l'0|K0\rangle \langle LMK - q|2q'\rangle \begin{Bmatrix} j & j' & 2 \\ 1 & 1 & J_c \end{Bmatrix} \begin{Bmatrix} l & 1/2 & j \\ l' & 1/2 & j' \\ L & K & 2 \end{Bmatrix}, \end{aligned} \tag{3.8}$$

with the sum being over all the indices apart from J_c; the factors with the curly brackets are $6j$ and $9j$ symbols.

In case of photoemission in the plane perpendicular to the photon beam, called in the following perpendicular plane, the angular distribution (3.8) assumes the following form:

$$\frac{d\sigma}{d\theta_e} = \frac{\sigma_0}{4\pi}\left[1 + S_1 \frac{\beta_e}{4}(3\cos 2\theta_e + 1)\right], \tag{3.9}$$

where σ_0 is the integrated photoionization cross section:

$$\sigma_0 = \frac{4\pi^2}{3}\alpha E_\gamma \sum_{lj} |D_{lj}|^2, \tag{3.10}$$

with α the fine structure constant, E_γ the energy of the incident photons expressed in atomic units, and θ_e is the angle between the direction of emission and the axis of major linear polarization. The relative distribution (3.9) is controlled only by the parameter β_e,

that can be extracted experimentally by observing electrons emitted at two angles. For photoionization from a $p_{3/2}$ orbital, that is the case that is interesting in this thesis, the asymmetry parameter is:

$$\beta_e = \frac{2}{5}\left[\frac{-2|D_{3/2}|^2 + 2|D_{5/2}|^2 + 3Re(D_{3/2}D^*_{5/2})}{|D_{1/2}|^2 + |D_{3/2}|^2 + |D_{5/2}|^2} - \frac{\sqrt{5}Re(D_{1/2}D^*_{3/2}) + 3\sqrt{5}Re(D_{1/2}D^*_{5/2})}{|D_{1/2}|^2 + |D_{3/2}|^2 + |D_{5/2}|^2}\right]. \tag{3.11}$$

3.3 Angular distribution of Auger electrons

The angular distribution of Auger electrons is obtained using arguments similar to those used for the angular distribution of photoelectrons. The initial state is the ion with an inner shell vacancy, with total angular momentum J_c; as a result of photoemission this state can be aligned and/or oriented. The degree of alignment depends on the photoionization process and on the light polarization, and is described by the statistical tensor. The equations for the angular distribution of Auger electrons contain the matrix elements of both the dipole $\mathbf{D}$ and of the Coulomb interaction V; the former because it characterizes the alignment of the intermediate state, and the latter because it controls the Auger decay. The angular distribution of Auger electrons has the following form [6]:

$$\frac{d\sigma}{d\mathbf{\Omega}_A} = \frac{\sigma_0\omega_A}{4\pi}\left[1 + \frac{\alpha_2}{\sigma_0}\sqrt{\frac{4\pi}{5}}\sum_q \rho_{2q}Y_{2q}(\mathbf{\Omega}_A)\right], \tag{3.12}$$

where σ_0 is the photoionization cross section as in equation (3.10), ω_A is the Auger yield and $\mathbf{\Omega}_A$ is the direction of emission. The statistical tensor of the ion ρ_{2q} depends on the light polarization ρ^γ_{2q} and on the photoemission dipole matrix elements D_{lj} [2]:

$$\rho_{2q} = 3\left(\sum_{lj}|D_{lj}|^2\right)^{-1}\rho^\gamma_{2q}\sum_{lj}(-1)^{j+J_c+1}\left\{\begin{array}{ccc} 1 & J_c & j \\ J_c & 1 & 2 \end{array}\right\}D_{lj}D^*_{lj}. \tag{3.13}$$

The coefficient α_2 depends on the matrix elements of the Coulomb operator and on the angular momenta J_c and J_f of intermediate and final states:

$$\alpha_2 = \left(\sum_{lj}|\langle J_f(ls)j : J_c\|V\|J_c\rangle|^2\right)^{-1}\hat{J}_c(-1)^{J+J_f-s} \times \sum_{ll'jj'}\hat{l}\hat{l}'\hat{j}\hat{j}'\langle l0l'0|20\rangle\left\{\begin{array}{ccc} J_c & j & J_f \\ j' & J_c & 2 \end{array}\right\}\left\{\begin{array}{ccc} l & j & s \\ j' & l' & 2 \end{array}\right\}$$

$$\times \quad \langle J_f(ls)j : J_c \| V \| J_c \rangle \langle J_f(l's)j' : J_c \| V \| J_c \rangle^*. \tag{3.14}$$

The following notation has been used:

$$\hat{J} \equiv \sqrt{2J+1} \tag{3.15}$$

The case of a ^1S doubly charged state is of particular interest because only one partial wave is allowed for the Auger electron; as a results α_2 assumes the following simplified form:

$$\alpha_2 = (-1)^{J_c+s} \hat{J}_c \hat{l}^2 \langle l0l0|20\rangle \begin{Bmatrix} J_c & J_c & 2 \\ l & l & s \end{Bmatrix}. \tag{3.16}$$

In this case the angular distribution does not depend on the matrix elements of the Auger decay, but only on the photoionization process.

In the perpendicular plane equation (3.12) can be simplified as follows:

$$\frac{d\sigma}{d\theta_A} = \frac{\sigma_0 \omega_A}{4\pi} \left[1 + S_1 \frac{\beta_A}{4} (3\cos 2\theta_A + 1) \right]. \tag{3.17}$$

Apart from the presence of β_A rather than β_e, and the presence of ω_A, equation (3.17) is identical to equation (3.9).

For a $p_{3/2}$ hole decaying to a ^1S state, that is the case of interest in this work, the anisotropy parameter of the Auger electron has the following form:

$$\beta_A = \frac{|D_{1/2}|^2 - 0.8|D_{3/2}|^2 + 0.2|D_{5/2}|^2}{|D_{1/2}|^2 + |D_{3/2}|^2 + |D_{5/2}|^2}. \tag{3.18}$$

3.4 The lsj coupling approximation

If the spin-orbit interaction in the intermediate ionic state is weak, the total spin and orbital angular momentum can be considered good quantum numbers and the state is labeled using the values of the quantum numbers L, S, and J. This is called LSJ approximation. LS coupling is not neglected, but its only effect is considered to be the splitting of the multiplet. If ls coupling is neglected for the continuum electron, the radial parts of the components of its wavefunction become independent of j. This is the lsj approximation; in this case the reduced matrix elements (3.4) of the dipole operator can be simplified as follows [2], [5]:

$$\langle (L_c S_c) J_c (ls) j : J = 1 \| D \| J = 0 \rangle = \frac{(-1)^{L_c+j+s}}{\sqrt{2}} \hat{j} \hat{J}_c$$

$$\times \left\{ \begin{array}{ccc} l & j & s \\ J_c & L_c & 1 \end{array} \right\} \langle Ll : J = 1 || D || J = 0 \rangle. \tag{3.19}$$

This approximation reduces the number of the dipole matrix elements for $p_{3/2}$ photoionization to the following:

$$D_{1/2} = -\frac{\sqrt{2}}{\sqrt{3}} D_s, \qquad D_{3/2} = -\frac{\sqrt{2}}{3\sqrt{5}} D_d, \qquad D_{5/2} = -\frac{\sqrt{2}}{\sqrt{5}} D_d. \tag{3.20}$$

Note that if this approximation is valid then $D_{3/2}/D_{5/3} = 1/3$. If it is possible to extract all the elements D_j this ratio can be used to determined whether the lsj approximation is valid or not. This approach has been attempted in the course of the present work; the results are presented in chapter 8.

For p photoionization followed by decay to a ^1S doubly charged state, the lsj approximations simplify the angular distribution parameters to the following:

$$\beta_e = \frac{|D_d|^2 - 2\sqrt{2}|D_s D_d| \cos \Delta_{sd}}{|D_s|^2 + |D_d|^2}, \qquad \beta_A = \frac{|D_s|^2 + 0.1|D_d|^2}{|D_s|^2 + |D_d|^2}. \tag{3.21}$$

3.5 Two-step double photoionization: angular correlation between the photoelectron and the associated Auger electron

The previous equations are valid if the Auger electron and the photoelectron are detected independently. If they are detected in coincidence the coincidence angular pattern reflects their angular correlation, in this case the differential cross section assumes the following form [7]:

$$\frac{d\sigma}{d\mathbf{\Omega}_e d\mathbf{\Omega}_A} = \frac{\sigma_0 \omega_A}{4\pi} \left[1 + \frac{\alpha_2}{\sigma_0} \sqrt{\frac{4\pi}{5}} \sum_q \rho_{2q}(\mathbf{\Omega}_e) Y_{2q}(\mathbf{\Omega}_A) \right]. \tag{3.22}$$

The difference between the distribution (3.22) and the non-coincidence Auger angular distribution (3.12), is that in equation (3.22) the statistical tensor of the ion ρ_{2q} contains also information on the direction of the photoelectron. Equation (3.13) is now replaced by:

$$\rho_{2q}(\mathbf{\Omega}_e) = \sum_{k'q'q''} \frac{3}{\sqrt{4\pi}\sqrt{5}} \langle 2qK'q' | 2q'' \rangle Y_{LM}(\mathbf{\Omega}_e) \rho^{\gamma}_{2q''}$$

$$\times \sum_{l'l''j'j''} (-1)^{j''+1/2} \hat{l}'\hat{l}''\hat{j}'\hat{j}'' \langle l'0l''0|L0\rangle \begin{Bmatrix} j' & l' & 1/2 \\ l'' & j'' & L \end{Bmatrix}$$
$$\times \begin{Bmatrix} J_c & j' & 1 \\ J_c & j'' & 1 \\ 2 & L & 2 \end{Bmatrix} D_{l'j'} D^*_{l''j''}. \tag{3.23}$$

Kabachnik and Schmidt in 1995 [8] studied theoretically the circular dichroism for the angular correlation between the $3p_{3/2}$ photoelectron and the $M_3N_1N_1$ Auger electron of Ca, assuming the lsj approximation and using the relativistic random phase approximation with exchange (RRPAE). Kabachnik and Ueda in 1995 [9] studied the $3p_{3/2}$ photoionization of Ca followed by decay to a ^1S doubly charged ion. In this thesis the general equations of reference [9] have been restricted to the case of the Auger electron being emitted in the direction of the major polarization; with this restriction the angular correlation (3.22) assumes the following form:

$$\frac{d\sigma}{d\theta_e} = A_0 + A_2 \cos(2\theta_e) + A_4 \cos(4\theta_e), \tag{3.24}$$

where

$$A_i = A_{i0} + (1 - S_1)A_{0i} \tag{3.25}$$

with

$$\begin{aligned} A_{00} &= \frac{1}{\sqrt{3}}B_{000} - \frac{\sqrt{2}}{4\sqrt{3}}B_{202} + \sqrt{\frac{2}{3}}B_{022} \\ &- \frac{1}{4\sqrt{15}}B_{220} - \frac{1}{2\sqrt{21}}B_{222} + \frac{3\sqrt{3}}{32\sqrt{7}}B_{422}, \end{aligned} \tag{3.26}$$

$$A_{20} = -\sqrt{\frac{3}{8}}B_{202} - \frac{\sqrt{3}}{4\sqrt{5}}B_{220} - \frac{\sqrt{3}}{2\sqrt{7}}B_{222} + \frac{5}{8\sqrt{21}}B_{422}, \tag{3.27}$$

$$A_{40} = \frac{5\sqrt{7}}{32\sqrt{3}}B_{422}, \tag{3.28}$$

and

$$A_{01} = -\sqrt{\frac{3}{8}}B_{022} + \frac{\sqrt{3}}{4\sqrt{7}}B_{222} - \frac{3}{32\sqrt{21}}B_{422}, \tag{3.29}$$

$$A_{21} = \sqrt{\frac{3}{8}}B_{202} + \frac{3}{4\sqrt{7}}B_{222} - \frac{5}{16\sqrt{21}}B_{422}, \tag{3.30}$$

$$A_{41} = -\frac{5\sqrt{7}}{4\sqrt{3}}B_{422}. \tag{3.31}$$

The expressions for the elements $B_{k_1 k_2 k_3}$ in terms of the elements $D_{1/2}$, $D_{3/2}$, and $D_{5/2}$ are in reference [9] and are not reported here.

In this work the initial plan was to detect the photoelectron in the direction of the major linear polarization, and the Auger electron in the perpendicular plane at variable angle, for experimental reasons. However, this is a trivial case because the dependence on the dipole matrix elements is cancelled from the angular correlation .

3.6 Complete photoionization experiments

Photoionization experiments that, within a selected theoretical frame, allow all the matrix elements such as (3.4) to be extracted are called complete.

The first complete experiment for photoionization was reported by Heinzmann in 1980 [10]; measurements of the angular distribution and spin polarization of photoelectrons from the $5p$ shell of Xe allowed the dipole matrix elements for that process to be extracted.

In the work described in this thesis the parameter β_e, β_A, A_2/A_0 and A_4/A_0 have been measured for $3p_{3/2}$ and $4p_{3/2}$ photoionization of Ca and Sr, followed by $M_3N_1N_1$ and $N_3O_1O_1$ decay respectively. The equations obtained in the previous sections allow these parameters to be expressed in terms of the dipole matrix elements. If these parameters are measured the task of the analysis is to extract the dipole elements from the measured quantities by inverting these equations.

In this context two-step DPI makes inner-shell photoionization a complete experiment; the type of information that can be extracted from such measurements is very much different from that obtained from studies of direct DPI. Such an approach to complete experiment was taken by Kämmerling and Schmidt in 1991 [11], and in 1997 [12] for $4d_{5/2}$ photoionization of Xe followed by $N_5O_{23}O_{23}$ decay. A similar treatment is presented here for atomic Ca and Sr. Non coincident angular distribution measurements of the photoelectron and the associated Auger electron allowed Kämmerling *et al.* in 1992 [13] and Lörch *et al.* in 1999 [14] (see section 8.3.1) to perform complete experiments for $2p$ photoionization of Mg and $3p$ photoionization of Ca respectively.
For $p_{1/2}$ photoionization, such an attempt to perform a complete experiment would fail because a state with $J_c = 1/2$ cannot be aligned, and the corresponding Auger and coincidence parameters do not contain the D_j elements.

Measurements of angular distributions and angular correlation that are on a relative scale contain information on the relative amplitudes of the dipole matrix elements, but not on their absolute values. The absolute values of these elements can be obtained from

equation (3.10) if absolute cross sections are known. Absolute cross sections could not be measured in this work and are not available, this makes impossible to obtain the absolute value of each dipole amplitude.

The measurements and their analysis are presented in detail in chapter 8.

3.7 Random phase approximation with exchange. Calculations of dipole matrix elements

Dipole matrix elements for $3p$ photoionization of Ca have been calculated using the RPAE by M Ya Amusia and LV Chernysheva [15] for comparison with the values extracted from the present experimental measurements. The basis of the calculations has been described in details in reference [16]. For this calculations the lsj approximation was assumed. The starting point of the RPAE is the Hartree-Fock (HF) approximation, where the reduced dipole amplitudes are expressed as

$$D_l \equiv e^{i\delta_l}\langle 3p|d|\epsilon l\rangle \tag{3.32}$$

with

$$\langle 3p|d|\epsilon l\rangle \equiv \int_0^\infty R_{np}(r) r R_{\epsilon l}(r) r^2 dr, \tag{3.33}$$

where δ_l are the real elastic scattering phase of the photoelectron wave and the integral in (3.32) is the amplitude of the matrix element, determined as a one-dimensional integral over the radial parts of the HF bound and continuous wave functions $R_{3p}(r)$ and $R_{\epsilon l}(r)$. The dipole operator is represented by its radial part r. The functions $R_{np}(r)$ and $R_{\epsilon l}(r)$ are obtained by solving the radial HF equations. The phase shifts δ_l are determined by the asymptotic limits of the $R_{\epsilon l}(r)$ functions:

$$R_{\epsilon s/d}(r) \sim \frac{1}{r\sqrt{p}} \sin\left(pr + \frac{1}{p}\log(2pr) - \frac{\pi l}{2} + \delta_l\right). \tag{3.34}$$

Here $p = \sqrt{\epsilon}$, where ϵ is the kinetic energy of the photoelectron in atomic units: $e = m = \hbar = 1$.

The HF approximation is inadequate for calculations of photoionization cross sections and other characteristic of the photoabsorption process where many-electron correlation must be included. For this reason the RPAE method is preferred, since it takes into accounts the dynamic polarization of the atom by the photon as it is absorbed, followed by ionization. In the RPAE method the amplitudes D_l are determined by solving numerically an integral

equation, which in our case is:

$$\langle 3p|D(\omega)|\epsilon_{s,d}\rangle = \langle 3p|d|\epsilon_{s,d}\rangle + \left(\sum\!\!\!\!\!\!\int_{n>F,\ j\leq F} - \sum\!\!\!\!\!\!\int_{n\leq F,\ j>F}\right) \frac{\langle j|D(\omega)|n\rangle\langle n;3p|U|j;\epsilon s,d\rangle}{\omega - \epsilon_n + \epsilon_j + i\eta(1-2n_n)}. \tag{3.35}$$

Here $\langle n;3p|U|j;\epsilon s,d\rangle \equiv \langle n;3p|V|j;\epsilon s,d\rangle - \langle n;3p|V|j;\epsilon d,s\rangle$; V is the Coulomb interelectron interaction; the summation is performed over occupied ($\leq F$) and vacant ($\geq F$) states; ϵ_n and ϵ_j are HF energies. Vacant states include the continuous spectrum over which the integration is performed, with $\eta \to 0$. The calculation for $3p$ photoionization of Ca includes the occupied $4s$, $3p$, and $3s$ subshells and the transitions $\epsilon p \leftarrow 4s$, $\epsilon(s,d) \leftarrow 3p$, and $\epsilon p \leftarrow 3s$. The inner $2p$, $2s$, and $1s$ levels need not to be considered in the energy region of interest. In reference [15] equation (3.35) was solved numerically using the code described by Amusia [17]. In solving this equation the imaginary parts $e^{i\delta_l}$ were eliminated from the $\langle 3p|d|\epsilon s,d\rangle$ matrix elements, even so the solutions of equation (3.35) are still complex because of the presence of $i\eta$ in the denominator and therefore the amplitudes D_l have been written in the form

$$D_l = |D_l|\, e^{i(\delta_l+\lambda_l-l\pi/2)}, \tag{3.36}$$

λ_l is the additional multichannel phase shift due to mixed configurations. The total phase shift Δ, which can be measured experimentally, is then given by

$$\Delta = \lambda_s + \delta_s - \lambda_d - \delta_d - \pi. \tag{3.37}$$

3.8 Direct double photoionization

3.8.1 Selection rules

Selection rules for differential DPI process have been obtained by Berakdar and Klar in 1992 [18] and by Maulbetsch and Briggs in 1995 [19] in the LS scheme. Their derivations are not reported here, and only the selection rules most relevant to this work are summarized in this section. These selection rules are valid for initial neutral and final doubly charged states both of ^1S symmetry.

The TDCS is independent of the degree of linear polarization, S_3, when the two electrons have the same kinetic energy [18]. This is good because in the VUV-XUV range S_3 is difficult to measure.

Antiparallel emission of the two electrons is forbidden if the two electrons have the same kinetic energy [19]. This is due to the Pauli principle, and is valid for odd values of $(\pi + S)$, where π and S are the exchange symmetry (e/o) and the spin of the two electron continuum respectively .

Parallel emission of the two electrons is forbidden when they have the same kinetic energy [19]. This is due to the Coulomb electron-electron repulsion.

3.8.2 Parameterization of TDCS by expansion in continuum electronic configurations

From section 3.5 it is clear that the coincidence measurements for the two-step DPI can be parameterized in terms of dipole and Coulomb matrix elements. This parameterization relies on the factorization of the DPI into two steps, and takes advantage of the selection rules for the dipole and Coulomb operators that reduce the infinite channels in the expansion (3.2) to a limited number. For direct DPI a similar parametrization was proposed by Malegat *et al.* in 1997 [20]. In this case, because of the simultaneous presence of two electrons in the continuum, the partial wave expansion for the final state Φ_f contains an infinite number of electronic configurations:

$$\Phi_f = \sum_{l_1 l_2 m_1 m_2} \langle l_1 m_1 l_2 m_2 | 1 m_1 + m_2 \rangle \Phi_c Y_{l_1 m_1}(\mathbf{\Omega_1}) Y_{l_2 m_2}(\mathbf{\Omega_2}) R^{u/g}_{l_1 l_2}(r_1, r_2). \tag{3.38}$$

In equation (3.38) l_1 and l_2 are the orbital angular momenta of the individual electrons and m_i are their projections, Φ_c is the wavefunction of the residual ion, of ^1S symmetry, the Clebsch-Gordan coefficients ensure that the overall symmetry is P, the spherical harmonics and the $R^{u/g}$ terms represent the angular and radial part of the two-electron continuum with gerade/ungerade symmetry with respect to the exchange of the two electrons. Such an expansion allows the TDCS to be expanded in the following form:

$$TDCS = \frac{1 + S_1}{2} \sigma_{pol} + \frac{1 - S_1}{2} \sigma_{unpol}, \tag{3.39}$$

where it is assumed $S_2 = S_3 = 0$. The contributions from polarized and unpolarized radiation are:

$$\frac{\sigma_{pol}}{2\sigma_0} = |(\cos\theta_1 + \cos\theta_2) M^g - (\cos\theta_1 - \cos\theta_2) M^u|^2 \tag{3.40}$$

and

$$\frac{\sigma_{unpol}}{\sigma_0} = (\sin\theta_1 + \sin\theta_2)^2 |M^g|^2 + (\sin\theta_1 - \sin\theta_2)^2 |M^u|^2, \tag{3.41}$$

with

$$\sigma_0 = 8\pi^2 \alpha E_\gamma \sqrt{E_1 E_2}, \tag{3.42}$$

where α is the fine structure constant, E_γ is the energy of the incident photon, and E_1 and E_2 are the asymptotic energies of the ejected electrons, all expressed in atomic units.

The gerade/ungerade amplitudes are defined in terms of the possible electronic configurations:

$$\begin{aligned} M^{g/u} = & \sum_{l=1}^{\infty} (-1)^l \sqrt{\tfrac{3(2l-2)!}{4(2l+1)!}} \langle \Phi_i \| D \| \Phi_c \left(R^{g/u}_{(l-1)l} \pm R^{u/g}_{l(l-1)} \right) \rangle \\ & \times \left[l P_{l-1}(\cos\theta_{12}) + (\cos\theta_{12} \mp 1) P'_{l-1}(\cos\theta_{12}) \right] \end{aligned} \tag{3.43}$$

where P_l are Legendre polynomials. Note that in expression (3.39) the second term does not provide additional information to the first and vice versa as they depend on the same set of parameters (3.43).

If direct DPI proceeds through an intermediate resonant state of the neutral, as in the case of the work of this thesis, the parameterization (3.39)-(3.43) is still valid provided that the dipole operator D is replaced by an appropriate linear combination of D and $V|R\rangle(h\nu - E_R + i\Gamma)^{-1}\langle R|D$, where V is the Coulomb operator, R is the resonant state, E_R its excitation energy and Gamma its natural width.

The partial wave decomposition (3.38) allowed to obtained the parametrization (3.39)-(3.43) but the price that had to be paid is an infinite numbers of parameters.

It is tempting to hope that only a limited number of configurations $l_1 l_2$ are enough to describe the experimentally measured TDCS, in this case the infinite sum in (3.38) and (3.43) could be truncated to a finite l_{max}, and a parameterization such as (3.39)-(3.43) would be very useful. However, the more structure is present in the TDCS, the higher the expected value of l_{max} in (3.39) and (3.43). This leads to a higher number of parameters, making their extraction more complicated and their meaning less transparent.
Such an attempt to reproduce the measured TDCS has been tried with the parameterization (3.39)-(3.43), the results are reported in detail in chapter 7.

3.8.3 Parameterization of TDCS with an angular and a correlation factor

The expansion (3.39)-(3.43) can be rewritten in the following general form:

$$\frac{\sigma}{2N} = \left\{ \frac{1+S_1}{2} |(\cos\theta_1 + \cos\theta_2)A_g - (\cos\theta_1 - \cos\theta_2)A_u|^2 + \frac{1-S_1}{2} \left[(1+\cos\theta_{12})|A_g|^2 + (1-\cos\theta_{12})|A_u|^2\right] \right\} \times C(E_1, E_2, \theta_{12}). \quad (3.44)$$

The factor within the curly brackets in (3.44) is normally called the angular factor. As above, the second term in the angular factor does not contain additional information but it is nevertheless included in (3.44) because it will be used in chapter 7. The factor $C(E_1, E_2, \theta_{12})$ is conventionally called the correlation factor and is often modeled by a smooth distribution with a single peak at $\theta_{12} = 180°$, where the angular factor is zero, that tends to favor emission of the two electrons in opposite direction.

In the work of Huetz in 1991 [21], and in subsequent work, a gaussian shape for $C(E_1, E_2, \theta_{12})$ was predicted on the basis of the Wannier theory [22], with full width at half maximum (FWHM) $\propto E_{exc}^{1/4}$. E_{exc} here is the excess energy. This model gained popularity and has often been applied to compare the best-fit FWHM to the $E_{exc}^{1/4}$ trend predicted from the Wannier theory, reproducing well the measured TDCS in He.

A modification to the previous model comes from the expansion for the final state with three Coulomb wavefunctions used by Maulbetsch and Briggs [23]. This leads to the following representation of the correlation factor:

$$C(E_1, E_2, \theta_{12}) = \frac{2\pi\alpha_{12}}{exp(2\pi\alpha_{12}) - 1}, \quad (3.45)$$

with

$$\alpha_{12} = \frac{1}{|\mathbf{p}_1 - \mathbf{p}_2|}, \quad (3.46)$$

where $\mathbf{p}_i$ are asymptotic linear momenta of the ejected electrons in atomic units. The TDCS predicted by this model is very similar to the previous and it always reproduced the measured TDCS in He very well. Both models gained popularity because: 1) they reproduce the measured TDCS in He well, 2) they have a limited number of parameters, that can be extracted from measurements and calculated without using an expensive procedure, and 3) they allow a very simple interpretation of the results in term of the Coulomb correlation.

These models with a smooth singly peaked correlation factor fail to reproduce the measured TDCS if the latter shows more than a single pair of lobes. This point will be addressed in chapter 7.

Further information on direct DPI of He can be found in a recent review by Briggs and Schmidt [24].

Bibliography

[1] U Fano, *Physical Review*, **90** 577-579 (1953).
Angular Correlation Methods in Gamma-Ray Spectroscopy.
A Ferguson, North Holland Publishing Company, Amsterdam (1965).
Density Matrix Theory and Applications.
K Blum, Plenum, New York (1981).

[2] Polarization and Correlation Phenomena in Atomic Collisions.
NM Kabachnik, Cambridge University Press, in press.

[3] VL Jacobs, *Journal of Physics B: Atomic, Molecular and Optical Physics*, **5** 2257-2271 (1972).

[4] N Kabachnik and IP Sazhina, *Journal of Physics B: Atomic, Molecular and Optical Physics*, **9** 1681-1697 (1976).

[5] K-N Huang, *Physical Review A*, **22** 223-239 (1980).

[6] N Kabachnik and IP Sazhina, *Journal of Physics B: Atomic, Molecular and Optical Physics*, **17** 1335-1342 (1984).

[7] N Kabachnik, *Journal of Physics B: Atomic, Molecular and Optical Physics*, **25** L389-L393 (1992).

[8] NM Kabachnik and V Schmidt, *Journal of Physics B: Atomic, Molecular and Optical Physics*, **28** 233-243 (1995).

[9] N Kabachnik and K Ueda, *Journal of Physics B: Atomic, Molecular and Optical Physics*, **28** 5013-5014 (1995).

[10] U Heinzmann, *Journal of Physics B: Atomic, Molecular and Optical Physics*, **13** 4353-4366 (1980).
U Heinzmann, *Journal of Physics B: Atomic, Molecular and Optical Physics*, **13** 4367-4381 (1980).

[11] B Kämmerling and V Schmidt, *Physical Review Letters*, **67** 1848-1851 (1991).

[12] B Kämmerling and V Schmidt, *Journal of Physics B: Atomic, Molecular and Optical Physics*, **26** 1141-1161 (1993).
SJ Schaphorst, Q Qian, P van Kampen, N Scherer and V Schmidt, *Journal of Physics B: Atomic, Molecular and Optical Physics*, **30** 4003-4017 (1997).

[13] B Kammerling, A Hausmann, J Lauger and V Schmidt, *Journal of Physics B: Atomic, Molecular and Optical Physics*, **25** 4773-4779 (1992).

[14] H Lörch, JM Bizeau, N Scherer, S Diehl, D Cubaynes, O Zerouni, FJ Wuilleumier, V Schmidt and RW Johnson, *Journal of Physics B: Atomic, Molecular and Optical Physics*, **32** 2215-2226 (1999).

[15] A De Fanis, JB West, KJ Ross, K Ueda, H-J Beyer, M Ya Amusia and LV Chernisheva, *Journal of Physics B: Atomic, Molecular and Optical Physics*, **32** 5739-5749 (1999).

[16] Atomic Photoeffect.
M Ya Amusia, Plenum Press, New York and London, (1990).

[17] Computation of Atomic Processes.
M Ya Amusia and LV Chernysheva, IoP Publishing, Bristol and Philadelphia (1990).

[18] J Berakdar and H Klar, *Physical Review Letters*, **69** 1175-1177 (1992).

[19] F Maulbetsch and JS Briggs, *Journal of Physics B: Atomic, Molecular and Optical Physics*, **28** 551-564 (1995).

[20] L Malegat, P Selles and A Huetz, *Journal of Physics B: Atomic, Molecular and Optical Physics*, **30** 251-261 (1997).
L Malegat, P Selles, P Lablanquie, J Mazeau and A Huetz, *Journal of Physics B: Atomic, Molecular and Optical Physics*, **30** 263-276 (1997).

[21] A Huetz, P Selles, D Waymel and J Mazeau, *Journal of Physics B: Atomic, Molecular and Optical Physics*, **24** 1917-1933 (1991).

[22] HH Wannier, *Physical Review*, **90** 817-825 (1953).

[23] F Maulbetsch and JS Briggs, *Journal of Physics B: Atomic, Molecular and Optical Physics*, **26** 1679-1696 (1993).
F Maulbetsch and JS Briggs, *Journal of Physics B: Atomic, Molecular and Optical*

Physics, **26** L647-L652 (1993).

F Maulbetsch and JS Briggs, *Journal of Physics B: Atomic, Molecular and Optical Physics*, **27** 4095-4104 (1994).

F Maulbetsch and JS Briggs, *Journal of Physics B: Atomic, Molecular and Optical Physics*, **28** L341-L347 (1995).

[24] JS Briggs and V Schmidt, *Journal of Physics B: Atomic, Molecular and Optical Physics*, **33** R1-R48 (2000).

Chapter 4

Background to the study of triple differential cross sections for atomic double photoionization

4.1 Introduction

This chapter gives an overview of previous work on triple differential cross section (TDCS) studies of atomic double photoionization (DPI). Only work on non resonant direct DPI is considered here.

4.2 Helium

To date most of the studies of DPI have been focused on He; helium is the only system where DPI can happen only as a direct process: both resonant and two-step DPI are energetically forbidden. The absence of electronic structure in the doubly charged ion makes the electronic correlation in the initial state and in the final continuum the only origin of the DPI.

For these reasons He is the system that best suits experiments and theories aimed at understanding the physics of three bodies in Coulomb interaction. For the work of this thesis DPI of He is interesting because, within the single electronic configuration picture, the two outermost electrons that are ionized in Ca and Sr are also in an s^2 shell around a closed subshell. Because initial and final states for valence DPI of Ca and Sr have the same symmetry as He, the same selection rules apply.

The first experimental work on DPI of He was reported by Schwarzkopf *et al.* in 1993

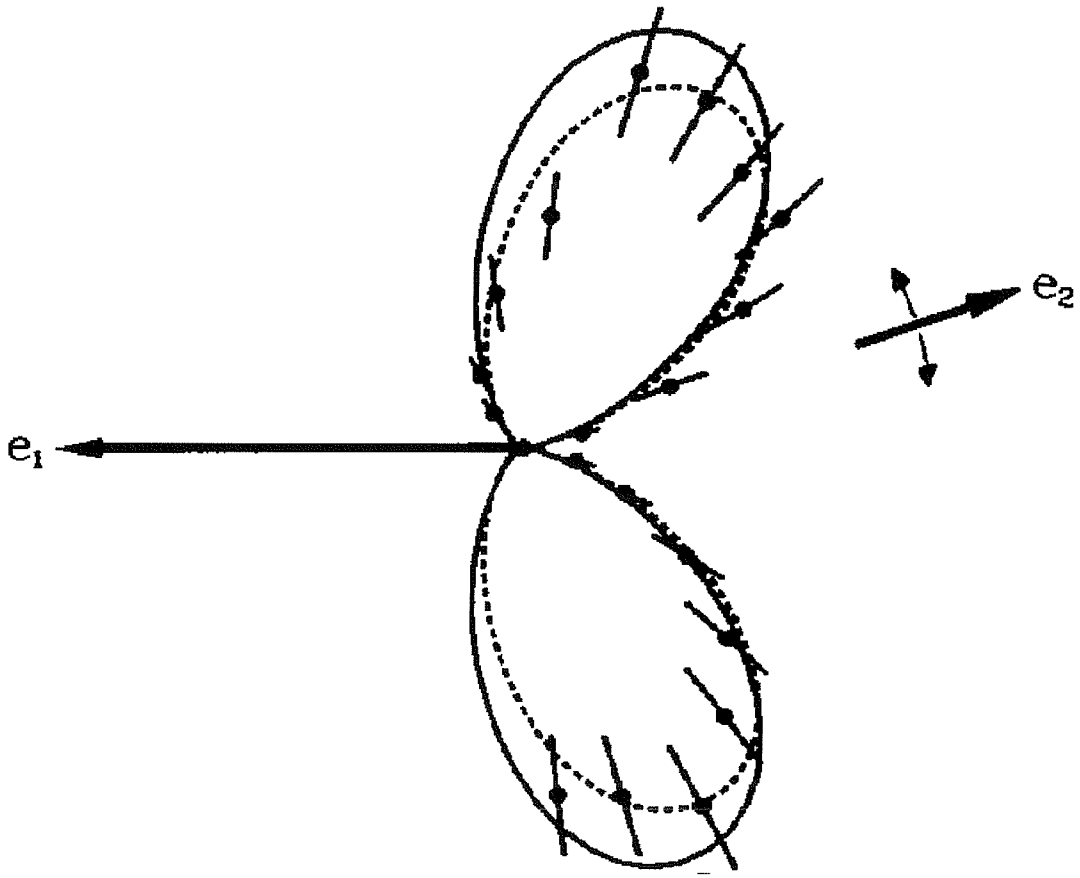

Figure 4.1: TDCS for DPI of He measured by Schwarzkopf *et al.*, with $h\nu = 79\,eV$, $E_1 = E_2 = 10\,eV$.

[1]. Electrons were analysed in kinetic energy and direction of emission and detected in coincidence. Elliptically polarized radiation produced by the BESSY electron synchrotron was tuned to $h\nu = 99\,eV$, $20\,eV$ above threshold. Measurements were taken in the perpendicular geometry: both electrons were emitted perpendicularly to the light beam, with one electron parallel to the electric field: $\theta_1 = 0^0$, and the other electron in the angular range $90^0 \leq \theta_2 \leq 270^o$. Measurements were initially taken for the equal energy sharing case: $E_1 = E_2 = 10\,eV$ [1], and subsequently also for different energy sharing: $E_1 = 5\,eV$, $E_2 = 47.9\,eV$ [2]. The results for the symmetric energy sharing are shown in figure 4.1; the full and broken curves are three-body Coulomb wavefunctions (3C) calculation of Maulbetsch and Briggs [3] and fit with the model of Huetz *et al.* [4] (see later) respectively.

The experimental results of Schwarzkopf *et al.* [1] showed differences from the theoretical predictions of Le Rouzo and Dal Cappello [5], who, in 1991 computed the TDCS using a multiconfigurational Hartree-Fock (HF) calculation for the initial state and Coulomb waves for the two-electron continuum, that neglect the electron correlation in the continuum. The results of Schwarzkopf *et al.* [1], [2] were also different from the calculations of Huetz *et al.* [4], that in 1991 applied the Wannier theory [6] to calculate the TDCS for DPI of He near threshold. The Wannier theory predicted the following general parame-

terization of the TDCS in the perpendicular plane:

$$TDCS \equiv \frac{d^3\sigma}{dE_1 d\theta_1 \theta_2} = |A_u(E_1, E_2, \theta_{12})(\cos\theta_1 - \cos\theta_2) + A_g(E_1, E_2, \theta_{12})(\cos\theta_1 + \cos\theta_2)|^2, \quad (4.1)$$

where A_g and A_u, called *gerade* and *ungerade* amplitudes, have to be calculated numerically and are respectively symmetric and antisymmetric with respect to exchange of the energies:

$$\begin{aligned} A_g(E_1, E_2, \theta_{12}) &= A_g(E_2, E_1, \theta_{12}) \\ A_u(E_1, E_2, \theta_{12}) &= -A_u(E_2, E_1, \theta_{12}). \end{aligned} \quad (4.2)$$

In the case of equal energies the *gerade* amplitude, also called the correlation factor $C(1,2)$, was assumed to have a gaussian shape peaked at $\theta_{12} = 180°$:

$$|A_g(E_1, E_2, \theta_{12})|^2 \equiv C(1,2) \propto \exp\left[-\ln 2 \left(\frac{\theta_{12} - 180}{\theta_{fwhm}}\right)^2\right], \quad (4.3)$$

with the width θ_{fwhm} scaling as:

$$\theta_{fwhm} = \Theta_0 E_{exc}^{1/4}, \quad (4.4)$$

and Θ_0 is a fixed parameter. In this case the TDCS of equation (4.1) is parameterized as

$$TDCS \propto (\cos\theta_1 + \cos\theta_2)^2 C(1,2). \quad (4.5)$$

The Wannier theory was expected to be valid near threshold and predicted the following scaling behaviours for A_u and A_g:

$$\begin{aligned} |A_g|^2 &\propto E_{exc}^{n-2}, \\ |A_u|^2 &\propto E_{exc}^{3n-3/2}, \end{aligned} \quad (4.6)$$

with $n = 1.056$. At low excess energy A_g dominates over A_u, as a results the effect of unequal energy sharing should be small. Although the experimental result of Schwarzkopf *et al.* [1] did not agree with the calculations from the Wannier theory, if the width θ_{fwhm} of the $C(1,2)$ distribution was fitted as a free parameter the data points were reproduced by the parameterization (4.1) well. The experimental data points were also reproduced

well by the 3C calculation; further comparison between experiments and theory confirmed the good agreement between the experimental data and the 3C calculations in the cases $E_1 + E_2 = 10 + 10\,eV$, $\theta_1 = 0^o$ and 76^o; $E_1 + E_2 = 5 + 5\,eV$, $\theta = 76^o$ and $E_1 + E_2 = 5 + 47.9\,eV$, $\theta_1 = 76^o$ [3], [7] and [8]. It was noticed that different wavefunctions for the initial state give very similar results; this is particularly interesting because it makes the electron correlation in the continuum the most important contribution to the TDCS.

The TDCS was measured on an absolute scale by Schwarzkopf and Schmidt in 1995 [9] with a similar experimental arrangement to that of their previous work [1], and under the same kinematic conditions. Their measurements showed excellent agreement with the velocity form of the calculation of Maulbetsch and Briggs [3], [7] and [8].

Huetz *et al.* in 1994 [10] and Lablanquie *et al.* in 1995 [11] studied the TDCS near threshold at the Super ACO synchrotron in Paris. The threshold region is believed to be particularly interesting because the TDCS is expected to reveal more pronounced features characteristic of the electron repulsion. The interest in low excess energy is also due to the fact that it allows a more appropriate comparison with the prediction of the Wannier theory. They observed electrons emitted in the plane of the light beam and of the electric field (coplanar geometry), with excess energy as low as $4\,eV$. One electron was analysed in kinetic energy by a toroidal analyser fitted with a position sensitive detector. This analyser collects electrons emitted in different directions. The result of this work was that at the lowest excess energy the TDCS does not show dependence on the energy sharing, in agreement with the *gerade* amplitude being dominant over the *ungerade* term as discussed before. The width of the correlation factor θ_{fwhm} was found to be rather constant, in disagreement with the $E_{exc}^{1/4}$ dependence predicted by the Wannier theory.

The TDCS near threshold was also measured by Dawber *et al.* in 1995 [12] on beam-line 3.3 at the Daresbury SRS. Their apparatus consisted of two electron energy analysers which collected electrons in the perpendicular geometry, with one electron emitted parallel to the electric field. Excess energies of 0.6, 1.0 and $2.0\,eV$ were investigated. They found deviations on the energy dependence of the θ_{fwhm} parameter from the $E_{exc}^{1/4}$ prediction of the Wannier model, and very little change in the TDCS for different conditions of energy sharing.

Viefhaus *et al.* in 1995 [13] studied the DPI of He using three time-of-flight (TOF) spectrometers. The advantage of TOF tubes is that they collect simultaneously electrons with all the possible kinetic energies; however, they have the disadvantage that the synchrotron radiation has to operate in single or double bunch mode, with an overall photon flux lower by at least one order of magnitude. These authors reported a study of the *ungerade* con-

tribution to the TDCS by coincidence detection of electrons emitted in opposite directions in the coplanar geometry, with selected photon energies of 94, 99, 104 and $130\,eV$, and energy sharing from $E_1 + E_2 = 1.5 + 9.5\,eV$ up to $E_1 + E_2 = 45 + 6\,eV$. By using a circularly polarizing multilayer filter they could also study circular dichroism (CD) in DPI. CD in DPI is defined as

$$\Delta(E_1, E_2, \mathbf{Omega}_1, \mathbf{Omega}_2) = \frac{1}{|S_3|} \frac{TDCS(\sigma^+) - TDCS(\sigma^-)}{TDCS(\sigma^+) + TDCS(\sigma^-)}, \tag{4.7}$$

where σ^+ and σ^- represent right and left circularly polarized light respectively. Δ was extracted for three different sets of angles in the coplanar geometry, at $h\nu = 94\,eV$, and for different energy sharing.

Dörner *et al.* in 1996 [14] and in 1998 [15] studied He DPI by using the cold target recoil ion momentum spectroscopy (COLTRIMS) technique [16]. They used simultaneously two three-dimensional (3D) TOF tubes that collect all the particles over a $4\pi\,sr$ solid angular range. The kinetic energy and angle of emission of the particles were extracted by the difference in their time of flight and the position of detection on two-dimensional position sensitive multichannel detectors. Together with energy and momentum conservation laws the kinematics of the DPI is extracted for all the DPI events, without restriction to specific energies and angles. Measurements of cross section were on an absolute scale. The limitation of the COLTRIMS technique is that, because it relies on a cooling process by supersonic expansion, it can be used only for stable species in the gas phase. Dörner *et al.* [14] reported the TDCS at $h\nu = 80$, 85 and $99\,eV$ in the perpendicular and in the out-of-plane geometry, with $\theta_1 = 40 - 65^o$ and $\theta_1 = 90^0$, and $0.1 \leq E_1/E_2 \leq 10$. In the perpendicular plane the TDCS resembles that for $\theta_1 = \varphi_1 = 0^o$ first measured by Schwarzkopf *et al.* in 1993 [1]. For $\theta_1 = 40 - 65^o$, when moving out of plane the TDCS shows a decrease in the major lobe while the minor lobe does not change intensity. Their fitted value for θ_{fwhm} of the gaussian correlation factor $C(1,2)$ agreed with those previously measured by Dawber *et al.* [12] at $E_{exc} = 1\,eV$, and by Schwarzkopf *et al.* at $E_{exc} = 20\,eV$ [9]. In 1998 the same authors studied the CD in the DPI of He at $20\,eV$ above threshold, at the helical undulator beam-line at the Photon Factory [17]. They found that in the coplanar geometry, with $\theta_1 = \varphi_1 = 0^o$, the angular separation between the two lobes present for $E_1 = E_2 = 10\,eV$ is progressively reduced when moving to unequal energy, and one single maximum is present at $\theta_{12} = 180^o$ for $E_1 + E_2 = 19.5 + 0.5\,eV$. Their measurements were not reproduced by the calculation with a 3C wavefunction for the final state.

Better agreement between measurements and theory for the CD on He DPI was obtained

by Soejima *et al.* [18] and by Kheifets *et al.* [19] in 1999, at the Photon Factory. Their data at $9\,eV$ above threshold, with $E_1 + E_2 = 1 + 8\,eV$, $4.5 + 4.5\,eV$ and $3.6 + 3.6\,eV$, were reproduced by calculations that used the convergent closed coupling (CCC) formalism for the final state.

The review of Briggs and Schmidt in 2000 [20] contains most of the results of investigations on DPI of He.

4.3 Heavier rare gases

The TDCS for DPI in rare gases other than He has received considerably less attention. In heavier rare gases DPI from the valence shell leaves the final ionic state with a p^4 external configuration, that can give $^3P^e$ (ground state), $^1D^e$ and $^1S^e$ symmetries. DPI leading to different final ionic states can be studied by selecting appropriately the kinetic energies of the electrons. DPI to the $^1S^e$ state is an interesting case because the two-electron continuum is restricted to having a $^1P^o$ symmetry, as in the case of He, whereas the $^3P^e$ ionic state results in the $^3P^o$ and $^3D^o$ degenerate continuum states, and the $^1D^e$ ionic state allows $^1P^o$, $^1D^o$ and $^1F^o$ two-electron continuum states.

In rare gases heavier than He, DPI can also happen as a two-step process through a singly charged intermediate state leading to Auger decay. The direct process can be isolated by selecting appropriate electron energies if the Auger spectrum is known.

The first measurements of the TDCS for DPI of a rare gas were reported by Mazeau *et al.* in 1991 [21]. They studied the DPI of Kr to the $4p^4\,{}^3P_2^e$ state using HeI α radiation, with $E_1 = E_2 = 1.13\,eV$ and with the two electrons emitted in the plane of the light beam. The TDCS showed a single maximum for antiparallel emission.

Waymel *et al.* in 1993 [22] measured the TDCS for DPI of Xe to the $5p^4\,{}^1S^e$ state, with $E_1 = E_2 = 1.64\,eV$. Two maxima were found in the range $60^o \leq \theta_{12} \leq 180^o$, rather than only one as in the case of He. As in the case of He, but not in Kr, a node was present for antiparallel emission.

Krässig *et al.* in 1993 [23], and Schaphorst *et al.* in 1996 [24], studied at BESSY in Berlin and at Super ACO in Paris, the TDCS of Ar and Ne respectively, leading to the $p^4\,{}^1D^e$ states. They investigated the evolution of the TDCS when moving from a direct to a two-step process, for the case of equal energies. In the direct process the TDCS was found to consist of two symmetric maxima with zeros for antiparallel emission, as in the case of He; in the two-step DPI the antiparallel nodes were filled to become maxima.

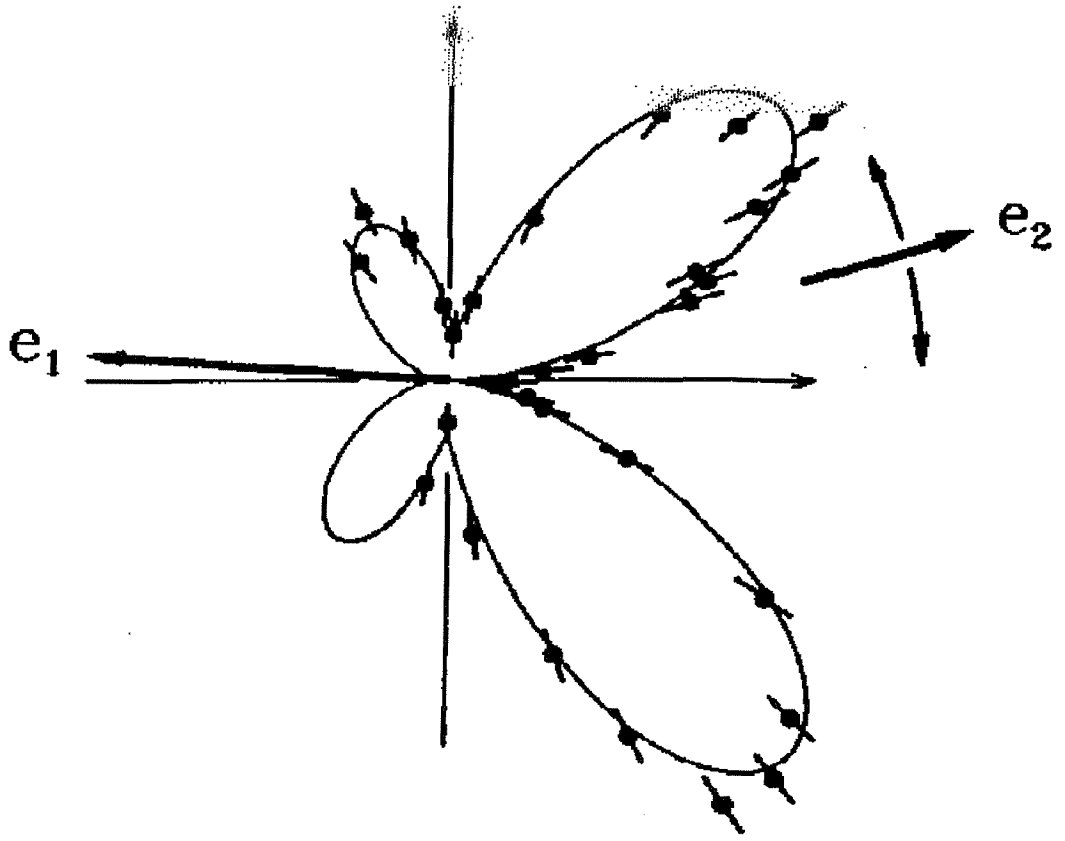

Figure 4.2: TDCS for DPI of Ne to the $2p^4\,{}^1S^e$ state measured by Schaphorst *et al.*, with $h\nu = 110\,eV$, $E_1 = E_2 = 20.3\,eV$.

The measurements reported by Schaphorst *et al.* in 1995 [25] for the TDCS for DPI of Ne to the $2p^4\ {}^1S^e$ state are displayed in figure 4.2. They show four maxima in the range $0^o \leq \theta_{12} \leq 180^o$ rather than two, and zeros for $\theta_{12} = 180^o$. Their explanation for the additional structure was based on the contribution from different configurations in the two-electron continuum. The final continuum was described by a superposition of configurations where each pair of electrons has defined orbital angular momenta $l_1 l_2$. In the case of He, starting from an s^2 valence configuration, the *sp* configuration is likely to be predominant, also in agreement with the expectation from the shake-off description. If all but the *sp* configurations are neglected, and a gaussian correlation factor $C(1,2)$ is included *ad-hoc*, the TDCS can be calculated and it has the form of equation (4.5). Starting from a p^6 configuration it would be most likely that the channels *sp* and *pd* are both important. In this case the TDCS is parameterized in the following form:

$$TDCS \propto (\cos\theta_1 + \cos\theta_2)^2 \left| D_{sp} + \frac{3\cos\theta_{12} - 1}{\sqrt{2}} D_{pd} \right|^2 C(\theta_{12}, E), \qquad (4.8)$$

where $D_{l_1 l_2}$ are the amplitudes of the two different partial waves. Such a parameterization was allowed to reproduce the TDCS for DPI to the $2p^4\,{}^1S^e$ state of Ne^{++} for different energies and geometries. The presence of only two channels (*sp* and *pd*) and of the gaussian

correlation factor were not rigorously justifiable.

A detailed study of the dependence of the TDCS on the L value of the $Ne^{++}2p^4$ states was reported by Krässig *et al.* [26] and by Schmidt *et al.* in 1996 [27]. By including the *sp* and *pd* configurations in the above mentioned partial wave expansion they fitted the measured TDCS with the parameterization (4.8), for different conditions of geometry and energies. The consistency of the fitted parameters and the agreement between the fitted curves and the measured TDCS was excellent, but a comparison with ab-initio calculations was still missing.

Malcherek *et al.* in 1996 [28] presented the result of an ab-initio calculation for the TDCS of Ne, for all the three possible final states. They adopted a similar approach to that of Maulbetsch and Briggs in the case of He [7], [8], using an uncorrelated HF wavefunction for the ground state, and three two-body Coulomb functions for the continuum, with the *ad-hoc* assumption of a gaussian correlation factor. These calculations were in reasonable agreement with the measured TDCS, but the widths, relative intensities and angular positions of the lobes were not in as good agreement with the experimental data as in the case of He.

A different approach to calculate the TDCS for He and other rare gases was adopted by Kazansky and Ostrovsky [29]-[32]. The so-called extended Wannier-ridge model (EWRM) calculates the evolution in time of the two-electron wavefunction as the electrons fly apart, solving the inhomogeneous Scroedinger equation for the two-electron wavefunction coupled to the radiation field. The initial state is described either by uncorrelated HF functions or by configuration interaction (CI); the interaction with the nucleus can be either the long range Coulomb potential $-2/r$, or a more realistic potential $V(r)$. Both CI rather than HF, and $V(r)$ rather than $-2/r$, make a negligible difference to the result. What is remarkable about this theory is that it solves the equation of motion without any *ad-hoc* assumption or adjustable parameters, unlike the calculations of Maulbetsch and Briggs [3]-[7]. Unfortunately the EWRM theory is restricted to the Wannier-ridge; the electrons have the same distance from the nucleus, and therefore the model can be applied only to the case of equal energy sharing. According to the EWRM, the differences in the TDCS for different elements are due to the initial orbital radial distributions $R_{nl}(r)$, and to the symmetries of the final state. In addition, for DPI leading to the $^1S^e$ state in heavier rare gases, the p^2 orbitals are coupled to an overall $^1S^e$ symmetry:

$$\Psi_0 \sim R_{np}(r_1)R_{np}(r_2)\cos\theta_{12}, \tag{4.9}$$

while in the case of He the angular dependence is absent:

$$\Psi_0 \sim R_{1s}(r_1)R_{1s}(r_2). \tag{4.10}$$

The $\cos\theta_{12}$ factor in equation (4.9) is considered partly responsible for the additional structure in the TDCS. The EWRM has been applied to calculate the TDCS for He [29], Ne ($^1S^e$) [30], Kr ($^3P^e$) [31], [32], Xe ($^1S^e$) [30], and Be, Mg, Ca and Sr ([35], see below). The agreement with the experimental data of Schwarzkopf *et al.* [1], Mazeau *et al.* [21], Waymel *et al.* [22] and Schaphorst *et al.* [25] is not as good as that of the 3C calculations of Maulbetsch and Briggs [7] and [8].

4.4 Alkaline earth atoms

Very little interest has been focused to the TDCS of DPI for atoms other than the rare gases. Apart from the rare gases, TDCS for DPI have been studied only for alkaline earth atoms. Ceraulo *et al.* in 1994 [33] calculated the valence TDCS for He, Mg and Ca. They considered linearly polarized light, perpendicular geometry ($\varphi_1 = \varphi_2 = 0^o$), equal and unequal energy sharing: $E_1 = E_2 = 15\,eV$ and $E_1 + E_2 = 5 + 25\,eV$, for $\theta_1 = 0^o$, 45^o and 90^o. The initial states were simulated by HF or CI wavefunctions, uncorrelated Coulomb functions were used for the final states and the electron correlation was taken into account by the inclusion of a Coulomb hole. The term Coulomb hole is used when the wavefunction is multiplied by a factor such as

$$1 - e^{-r_{12}/r_C}, \tag{4.11}$$

with r_c a fixed parameter, to partly take into account the radial correlation. These calculations failed to reproduce the experimental data of Schwarzkopf *et al.* [1] on He. In the case of Mg and Ca, the TDCS for equal energies were quite similar to each other, and showed several pairs of lobes rather then only a single pair as in He. In the case of unequal energies more lobes appear and the TDCS for Mg and Ca looked different when CI was used. HF rather than CI reduces the number of lobes for both Mg and Ca; with HF wavefunctions the TDCS does not change when moving from equal to unequal energies. The inclusion of a Coulomb hole made virtually no difference to the calculated TDCS.

These results would suggest that in the alkaline earth atoms the additional orbital angular momenta l in the mixed initial configuration, rather than correlation in the continuum, are responsible for the additional structure in the TDCS, in contrast to what was found

for He. One would therefore expect that when moving from Mg to Ca, and then to Sr, the TDCS would become more structured as a consequence of stronger mixing in the initial configuration. This would also be in line with the model of Malegat *et al.* [34] discussed in section 3.5.

In 1997 Kazansky and Ostrovsky [35] applied the EWRM to calculate the TDCS for the alkaline earth atoms Be, Mg, Ca and Sr. They considered completely linearly polarized light, equal energies and excess energies from 0.5 to 5.0 eV, for perpendicular geometry. HF wavefunctions plus a Coulomb hole were used for the initial states, relying on the fact that CI rather than HF made minimal changes to the TDCS for both Ne and Xe calculated with the EWRM. Their result was that in all cases the TDCS is zero for $\theta_{12} = 180^o$ and two maxima were present in the angular range $50^o \leq \theta_{12} \leq 180^o$ for Mg, while for Be, Ca and Sr the number of maxima ranged from three (lowest excess energy) to two (highest excess energy).

The experimental results obtained by Ross *et al.* in 1997 [36] for the TDCS of Ca are presented in chapter 7.

Bibliography

[1] O Schwarzkopf, B Krässig, J Elmiger and V Schmidt, *Physical Review Letters*, **70** 3008-3011 (1993).

[2] O Schwarzkopf, B Krässig, V Schmidt, F Maulbetsch and JS Briggs, *Journal of Physics B: Atomic, Molecular and Optical Physics*, **27** L347-L350 (1994).

[3] F Maulbetsch and JS Briggs, *Journal of Physics B: Atomic, Molecular and Optical Physics*, **28** 551-564 (1995).

[4] A Huetz, P Selles, D Waymel and J Mazeau, *Journal of Physics B: Atomic, Molecular and Optical Physics*, **24** 1917-1933 (1991).

[5] H Le Rouzo and C Dal Cappello, *Physical Review A*, **43** 318-329 (1991).

[6] HH Wannier, *Physical Review*, **90** 817-825 (1953).

[7] F Maulbetsch and JS Briggs, *Journal of Physics B: Atomic, Molecular and Optical Physics*, **26** 1679-1696 (1993).
F Maulbetsch and JS Briggs, *Journal of Physics B: Atomic, Molecular and Optical Physics*, **26** L647-L652 (1993).
F Maulbetsch, M Pont, JS Briggs and R Shakeshaft, *Journal of Physics B: Atomic, Molecular and Optical Physics*, **28** L341-L347 (1995).

[8] F Maulbetsch and JS Briggs, *Journal of Physics B: Atomic, Molecular and Optical Physics*, **27** 4095-4104 (1994).

[9] O Schwarzkopf and V schmidt, *Journal of Physics B: Atomic, Molecular and Optical Physics*, **28** 2847-2862 (1995).

[10] A Huetz, P Lablanquie, L Andric, P Selles and J Mazeau, *Journal of Physics B: Atomic, Molecular and Optical Physics* , **27** L13-L18 (1994).

[11] P Lablanquie, J Mazeau, L Andric, P Selles and A Huetz, *Physical Review Letters*, **74** 2192-2195 (1995).

[12] G Dawber, L Avaldi, AG McConkey, H Rojas, MA MacDonald and GC King, *Journal of Physics B: Atomic, Molecular and Optical Physics*, **28** L271-L277 (1995).

[13] J Viefhaus, L Avaldi, F Heiser, R Hentges, O Gessner, A Rüdel, M Viedenhöft, K Wieliczek and U Becker, *Journal of Physics B: Atomic, Molecular and Optical Physics*, **29** L729-L736 (1996).
J Viefhaus, L Avaldi, G Snell, M Wiedenhöft, R Hentges, A Rüdel, F Schäfers, D Menke, U Heinzmann, A Engelns, J Berakdar, H Klar and U Becker, *Physical Review Letters*, **77** 3975-3978 (1996).

[14] R Dörner, T Vogt, V Mergel, H Khemliche, S Kravis, CL Cocke, J Ullrich, M Unverzagt, L Spielberger, M Damrau, O Jagutzki, I Ali, B Weaver, K Ullmann, CC Hsu, M Jung, EP Kanter, B Sonntag, MH Prior, E Rotenberg, J Denlinger, T Warwick, ST Manson and H Schmidt-Böcking, *Physical Review Letters*, **76** 2654-2657 (1996).
R Dörner, JM Feagin, CL Cocke, H Braüning, **O** Jagutzki, M Jung, EP Kanter, H Khemliche, S Kravis, V Mergel, MH Prior, H Schmidt-Böcking, L Spielberger, J Ullrich, M Unversagt and T Vogt, *Physical Review Letters*, **77** 1024-1027 (1996).

[15] R Dörner, H Braüning, JM Feagin, V Mergel, O Jagutzki, L Spielberger, T Vogt, H Khemliche, MH Prior, J Ullrich, CL Cocke and H Schmidt-Böcking, *Physical Review A*, **57** 1074-1090 (1998).
H Bräuning, R Dörner, CL Cocke, MH Prior, B Krässig, AS Kheifets, I Bray, A Bräuning-Demian, K Carnes, S Dreuil, V Mergel, P Richard, J Ulrich and H Schmidt-Böcking, *Journal of Physics B: Atomic, Molecular and Optical Physics*, **31** 5149-5160 (1998).

[16] J Ullrich, R Moshammer, R Dörner, O Jagutzki, V Mergel, H Schmidt-Bocking and L Spielberger, *Journal of Physics B: Atomic, Molecular and Optical Physics*, **30** 2917-2974 (1997).

[17] V Mergel, M Achler, R Dörner, KH Kayyat, T Kambara, Y Awaya, V Zoran, B Nyström, L Spielberger, JH McGuire, J Feagin, J Berakdar, Y Azuma and H Schmidt-Böcking, *Physical Review Letters*, **80** 5301-5304 (1998).

[18] K Soejima, A Danjo, K Okuno and A Yagishita, *Physical Review Letters*, **83** 1546-1549 (1999).

[19] A Kheifets, I Bray, K Soejima, A Danjo, K Okuno and A Yagishita, *Journal of Physics B: Atomic, Molecular and Optical Physics*, **32** L501-L509 (1999).

[20] JS Briggs and V Schmidt, *Journal of Physics B: Atomic, Molecular and Optical Physics*, **33** R1-R48 (2000).

[21] J Mazeau, P Selles, D Waymel and A Huetz, *Physical Review Letters*, **67** 820-823 (1991).

[22] D Waymel, L Andric, J Mazeau, P Selles and A Huetz, *Journal of Physics B: Atomic, Molecular and Optical Physics*, **26** L123-L128 (1993).

[23] B Krässig, O Schwarzkopf and V Schmidt, *Journal of Physics B: Atomic, Molecular and Optical Physics*, **26** 2589-2599 (1993).

[24] SJ Schaphorst, A Jean, O Schwarzkopf, P Lablanquie, L Andric, A Huetz, J Mazeau and V Schmidt, *Journal of Physics B: Atomic, Molecular and Optical Physics*, **29** 1901-1911 (1996).

[25] SJ Schaphorst, B Krässig, O Schwarzkopf, N Scherer and V Schmidt, *Journal of Physics B: Atomic, Molecular and Optical Physics*, **28** L233-L238 (1995).
SJ Schaphorst, B Krässig, O Schwarzkopf, N Scherer, V Schmidt, P Lablanquie, L Andric, J Mazeau and A Huetz, *Journal of Electron Spectroscopy and Related Phenomena*, **76** 229-235 (1995).

[26] B Krässig, SJ Schaphorst, O Schwarzkopf, N Scherer and V Schmidt, *Journal of Physics B: Atomic, Molecular and Optical Physics*, **29** 4255-4265 (1996).

[27] V Schmidt, SJ Schaphorst, B Krässig, O Schwarzkopf and N Scherer, *Journal of Electron Spectroscopy and Related Phenomena*, **79** 279-281 (1996).

[28] AW Malcherek, F Maulbetsch and JS Briggs, *Journal of Physics B: Atomic, Molecular and Optical Physics*, **29** 4127-4138 (1996).

[29] AK Kazansky and VN Ostrovsky, *Physical Review A*, **51** 3698-3702 (1995).

[30] AK Kazansky and VN Ostrovsky, *Physical Review A*, **52** 1775-1778 (1995).

[31] AK Kazansky and VN Ostrovsky, *Journal of Physics B: Atomic, Molecular and Optical Physics*, **28** L333-L339 (1995).

[32] PO Bogdanovich, AK Kazansky and VN Ostrovsky, *Journal of Physics B: Atomic, Molecular and Optical Physics*, **30** 921-940 (1997).

[33] SC Ceraulo, RM Stehman and RS Berry, *Physical Review A*, **49** 1730-1744 (1994).

[34] L Malegat, P Selles and A Huetz, *Journal of Physics B: Atomic, Molecular and Optical Physics*, **30** 251-261 (1997).
L Malegat, P Selles, P Lablanquie and A Huetz, *Journal of Physics B: Atomic, Molecular and Optical Physics*, **30** 263-276 (1997).

[35] AK Kazansky and VN Ostrovsky, *Journal of Physics B: Atomic, Molecular and Optical Physics*, **30** L835-L841 (1997).

[36] KJ Ross, H-J Beyer and JB West, *Journal of Physics B: Atomic, Molecular and Optical Physics*, **30** L735-L740 (1997).

Chapter 5

Previous experimental and theoretical work on the electron spectroscopy of Ca and Sr

5.1 Introduction

This chapter provides a summary on the previous work on electron spectroscopy of Ca and Sr.

Due to their similar electronic configuration Ca and Sr have often received attention in parallel, both experimentally and theoretically. Most of the references in this chapter report work carried out on both Ca and Sr, leading to similar results.

Because of their astrophysical importance Ca and Sr have been studied using electron spectroscopy by numerous workers. For example, the interest in electron correlation effects in these atoms dates back as early as 1925 when Russell and Saunders recognised multiplets in the emission spectra of these elements as being due to the simultaneous excitations of the valence electrons [1].

5.2 Early work with PES

Although several ionization energies (Ie) of both Ca and Sr were known from optical data tabulated by Moore in 1949 [2], the first photoelectron (PE) spectra of Ca and also of Sr were reported by Süzer *et al.* in 1976 [3]. They observed the main photoline and satellite peaks on effusive beams of metal vapour with HeI α radiation. The measurements were not at sufficiently high resolution to resolve the spin-orbit splitting in the final ionic states,

Assignment	Energy [eV]	comment
$3p^5(3d^3\ ^4P)\ ^5P_1$	31.2155(7)	quite strong
-	31.2534(7)	quite strong
$3p^5(3d^3\ ^2P)^3S_1$	31.2672(7)	strong
$3p^54s^2(^2P_{1/2})3d\ ^1P_1$	31.4067(14)	extremely strong, broad
$3p^5(3d^3\ ^3D_2)^1P_1$	31.5194(2)	very strong
$3p^5(4p^2\ ^1D)(^2P)3d\ ^3D_1$	31.5426(2)	very strong
$3p^5(3d^2\ ^1S)\ (^2P)4s\ ^1P_1$	31.5804(13)	very strong
$3p^54s^24d\ ^3P_1$	31.6191(1)	very strong

Table 5.1: Resonances in the Ca photoabsorption spectrum of Mansfield and Newsom close to the *giant* resonance.

and the reported uncertainty was $\pm 20meV$. This work aimed to show the importance of electron correlation effects in alkaline-earth atoms, and concluded that contributions of configurations like $4p^2$ and $3d^2$ in the initial state were important to explain the presence of satellite peaks in the PE spectra of these elements. It also demonstrated the feasibility of photoelectron spectroscopy (PES) for the study of electron correlation effects. The interpretation of these experimental results was corroborated by the previous results of Kim and Bagus in 1973 [4], who calculated generalized oscillator strengths (GOS) using the multiconfigurational Hartree-Fock method (MCHF) and found that electron correlations such as $4p^2$ and $3d^2$ had to be included to bring the calculated GOS into agreement with experiments. The first ionization energy of Ca (Sr), as measured by PES and photoabsorption, is 6.11 and $6.111\,eV$ respectively (5.69 and $5.692\,eV$).

In 1980 Lee and Potts reported HeII α PE spectra of Ca and Sr vapour, where they observed photolines corresponding to the removal of $3p$ and $4p$ removal [11]. Their results are in the fourth column of table 5.3 for Ca, and in the third column of table 5.4 for Sr.

5.3 Photoabsorption

The most important photoabsorption spectrum of Ca in the context of the present work is that of Mansfield and Newsom in 1977 [5]. They observed the absorption spectrum of Ca vapour in the photon energy range $25 - 41\,eV$, and discovered 125 lines, most of them associated with Rydberg series based on the $3p^54s^2\ ^2P_{1/2,3/2}$ ionic cores, with principal quantum number n up to 16. Assignments were made by comparison with single configuration Harteee-Fock (SCHF) calculations. In their work they observed for the first time a very strong resonance at $h\nu = 31.41\,eV$, that was assigned to the $3p^53d4s^2\ ^1P_1$

Assignment	Energy [eV]	Relative intensity
$4p^5(4d^2\ ^1D)5s\ ^1P$ 21%	24.264	3
$4p^5(4d^2\ ^3P)5s\ ^3D$ 39%	24.323	0
$4p^5(4d^3\ ^4F)\ ^3D$ 35%	24.755	0
$4p^5 5s(^3P)(5p^2\ ^3P)\ ^3P$ 58%	24.940	2
$4p^5(4d^3\ ^4F)^3D$ 24%	25.040	6
$4p^5(4d^3\ ^4F)^3D$ 37%	25.091	6
$4p^5(4d^2\ ^3P)5s\ ^3S$ 61%	25.196	7
$4p^5 4d5s^2\ ^1P$ 97%	25.243	10
$4p^5 4d(^3P)(5p^2\ ^3P)\ ^5D$ 35%	25.304	6
$4p^5(4d^2\ ^1D)5s\ ^3D$ 50%	25.393	4
unassigned	25.418	3
unassigned	25.502	1

Table 5.2: Resonances in the Sr photoabsorption spectrum in the region of the *giant* resonance.

excited state. The explanation for the strength of this so called *giant* resonance was based on the influence of the effective central potential on the $3d$ wavefunction. The potential curves for the $3d$ orbital is significantly deeper than those for the $4d$ and $5d$ orbitals, and as a result the $3d$ orbital is much closer to the nucleus. This creates a very high overlap between the $3d$ and $3p$ radial wavefunctions, that leads to a very high cross section for the excitation to the $3p^5 3d4s^2\ ^2P$ state and in a high quantum defect ($\delta = 0.95$). This collapse of the d orbital is present also in other alkaline earth atoms, but in Ca it is particularly strong, probably due to the position of Ca (Z=20) in the periodic table, just before the first transition period (Sc, Z=21 to Zn, Z=30) where the $3d$-subshell starts to be filled. Table 5.1 lists some of the Ca resonances in the region of $31.41\,eV$; errors on the last digits are in brackets.

In 1981 Mansfield and Newsom [6] reported the results of a photoabsorption spectrum of Sr vapour, recorded at the 500 MeV Bonn synchrotron, between 25 and 36 eV. They assigned most of the resonances to Rydberg series converging to the ionic limits arising from a hole in the $4p$ subshell, with principal quantum number n up to 17. However, because of severe configuration mixing not all the resonances could be assigned to Rydberg series. As for the case of Ca, a *giant* resonance was found at $h\nu = 25.24\,eV$, assigned to a 97% pure $4d \leftarrow 4p$ excitation. Assignments were made with the help of the Auger electron spectra measured by White *et al.* (see later) and by comparison with MCHF calculations. Because Sr has a greater atomic number Z than Ca, configuration mixing is more important when ab-initio calculations are performed. Energies of resonances close to the *giant* resonance are

listed in table 5.2 together with their assignment and the percentage of the predominant configuration. Ionization energies extracted from the Sr Rydberg series are listed in table 5.4.

Ionic state	KE	Ie from PES with SR	Ie from HeIIα PES
$3p^5 3d4s\ ^4P_{1/2}$	12.94	-	-
$3p^5 3d4s\ ^4P_{3/2}$	13.00	-	-
$3p^5 3d4s\ ^4P_{5/2}$	13.09	-	-
$3p^5 3d(^3P)4s\ ^2P_{3/2}$	13.49	31.68	-
$3p^5 3d(^3P)4s\ ^2P_{1/2}$	13.60	31.68	-
$3p^5 3d4s\ ^4F_{7/2}$	14.065	-	-
$3p^5 3d4s\ ^4F_{5/2}$	14.15	-	-
$3p^5 3d4s\ ^4F_{3/2}$	14.245	-	-
$3p^5 3d(^3F)4s\ ^2F_{7/2}$	14.51	32.65	-
$3p^5 3d(^3F)4s\ ^2F_{5/2}$	14.65	32.65	-
$3p^5 3d(^4D)4s\ ^4D_{7/2}$	15.615	33.82	-
$3p^5 3d(^4D)4s\ ^4D_{5/2}$	15.665	33.82	-
$3p^5 3d(^4D)4s\ ^4D_{3/2}$	15.69	33.82	-
$3p^5 3d(^4D)4s\ ^4D_{1/2}$	15.74	33.82	-
$3p^5 3d(^1F)4s\ ^2F_{7/2}$	15.875	-	-
$3p^5 3d(^1F)4s\ ^2F_{5/2}$	16.005	-	-
$3p^5 3d(^3D)4s\ ^2D_{5/2}$	16.25	-	-
$3p^5 3d(^3D)4s\ ^2D_{3/2}$	16.296	-	-
$3p^5 4s^2\ ^2P_{3/2}$	16.329	-	34.34
$3p^5 4s^2\ ^2P_{1/2}$	16.675	-	34.69
$3p^5(3d^2\ ^1S_0)\ ^2P_{3/2}$	18.13	36.27	-
$3p^5(3d^2\ ^1S_0)\ ^2P_{1/2}$	18.40	36.27	-

Table 5.3: Second column: kinetic energies (KE) of Ca Auger lines measured by electron impact, the doubly ionized state is $3p^6$. Third and fourth column: ionization energies (Ie) from the $4s^2$ state, measured from PES with SR and with HeIIα.

5.4 Electron emission following electron impact

Schmitz *et al.* in 1976 [7] and Pejcev *et al.* in 1978 [8] reported the results of studies of the ejected-electron spectrum of Ca vapour following electron impact. A preliminary assignment of this spectrum was based on the optical data of Mansfield and Newsom [5]; and a more extensive analysis was reported by Mansfield and Ottley in 1979 [9] by

Ionic state	Ie from photoabsorption	Ie from He II α PES	KE
$4p^5 4d5s\ ^4P_{1/2}$	26.898	-	10.20
$4p^5 4d5s\ ^4P_{3/2}$	27.037	27.08 ± 0.03	10.34
$4p^5 4d(^3P)5s\ ^2P_{1/2}$	27.477	27.64 ± 0.02	10.61
$4p^5 4d(^3P)5s\ ^2P_{3/2}$	27.370	unresolved	10.89
$4p^5(4d^2\ ^3F)(^3P)^4D_{1/2}$	27.734	-	11.03
$4p^5 5s^2\ ^2P_{3/2}$	28.160	28.23 ± 0.03	11.46
$4p^5 5s^2\ ^2P_{1/2}$	29.134	29.13 ± 0.02	12.43
$4p^5 4d5s\ ^4D_{1/2}$	29.401	29.41 ± 0.03	-
$4p^5(4d^2\ ^1D)^2P_{1/2}$	29.670	30.00 ± 0.03	-
$4p^5(5p^2\ ^3P)^4S_{1/2}$	30.706	30.85 ± 0.03	-
$4p^5(4d^2\ ^1S)^2P_{3/2}$	31.521	-	-
$4p^5(4d^2\ ^1S)^2P_{1/2}$	32.267	-	-
$4p^5(5p^2\ ^1S)^2P_{3/2}$	35.038	-	-

Table 5.4: Ionization energies (Ie) of Sr extracted from the optical data of Mansfield and Newsom, and measured by HeII α PE spectra. Fourth column: kinetic energies (KE) of Auger lines to the $3p^6$ state.

comparison with SCHF calculations. Table 5.3 lists some of those Auger lines that are most relevant to this work. It is worth noting how the structure of the $3d$ subshell affects the energy of the highly correlated $4s$ and $3d$ orbitals. In neutral Ca the $4s3d$ levels are higher than the $4s^2$, but a hole in the $3p$ subshell draws the $3d$ orbital closer to the nucleus and the $3p^5 3d4s$ levels are lower than those of $3p^5 4s^2$.

Schmitz *et al.* in 1976 [7] and White *et al.* in 1979 [10] reported the measured kinetic energies of ejected electrons after electron impact ionization on Sr vapour. Unlike the case of Ca, these Auger spectra were published before the corresponding photoabsorption spectra and ab-initio calculations of Mansfield and Newsom were available, and most of the lines were left unassigned. The fourth column on table Table 5.4 lists the kinetic energies of the most important Auger lines observed by White *et al.* [10], the assignments are taken from the work of Mansfield and Newsom [5].

5.5 Photoionization mass spectroscopy with synchrotron radiation

Synchrotron radiation was used to study photoionization of Ca and Sr by Holland and Codling in 1981 at the $2.3\,GeV$ Bonn electron synchrotron [12]. They measured the relative ion yields for the singly and doubly charged ions in the region of the subvalence shell resonances. They observed that the intensity ratio Ca^{++}/Ca^{+} increases steeply at photon energies corresponding to the creation of $3p$ holes ($3p^5 3d(^3P)4s$ and $3p^5 4s^2$), and interpreted this in terms of a DPI process which proceeds mainly as a two-step process: the creation of a hole in the $3p$ subshell, followed by its Auger decay, rather than a direct two-electron emission. The interpretation of the Sr^{++}/Sr^{+} ratio was not as simple. Although the ratio showed enhancements for wavelengths corresponding to ionization energies, it also showed falls in intensity for resonant wavelengths.

Sato *et al.* in 1985 [13] repeated the work of Holland and Codling on Ca at the Photon Factory in Japan, with an improved resolution of $5\,meV$ and a finer wavelength grid, in the same wavelength region of the work of Holland and Codling [12]. They also observed in both Ca^{+} and Ca^{++} photoion yields Rydberg series based on the ionic cores with a $3p$ hole, and the *giant* resonance $3p^5 3d4s^2\ ^1P_1$ at $31.41\,eV$, in agreement with the photoabsorption spectrum of Mansfield and Newsom in 1977 [5]. Again, the increase in the Ca^{++}/Ca^{+} ratio was interpreted as DPI proceeding primarily as a two-step process.

Nagata *et al.* in 1986 [14] repeated the work of Holland and Codling on Sr at the Photon Factory, in similar conditions of the work of Sato *et al.* [13]. They observed the predominance of the $4p^5 5s^2(^2P_{1/2,3/2})nl$ ($l = s$ or d) Rydberg series, with the *giant* resonance at $h\nu = 25.25\,eV$. In this context the important difference between Ca and Sr is that, while in Ca the $3d \leftarrow 3p$ *giant* resonance lies above the lowest $3p$-hole ionic states ($3p^5 3d4s\ ^4P$), in Sr the $4d \leftarrow 4p$ *giant* resonance lies below any $4p$-hole ionic state. Therefore, the only possible DPI process at this resonance in Sr is the direct emission of the two $5s^2$ electrons, a process expected to have a very low cross section. However, a strong enhancement in the Sr^{++} ion yield was observed at $h\nu = 25.25\,eV$. At resonances above the lowest $4p$-hole ionic level both the Sr^{+} and the Sr^{++}/Sr^{+} intensities showed strong enhancement, again leading to the conclusion that DPI proceeds primarily as a two-step process through a $4p$-hole intermediate state.

5.6 PES with synchrotron radiation

Yagishita *et al.* in 1988 [15] measured at BESSY in Berlin CIS spectra for the $5s$, $4d$ and $5p$ states of Sr^+ and Auger yields from the $4p^5 4d(^3P)5s\ ^2P_{3/2}$, $4p^5 5s^2\ ^2P_{1/2,3/2}$ and $4p^5 4d5s\ ^4D_{1/2}$ states of Sr^+, in the region of the $4p$ excitations, with a resolution of the order of $60\,meV$. The relative intensities of the resonances in the CIS spectra resembled those in the Sr^{++} ion yields only up to the threshold for the $4p$-hole ionic states; this was explained in terms of a two-step DPI channel that opens at the $4p$-hole threshold, increasing the DPI and reducing valence photoionization. At the *giant* resonance the $5s/4d$ intensity ratio is 10 times lower than the $4s/3d$ ratio in Ca. This corresponds to the lower intensity of the *giant* resonance in photoabsorption, which results from a lower $p-d$ overlap in the subvalence shell. Differences between Auger yield spectra and the Sr^{++} yield spectra of Nagata *et al.* [14] were explained by post collision interaction (PCI) and shake up/down effects.

Cowan *et al.* in 1985 [16] calculated the Ca $4s$, $3d$ and $4p$ photoionization cross section in the photon energy range $11-28\,eV$, using a code developed by Cowan in 1981 [17]. The inclusion of mixed configurations resulted in a decreased strength of the main $4s$ photoline in favour of the $3d$ and $4p$ line; the latter could also become more intense than the 4s. In the same year Altun and Kelly [18] presented the result of a calculation for the photoionization cross section of Ca to the $4s$, $3d$ and $4p$ ionic state from the $3d$ threshold up to $h\nu = 50\,eV$, using many body perturbation theory (MBPT). All the channels showed a strong increase corresponding to the presence of the *giant* resonance at $31.41\,eV$. At this resonance the cross section to the 4s, 3d and 4p states were computed to be 200, 24 and 67 Mb; these results suggested that the $3d \leftarrow 3p$ resonance decays mainly to the 4s ionic state rather than to the 3d or 4p satellite.

Bizeau *et al.* in 1984 [19], and in 1987 [20], measured PES spectra of Ca using SR, and compared their results with calculations using the random phase approximation (RPA) and many body perturbation theory (MBPT). Synchrotron radiation was produced by the ACO storage ring and electrons emitted by the interaction of the photon beam with an effusive atomic beam were energy analysed by a CMA analyser at the magic angle $\theta = 54.44^o$. Apart from conventional PE spectra of Ca vapour at selected wavelengths they also reported measurements of relative photoionization cross sections for the $4s$, $3p$ and $3s$ main lines, from threshold up to $h\nu = 120\,eV$, and relative intensities of PE satellite and Auger lines in the region of the $3p$ resonances. From that work it was evident that any intermediate $3p$ resonance leads to enhancements of large groups of photo and Auger lines.

Connerade *et al.* in 1987 [21] repeated the measurements of the photoabsorption spectrum of Ca vapour in the region of the $3p$ resonances, using the $500\,MeV$ Bonn synchrotron, with a resolution higher than that of Mansfield and Newsom in 1977 [5]. The spectrum was re-assigned by Connerade and Sarpal [22] in 1992 on the basis of a multiconfigurational Dirac-Fock (MCDF) calculation.

Beier *et al.* in 1992 [23] studied the electronic decay of excited Ca atoms in the $3p^5 3d4s4p$ levels using PES with synchrotron radiation combined with optical pumping. Visible laser radiation at $422.7\,nm$ ($h\nu = 2.932\,eV$) prepared the Ca atoms in the $4s4p$ levels: $3p^6 4s4p \leftarrow 3p^6 4s^2$, and VUV SR produced the core excitation $3p^5 3d4s4p \leftarrow 3p^6 4s4p$. By observing PE spectra in a fixed direction, and rotating the axis of linear polarization of the laser radiation, they assigned resonances to the $3p^5 3d4s4p\ {}^1S_0$, ${}^1P_1$ and ${}^1D_2$ levels in the photon energy region between 31 and $33\,eV$.

Hamdy *et al.* in 1991 [24] measured at the Daresbury SRS the relative $Ca^+\ 4p \rightarrow 4s$ ($\lambda = 3933\mathring{A}$) and $Sr^+\ 5p \rightarrow 5s$ ($\lambda = 4078\mathring{A}$) fluorescence yields for incident photon energies in the region of the subvalence shell excitations, with a monochromator bandwidth of the order of $30\,meV$. They observed the $3p^5 4s^2({}^2P_{1/2,3/2})nl$ ($l = s$ or d) Rydberg series in the Ca spectrum. The *giant* resonance was present in their spectrum at $h\nu = 31.41\,eV$, with a smaller peak on its side at $31.53\,eV$, that according to the work of Mansfield and Newsom corresponded to the superposition of several resonances not resolved by Hamdy *et al.* (see table 5.1). In the Sr spectrum they observed resonances whose energies were in agreement with the photoabsorption spectrum of Mansfield and Newsom; Rydberg series were present which converged to the ionic cores $4p^5 5s^2\ {}^2P_{1/2,3/2}$ and $4p^5 4d({}^3P)5s\ {}^2P_{3/2}$. One of the main purposes of the work of Hamdy *et al.* was to extract the alignment of the $Ca^+\ 4p$ ($Sr^+\ 5p$) satellite by measuring the polarization of the $4p \rightarrow 4s$ ($5p \rightarrow 5s$) fluorescence radiation. From those measurements, and together with the anisotropy of the $4p$ ($5p$) PE line, it was planned to extract the relative dipole matrix amplitudes and phase difference for the s and d waves of the photoelectron which leaves the ion in the $4p$ state. Their work was hampered by the fact that the $4p$ ($5p$) states are populated not only by photoionization, but also by fluorescence from higher Ca^+ (Sr^+) levels. This was evident from the fact that in their fluorescence work the intensity ratio between the $3p^5 4s^2 nl$ ($4p^5 5s^2 nl$) resonances, with $n > 3$ ($n > 4$), and the $n = 3$ ($n = 4$) member, was much higher than in a photoabsorption or photoion yield spectrum. The polarization measurements could not be finally used to extract the alignment of the $4p$ ($5p$) state. This problem was solved in the case of Ca in 1995 [25] when the polarization of the $4p \rightarrow 4s$ fluorescence was measured in coincidence with the photoelectron that leaves the ion in the

$4p$ state, with the incident radiation tuned to the *giant* resonance. Assuming the validity of lsj approximation it was possible to extract the relative amplitudes and the absolute values of the phase difference of the s and d channels, $|D_s/D_d|$ and $|\Delta_s - \Delta_d|$. The validity of the lsj approximation scheme was confirmed by measurements of the polarization of the fluorescence in coincidence with the photoelectron at particular angles where the lsj approximation scheme predicted specific values for the polarization. Extending these measurement to the adjacent peak at $31.53\,eV$ showed that the lsj approximation was not valid at that energy.

Further measurements were necessary to extract the sign of the relative phase difference, and this was done by West *et al.* in 1996 [26] by repeating the previous measurements of Hamdy *et al.* [24], but introducing a component of circularly polarized light ($S_3 \neq 0$).

The electronic decay of the excited states of Ca in the region of the *giant* resonance was studied in details by Ueda *et al.* in 1993 [27] and in 1997 [28] by using angle resolved photoelectron and Auger spectroscopy at the Daresbury SRS. They noticed that the *giant* resonance decays preferably by autoionizing to the 4s state, rather than to the $3d$ or $4p$ states. They measured the $4s$: $3d$ and $4s$: $4p$ branching ratios and found agreement with both the previous measurements of Bizeau *et al.* [20] and with the ab-initio calculations of Altun and Kelly [18]. The presence of the $3p^5 3d4s\ ^4P \rightarrow 3p^6\ ^1S_0$ Auger line in their electron spectrum also suggested a coupling mechanism between the $3p^5 3d4s^2\ ^1P_1$ resonance and the $3p^5 3d4s\ ^4P\epsilon l$ continuum, allowing the *giant* resonance to autoionize to the $3p^5 3d4s\ ^4P$ states. They also suggested several possible other coupling mechanisms for the $3p^5 3d4s^2\ ^1P_1$ resonance with nearby configurations in order to explain the enhancement of satellite PE peaks in terms of the breakdown of the LSJ coupling scheme and of the spectator model for autoionizing decay.

Kämmerling *et al.* in 1994 [29] studied the $3p$ photoionization process in the photon energy range between 40 and $100\,eV$, where a Cooper minimum was expected. A Cooper minimum occurs when the ϵd channel for the outgoing electron vanishes [30]. The $3p$ photoionization process controls the alignment of the ionic state, which controls the angular distribution of its decay products. Kämmerling *et al.* measured the anisotropy parameter of the $3p^5 4s^2\ ^2P_{1/2,3/2} \rightarrow 3p^6\ ^1S_0$ Auger electrons and of the $3p_{3/2}$ photoelectron, to extract information on the $3p$ photoionization. They found the presence of a Cooper minimum at $h\nu = 60\,eV$. They also found that the single configuration relativistic random phase approximation (SCFRRPA) describes the photon energy dependence of the anisotropy parameter for the $3p^5 4s^2\ ^2P_{1/2,3/2} \rightarrow 3p^6\ ^1S_0$ Auger decay well.

Jiménez-Mier *et al.* in 1993 [31] at the Aladdin SRS in Wisconsin, studied the electronic

decays of $4p$ excitations in Sr. They performed high resolution CIS spectra of the $5s$, $4d$, $5p$, $6s$, $5d$, $6p$ and $4f$ states of Sr^+ and Auger yields from the $4p^5 4d(^3P)5s\ ^2P_{3/2}$ and $4p^5 5s^2\ ^2P_{3/2}$ levels in the photon energy region $20 - 30\,eV$, with an optical resolution of $5.5\,meV$. The resolution was good enough to resolve individual components of the *giant* resonance reported by Mansfield and Newsom. It was noticed that close resonances, unresolved in the work of Yagishita *et al.* [15] where the resolution was $60\,meV$, result in different decay patterns. This is particularly true for the *giant* resonance, that in the work of Yagishita *et al.* appeared as a superposition of three resonances between 25.196 and $25.304\,eV$. From their spectra it was clear that resonances at lower energies decay preferably to lower ionic state, while decay from higher resonances tends to decay to higher ionic states. CIS spectra confirmed that the $5p \rightarrow 5s$ fluorescence yield of Hamdy *et al.* [24] suffered severely from cascade effects.

Ueda *et al.* in 1998 [32] studied the $3p$ resonances in neutral Ca, in the photon energy range $31 - 34\,eV$. They measured the relative intensities and angular distribution parameters of Auger transitions to the $Ca^{++}\ 3p^6$ ground state from the $3p^5 3d4s\ ^4P$, ^2P and ^4F states of Ca^+, and noticed sharp variations at resonant wavelengths. Thes resonance not only enhanced the ionization cross section, but also changed the alignment parameter of the final state.

Bibliography

[1] HN Russell and FA Saunders, *Astrophysical Journal*, **61** 38 (1925).
HN Russell and FA Saunders, *Astrophysical Journal*, **62** 1 (1925).

[2] Atomic Energy Levels.
C Moore, circular 467 United States National Bureau of Standards, Washington (1949).

[3] S Süzer, S-T Lee and DA Shirley, *Physical Review A*, **13** 1842-1849 (1976).

[4] Y-K Kim and PS Bagus, *Physical Review A*, **8** 1739-1747 (1973).

[5] MWD Mansfield and GH Newsom, *Proceedings of the Royal Society of London*, **357** 77-102 (1977).

[6] BWD Mansfield and TW Ottley, *Proceedings of the Royal Society of London*, **377** 431-448 (1981).

[7] W Schmitz, B Breuckmann and W Mehlhorn, *Journal of Physics B: Atomic, Molecular and Optical Physics*, **9** 1493-1497 (1976).

[8] V Pejcev, TW Ottley, D Rassi and KJ Ross, *Journal of Physics B: Atomic, Molecular and Optical Physics*, **11** 531-539 (1978).

[9] BWD Mansfield and TW Ottley, *Proceedings of the Royal Society of London*, **365** 413-424 (1979).

[10] MD White, D Rassi and KJ Ross, *Journal of Physics B: Atomic, Molecular and Optical Physics*, **12** 315-322 (1979).

[11] EPF Lee and AW Potts, *Journal of Physics B: Atomic, Molecular and Optical Physics*, **14** L61-L65 (1981).

[12] DMP Holland and K Codling, *Journal of Physics B: Atomic, Molecular and Optical Physics*, **14** 2345-2351 (1981).

[13] Y Sato, T Hayaishi, Y Itikawa, Y Itoh, J Murakami, T Nagata, T Sasaki, B Sonntag, A Yagishita and M Yoshino, *Journal of Physics B: Atomic, Molecular and Optical Physics*, **18** 225-231 (1985).

[14] T Nagata, JB West, T Hayaishi, Y Itikawa, Y Ito, T Koizumi, J Murakami, Y Sato, H Shibata, A Yagishita and M Yoshino, *Journal of Physics B: Atomic, Molecular and Optical Physics*, **19** 1281-1290 (1986).

[15] A Yagishita, S Aksela, TH Prescher, M Meyer, M Richter, E von Raven and B Sonntag, *Journal of Physics B: Atomic, Molecular and Optical Physics*, **21** 945-953 (1988).

[16] RD Cowan, JE Hansen and H Smid, *Physical Review A*, **31** 2750 (1985).

[17] The Theory of Atomic Structure and Spectra
RD Cowan, University of California Press, Berkeley (1981).

[18] Z Altun and HP Kelly, *Physical Review A*, **6** 3711-3717 (1985).

[19] JM Bizeau, P Gerard, FJ Wuillemier and G Wendin, *Physical Review Letters*, **53** 2083 (1984).

[20] JM Bizeau, P Gerard, FJ Wuillemier and G Wendin, *Physical Review A*, **36** 1220-1248 (1987).

[21] JP Connerade, MA Baig and M Sweeney, *Journal of Physics B: Atomic, Molecular and Optical Physics*, **20** L771-L775 (1987).

[22] JP Connerade and BK Sarpal, *Journal of Physics B: Atomic, Molecular and Optical Physics*, **25** 2245-2256 (1992).

[23] S Beier, W Fiedler, BR Müller, M Schulze, P Zimmermann, M Meyer, M Pahler, TH Prescher, E von Raven, M Richter, J Rüder and B Sonntag, *Journal of Physics B: Atomic, Molecular and Optical Physics*, **25** 923-930 (1992).

[24] H Hamdy, H-J Beyer, JB West and H Kleinpoppen, *Journal of Physics B: Atomic, Molecular and Optical Physics*, **24** 4957-4972 (1991).

[25] H-J Beyer, JB West, KJ Ross, K Ueda, NM Kabachnik, H Hamdy and H Kleinpoppen, *Journal of Physics B: Atomic, Molecular and Optical Physics*, **28** L47-L52 (1995).

[26] JB West, K Ueda, NM Kabachnik, KJ Ross, H-J Beyer and H Kleinpoppen, *Physical Review A*, **53** R9-R11 (1996).

[27] K Ueda, JB West, KJ Ross, H Hamdy, H-J Beyer and H Kleinpoppen, *Physical Review A*, **48** R863-R866 (1993).

[28] K Ueda, JB West, KJ Ross, NM Kabachnik, H-J Beyer, H Hamdy and H Kleinpoppen, *Journal of Physics B: Atomic, Molecular and Optical Physics*, **30** 2093-2108 (1997).

[29] B Kämmerling, J Läuger and V Schmidt, *Journal of Electron Spectroscopy and Related Phenomena*, **67** 363-371 (1994).

[30] J Cooper, *Physical Review A*, **128** 681 (1962).
U Fano and J Cooper, *Review of Modern Physics*, **40** 441-507 (1968).

[31] J Jiménez-Mier, CD Caldwell, MG Flemming, SB Whitfield and P van der Meulen, *Physical Review A*, **48** 442-451 (1993).

[32] KUeda, NM Kabachnik, JB Westn KJ Ross, H-J Beyer, H Hamdy and H Kleinpoppen, *Journal of Physics B: Atomic, Molecular and Optical Physics*, **31** 4331-4337 (1998).

Chapter 6

Experimental apparatus for the study of double photoionization of metal vapours

6.1 Introduction

This chapter describes the experimental arrangement for the study of double photoionization of metal atoms using synchrotron radiation.

The spectrometer chamber is constructed of stainless steel and is maintained at a vacuum better than $5 \times 10^{-6}\, mbar$, described in section 6.2. Section 6.3 describes the oven inside the chamber that produces the metal vapour beam. Electrons produced by the interaction of the atomic beam with the synchrotron radiation are energy analysed by two dispersive spherical sector analysers, and detected by channeltron electron multipliers, described in sections 6.4 and 6.5 respectively. After detection the electron pulses are processed and stored in a pulse height analyser, this is described in section 6.6.

6.2 Vacuum system

High vacuum ($P < 10^{-5}\, mbar$) is required in the experimental chamber for the transmission of the radiation and low energy electrons and for the operation of the metal vapour source.

The experimental chamber, whose schematic drawing is in figure 6.1, is maintained under high vacuum in Daresbury by a Pfeiffer 500 l/s turbomolecular pump backed by an Edwards $5\, m^3/h$ rotary pump. When the system was at Elettra an ALCATEL ABBECY

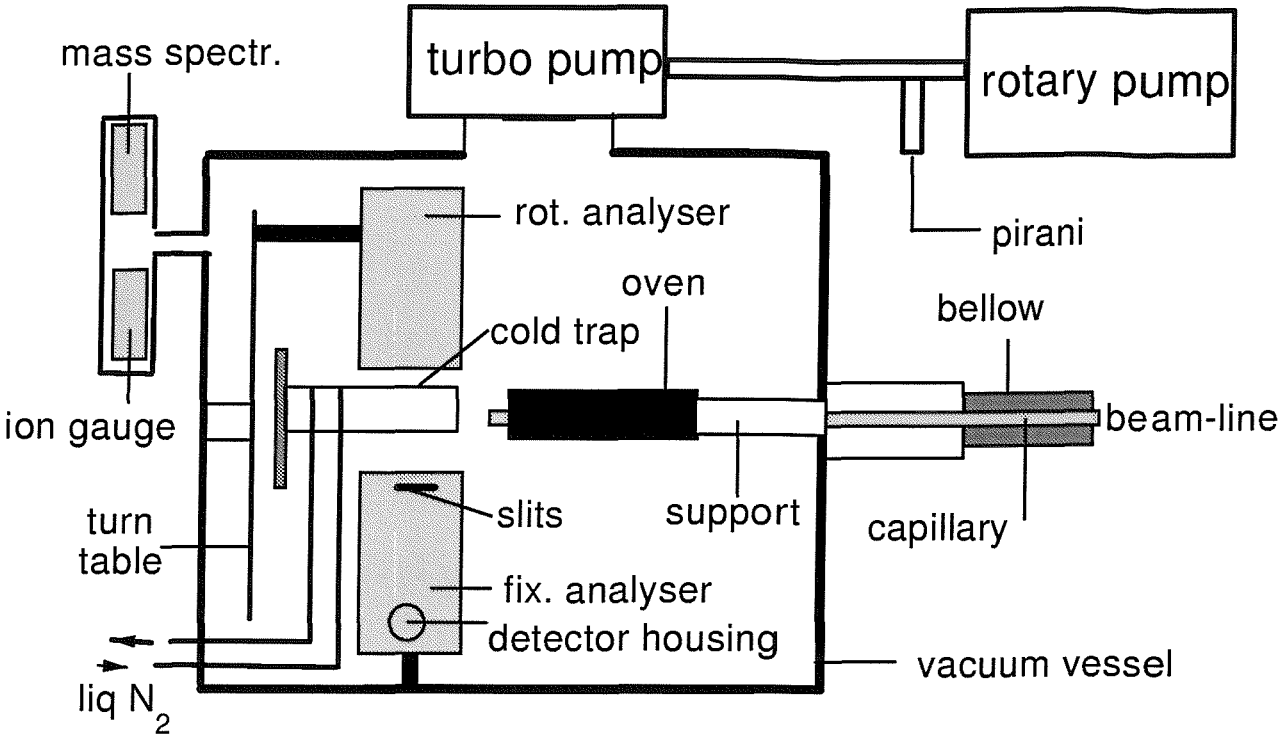

Figure 6.1: A schematic drawing of the whole spectrometer.

5402 OP grease bearing 500 l/s turbomolecular pump and an RV Edwards 3 oil free rotary pump were used.

High pump speed is not a requirement for this system as no gas throughput is externally added. The pumps are needed to extract the gas released by the surfaces, and also to pump away the gases produced by the hot metal vapour source. The chamber has a volume of approximately $100\,l$ and it normally takes 3 hours to reach a background pressure of $10^{-6}\,mbar$.

In order to reduce the contamination of the pre-entrance slits of the analysers there is a cold trap around the interaction region, in front of the entrance to the analysers. The trap is cylindrical, $50\,mm$ diameter and $100\,mm$ length, and cooled by liquid nitrogen which flows through a pipeline brazed to the trap. The temperature of the cold trap is monitored by a Cr/Al thermocouple and in normal condition it is constant at approximately $-180\,^{\circ}C$. The trap has one hole and a slot that faces the entrance slits of the analysers, where electrons can pass through. The diameter of the hole and the width of the slot are $2\,cm$.

Typical working pressure is 2 to 3 $\times\ 10^{-7}\,mbar$, measured by an ionization gauge. A quadrupolar mass analyser is also attached to the chamber. When the pressure is relatively high, particularly during initial heating of the metal vapour source, it can be very useful to know the mass composition of the residual internal gas. Abundance of H_2O would

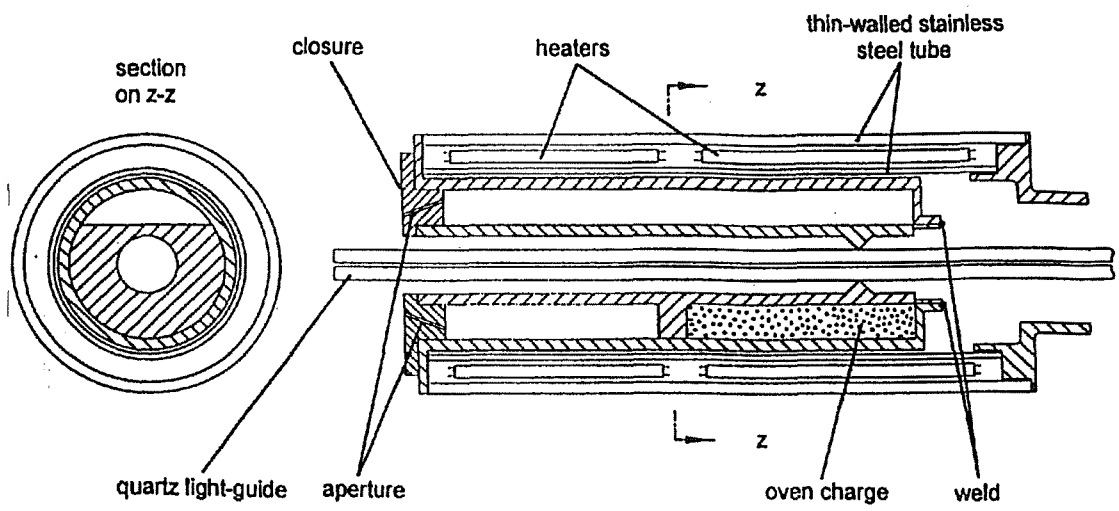

Figure 6.2: Drawing of the oven.

suggest a slow release of water vapour from the surfaces, while an N_2 signal stronger than that of H_2O would indicate a leak in the system.

The pressure in the backing line is measured by a Pirani gauge. Both the ionization gauge and the Pirani gauge are connected to a safety circuit which switches off the high voltages to the channeltron and the power supply to the oven when the pressure rises $\geq 10^{-5}\,mbar$ in the main chamber or $\geq 10^{-2}\,mbar$ in the backing line.

6.3 The atomic beam

6.3.1 The oven

The metal vapour beam is produced by an oven that heats the solid sample, which is contained in a crucible [1]. A drawing of the oven and a photograph of the oven mounted on the chamber are shown in figures 6.2 and 6.3 respectively. The oven is resistively heated and consists of two concentric tubes with diameters 30 and $40\,mm$ and thickness 1 and $2\,mm$, mounted on a common base, with the heating elements between them. The solid sample is loaded inside a crucible placed in the centre of the oven. The oven has been designed to allow the synchrotron radiation to pass through the center of it.

The material from which the oven and the crucible are fabricated must satisfy a number of conditions [2]. It must have a negligible vapour pressure ($< 10^{-8}\,mbar$) at the working temperature and its melting point must be at least $200\,^{o}C$ higher than the operating temperature. It must also not react with species present inside the crucible. It is also

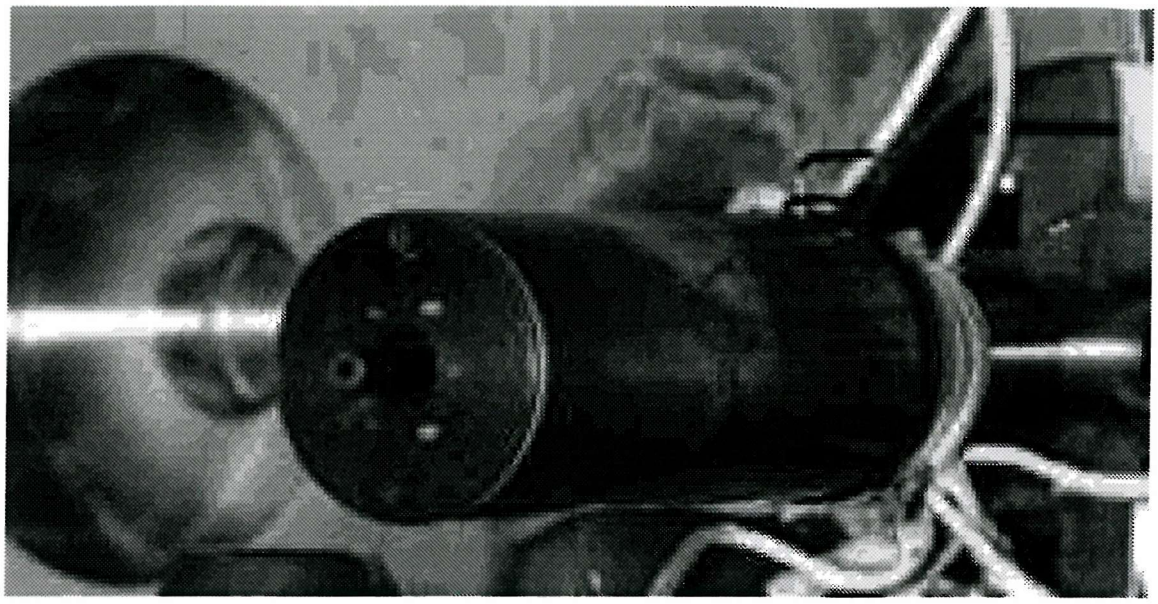

Figure 6.3: A photograph of the oven.

convenient to choose a material easy to machine. For the present study the oven and the crucible are made from stainless steel.

The oven heaters are made using $0.5\,mm$ diameter molybdenum wires inside twin bore alumina sleevings (Al_2O_3), wired in such a way as to minimize the magnetic fields produced. The electrical resistances of the front and rear heaters are approximately 0.8 and $1.5\,\Omega$ at room temperature. Two filaments are used in order to have independent control of the front and the rear temperatures of the oven. Boron nitride rings are used to isolate the heaters from each other and from the front and the rear of the oven case. In working conditions the rear part of the oven is at approximately $600^o\,C$ for Ca and 550^o for Sr. The powers supplied to the front and rear heaters are approximately 35 and $55\,W$. A temperature difference of approximately $50\,^oC$ is maintained between the front and the rear of the oven to prevent the metal vapour from condensing around the oven apertures; the temperatures of the crucible are measured by two Cr/Al thermocouples. As shown in figure 6.2, the crucible containing the charge consists of two coaxial cylinders of stainless steel welded at one end. The outer cylinder is made to slide easily into the inner tube of the oven and the inner cylinder has a diameter of $11\,mm$. The charge is loaded in the rear compartment of the crucible in the region between the two cylinders and is kept away from the front of the crucible by a flange machined around the inner tube at two thirds of its length; the top section of the flange is cut away to allow the vapourised charge to reach the crucible apertures.

The crucible terminates with a loose fitting flange with a central hole. This closure has

also six symmetrical holes around the central axis, 1.5 mm diameter and 9 mm in length. These holes point towards a point on the oven axis, approximately 60 mm in front of the crucible.

To reduce radiation heat losses three layers of 0.1 mm thickness tantalum foil are wrapped around the oven. The degree of radiation shielding is a compromise between reducing the input power required, and the time required for the oven to cool down.

For a charge of 15 g the atomic beam produced by the oven lasts for at least 4 weeks.

6.3.2 Collimation and intensity of the atomic beam

In this experiment it was important to have a relatively high atomic density, and also directionality of the atomic beam. These conditions were achieved by combination of suitable crucible apertures and an atomic effusive regime. An effusive regime is when the mean free path of the atoms λ is greater than the diameter of the aperture a in the crucible:

$$\lambda > a. \tag{6.1}$$

The mean free path λ is

$$\lambda[cm] = 7 \times 10^{-20} \frac{T[K]}{P[mbar]\sigma[cm^2]}, \tag{6.2}$$

with T the absolute temperature and σ the atomic collision cross section, that can be approximated by

$$\sigma = \pi\delta^2, \tag{6.3}$$

with δ the atomic or molecular size. For an element like Ca ($\delta \approx 1.7\mathring{A}$) at $600^o\,C$ and $2 \times 10^{-2}\,mbar$ the mean free path λ is approximately 8 mm.

Under these conditions the number of atoms emerging from a thin aperture of diameter a, at an angle θ in the solid angle $d\Omega$ has a cosine distribution, given by Giordmaine and Wang in 1960 [3]:

$$dN = \frac{d\Omega}{4} nva^2 \cos\theta, \tag{6.4}$$

where n is the particle density in the source and v the mean atomic velocity:

$$v[cm/s] = 1.4 \times 10^{-4} \sqrt{\frac{T}{M}}, \tag{6.5}$$

with M the mass number of the elements. With a thin aperture geometry the resulting

atomic beam is broad and uncollimated, the beam can be made highly directional by having tubes rather than a thin hole. If the mean free path λ is such that $\lambda \geq L$, with L the length of the tube, and $L >> a$, the flow of atoms through such a tube is said to be *transparent*. In this condition the angular full width at half maximum of the atomic beam is reduced to

$$\theta_{1/2} = 1.7\frac{a}{L}. \tag{6.6}$$

For transparent flow, in a atomic effusive regime, the atomic density on the axis of the tube at a distance d can be approximated by the expression given by Ramsey in 1956 [4]:

$$I[atoms/cm^3] = 10^{18}\frac{P[mbar]}{M}\left(\frac{a}{d}\right)^2. \tag{6.7}$$

If more than one tube is present, equation (6.7) must be multiplied by the number of tubes. In the present oven 6 tubes are used, with $a = 1.5\,mm$, $d = 50\,mm$, $P = 10^{-2}\,mbar$ and $M = 40$ for Ca and 88 for Sr; in this condition equation (6.7) results in a beam density of the order of $10^{11} - 10^{12}\,atoms/cm^3$.

6.4 Electron energy analysers

6.4.1 General information

The majority of experiments involving photoionization involve analysis of electron kinetic energy. Most of the electron energy analysers are of the deflection type, which use electrostatic fields to spatially separate electrons with different kinetic energy.

When designing an electron spectrometer several characteristic of the electron analysers must be taken into account. One of the most important features of an analyser is its electron energy resolution ΔE, normally defined as the full width at half maximum (FWHM) of a measured energy distribution resulting from a beam of monoenergetic electrons entering the analyser. Taylor expansion of the trajectory of the electrons in the dispersive elements leads to the following expression for the resolution [5]:

$$\frac{\Delta E}{E} = C_w\left(\frac{w}{L}\right) + C_\alpha\left(\Delta\alpha\right)^2 + C_\beta\left(\Delta\beta\right)^2 + C_h\left(\frac{h}{L}\right)^2, \tag{6.8}$$

where w and h are the average width and length of entrance and exit slits, L is a typical dimension of the analyser, and $\Delta\alpha$ and $\Delta\beta$ are the opening angles in the dispersive and non-dispersive planes. The numerical coefficients C_w, C_α, C_β and C_h have been tabulated

Analyser		C_w	C_α	C_β	C_h
CMA	$\alpha = 54.5^o$	1.29	1.65	0	0
Spherical deflection analyser	$\Phi = 180^o$	1	1	0	1/8
	$\Phi = 90^o$	1	2	1/2	1/16
Cylindrical deflection analyser	$\Phi = 127^o$	2	4/3	1	0

Table 6.1: Typical constants, for various types of electron energy analysers.

by Granneman in 1983 [5] for the most common analysers and are reported in table 6.1. The main contribution in equation (6.8) normally comes from the first term. Narrower slits result in a better resolution, but at the expense of intensity. Increasing the dimension of the analyser would also improve the resolution, but this could be inconvenient.

Equation (6.8) does not include contributions from fringe fields effects, which can also be important.

Other important characteristic of electron energy analysers are:

Transmission: the ratio between the emergent flux of particles and the flux entering the analyser.

Efficiency of the entire system, including source area, solid angle and detector efficiency; this could be the most important criterium for processes with very low cross sections.

Etendue: the product of the entrance solid angle and the entrance area.

Two basic modes of operation of an electron analyser exist. In the *variable* pass energy mode the voltages creating the electrostatic dispersive field are scanned when recording a spectrum. This mode has the disadvantages of giving different resolutions at different energies. In the *fixed* pass energy mode all the electrons passing through the analyser have the same energy, and an electron energy spectrum is recorded by accelerating/retarding the electrons before they enter the analyser. This mode of operation has the advantage of providing a constant resolution over the entire spectrum, but the efficiency changes as a function of energy due to different efficiency of the acceptance apertures.

The following is a list of some common dispersive analysers.

Parallel plate analyser. In this analyser, firstly introduced by Pierce in 1939 [6], the deflecting field is between two parallel plates kept at different voltages. The field also provides a focusing effect in the planes perpendicular to the plates. Entrance and exit slits are in one of the plates. The potential between the plates repels the particles towards the

plate containing the slits, and only electrons with a certain energy can emerge through the exit slit. This analyser was chosen in the past mainly for its relatively simple mechanical construction.

Cylindrical mirror analyser (CMA). This analyser consists of two concentric cylinders maintained at different potentials. Electrons created at the cylinders' axis enter the analyser through a circular entrance slit on the inner cylinder. Electrons emerging from the exit slits are focused onto the detector, which is located on the axis of the system. The main advantage of this analyser is to have a large solid angle acceptance, due to its full 2π azimuthal symmetry. It also has the property of being independent of angular distribution effects. One disadvantage is that in the case of a non-negligible radial dimension of the source the resolving power is strongly reduced.

Cylindrical deflector analyser. In this type of analyser two concentric cylindrical sectors with different radii are kept at different voltages. The electrons travel in the plane perpendicular to the cylinders axis, the deflection field also provides focusing effect in this plane. If the angle of the cylindrical sectors is 127^o, the source and its image of the system are located at the entrance and exit slits planes. The reason this analyser is currently widely used is its simple mechanical construction.

Spherical sector analyser. In this analyser, firstly introduced by Purcell in 1938 [7], the electrons travel between concentric hemispherical plates. The relation between the pass energy, the voltages to the inner and the outer sector V_i and V_o, and the radii of these sectors R_i and R_o is:

$$E_p = \left(\frac{R_o}{R_i} - \frac{R_i}{R_o}\right)^{-1} (V_i - V_o). \tag{6.9}$$

Two great advantages of this analyser are that *(i)* it has focusing properties both in the dispersive and in the non-dispersive planes, and *(ii)* for any angle of the spherical sectors the center of curvature, the source and its image lie all on the same plane. Entrance and exit slits are placed on this plane. Fringe-field correctors, as described by Herzog in 1935 [8] and subsequently by Jost in 1979 [9], are often used with these analysers.

6.4.2 Electron analysers used throughout this work

Two hemispherical sectors analysers are used for the study of double photoionization of metal vapours. A scheme of the two analysers is in figure 6.4 and a photograph of them attached to the lid of the chamber is shown in figure 6.5. In the photograph the housings for the detectors, the entrance slits, the cold trap and the pipeline brazed to it can be

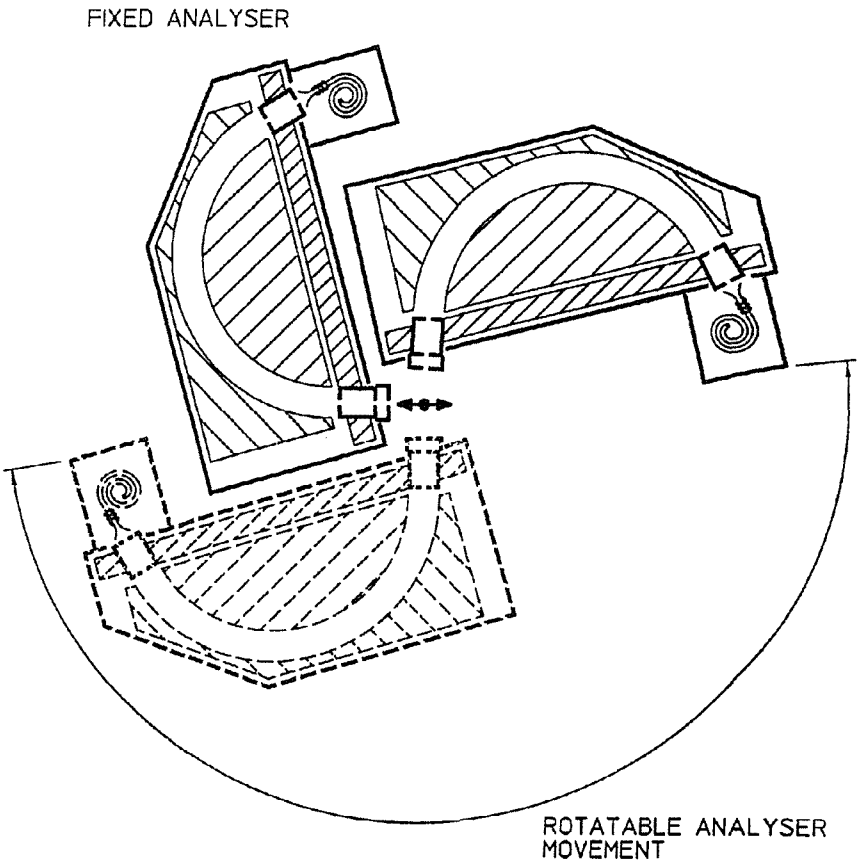

Figure 6.4: Scheme of the two hemispherical analysers used in this work. The radiation propagates perpendicularly to the plane, the arrow shows the direction of polarization.

clearly seen. One analyser is in one of two fixed positions, bolted to the chamber's lid and can accept electrons emitted either horizontally, parallel to the **E** field of the radiation beam, or vertically, perpendicular to it. This analyser is referred to as the *fixed* analyser. The second analyser is mounted on a turn-table that can be rotated around the axis of the light beam; this is referred to as the *rotatable* analyser.

The turn-table can be rotated using an external rotary drive mechanism; the angular position of the turn-table can be determined either by viewing a scale through a vacuum window on the side of the chamber or from graduations on the rotary feedthrough. The minimum and maximum relative angles between the two analysers are $\theta_{12} = 93^\circ$ and $\theta_{12} = 266^\circ$ for either position of the fixed analyser.

Both analysers accept electrons emitted perpendicularly to the direction of the light beam, with $\pm 2^\circ$ acceptance angle in the plane of propagation of the light, and $\pm 1^\circ$ in the plane

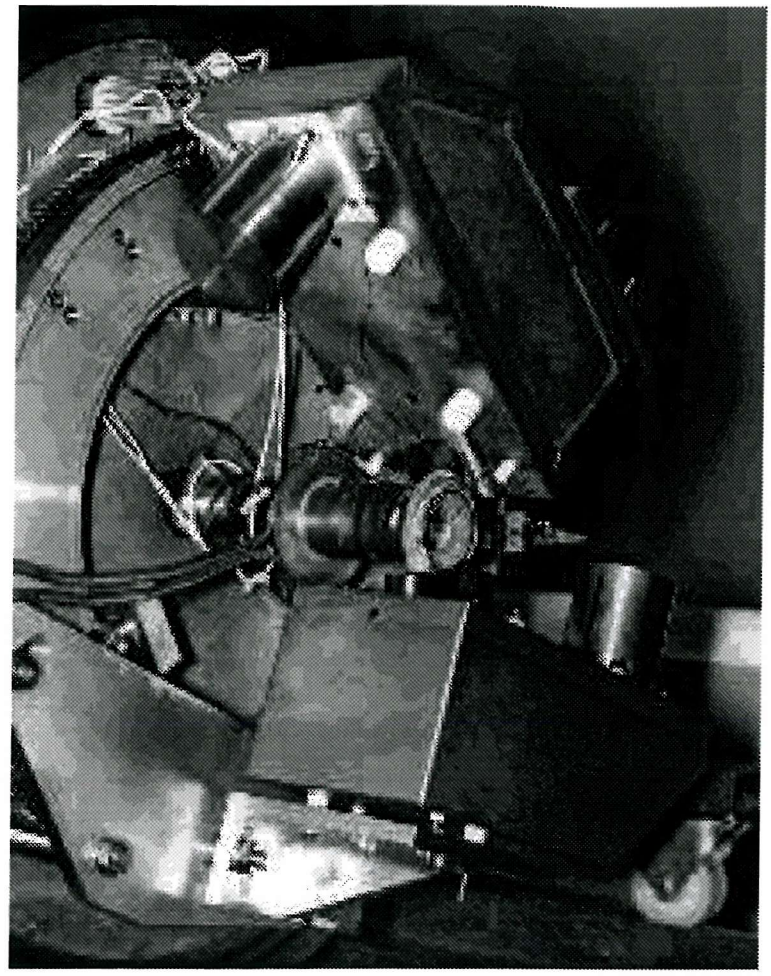

Figure 6.5: A photograph of the two analysers used in this work.

perpendicular to it.

The spherical sectors, which have radii R_i and R_o of 81 mm and 99 mm respectively, are mounted on a common plate which is electrically isolated from them. Both analysers are constructed from aluminum alloy 6082; they are coated with colloidal graphite in order to obtain uniform contact potential and reduce stray fields effects.

Herzog end-field correctors [8] are fitted before the entrance to the spherical sectors. The sizes of the entrance and exit slits are both $2 \times 10\,mm^2$. The exit slits are covered with a fine metallic mesh coated with graphite to prevent fields from the channeltrons entering the analysers.

The analysers can operate at pass energies in the range $5 - 24\,eV$; they normally operate at a constant pass energy of $E_p = 10\,eV$.

Lenses are not present with these analysers, but an accelerating/retarding field is created using a set of titanium pre-entrance slits placed before the entrance slits; these

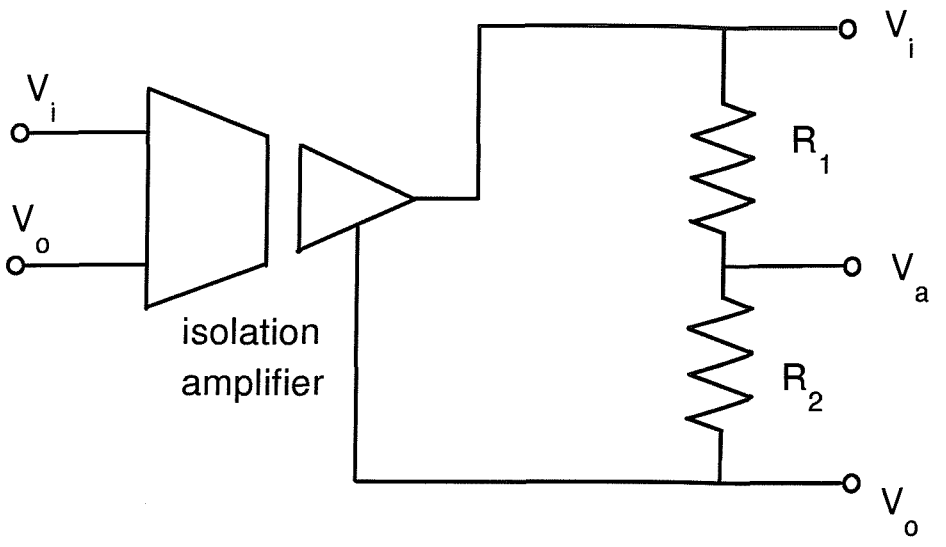

Figure 6.6: Scheme of the circuit that sets the voltages to the plate (V_a) and to the inner and outer hemispheres (V_i and V_o).

pre-entrance slits are electrically earthed. After this set of slits all the electrons are accelerated by the potential V_a applied to the plate. Electrons that are accelerated to the pass energy travel through the analyser and reach the detector after the exit slits. The voltages V_i and V_o applied to the inner and outer hemispheres are such that the plate is at the same potential as the centre line between the spherical sectors:

$$V_a = \frac{R_i V_i + R_o V_o}{R_i + R_o}. \tag{6.10}$$

V_a is the accelerating/retarding voltage applied to the plate; the desired pass energy, as defined by equation (6.9), for these analysers is given by

$$E_p \simeq 2.5(V_i - V_o). \tag{6.11}$$

The voltage $V_i - V_o$ is provided by an isolation amplifier, and V_a is added as shown in the circuit in figure 6.6. In such a circuit the voltage V_a corresponds to

$$V_a = \frac{R_1 V_i + R_2 V_o}{R_1 + R_2}, \tag{6.12}$$

which coincides with equation (6.10) if $R_1/R_2 = R_i/R_o$.

For the present geometry, and for $E_p = 10\,eV$, the first term in equation (6.8) is $50\,meV$. Other factors which contribute to the line-width in an energy spectrum are the finite band-width of the radiation, the angular spread of the electrons entering the analyser, the

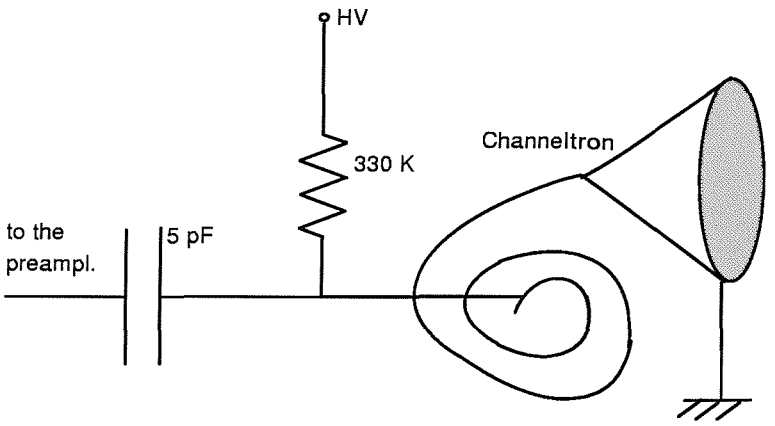

Figure 6.7: Channeltron detector and circuit applied to it.

Doppler broadening and unresolved relativistic or hyperfine structure. Typical full widths at half maximum (FWHM) are $200\,meV$ for a photoline, and $100\,meV$ for an Auger line; the photon band-width does not contribute to the Auger line-widths.

Each analyser is enclosed in its box of μ-metal ($1\,mm$ thickness) to reduce effects of stray magnetic fields.

6.5 Detection of the electrons

The electrons emerging from the exit slits of an energy analyser can be detected by a single channel electron multiplier (channeltron). In the present work PHILIPS X919BL channeltrons were used. Figure 6.7 shows a schematic of a channeltron and the high voltage circuit applied to it. Channeltrons consist of a $2\,mm$ bore glass tube, approximately $25\,mm$ long, internally coated with a secondary electron emitter. The tube has a typical resistance of $1\,M\Omega$ and a high voltage is applied to the end, while its front is earthed. The front of the channeltron has the shape of a funnel, with the widest radius of approximately $10\,mm$. Electrons hitting the input funnel produce secondary electrons which are accelerated by the voltage gradients in the tube. The collisions with the walls as the charge is accelerated down the tube result in a final gain of between 10^6 and 10^8. The negative pulses at the end of the multiplier are then electronically amplified (LECROY 612A) and recorded in *coincidence* (see section 6.6).

The channeltron itself has a curved shape to prevent ions produced from the electron impact with the background gas from travelling back to the input cone, where they may start a new avalanche. Maximum acceptable pulse rates are of the order of 3×10^4; at higher input rates the detector saturates.

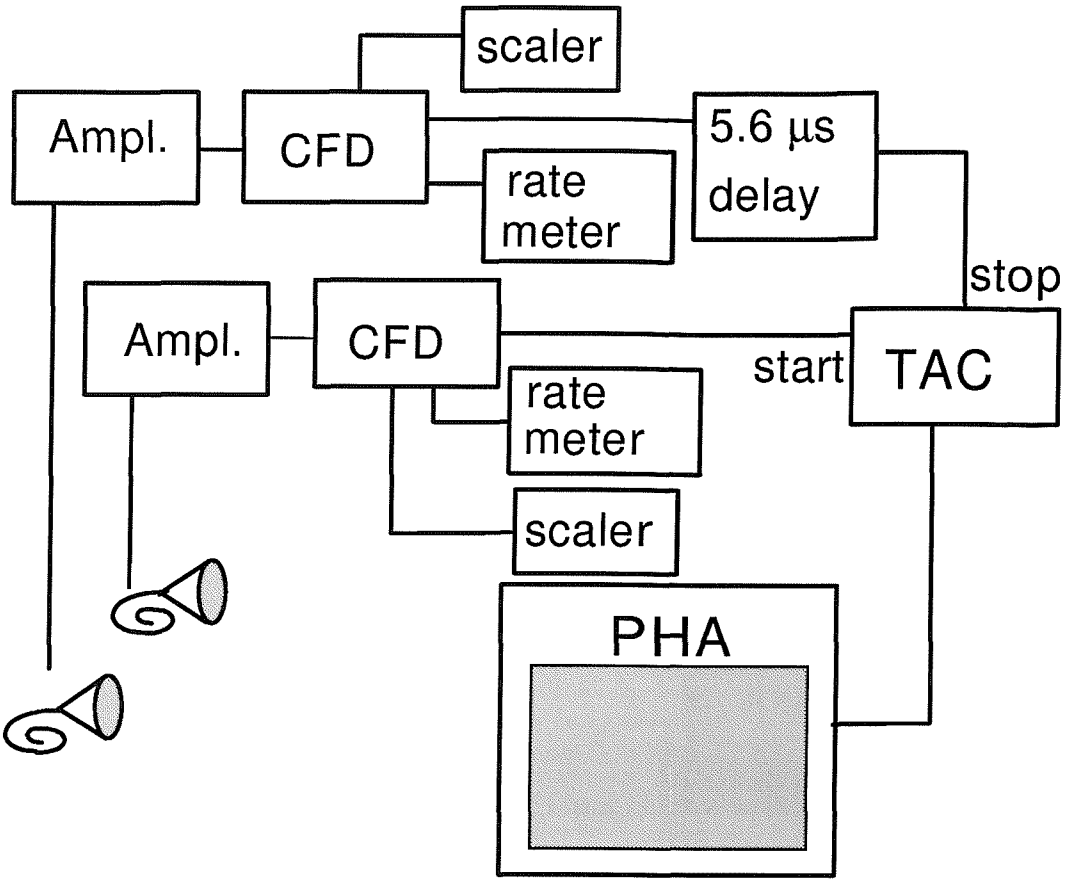

Figure 6.8: Block diagram of the coincidence circuit.

The output pulse rate is dependent on the applied high voltage: it is zero until $1.2\,kV$, where it starts to rise steeply, and it reaches a plateau at $3.0 - 3.5\,kV$. The optimum voltage is some $50\,V$ higher than the start of the plateau. Too high voltage must be avoided as they may lead to deterioration in the performance of the multiplier tube.

6.6 Coincidence set-up

In order to study double photoionization the two specific electrons must be isolated from all other processes by observing them in *coincidence*. The word *coincidence* is used because the two electrons are emitted simultaneously, or nearly so.

The experimental set-up for the coincidence measurements is shown in figure 6.8. The two outputs from the amplifier are fed into constant fraction discriminators (CFD, CANBERRA 2128, threshold $\equiv 100\,meV$). The CFD is used in coincidence experiments for the following reason: it is preferable to have the time-width of the coincidence signal as low as possible, because the narrower the signal, the better the estimate of its intensity. One contribution to the time-width of a coincidence signal arises from the time-widths of individual electron pulses. Electron pulses from the detectors have different time-spreads,

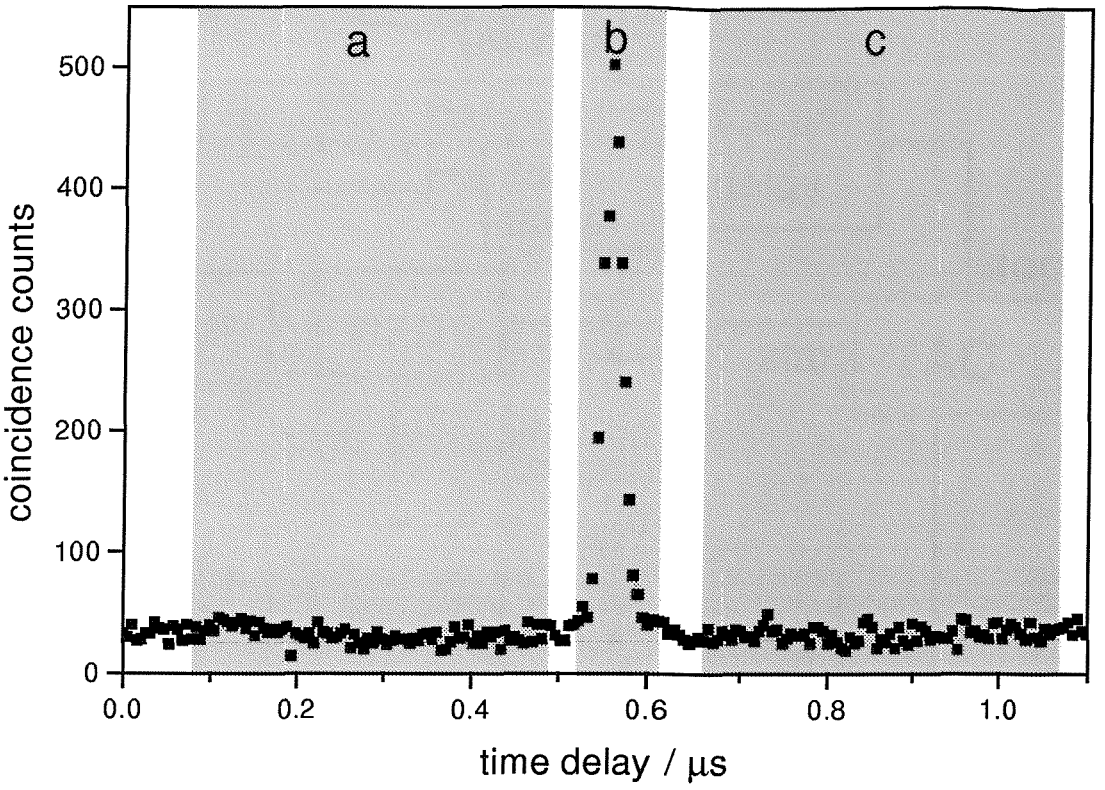

Figure 6.9: Coincidence measurements as output from the TAC, displayed by the PHA. The plot represents sum of measurements recorded over a period of a week.

of several ns, because of the statistical nature of the electron multiplication process, and are therefore unsuitable for coincidence detection. The CFD triggers at a constant fraction of the pulse height, thus overcoming the problem of different time-widths of individual electron pulses. Consequently the time-width of the coincidence signal is reduced to $\sim 100\,ps$. One of the two outputs from the CFDs is delayed by $550\,ns$ (ORTEG 416A GATE and DELAY generator) and then the two signals are fed into rate counters, scalers and also into the START and STOP inputs of a time-to-amplitude-converter (TAC ORTEG NE4670). The time delay of one of the signals is needed to distinguish between a START and a STOP signal in the TAC.

The TAC output is a digital signal whose amplitude is proportional to the time difference between the START and STOP pulses ($1.1\mu s \equiv 10\,V$). Because the electron pulses from double photoionization appear nearly simultaneously and one channel is delayed by $550\,ns$, the coincidence signal is expected as a $5\,V$ digital signal from the TAC.

The output from the TAC goes to a pulse height analyser (PHA ORTEG 7100) that sorts the pulses according to their amplitude in a histogram, as shown in figure 6.9. In such a histogram both *true* and *false* coincidences are present. The *true* counts appear as a peak (region b), superimposed on the flat distribution of the background counts. The

false counts are estimated from a window at each side of the peak (regions a and c) and this background is then subtracted from the central region.

Each coincidence measurement is recorded over a period of time of 30-120 minutes, each final coincidence data point is usually the average of several measurements, normally 4 or 5, recorded at different times during the same set of measurements.

The intensity of the coincidence signal can vary for several reason. Among these there are fluctuations in the photon flux, changes in analyser and detector efficiencies and target density. It is therefore necessary to normalize the *true* counts to correct for these factors. This is done by dividing the *true* counts by the number of counts from the fixed analyser as measured by one scaler.

6.7 Conclusions

The experimental apparatus that was used for the study of double photoionization of Ca and Sr in the vapour phase with synchrotron radiation, described in chapters 7 and 8 respectively, has been described in this chapter. Particular emphasis is placed on the production of a suitable atomic beam, the electron energy analysers and the coincidence detection technique.

Bibliography

[1] KJ Ross and JB West, *Measurement Science & Technology*, **9** 1236-1238 (1998).

[2] KJ Ross and B Sonntag, *Review of Scientific Instruments*, **66** 4409-4433 (1995).

[3] JA Giordmaine and TC Wang, *Journal of Applied Physics*, **31** 463-471 (1960).

[4] Molecular Beams.
NF Ramsey, Oxford University Press, Oxford (1956).

[5] Transportion, Dispersion and Detection of Electrons, Ions and Neutral.
EHA Granneman and MJ Van der Wiel, in *Handbook on Synchrotron Radiation*, edited by EE Koch, North Holland, Amsterdam (1983).

[6] DT Pierce CE Kuyatt and RJ Celotta, *Review of Scientific Instruments*, **50** 1467-1473 (1979).

[7] EM Purcell, *Physical Review*, **54** 818-826 (1938).

[8] R Herzog, *Zeitschrift der Physik*, **97** 5327-5331 (1935).

[9] K Jost, *Journal of Physics E: Scientific Instruments*, **12** 1001-1005 (1797).

[10] A Van Veen, AGJ De Wit, GA Van de Shootbrugge and JM Fluit, *Journal of Physics E: Scientific Instruments*, **12** 861-864 (1979).

[11] E Blauth, *Zeitschrift der Physik*, **147** 288-291 (1957).

[12] W Mehlhorn, *Zeitschrift der Physik*, **160** 247-250 (1960).

[13] PH Citrin, RW Shaw Jr and TD Thomas, edited by DA Shirley, North Holland, Amsterdam (1972).

[14] S Aksela, *Review of Scientific Instruments*, **42** 810-812 (1972).

[15] S Aksela, *Review of Scientific Instruments*, **43** 1350-1356 (1973).

[16] CE Kuyatt and JA Sympson, *Review of Scientific Instruments*, **38** 103-111 (1967).

[17] H Ewald and H Liebl, *Zeitschrift der Naturforschalung*, **10a** 872-877 (1955).

[18] AC Parr, SH Southworth, JL Dehmer and DMP Holland, *Nuclear Instruments and Methods in Physics Research*, **222** 221-229 (1984).

Chapter 7

Double photoionization of atomic Ca and Sr

7.1 Introduction

This chapter presents the studies of TDCS for DPI of Ca and Sr in the vapour phase. Parts of the results included here have been recently published in reference [1]. This chapter is organized as follows. Sections 7.2 and 7.4 are dedicated to the discussion of the results and to the analysis of the data for DPI via neutral resonances in Ca and Sr respectively. Section 7.3 presents the results and the analysis of the off-resonant DPI data for Ca.

7.2 TDCS of Ca via a neutral resonance

The DPI process in Ca which is the subject of the main interest in this work is the following:

$$Ca^{*}\, 3p^5 3d4s^2\, {}^1P_1 \leftarrow Ca\, 3p^6 4s^2\, {}^1S_0 + h\nu \tag{7.1}$$

$$Ca^{*}\, 3p^5 3d4s^2\, {}^1P_1 \rightarrow Ca^{++}\, 3p^6\, {}^1S_0 + e_1^- + e_2^- \tag{7.2}$$

$$Ie^{++} = 17.98\, eV,$$

where double photoionization takes place in the region of the $3d \leftarrow 3p$ *giant* resonance at $h\nu = 31.41\, eV$ (see section 5.5 and also reference [2]). In this condition the two electrons share an excess energy E_{exc} of

$$E_{exc} = E_1 + E_2 = h\nu - Ie^{++}. \tag{7.3}$$

For one photon dipole absorption, LSJ coupling and single electron configuration the first step (7.1) is allowed, whereas the second step (7.2) is forbidden by selection rules. In fact this is not surprising, as DPI happens only as a consequence of interelectron correlation that breaks the selection rules based on the one-electron picture.

The two electrons are emitted with energies E_1 and E_2, called E_F and E_R in section 7.3, in the plane perpendicular to the radiation beam, at angles θ_F and θ_R with respect to the direction of major linear polarization. The indices F and R refer to the electrons accepted by the fixed and rotatable analyser respectively.

During the work of this thesis measurements have been recorded with the fixed analyser at $\theta_F = 0^o$, parallel to the direction of the **E** vector of the photon beam. However, the complementary work of Ross *at al.* published in 1997 [3] is also included here for the sake of completeness.

7.2.1 The Ca $3d \leftarrow 3p$ resonance region

Both in the present work and in that of reference [3], measurements were made at a photon energy resonant with an excitation of the neutral atom in order to resonantly enhance the DPI process; the cross section for DPI is very low and the coincidence rate is further reduced by the selection in directions and energies.

The need to make measurements at a resonant energy restricts the total excess energy E_{exc} to the following:

$$E_{exc} = E_F + E_R = h\nu_{res} - Ie^{++} = 31.41 - 17.98 = 13.43\,eV. \tag{7.4}$$

Calculations of DPI become more complicated if the resonance is considered. Even though some theoretical work on DPI of alkaline earth atoms exist, none of them includes DPI via a neutral resonance (see section 4.4 and references [4] and [5]).

Several resonances are present in the region of the $3d \leftarrow 3p$ excitation (see table 5.1 in chapter 5), and their positions were found by recording CIS spectra for the $4s$ state of Ca^+. Two such spectra are shown on the same relative scale in figure 7.1. It can be seen from these spectra that the structure of the *giant* resonance is not resolved, this means that in the present experimental conditions the measured DPI is an incoherent summation of several contributions, each of them arising from a different unresolved resonance state.

The DPI coincidence measurements were taken with a monochromator bandwidth of $100\,meV$. In this condition the strongest peak of figure 7.1, at $h\nu = 31.41\,eV$, is almost

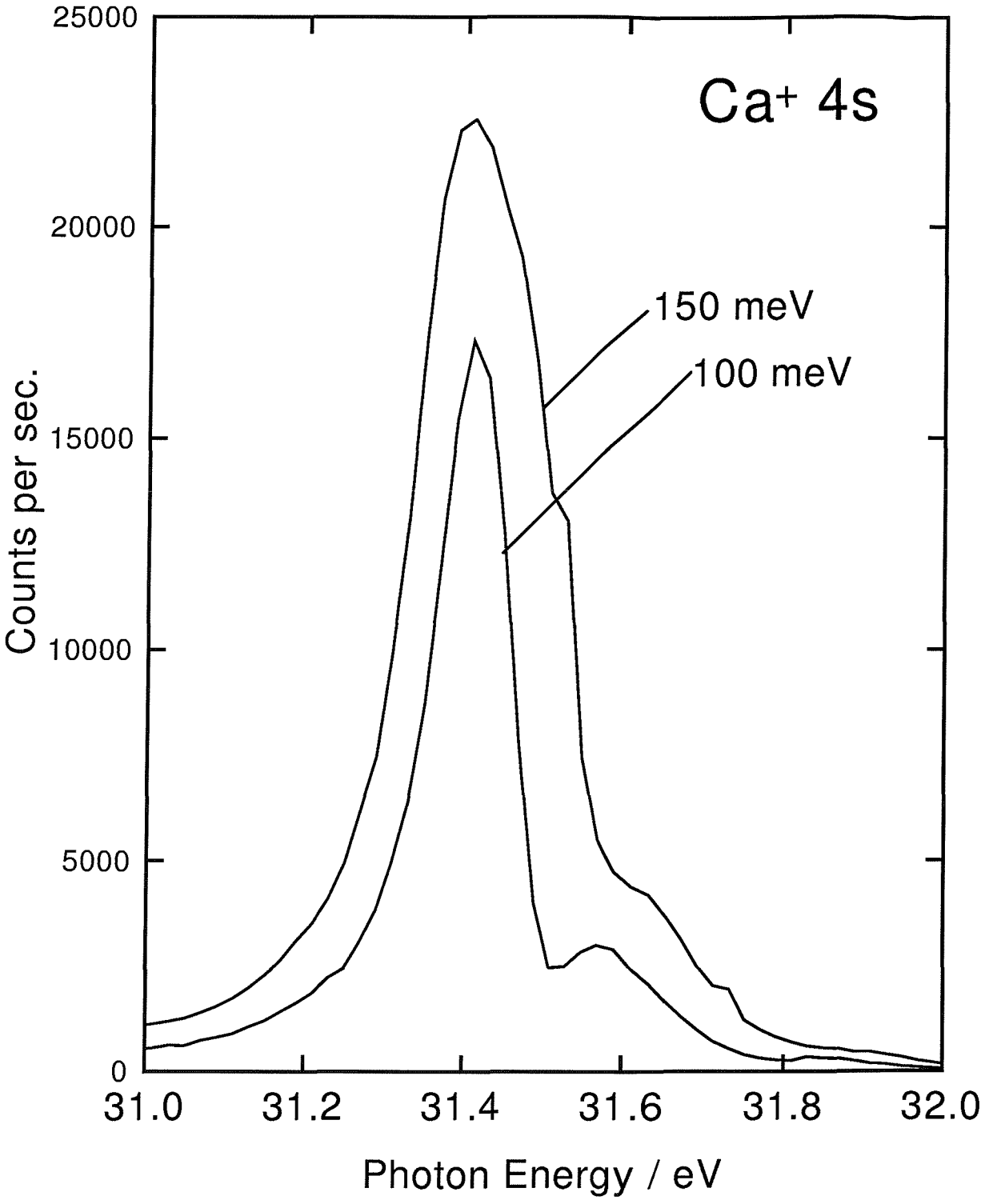

Figure 7.1: CIS spectra of the $4s$ state of Ca^+ for monochromator bandwidths of 100 and $150\,meV$. Both spectra have been recorded with the fixed analyser at $\theta_F = 0^o$ and $S_1 \simeq 0.75$; the pass energy of the analyser was $24\,eV$.

entirely due to the $3p^5 3d4s^2\,{}^1P_1$ *giant* resonance. In contrast, the side peak at $h\nu = 31.56\,eV$ contains unresolved contributions from several excited states.

7.2.2 Energy and angular resolution

The DPI coincidence measurements have been recorded with the pass energies of the analysers set to $24\,eV$, in order to maximize the efficiencies of the analysers, the pass energies were limited by the voltages available from the DACs to drive the analysers. The monochromator bandwidth was set to $100\,meV$, this value was chosen as a compromise between the need to maximise the coincidence count rate and the need to resolve the two resonances of figure 7.1. These conditions of bandwidths and pass energies resulted in full width at half maximum (FWHM) in PE spectra of approximately $200\,meV$;

The angular resolution is also important when angle resolved measurements are attempted, see for example reference [6]. The angular acceptance of the electron energy analyser is determined by the geometry of the input slits. In this work each analyser has a $2\,mm$ wide pre-entrance slit which is $50\,mm$ from the ionization region, followed by the entrance slit, also $2\,mm$ wide and $6.4\,mm$ further back. This gives an angular acceptance of $\pm 1^o$, which is expected to be narrower than any angular structure in the measured TDCS.

7.2.3 TDCS of Ca at the $31.41\,eV$ *giant* resonance: equal energy sharing

Figures 7.2 and 7.3 show the TDCS for DPI of Ca measured during the course of this work ($\theta_F = 0^o$), published in reference [1] and by Ross *et al.* in 1997 [3] ($\theta_F = 270^o$) respectively, both with $h\nu = 31.41\,eV$ and with equal energy sharing of the two outgoing electrons: $E_F = E_R = 6.71\,eV$.

It is very difficult to estimate the uncertainties in the measured data. A source of uncertainties comes from the efficiency of the analyser that could change with time, but this effect cannot be assessed quantitatively. The error bars in figures 7.2 and 7.3 contain only the statistical contribution from the *true* and *false* coincidence counts, assuming poissonian distributions for both.

It can be seen in figures 7.2 and 7.3 that the data are not symmetric about $\theta_{RF} = 180^o$. As it has been pointed out in reference [7], symmetry about $\theta_{RF} = 180^o$ in the present measurements must be expected because of absence of circularly polarized light. The asymmetry that can be observed in the present data is believed to be an instrumental

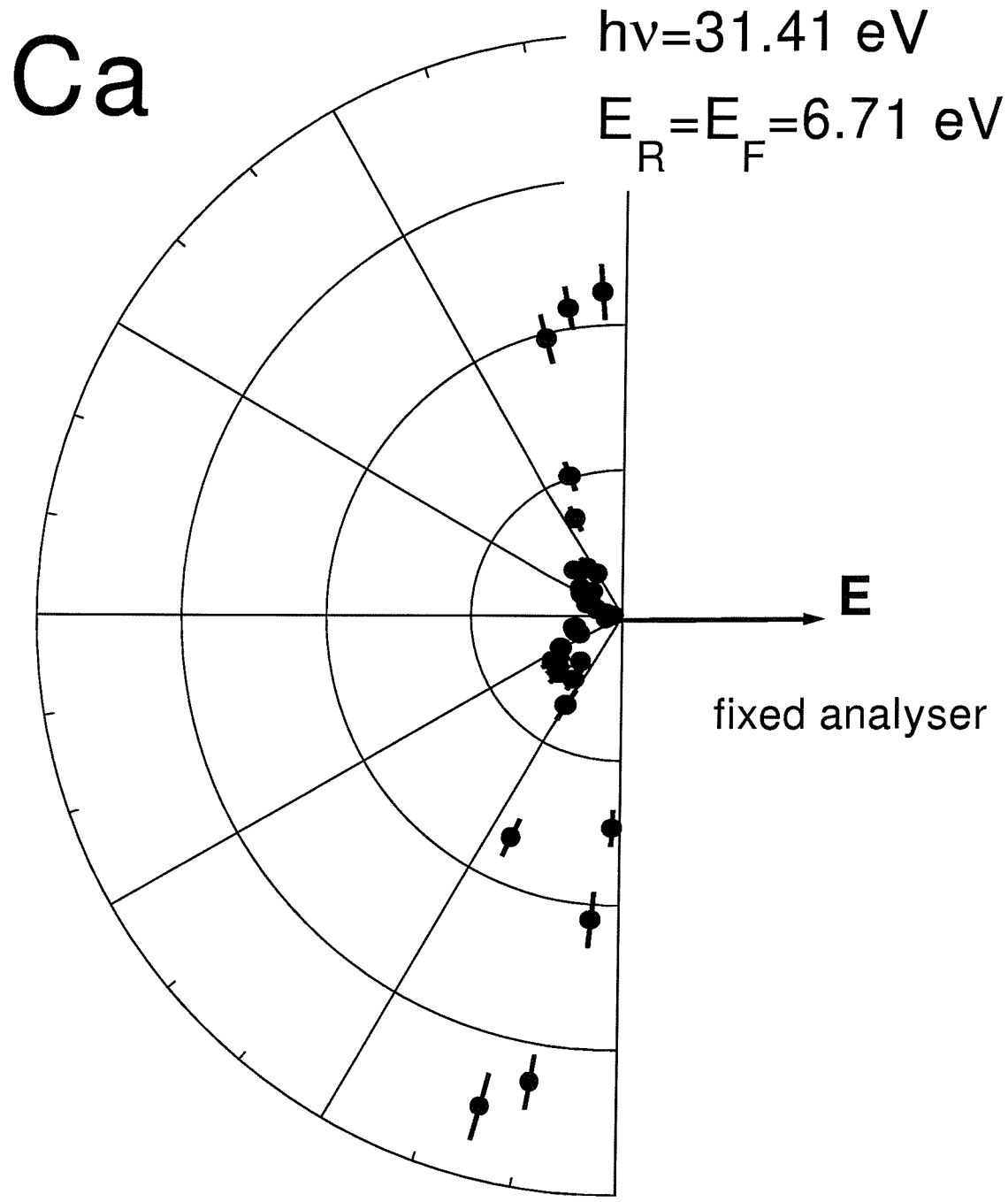

Figure 7.2: TDCS of Ca for equal energy sharing recorded at the resonant photon energy of 31.41 eV. The two electrons are emitted in the plane perpendicular to the photon beam; one electron is emitted in the direction of the **E** field of the radiation, indicated by the arrow, at $\theta_F = 0^o$.

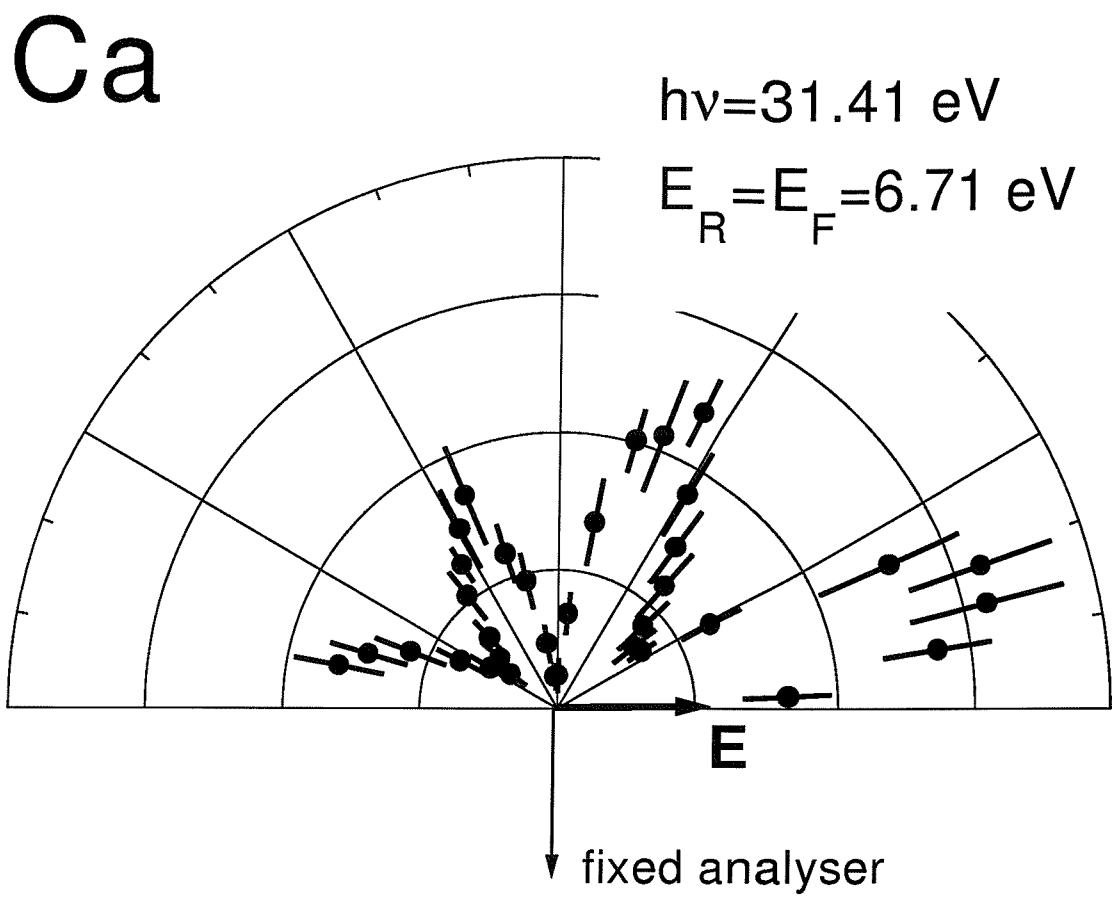

Figure 7.3: TDCS of Ca for equal energy sharing recorded at the resonant photon energy of 31.41 eV. The two electrons are emitted in the plane perpendicular to the photon beam; one electron is emitted in the direction perpendicular to the **E** field of the radiation, at $\theta_F = 270^o$.

effect rather than a real property of the TDCS. All available TDCS data for inert gases with the same experimental geometry as here show symmetry about $\theta_{RF} = 180^o$. One possible reason for this asymmetry is a slow change in the efficiency of the two analysers with time, as the electron analysers entrance slits are progressively coated with metal. Each data point takes on average two hours to measure, so that the data, which are an average of several measurements for each individual point, take many days to collect. Another reason for this asymmetry may be a change in the overlap between the space "seen" by the two analysers when one of them is rotated, although great care is taken to align the spectrometer before measurements are taken. A further possible explanation for the asymmetry might be a small constant angle of tilt between the direction of the major linear polarization and the direction of acceptance of the fixed analyser, although every previous systematic attempt to measure the degree and direction of linear polarization on the beam-line does not support this hypothesis [8]. The asymmetry in the data of figure 7.2 is not as strong as in figure 7.3; part of the reason is probably that this set of data has been corrected with the He calibration procedure as described in section 8.2.

Both figures 7.2 and 7.3 show a deep minimum at $\theta_{RF} = 180^o$, where in fact a zero is expected from the selection rules obtained in reference [9] and outlined in chapter 4; this zero is due to the unfavoured character of the ^1P symmetry for the electron continuum. Only a minimum rather than a zero is present, probably due to the finite angular acceptance of the electron analysers, as pointed out before. The fact that the minima at $\theta_{RF} = 180^o$ are very deep can be taken as an indication of the fact that the present angular and energy resolution are sufficiently high to resolve all the angular structure in the TDCS.

The main difference between the TDCS of He plotted in figure 4.1 of chapter 4 and those of Ca in figures 7.2 and 7.3 is the presence of an extra set of lobes. The four-lobe structures are reminiscent of the measured TDCS in the heavier rare gases where the DPI proceeds from the $3p^6$ shell, as can be seen, for example, in the TDCS of Ne in figure 4.2. Coupling between the $3p^4 4s^2\, ^1S_0$ and the $3p^6\, ^1S_0$ configurations in Ca were initially thought to be responsible for this four-lobe structure. However, the $3p^4 4s^2$ levels lie approximately $75\, eV$ higher than the $3p^6$ ground state and the mixing between these configurations must consequently be very small. A further point to observe in making comparison between the TDCS for rare gases other than He and the data for Ca, is that the lobes for the rare gases always extend outside the angular range $90^o \leq \theta_{RF} \leq 270^o$.

When figure 7.3 is compared with figure 7.2, it is initially surprising to notice that the two inner lobes for the case $\theta_F = 0^o$, in figure 7.2, are much smaller in size than those

for $\theta_F = 270^o$, in figure 7.3. This is in contrast to the case of He, where for equal energy sharing only two symmetric lobes appear, the relative TDCS for $\theta_F = 0^o$ and $\theta_F = 270^o$ being almost identical [10].

From the infinite expansion (3.39)-(3.43), and also from the limited $sp + pd$ expansion adopted in reference [12], it is clear that the highly structured TDCS can be interpreted as a consequence of strong correlation effects in the two-electron continuum.

The structure of the TDCS of Ca can be tentatively explained by considering the Ca atom to have a frozen core surrounded by two valence electrons that are described by a combination of l^2 configurations $(s^2 + p^2 + ...)$. Each l^2 configuration contributes to the $l(l+1)$ and $(l-1)l$ terms in the expansion (3.39)-(3.43), leading to more complicated functions of θ_{RF} in the expression for the TDCS, which in turn are responsible for the additional lobes in the TDCS of Ca. A similar discussion of the DPI of He would have only small contributions from l^2 configurations other than s^2, leaving the sp configuration as the dominant configuration in the continuum. Unfortunately this explanation is not able to give any role to the resonant state.

In view of the fact that the additional structure in the TDCS of Ca when compared to the TDCS of He is probably due to a more correlated initial state resulting from a higher atomic number Z, it would be very interesting to pursue a systematic study of TDCS in all the alkaline earth atoms, the higher the value of Z the more structure is expected in the TDCS. The work described in this thesis is the beginning of such a study. It would also be interesting to study the TDCS in an $np^2\,{}^1S$ system, in order to understand how an $np^2\,{}^1S$ configuration would contribute to the TDCS; unfortunately systems with np^2 configuration, such as C, have ground state of ${}^3P$ symmetry, not ${}^1S$.

The fact that in this work DPI proceeds via a resonant state further increases the degree of correlation in the continuum: higher values of l for the outgoing electrons can be built up by the coupling of angular momenta between those of the excited resonance orbital and of the ionic core during the finite lifetime of the excited state. This idea suggests that it would be interesting to pursue a systematic study of how different resonances affect the TDCS, this has been partly achieved in the work described in this chapter. If such resonant enhancement of high values of l occurs, it would have a parallel in what happens to the anisotropy parameters β for single photoionization of molecules when photoionization proceeds via resonant Rydberg states [11].

The above interpretation would suggest that the resonance enhances the correlation of the two electrons continuum. In this perspective the presence of the resonance may be considered responsible for the four-lobe structure in the data of figures 7.2 and 7.3. How-

ever, it is important to remember that both the theoretical works on off-resonant DPI of Ca by Kazansky and Ostrovsky in 1997 [4] and by Malegat *et al.* in 2000 [5], mentioned in section 4.4, showed a four-lobe structure in the TDCS and were made at off-resonant energies.

The expansion (3.39)-(3.43), with an additional gaussian correlation factor $C(\theta_{RF})$, has been tentatively applied to the data in figures 7.2 and 7.3. When a single *sp* configuration is included in the two-electron continuum this expansion has the following form:

$$(\cos\theta_R + \cos\theta_F)^2 |D_{sp}|^2 C(\theta_{RF}), \tag{7.5}$$

with

$$C(\theta_{RF}) = \exp\left[-\ln 2\left(\frac{\theta_{RF} - 180^o}{\theta_{fwhm}}\right)^2\right]; \tag{7.6}$$

when a *pd* configuration is also included the following factor replaces D_{sp} in equation (7.5):

$$D_{sp} - \frac{D_{pd}}{\sqrt{2}}(3\cos\theta_{RF} - 1); \tag{7.7}$$

if, in addition, the contribution from the *df* configuration is also considered, the following must be substituted for D_{sp} in equation (7.5):

$$D_{sp} - \frac{D_{pd}}{\sqrt{2}}(3\cos\theta_{RF} - 1) + \frac{2D_{df}}{\sqrt{7}}\left(\frac{15}{2}\cos^2\theta_{RF} - 3\cos\theta_{RF} - \frac{3}{2}\right). \tag{7.8}$$

The presence of values of l up to a certain value l_{max} in this expansion makes the second factor in (7.5) a polynomial in $\cos\theta_{RF}$ of order $2(l_{max} - 1)$, with $2(l_{max} - 1)$ linearly independent coefficients plus an overall scale factor.

In an attempt to reproduce the data in figures 7.2 and 7.3 the parameterization (7.5)-(7.8) was tentatively applied to these data, with up to a *d* wave ($l_{max} = 2$). It has not been possible in this work to reproduce the data in figures 7.3 and 7.2 with such a parameterization; fits with more parameters have not been attempted. If the parameters $M_{(l-1)l}$ could be extracted from the fitting of the data in figure 7.2 (or 7.3), they could then be applied to try to reproduce the data in figure 7.3 (or 7.2). Such an analysis would have been a test of consistency for both the analysis and the experiments.

A similar analysis was performed very recently by Maulbetsch *et al.* [13]: an *ansatz* was

made to fit the data in figure 7.3, those with $\theta_F = 270^o$, using the following expression:

$$TDCS = C \left| \sum_{l}^{l_{max}} A_l \left[B_{10}^{(l-1)l}(\mathbf{\Omega_R}, \mathbf{\Omega_F}) + B_{10}^{(l-1)l}(\mathbf{\Omega_F}, \mathbf{\Omega_R}) \right] \right|^2 , \tag{7.9}$$

where $B_{10}^{(l-1)l}$ are bipolar harmonics, $\mathbf{\Omega_F}$ and $\mathbf{\Omega_R}$ are spherical angles of emission of the two outgoing electrons and the coefficients A_l are complex numbers to be fitted. This expansion is a rearrangement of equations (3.39)-(3.43), with $S_1 = 1$. In the cited work the parameterization of equation (7.9) was found to reproduce the data in figure 7.3, where $\theta_F = 270^o$, with $l_{max} = 3$ (up to the fg configuration). The same parameters A_0, ..., A_3 extracted from the fit of the data in figure 7.3 could then reproduce the data of figure 7.2, where $\theta_F = 0^o$.

The results of these fittings are shown in figure 7.4. In this figure the data are made symmetric with respect to $\theta_{RF} = 180^o$ by taking the average of the data at $\theta_{RF} > 180^o$ and $\theta_{RF} < 180^o$. The upper figure contains the data for the TDCS of Ca from figure 7.3, and the solid line is the best fit to these data with the ansatz (7.9). The lower figure contains the data for the TDCS of Ca from figure 7.2; the solid line is the function (7.9) with the parameters obtained from the previous fit. The contribution to the TDCS from different terms are as given in the figure captions. It is clear that the contribution from the configurations pd and df are dominant and show destructive interference.

In this way Maulbetsch *et al.* [13] proved that the two sets of data in figures 7.2 and 7.3 are consistent, even though it is initially surprising to see that the inner lobes are small in figure 7.3 whereas in figure 7.2 they have approximately the same size as the outer lobes.

What has been achieved in the work of reference [13] is a success. However, in that work the fitted values of A_0, ..., A_3 are all of comparable amplitudes, making their physical meaning somewhat obscure for the following reason. In mixing electronic configurations it is desirable for one configuration to be strongly dominant and for a very limited number of other configurations to provide non negligible but small contribution; if this is not the case the following argument could apply: although equation (7.9), with $l_{max} = 3$, reproduces both sets of data in figures 7.2 and 7.3 with only one set of A_l, the inclusion of $l_{max} > 3$ could result in $|A_{l>3}|$ of the same order of magnitude of $|A_{l\leq 3}|$. Such a result would suppress possible physical interpretations of $|A_l|$ as weights of electronic configurations.

At the present time, the interpretation of the measured TDCS of Ca by an expansion in electronic configurations shows agreement with the experimental data but does not provide clear physical insight into the DPI process.

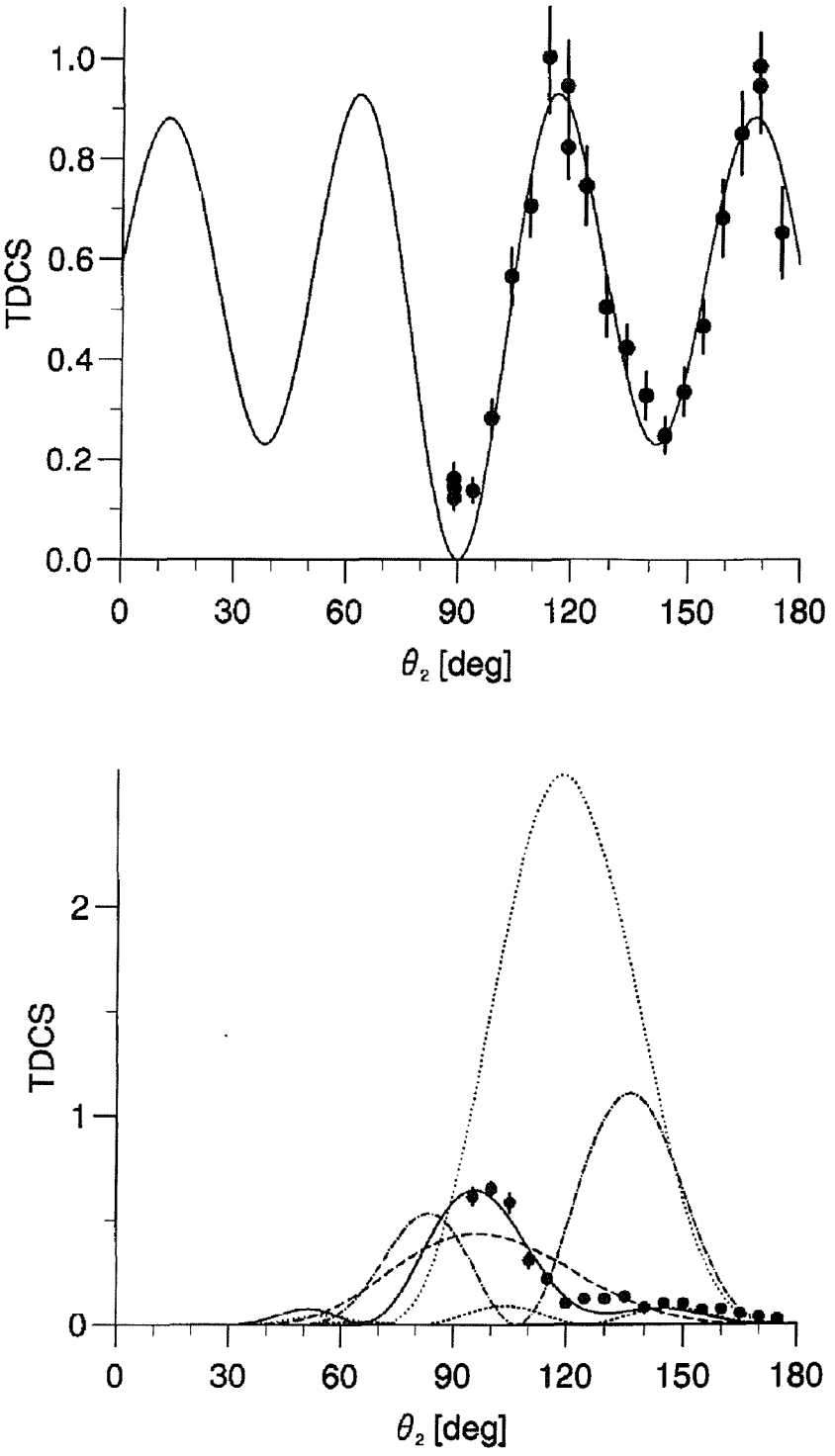

Figure 7.4: Upper: experimental data points for the TDCS of Ca with $\theta_F = 270°$, fitted with the ansatz of Maulbetsch *et al.*. Lower: experimental data points for the TDCS of Ca with $\theta_F = 0°$. The solid line is the best fit of the ansatz of Maulbestch *et al.*. The contribution to the TDCS from different terms are as follows: long dashed: *sp*, dotted: *pd*, dot-dashed *df*, short-dashed: *fg*.

7.2.4 TDCS of Ca at the $31.41\,eV$ *giant* resonance: unequal energy sharing

In this work studies were made on the TDCS of Ca at the $3d \leftarrow 3p$ resonance at $h\nu = 31.41\,eV$, also for unequal energy sharing. Figures 7.5 and 7.6 show the measured TDCS for $\theta_F = 0^o$ with $E_R = 4.48\,eV$, $E_F = 9.95\,eV$ and $E_R = 9.95\,eV$, $E_F = 4.48\,eV$ respectively. The data in figure 7.7 are from the work of Ross *et al.* [3] and were not recorded during the work of this thesis, they show the measured TDCS for $\theta_F = 270^o$, with $E_R = 8.8\,eV$, $E_F = 4.6\,eV$.

The data in figures 7.5 and 7.6 have been corrected with the He calibration procedure for change in efficiency of the two electron analysers outlined in section 8.2, nevertheless they show asymmetry, probably due to the factors already discussed in section 7.2.3.

As pointed out in section 7.2.3, the selection rules reported by Maulbetsch and Briggs in reference [9] forbid antiparallel emission of the two electrons when they have the same energy. When the electron energies are no longer equal these selection rules "progressively" break down: for nearly equal energies a minimum rather than a zero should be present at $\theta_{RF} = 180^o$, and for further unequal energies this minimum gains in intensity and it can become a maximum [14].

Minima are present for antiparallel emission in figures 7.5 and 7.6, and an even more marked minimum is present in figure 7.7 at $\theta_{RF} = 180^o$. It must be observed that the minima for antiparallel emission in figures 7.5, 7.6 and 7.7, that refer to unequal energy sharing, are not as marked as the one in figure 7.3, and in particular in figure 7.2, that are both for equal energy sharing. Optimistically, this could be considered as evidence for the breakdown of the selection rule that forbids antiparallel ejection, expected when moving from equal to unequal energy sharing.

From comparison between the plots in figures 7.5, 7.6 and 7.7, and those in figures 7.2 and 7.3 it seems that at this excess energy ($E_{exc} = 13.34\,eV$) the TDCS show little dependence on the energy sharing when moving from $E_R = E_F = 6.67\,eV$ to $E_R = 4.48\,eV$, $E_F = 8.95\,eV$ or to $E_R = 8.95\,eV$, $E_F = 4.48\,eV$. The fact that this happens for both $\theta_F = 0^o$ and $\theta_F = 270^0$ is an indication of consistency between the two sets of measured TDCS.

It is known both from theory [15] and experiment [16], that for the TDCS of He the lower the excess energy, the lower is the dependence on the energy sharing, and the same is expected for Ca. From the results published in reference [17] it is clear that in He at $E_{exc} = 6\,eV$, changing from $E_R = 3$, $E_F = 3\,eV$ to $E_R = 4.8$, $E_F = 1.2$ or to $E_R = 1.2$, $E_F = 4.8$ does not make a big difference to the TDCS. In the present work in

Ca the measured TDCS is at $13.43\,eV$ above threshold, and the non-dependence of the TDCS on energy sharing is against what would be expected at this excess energy. The low energy background in the electron analysers did not allow measurements at further unequal energy sharing to be recorded.

Figure 7.8 shows the measured TDCS of Ca at the photon energy of $h\nu = 31.41\,eV$, with the two electrons emitted at $\theta_F = 180^o$ and $\theta_R = 0^o$, as a function of the difference between their energies. The progressive breakdown of the selection rule that forbids antiparallel emission of the two electrons when they have the same energy is evident from the figure. The linear trend of the first 5 data should not be given too great weight as the efficiencies of both electron analysers depend on the energy of the electrons transmitted in an unknown way.

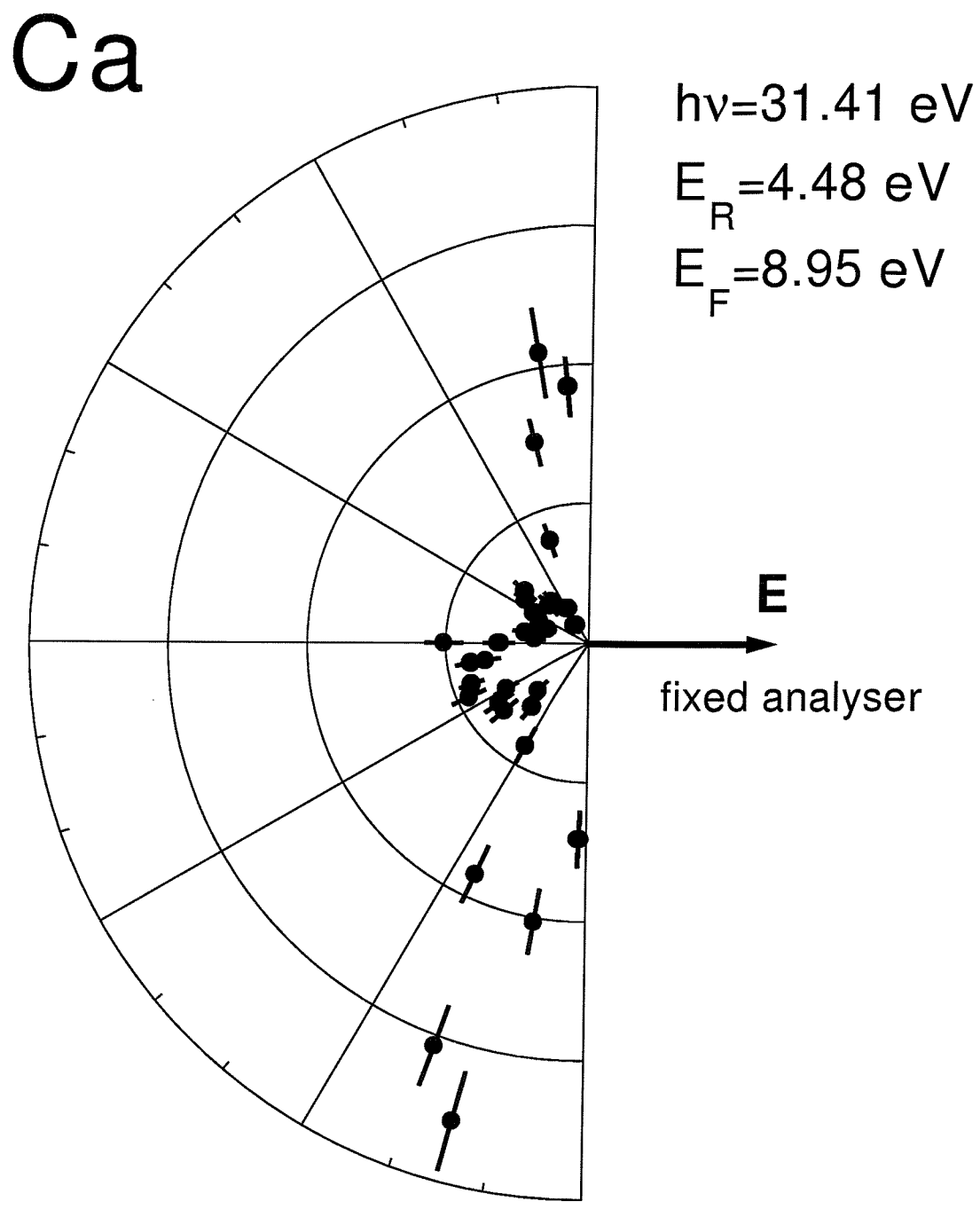

Figure 7.5: TDCS of Ca recorded at the resonant photon energy of 31.41 eV. The two electrons have different kinetic energies and are emitted in the plane perpendicular to the photon beam; one electron is emitted in the direction of the **E** field of the radiation, indicated by the arrow, at $\theta_F = 0^o$.

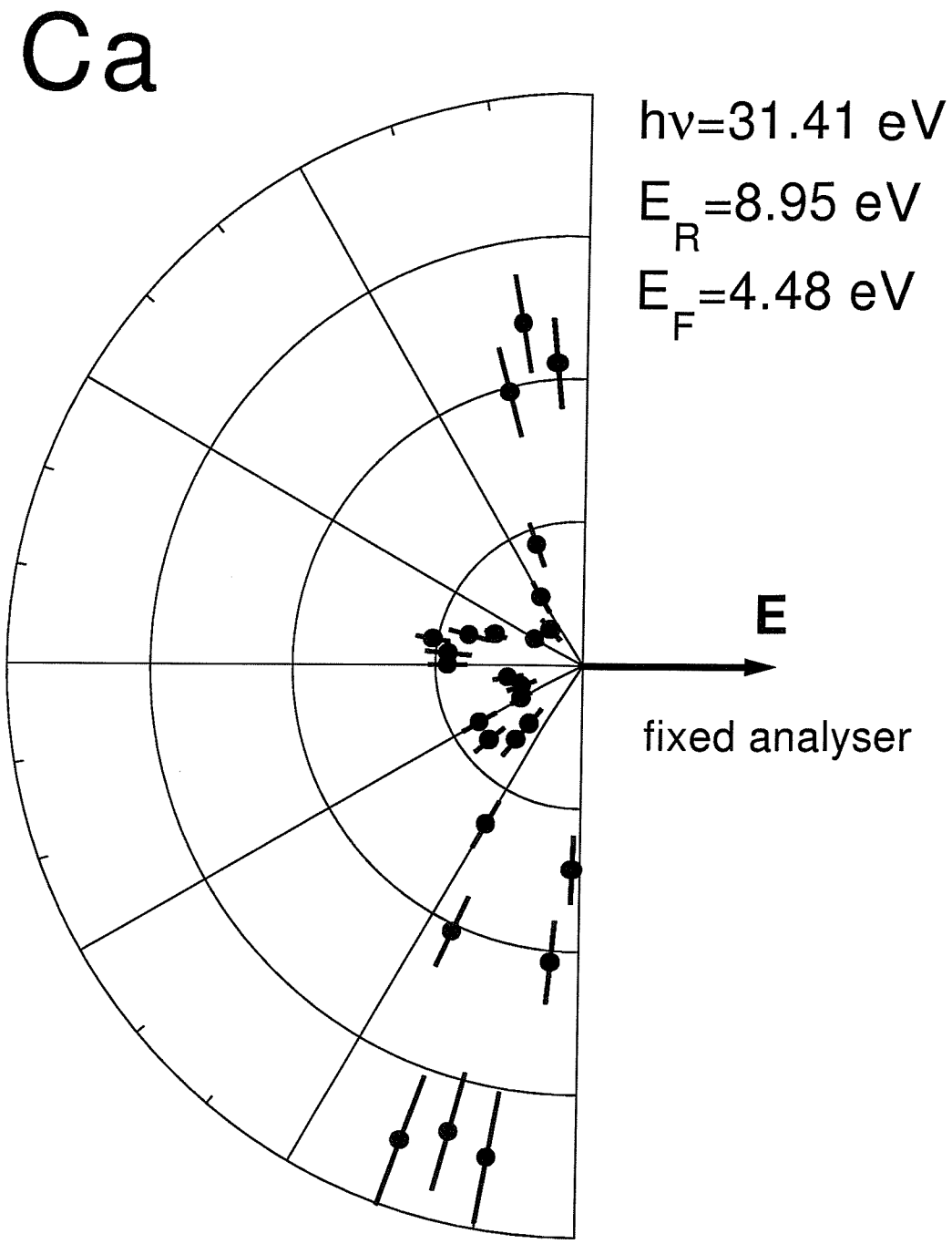

Figure 7.6: TDCS of Ca recorded at the resonant photon energy of $31.41\,eV$. The two electrons have different kinetic energies and are emitted in the plane perpendicular to the photon beam; one electron is emitted in the direction of the **E** field of the radiation, indicated by the arrow, at $\theta_F = 0^o$.

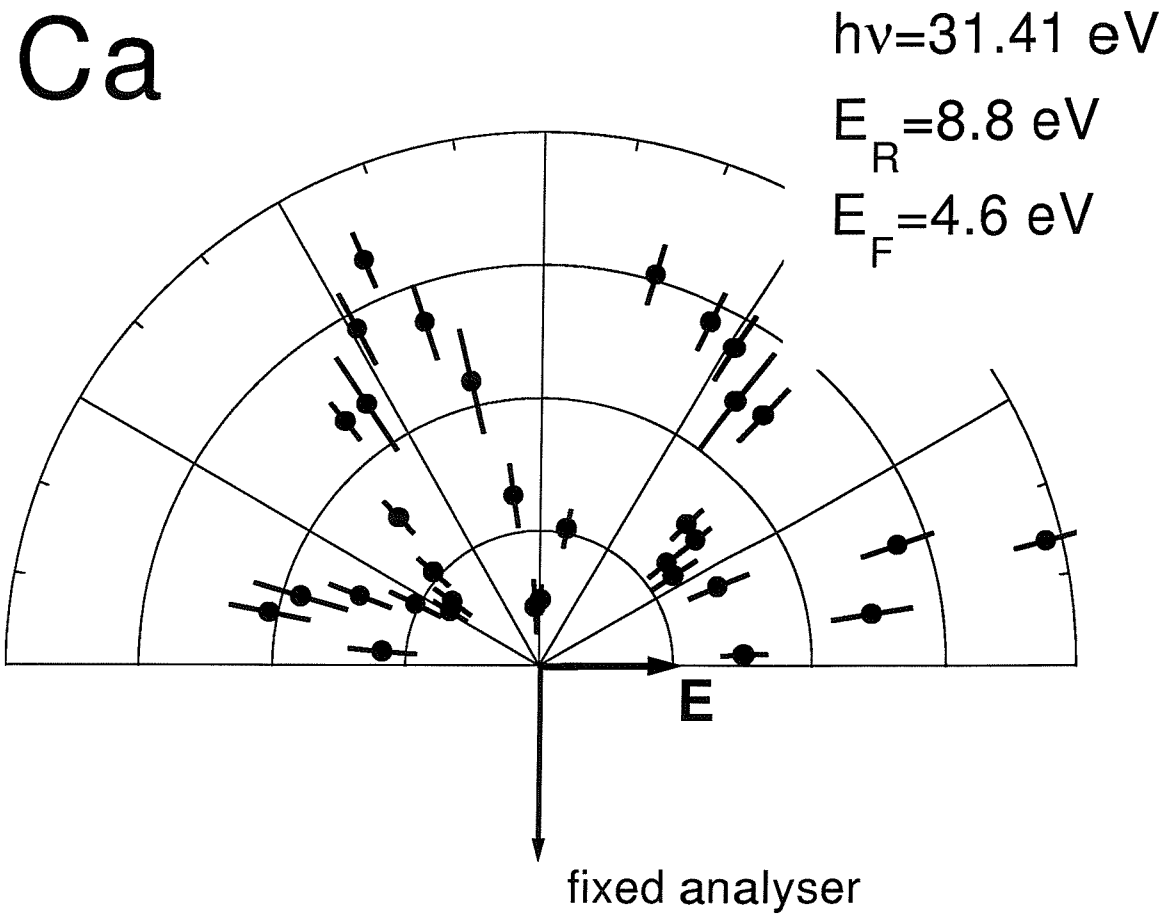

Figure 7.7: TDCS of Ca recorded at a resonant photon energy of 31.41 eV. The two electrons have different kinetic energies and are emitted in the plane perpendicular to the photon beam; one electron is emitted in the direction perpendicular to the **E** field of the radiation, at $\theta_F = 270^o$.

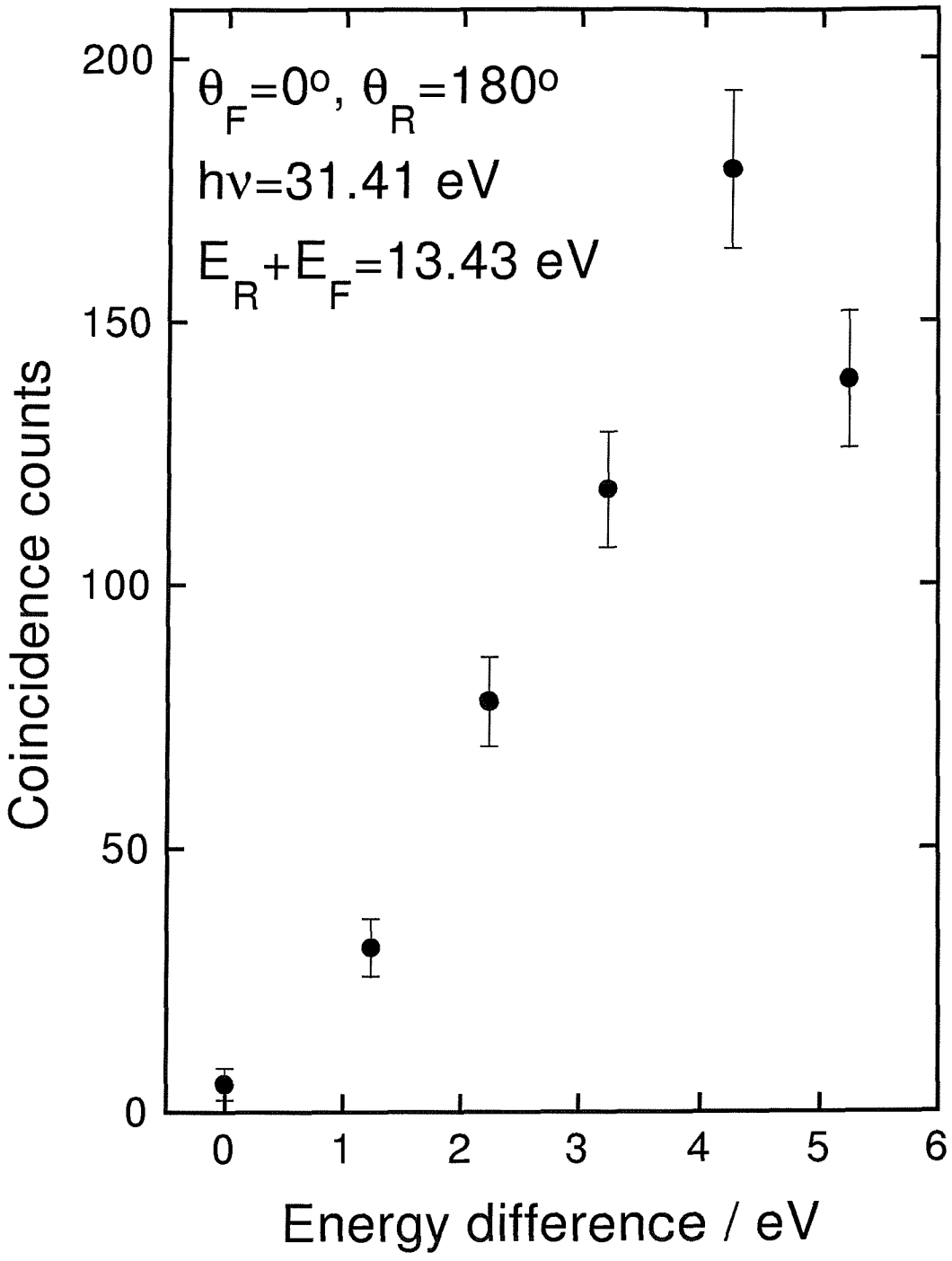

Figure 7.8: TDCS of Ca at $\theta_F = 180^o$ and $\theta_R = 0^0$ at the resonant photon energy of $h\nu = 31.41\,eV$, as a function of the difference between the energies of the two electrons.

7.2.5 TDCS of Ca at the $31.56\,eV$ side resonance: equal energy sharing

Measurements of TDCS were also recorded at the photon energy of $h\nu = 31.56\,eV$ for equal energy of the emitted electrons. At this photon energy the incident radiation is tuned to the side resonance in the CIS spectra of figure 7.1.

The results of these measurements are reported in figure 7.9. The fixed analyser was positioned to accept electrons emitted at $\theta_F = 0^o$, parallel to the **E** field of the radiation beam. The data in figure 7.10 are from the work of Ross *at al.* [3] and were not recorded during the work of this thesis. These latter measurements were obtained with the fixed analyser set at $\theta_F = 270^o$, perpendicular to the **E** field of the radiation.

The data in figures 7.9 and 7.10 are asymmetric about $\theta_{RF} = 180^o$, the possible reasons for this asymmetry have been discussed in section 7.2.3.

As it has been mentioned in section 4.2, from the selection rules of reference [9] a zero in the TDCS is expected at $\theta_{RF} = 180^o$, when the emitted electrons have the same energy. The data in figure 7.9, obtained with $\theta_F = 0^o$, show a zero for antiparallel emission, in agreement with what is expected from the selection rule.

In the data of figure 7.10 a deep minimum rather than a zero is present at $\theta_{RF} = 180^o$, in apparent disagreement with the above mentioned selection rule. A possible reason for the finite value of the measured TDCS for antiparallel emission is the finite angular acceptance of the analysers, as explained in section 7.2.3. The finite energy resolution of the analysers could also, in principle, be responsible for the finite value of the TDCS at $\theta_{RF} = 180^o$; however, at this excess energy the TDCS is expected to depend very smoothly on the energy difference of the two electrons, and the finite energy resolution of the analyser cannot have any observable effects on the measured TDCS.

It is interesting to observe that at this side resonance, unlike at the *giant* resonance at $31.41\,eV$, the TDCS measured for $\theta_F = 0^o$ and for $\theta_F = 270^o$, shown in figures 7.9 and 7.10 respectively, look very similar to each other. The reason for their similarity is unknown at the present time.

In both TDCS observed at the $31.56\,eV$ side resonance shown in figures 7.9 and 7.10 two nearly symmetric maxima are present at approximately $\theta_{RF} = 135^o$ and 225^o. After a minima at $\theta_{RF} = 250^o$ there is a clear indication of the TDCS rising up again, showing not only that the TDCS contains more than two lobes, but also that the maxima of the second pair of lobes lie in the forward direction, as observed in the TDCS of rare gases other than He [12].

It is also very interesting to notice that at the side resonance at $31.56\,eV$ both measured TDCS at $\theta_F = 0^o$ and at $\theta_F = 270^o$, shown in figures 7.9 and 7.10 respectively, are very different from those at $h\nu = 31.41\,eV$ at the same angles, shown in figures 7.2 and 7.3.

The difference between the TDCS measured at the $31.41\,eV$ *giant* resonance and at the $h\nu = 31.56\,eV$ side resonance clearly confirms that the TDCS is dependent on the resonance selected. The change in the TDCS when moving from $h\nu = 31.41\,eV$ to $h\nu = 31.56\,eV$ cannot be due to the different excess energy, as this changes only from $E_{exc} = 13.43\,eV$ at $h\nu = 31.41\,eV$ to $E_{exc} = 13.58\,eV$ at $h\nu = 31.56\,eV$; only the different characters of the resonances can be considered responsible for the difference in the measured TDCS. The dependence of the TDCS on the selected resonance also confirms that the process under investigation cannot be regarded as pure DPI, but it must be seen as double autoionization of the excited neutral state to the continuum of the doubly charge ion.

Kazansky and Ostrovsky in 1997 [4] sustained that the difference between the measured TDCS of He and Ca is only a consequence of the different radial distribution of the valence orbital in the initial neutral states. The results presented in this section clearly proves that the conclusion of reference [4] cannot be extended to resonant DPI, as this would have made the TDCS measured at the $31.41\,eV$ *giant* resonance to appear identical to the TDCS measured at the $31.56\,eV$ side resonance.

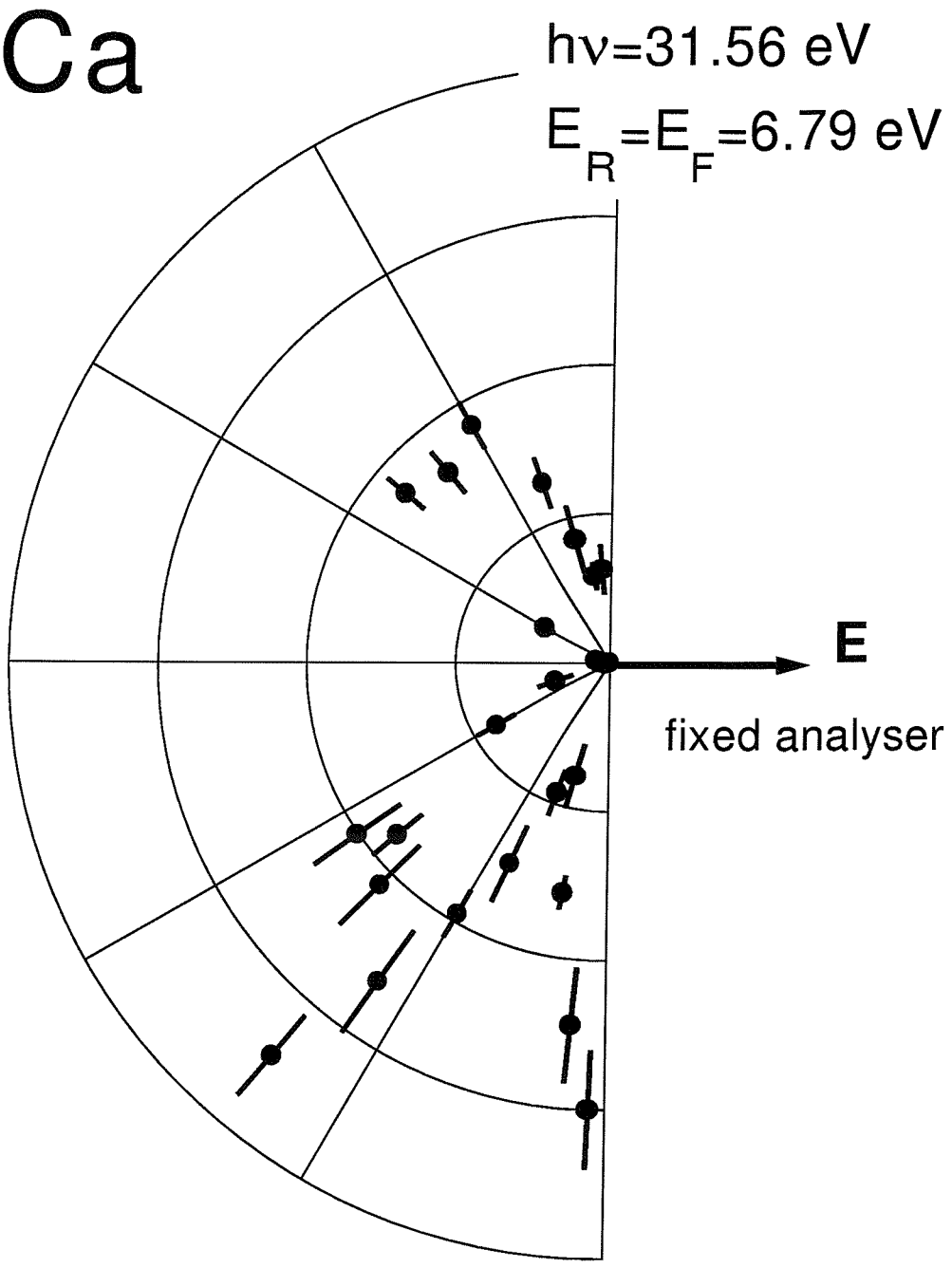

Figure 7.9: TDCS of Ca recorded at the resonant photon energy of 31.56 eV. The two electrons are emitted with the same energy in the plane perpendicular to the photon beam; one electron is emitted in the direction of the **E** field of the radiation, indicated by the arrow, at $\theta_F = 0^o$.

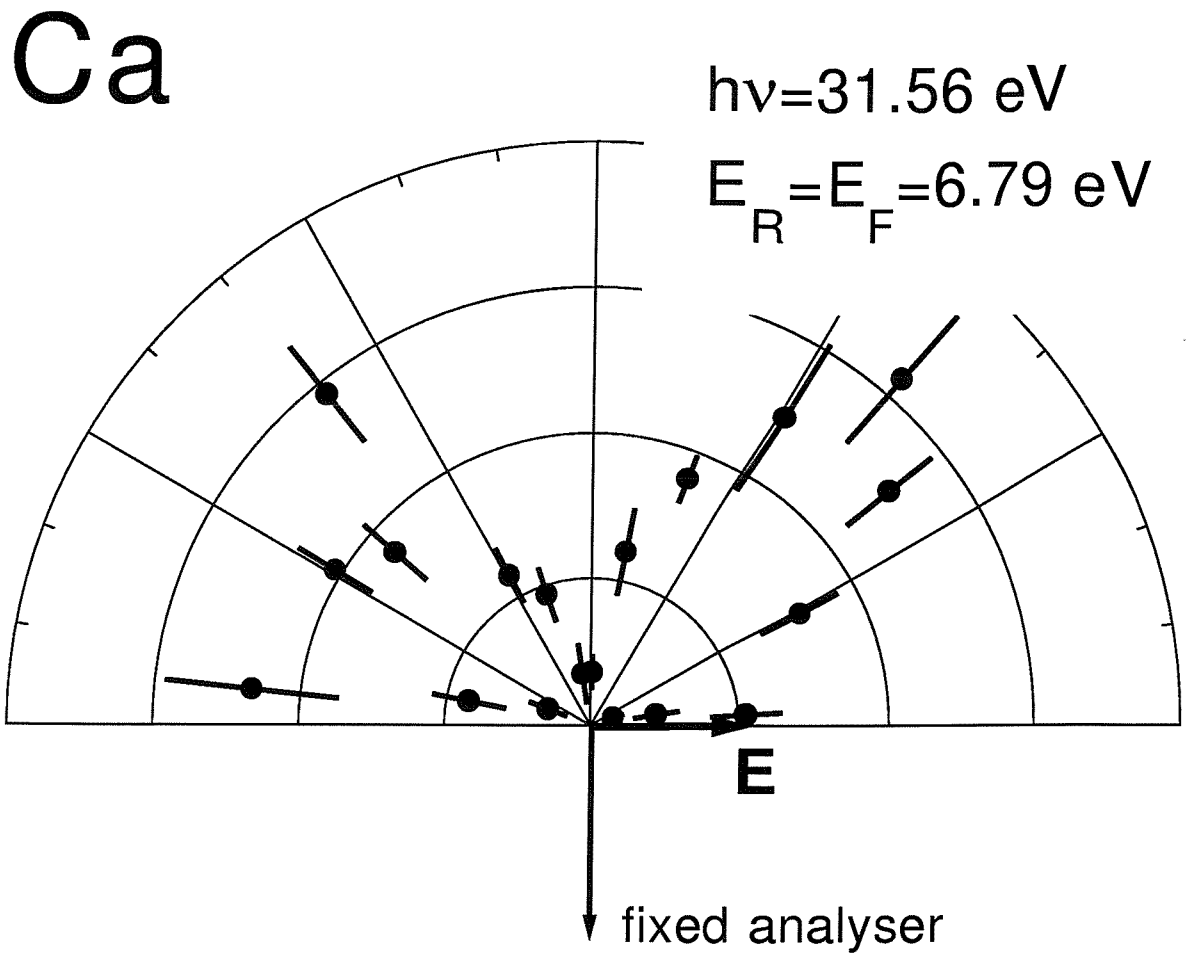

Figure 7.10: TDCS of Ca recorded at the resonant photon energy of $31.56\,eV$. The two electrons are emitted with the same energy in the plane perpendicular to the photon beam; one electron is emitted in the direction perpendicular to the **E** field of the radiation, at $\theta_F = 270°$.

7.3 Off-resonant TDCS of Ca at $h\nu = 43.03\,eV$

As it has been emphasized before, due to a very low coincidence counts rate, it was not possible to measure the TDCS of metal vapours at non resonant photon energies at the Daresbury SRS.

In the attempt to make measurements of TDCS of Ca at a non-resonant photon energy, where only the direct DPI process is possible, the spectrometer was transported to the Elettra SRS in Trieste, and attached to the gas phase photoemission beam-line described in section 2.6.

Before moving to Elettra, it was expected that in the region of interest, $h\nu = 30 - 40\,eV$, the photon flux at Elettra would have been higher by at least two orders of magnitude than on beam-line 3.3 at the Daresbury SRS; in the event it proved to be higher by approximately a factor of 25.

In choosing a continuum photon energy, an energy as close as possible to the $31.41\,eV$ *giant* resonance was desired, in order to study the change in the TDCS when moving off-resonance, but without introducing effects due to a different excess energy. Unfortunately, the undulator gap for the beam-line at Elettra could not be tuned below $40\,eV$, and as a result the photon energy was tuned to $43.03\,eV$; this value was carefully choosen in order to avoid both neutral resonances and two-step DPI processes.

At the photon energy of $43.03\,eV$ the excess energy is $E_{exc} = 25.05\,eV$, almost twice the excess energy of $13.43\,eV$ at the $31.41\,eV$ *giant* resonance. It was thought that although the difference in excess energy could be partly considered responsible for small differences between the resonant and the non-resonant TDCS, if they could be observed, it would not cause major changes in the general shape of the TDCS, such as the number of lobes. This opinion is supported by the fact that the TDCS of He does not show dramatic changes in shape when the excess energy is varied [18].

The degree of linear polarization of the radiation from the beam-line used at Elettra, $S_1 \simeq 0.95$, is higher than that of beam-line 3.3 at the Daresbury SRS, $S_1 \simeq 0.75$, this difference is not expected to make a considerable change in the measured TDCS.

The TDCS measured at the photon energy of $43.03\,eV$ is shown in figure 7.11 on a cartesian graph for equal energy of the two electrons: $E_R = E_F = 12.53\,eV$. One electron is observed in the direction of the **E** field of the radiation, and both electrons are emitted in the plane perpendicular to the photon beam. Each data point took approximately 12 hours to collect.

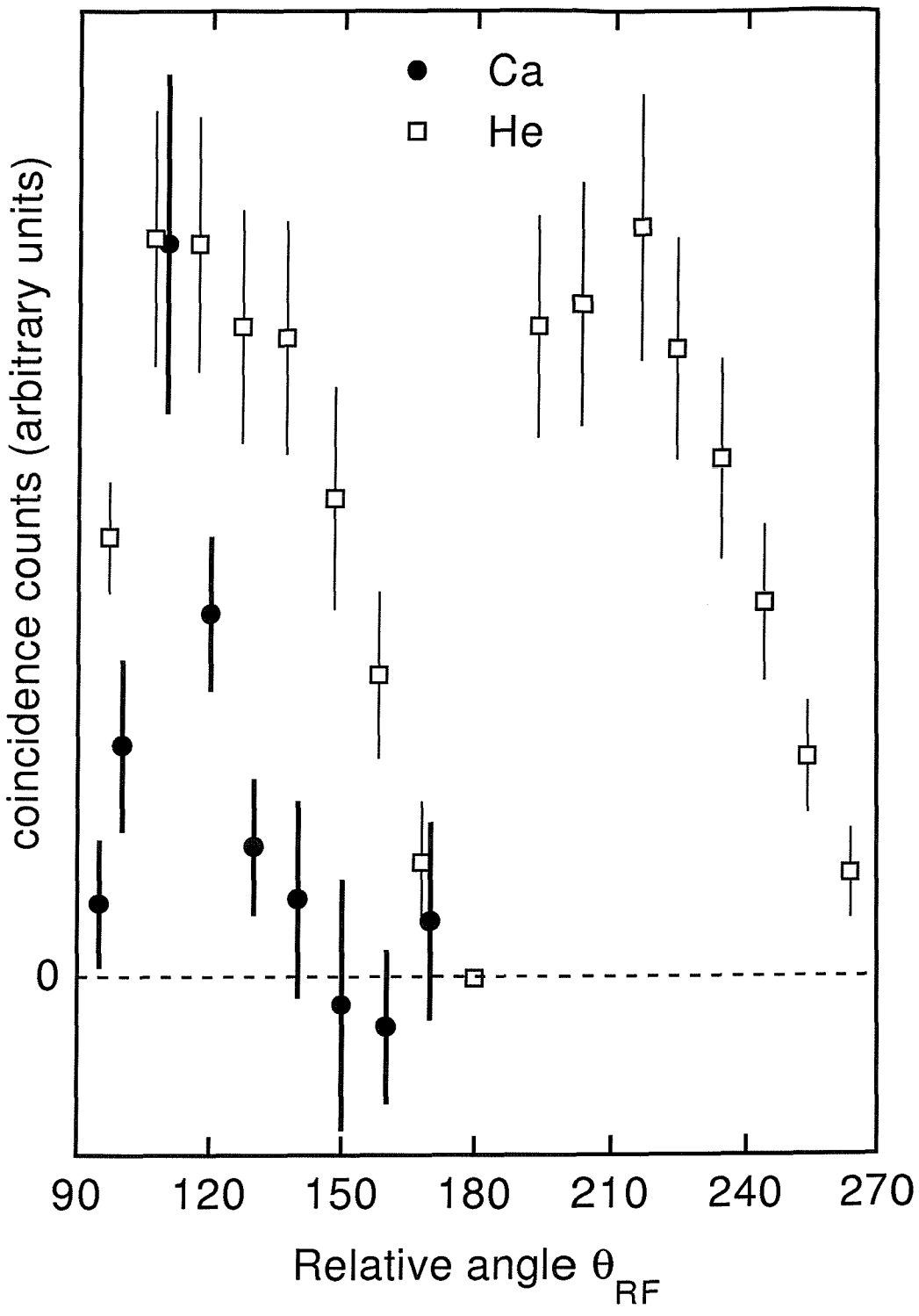

Figure 7.11: TDCS of Ca measured at the non resonant photon energy of $43.03\,eV$. The two electrons are emitted with the same energy in the plane perpendicular to the photon beam, that is almost completely polarized, $S_1 \geq 0.95$. One electron is emitted in the direction of the **E** field of the radiation, at $\theta_F = 0^o$.

The error bars in figure 7.11 contain only the statistical contribution from the *true* and *false* coincidences. It can be noticed that the relative accuracy of the data points in figure 7.11 is not as good as in the previous TDCS of Ca shown in this chapter; this is a consequence of an overall lower coincidence rate in this experimental condition. Each data point in the graph of figure 7.11 is the result of measurements over a period of time of several hours. The small He correction procedure for the efficiency of the analysers, as described in section 8.2, was not applied, as it would have brought only very small changes in the relative intensities of the points.

The most interesting feature of the Ca data in figure 7.11 is that only one maximum is present in the displayed angular range $90^o \leq \theta_{RF} \leq 180^o$. This is in striking contrast to the double lobe structure present in the TDCS measured at the 31.41 eV *giant* resonance, in particular with the measurements of figure 7.3 where the "fixed" electron is emitted at $\theta_F = 270^o$. It is also relevant to notice that the measured TDCS has a very low value at $\theta_{RF} = 170^0$, as is also the case for the other measurements of TDCS presented in this chapter, and also in agreement with the zero expected from the selection rules for antiparallel emission of reference [9].

The measured off-resonant TDCS of Ca shown in figure 7.11 is in evident discrepancy with the theoretical results of Kazansky and Ostrovsky in 1997 [4], and of Malegat *et al.* in 2000 [5], that have been discussed in section 4.4. In both these theoretical works two lobes were found in the angular quarter $90^o \leq \theta_{RF} \leq 180^o$. The excess energies considered in these works were up to 15.50 and 10.00 eV respectively, whereas in the experiment reported here the excess energy is 25.03 eV. This difference in excess energy may be partly responsible for the difference observed between experiments and theory. It is in fact clear from both the works of references [4] and [5] that the two-lobe structure in the TDCS of Ca becomes less pronounced at higher excess energy.

7.3.1 Comparison between the TDCS of Ca at resonant and non resonant photon energies

It is useful to make a comparison of the present data in figure 7.11 with the measurements of TDCS of Ca recorded at resonant photon energies shown in figures 7.2 and 7.9 and discussed in sections 7.2.4 and 7.2.5. To facilitate these comparisons the resonant and non-resonant TDCS of Ca are plotted on the same graphs in figure 7.12. With the quality of the present non-resonant data it can be concluded not only that the non-resonant TDCS is different from the TDCS at the 31.41 eV *giant* resonance, where two maxima with different relative intensities are clearly present in the angular quarter $90^o \leq \theta_{RF} \leq 180^o$, but also

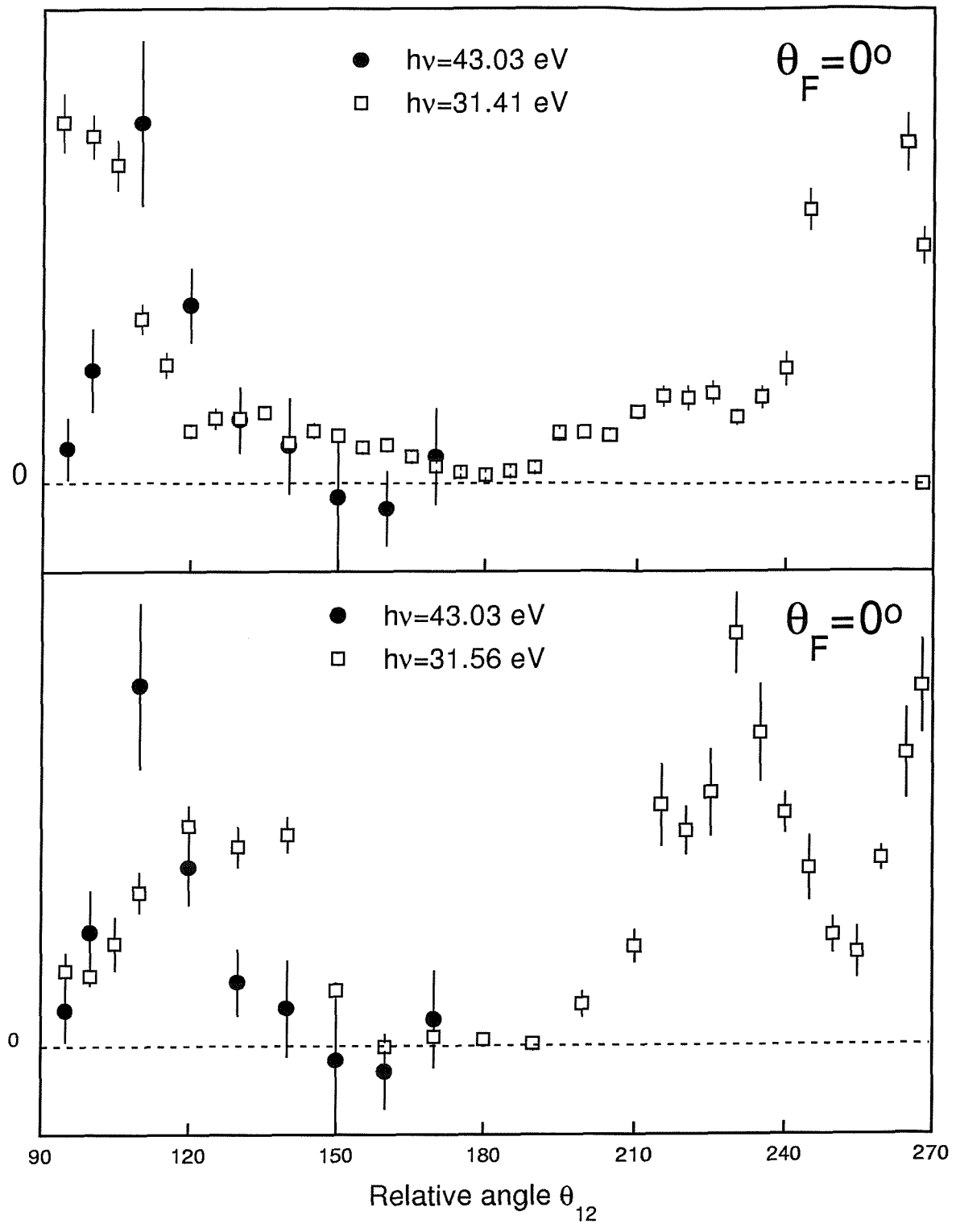

Figure 7.12: Upper: comparison between the TDCS of Ca at the non resonant photon energy of $43.03\,eV$ and at the $31.41\,eV$ *giant* resonance. Lower: TDCS of Ca at the non resonant photon energy of $43.03\,eV$ and at the $31.56\,eV$ resonance. In all sets of data the two electrons have the same energy, one electron is emitted in the direction of the **E** field of the polarized radiation, at $\theta_F = 0^o$, and both electrons are emitted in the plane perpendicular to the photon beam.

that the off-resonant TDCS is very different from the TDCS measured at the resonance at $31.56\,eV$, where only one maximum is present in the range $90 \leq \theta_{RF} \leq 180^o$. The single maximum in the TDCS measured at $h\nu = 31.56\,eV$ is broader that the maximum in the off-resonant TDCS, and is also centered in a different angular position: $\theta_{RF} = 130^o$ rather than $\theta_{RF} = 110^o$ for the non-resonant TDCS.

7.3.2 Comparison between the TDCS of Ca and of He

In figure 7.13 the data for the TDCS of He from reference [19] are included with the present Ca measurements on a cartesian graph for a direct comparison. The data have been scaled in such a way to give similar intensities to the maxima of Ca and He. The data for the TDCS of He were recorded at an excess energy of $20.00\,eV$ and equal energy sharing; one electron is emitted parallel to the **E** field of the photon beam, which is almost completely polarized. It is particularly interesting to observe that, although the main feature of a single peak in the angular quarter $90^o \leq \theta_{RF} \leq 180^0$, as well as the zero for antiparallel emission, are common to the Ca and He data, the TDCS of Ca and He appear clearly different. The peak in the TDCS of Ca is much narrower than in the data of He. Even though the measurements have been obtained for different excess energies, 20.00 and $25.05\,eV$ for He and for Ca respectively, it is believed that the different excess energies cannot be responsible for such an evident difference in the TDCS.

7.3.3 Absolute values of cross sections for the DPI of Ca

An attempt was made to extract the ratio between the absolute cross sections of DPI of Ca at the resonant and non resonant energies of 31.41 and $43.03\,eV$. In order to do this the TDCS at the photon energy of the *giant* resonance was measured during the beam-time at Elettra, for a relative angle of emission of $\theta_{RF} = 100^o$. From the number of coincidence per unit of time, at the photon energies of 31.41 and $43.03\,eV$, and with the relative photon flux obtained from the current measured by the photodiode at the back of the chamber, an estimate of the ratio between the cross sections at resonant and non-resonant photon energy could be obtained, and resulted in

$$DPI(h\nu = 31.41\,eV) : DPI(h\nu = 43.03\,eV) \approx 5310 : 1. \tag{7.10}$$

It is very difficult to estimate the error in this number, only the order of magnitude of this numerical result can be trusted.

The ratio (7.10) gives an indication of the difficulty of measuring the off resonant TDCS

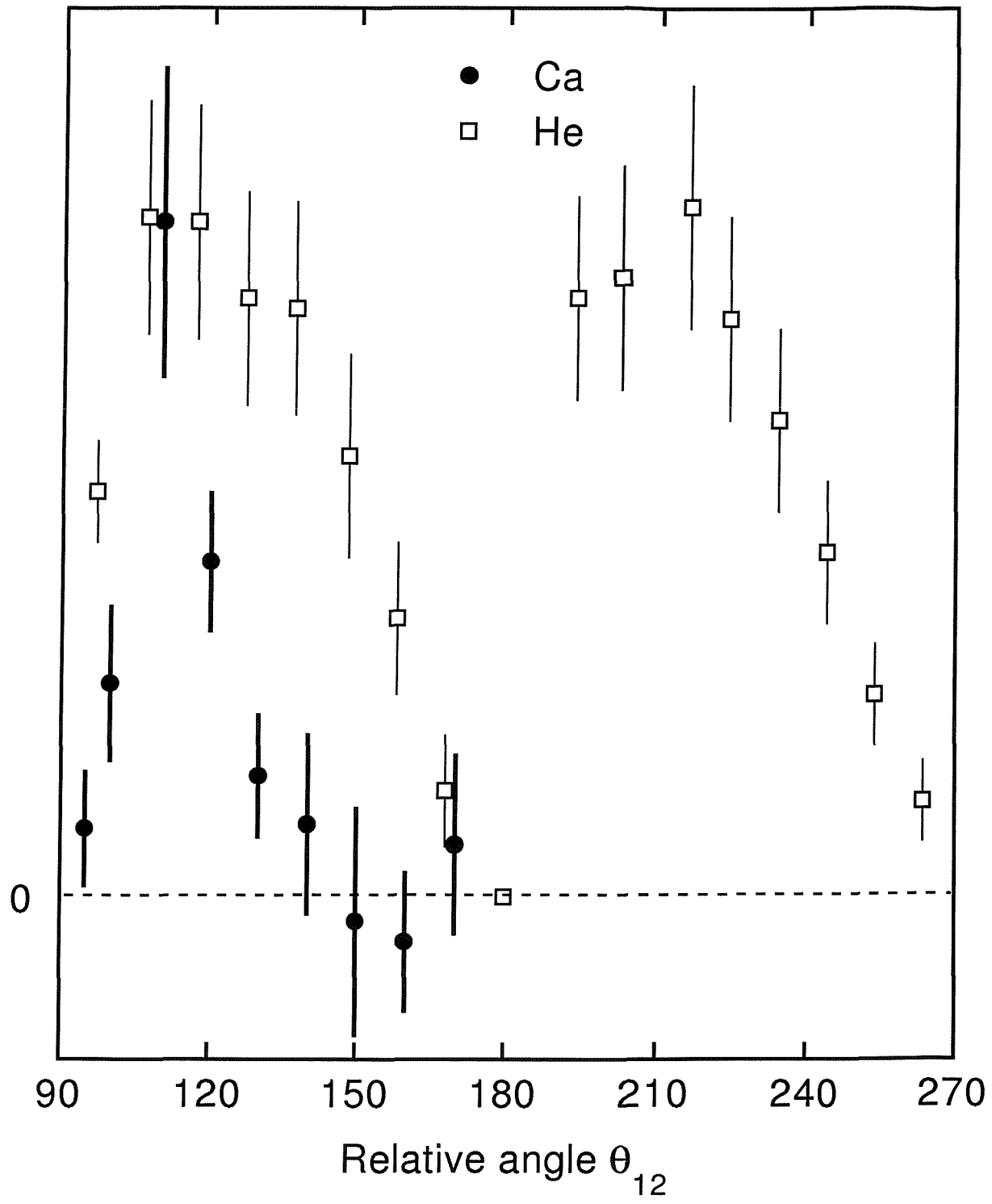

Figure 7.13: Comparison between the TDCS of Ca and of He measured at excess energies of 25.05 and 20.00 eV respectively. In both sets of data the two electrons have the same kinetic energy, one electron is emitted in the direction of the **E** field of the polarized radiation, and both electrons are emitted in the plane perpendicular to the photon beam.

of metal vapours, and it confirms that attempts to make measurements of TDCS of Ca at non-resonant energies on a second generation synchrotron radiation source are too ambitious. More important, it confirms that on a third generation synchrotron radiation facility the present experimental arrangement can allow such a measurement to be obtained only with great difficulty. Measurements of non-resonant DPI of metal vapours could be ideal candidate experiments on FEL.

7.4 TDCS of Sr via a neutral resonance

Unlike the case of Ca, no experimental studies of TDCS for Sr have been reported prior to the work of this thesis; the only theoretical work is the one of Kazansky and Ostrovsky in 1997 [4], cited in section 4.4.

The DPI process that has been investigated is the following:

$$Sr^{*}\, 4p^5 4d5s^2\, {}^1P_1 \leftarrow Sr\, 4p^6 5s^2\, {}^1S_0 + h\nu \tag{7.11}$$

$$Sr^{*}\, 4p^5 4d5s^2\, {}^1P_1 \rightarrow Sr^{++}\, 4p^6\, {}^1S_0 + e_1^- + e_2^- \tag{7.12}$$

$$Ie^{++} = 16.72\, eV.$$

This is very similar to the process (7.1)-(7.2) in Ca, DPI of the outermost s^2 electrons takes place with the photon energy tuned to the $4d \leftarrow 4p$ *giant* resonance at $h\nu = 25.24\, eV$. In this condition the two electrons share an excess energy E_{exc} of:

$$E_{exc} = E_1 + E_2 = h\nu - Ie^{++} = 25.24 - 16.72 = 8.52\, eV. \tag{7.13}$$

Several resonances are present in the region of the $4d \leftarrow 4p$ excitation, their positions were found by recording CIS spectra of the $5s$ state of Sr^+. Two CIS spectra in the photon energy range $24.8 - 25.6\, eV$ are plotted in figure 7.14, both recorded at $\theta = 0°$, with $S_1 \simeq 0.8$ and with monochromator bandwidths of approximately 100 and $150\, meV$. A CIS spectrum in the photon energy range $25.8 - 29.2\, eV$ is shown in figure 7.15, the monochromator bandwidth was set to $150\, meV$. The thick marks in figure 7.15 show the ionic limit of the states studied in chapter 8. The structure in these CIS spectra have been assigned to the states identified by Mansfield and Ottley in 1981 [20], these assignments are shown in the figures 7.14 and 7.15 together with the spectra.

No other resonances were considered other than the $4d \leftarrow 4p$ *giant* resonance at $25.24\, eV$. The CIS spectra in figures 7.14 and 7.15 indicate that other resonances would result in lower coincidence rates by at least an order of magnitude, resulting in excessively long

data collection times. For the coincidence detection the monochromator bandwidth was set to approximately $150\,meV$ and the pass energy of both electron analysers was set to $24\,eV$.

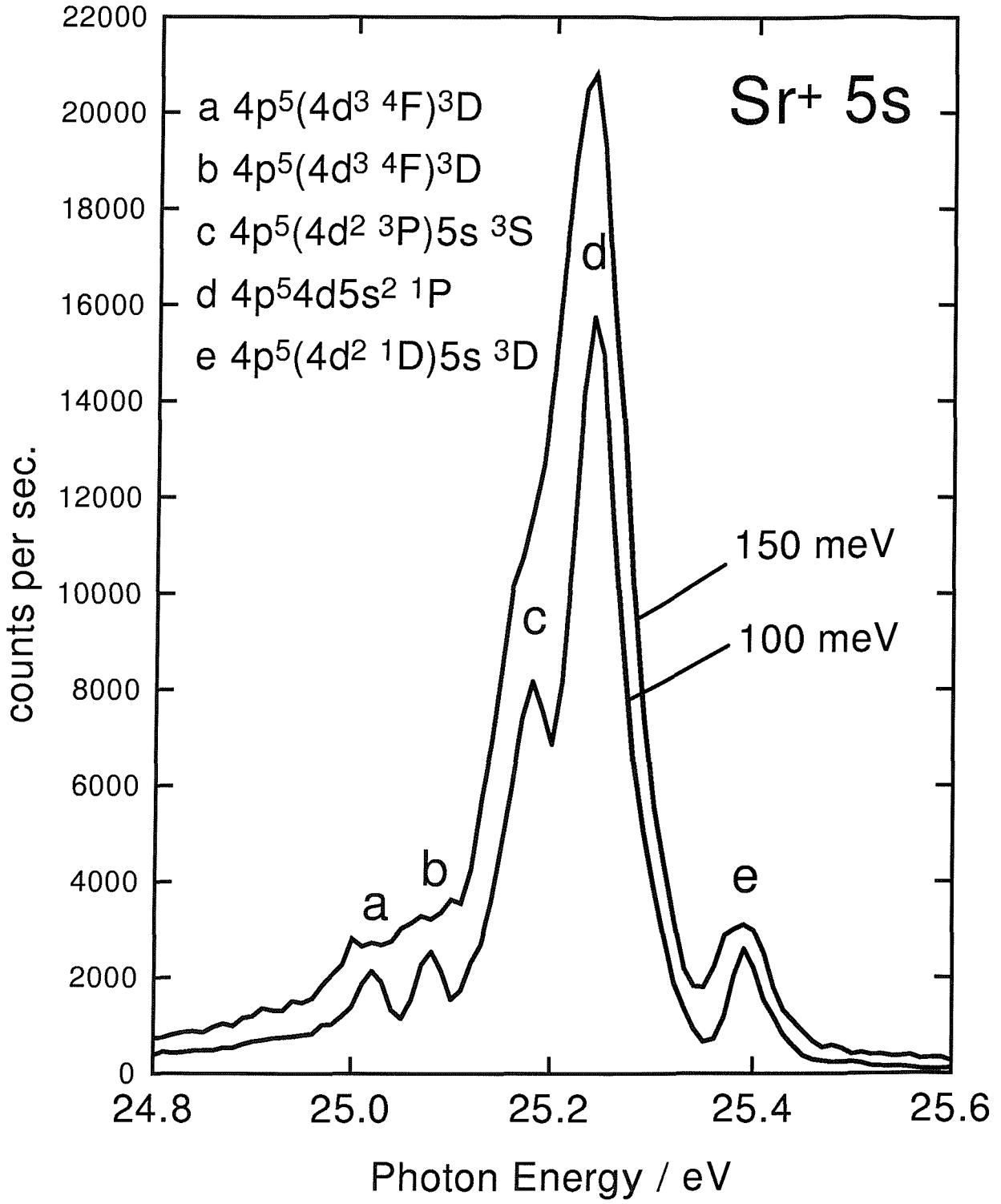

Figure 7.14: CIS spectra of the $5s$ state of Sr^+ recorded at $\theta = 0^o$ and with monochromator bandwidths of 100 and $150\,meV$.

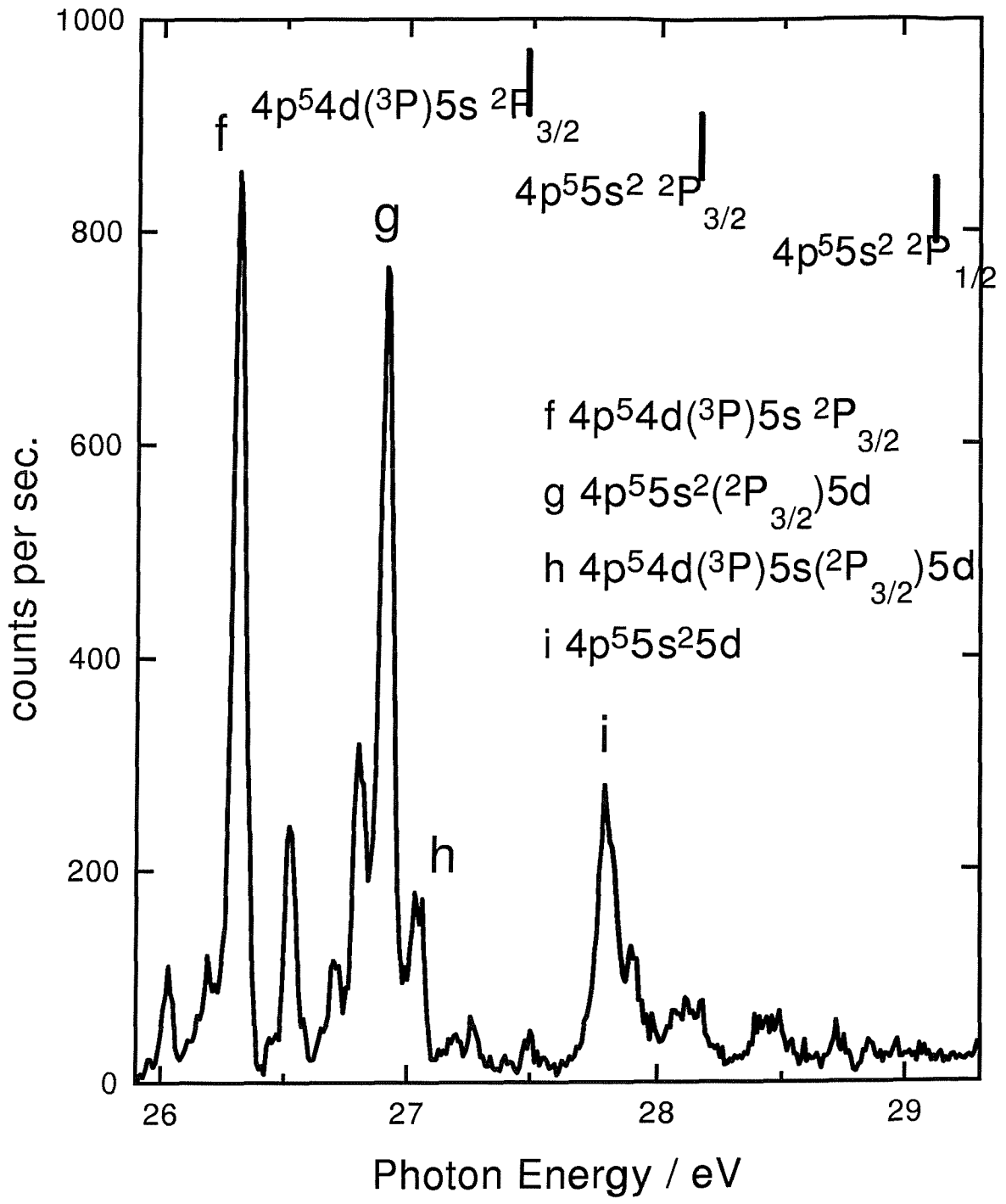

Figure 7.15: CIS spectra of Sr^+ $5s$ recorded at $\theta = 0^o$ and with a monochromator bandwidth of $150\,meV$.

7.4.1 TDCS of Sr for equal energy sharing

The TDCS of Sr measured at the $4d \leftarrow 4p$ *giant* resonance for equal energy sharing is shown on a polar plot in figure 7.16. The present set of data has been corrected for different efficiencies of the rotatable analyser at different angles with the He calibration procedure described in section 8.2, and is symmetric about $\theta_{RF} = 180^o$. A near zero value for the TDCS is found at $\theta_{RF} = 180^o$, where a zero is expected from the selection rules of reference [9]. The error bars in figure 7.16 show only the statistical contribution to the uncertainties that comes from the *true* and *false* coincidences. Each data point in the figure is the average of up to four independent data points, and each independent data point takes an average of two hours to collect.

Most interesting is the fact that in the TDCS in figure 7.16 only two lobes are present, thereby resembling more the TDCS of He (see section 4.2) than the TDCS of Ca at the $31.41\,eV$ *giant* resonance presented in section 7.2. This is very much in contrast to what would be expected from the tentative interpretation of the TDCS of Ca given in section 7.2, on the basis of correlation effects described by configuration interaction. Sr being heavier than Ca, configuration interactions are expected to be more important in Sr than in Ca. Following the expansion of the TDCS in electronic configurations (7.5)-(7.8) outlined in section 7.2.3, it was reasonable to expect a TDCS with more than two lobes. No reason is evident for the different number of lobes present in the TDCS of Sr compared to that of Ca.

As a result of the apparent similarity with the TDCS of He, the data for the TDCS of Sr in figure 7.16 have been tentatively fitted with the following expression, that is known to reproduce well the measured TDCS of He:

$$TDCS = \frac{1+S_1}{2} TDCS_{pol} + \frac{1-S_1}{2} TDCS_{unpol} \tag{7.14}$$

The two terms in equation (7.14) are:

$$TDCS_{pol} = |M_g|^2 (\cos\theta_R + \cos\theta_F)^2 \exp\left[-\ln 2 \left(\frac{\theta_{RF} - 180^o}{\theta_{fwhm}}\right)^2\right], \tag{7.15}$$

and

$$TDCS_{unpol} = |M_g|^2 (\sin\theta_R + \sin\theta_F)^2 \exp\left[-\ln 2 \left(\frac{\theta_{RF} - 180^o}{\theta_{fwhm}}\right)^2\right]; \tag{7.16}$$

θ_{fwhm} is the only free parameters in this fit, apart from the overall scaling factor $|M_g|^2$. The value of θ_{fwhm} resulting from the fit was found to be $75^o \pm 5^o$. Expressions (7.14)-

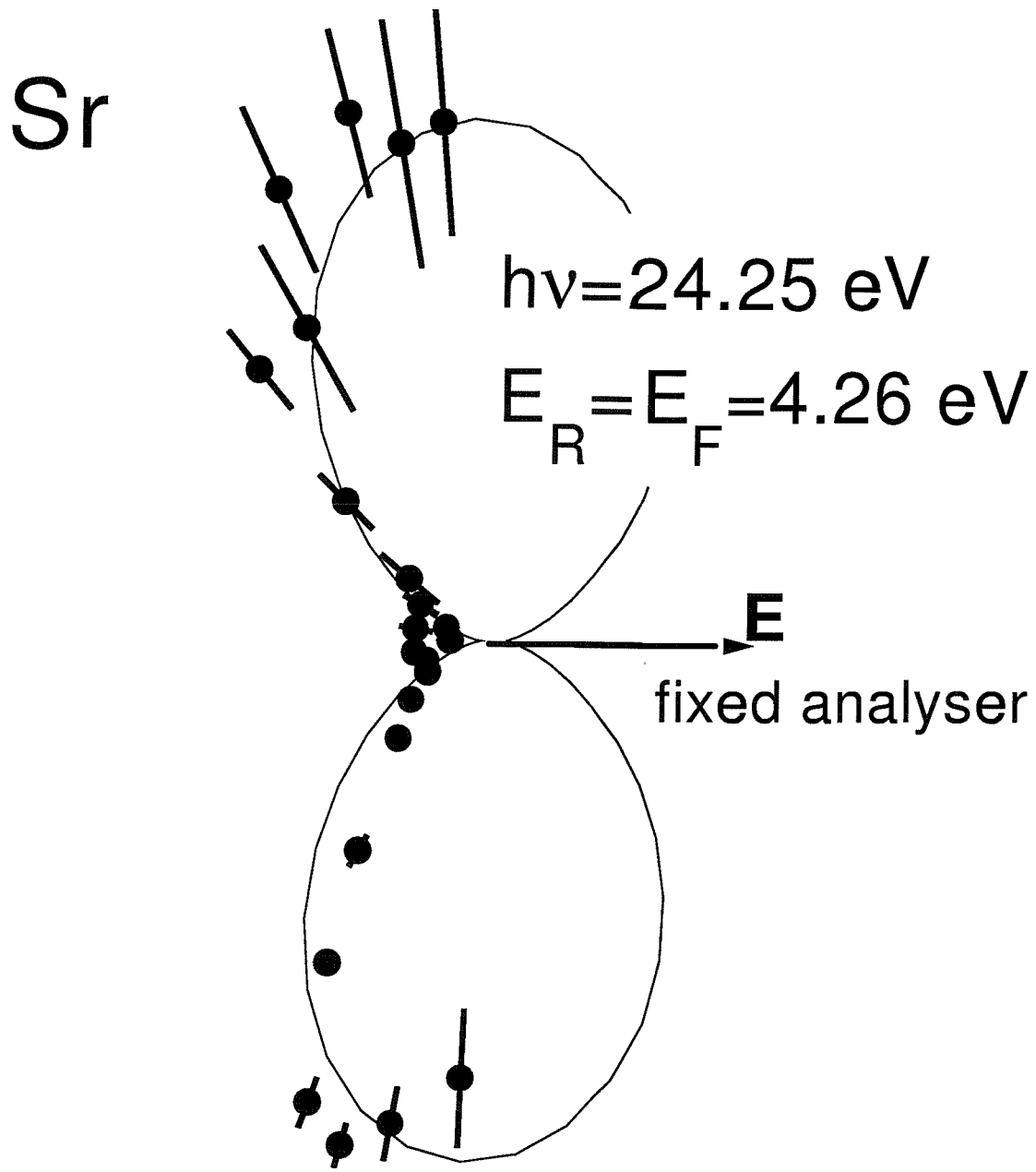

Figure 7.16: TDCS of Sr recorded at the resonant photon energy of $25.24\,eV$. The two electrons are emitted with the same energy in the plane perpendicular to the photon beam; one electron is emitted in the direction of the **E** field of the radiation, indicated by the arrow, at $\theta_F = 0^o$.

(7.16) have been derived in reference [15] from the Wannier theory applied to the DPI of closed shell atoms. It also corresponds to the expansion (3.39)-(3.43) truncated to only one partial wave, and the gaussian factor is added *ad hoc* to simulate correlation effects.

The curve in figure 7.16 is the least chi square fit of equations (7.14)-(7.16) to the data points, and it is clear that this is not a good fit to the measured data. The failure of this fit to reproduce the experimental data points well means that even though the two-lobes structure for the measured TDCS of Sr in figure 7.16 is apparently similar to the TDCS of He, a more detailed inspection shows that there are differences between the TDCS of these two elements.

Although a least chi square fit of the data points with expressions (7.14)-(7.16) has been undertaken, this work is only able to put emphasis on the qualitative aspects of the TDCS, such as the number of lobes and their angular positions. From this point of view the TDCS of Sr is closer to the TDCS of He than to the TDCS of Ca.

7.4.2 TDCS of Sr for unequal energy sharing

A study was also made of the TDCS of Sr at the $4d \leftarrow 4p$ resonance at the energy at $h\nu = 25.24\,eV$, for unequal energy sharing.

Figures 7.17 and 7.18 show the measured TDCS of Sr, for $E_R = 6.76$, $E_F = 1.76\,eV$ and $E_R = 1.76$, $E_F = 6.76\,eV$ respectively. Due to the limited beam-time available, measurements were only made in the angular quarter $90^o \leq \theta_{RF} \leq 180^o$. The TDCS shown in figures 7.17 and 7.18 have been plotted over the range $90^0 \leq \theta_{RF} \leq 270^o$ by reflecting the measured data points through $\theta_{RF} = 180^o$, assuming that the TDCS are symmetric about this point, which is to be expected from symmetry consideration, and it was further supported by the data for equal energy sharing shown in figure 7.16. Both sets of data in figures 7.17 and 7.18 have been corrected for change in the efficiency of the rotatable analyser at different angles with the He calibration procedure, as described in section 8.2. The error bars in both figures 7.17 and 7.18 show only the statistical contribution to the uncertainties. Each data point in figure 7.17 and 7.18 is the average of up to four independent data points, and each independent data point takes an average of two hours to collect.

In both conditions of energy sharing in figures 7.17 and 7.18, the filling of the former zeros for opposite ejection present in figure 7.16 is evident. In fact the selection rule of reference [9], that forbids the antiparallel emission of the two electrons when they have the same energy, is no longer valid when the electrons have different energies.

The intensity of the data points at $\theta_{RF} = 180^o$ must be the same in the two sets of data in figures 7.17 and 7.18. However, these two data points have been recorded with a time gap of approximately one week and they differ by more than a factor of two. This is an indication of the fact that within the time required to measure one TDCS, that is of the order of one week, the efficiencies of the analysers can change appreciably and this can affect the measurements.

Because of the apparent similarity with the TDCS of He at unequal energy sharing [14], [18], the data for the TDCS of Sr in figures 7.17 and 7.18 have been tentatively fitted with the expressions (7.14)-(7.16) extended to the case of unequal energy sharing, where also the *ungerade* contribution M_u is non zero. In this case equations (7.15) and (7.16) must be transformed to

$$TDCS_{pol} = |(\cos\theta_R + \cos\theta_F)M_g + (\cos\theta_R - \cos\theta_F)M_u|^2$$

$$\times \exp\left[-\ln 2\left(\frac{\theta_{RF}-180^o}{\theta_{fwhm}}\right)^2\right], \qquad (7.17)$$

and

$$TDCS_{unpol} = |(\sin\theta_R + \sin\theta_F)M_g + (\sin\theta_R - \sin\theta_F)M_u|^2 \times \exp\left[-\ln 2\left(\frac{\theta_{RF}-180^o}{\theta_{fwhm}}\right)^2\right] \qquad (7.18)$$

respectively. The curves in figures 7.17 and 7.18 are the least chi square fits of the expressions (7.14), (7.17) and (7.18) to the data points. The free parameters in the fit are $|M_g/M_u|$, $|\Delta_{gu}|$ the phase difference between M_g and M_u, θ_{fwhm}, and an overall scaling factor. The discrepancies between the experimental data points and the fitted curves in figures 7.17 and 7.18 show that the parameterization chosen is inadequate to reproduce the measured TDCS. The fitted values of $|M_g/M_u|$, $|\Delta_{gu}|$ and θ_{fwhm} for figures 7.17 and 7.18 are 7.7 ± 0.7, $0^o \pm 20^o$ and $63^o \pm 5^o$ and 15 ± 2, $0^o \pm 46^o$ and $45^o \pm 2^o$ respectively. However, since the parameterization that has been chosen to fit the measured TDCS does not reproduce the experimental data points well, no physical interpretation can be given to these numbers.

The two complementary TDCS of figures 7.17 and 7.18 are very similar to each other. It is interesting to compare these TDCS with the systematic study on the dependence of the TDCS of He on energy sharing, at an excess energy of $20.00\,eV$, reported by Braüning *et al.* in 1998 [21], cited in section 4.2. In the work of reference [21] a change from $E_F = 15$, $E_R = 5\,eV$ to $E_F = 5$, $E_R = 15\,eV$ made a significant change in the TDCS of He, whereas for the TDCS of Sr reported here a change from $E_F = 1.76$, $E_R = 6.76\,eV$ to $E_F = 6.76$, $E_R = 1.76\,eV$ does not have such a dramatic effect. The present measurements of the TDCS of Sr were made at an excess energy of $8.52\,eV$, compared to the value of $20.00\,eV$ for the work on He of reference [21]; it is known from theory [15] and confirmed by experiments [16], that at higher excess energy a stronger dependence on energy sharing is expected in the TDCS. This could be the reason why the TDCS of Sr at $E_{exc} = 8.52\,eV$ seems to be less dependent on energy sharing than the TDCS of He at $E_{exc} = 20.00\,eV$. However, the TDCS of Sr reported here was recorded at a resonant photon energy and the effect of the resonance on the energy sharing dependence is unknown.

The TDCS of Sr measured in this work show stronger dependence on energy sharing than the TDCS of Ca. Again, the fact that the excess energy is $8.52\,eV$ in Sr compared to $13.43\,eV$ in Ca makes this result difficult to understand, as the dependence on energy

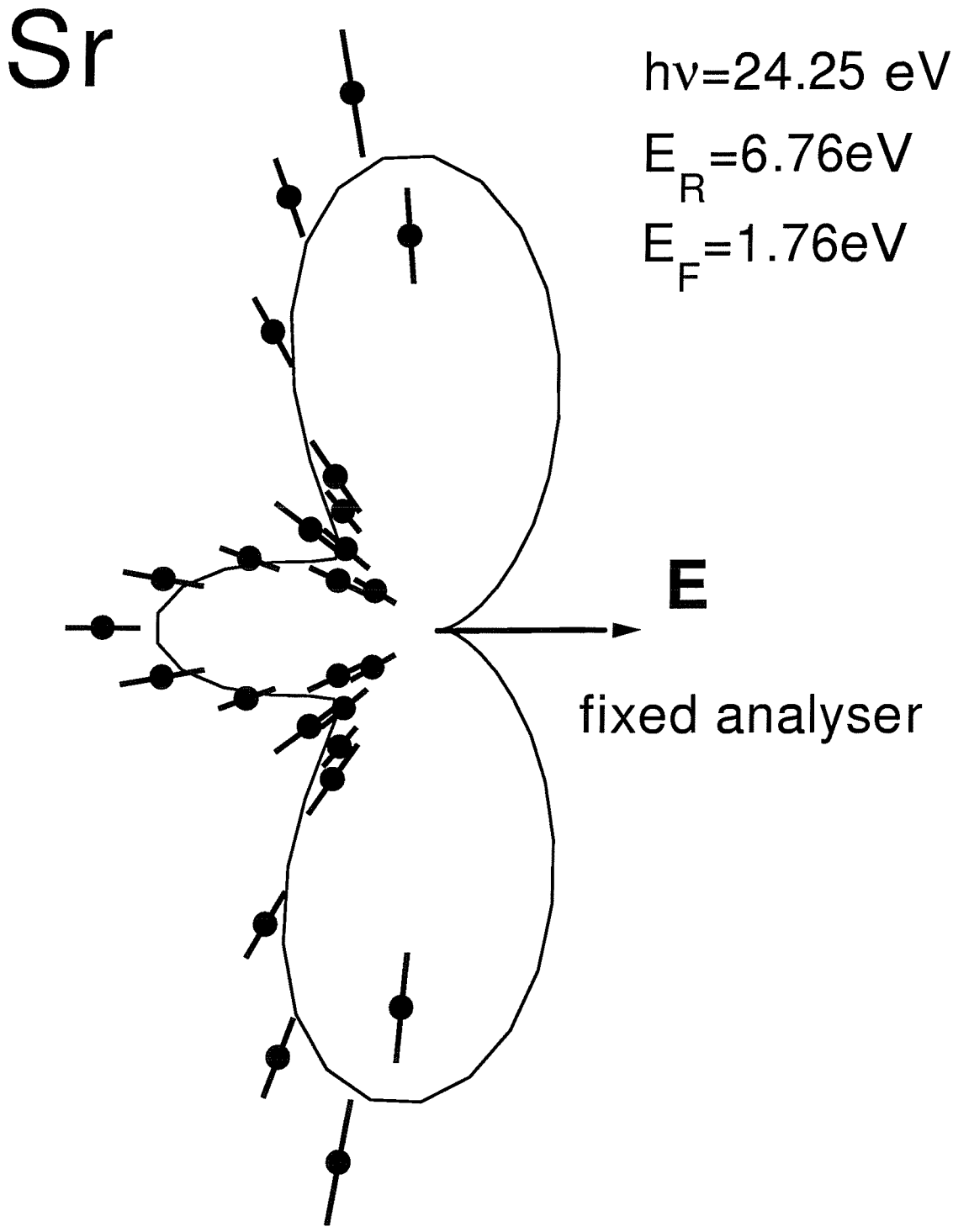

Figure 7.17: TDCS of Sr recorded at the resonant photon energy of $25.24\,eV$. The two electrons are emitted with different energies in the plane perpendicular to the photon beam; one electron is emitted in the direction of the **E** field of the radiation, indicated by the arrow, at $\theta_F = 0°$.

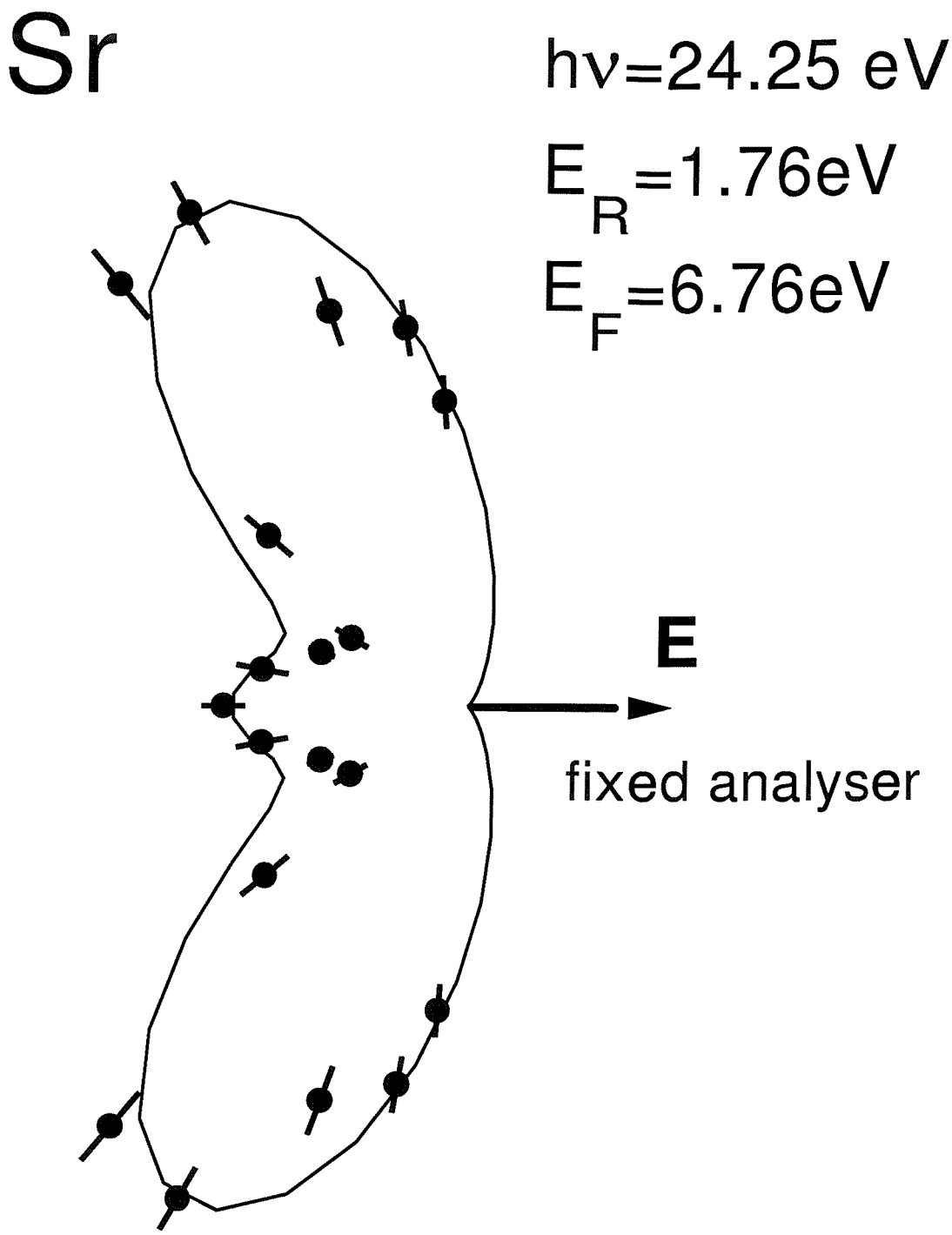

Figure 7.18: TDCS of Sr recorded at the resonant photon energy of $25.24\,eV$. The two electrons are emitted with different energies in the plane perpendicular to the photon beam; one electron is emitted in the direction of the **E** field of the radiation, indicated by the arrow, at $\theta_F = 0^o$.

sharing is expected to increase with the excess energy. One reason that may be partly responsible for the greater change in TDCS of Sr when moving from equal to unequal energy sharing, compared to the TDCS of Ca, is that in the TDCS of Sr measured for unequal energy sharing the difference in energy of the two electrons is greater in the case of Ca: 1.76 and 6.76 eV for Sr, 4.48 and 8.95 eV for Ca. However, it seems hard to believe that the difference in the dependence of the TDCS on energy sharing can be entirely due to the different energies. It would be easier to believe that the difference between the dependence on energy sharing of the TDCS of Ca and Sr is a consequence of the different resonant states to which they are excited. In this context it would have been interesting to measure the TDCS for unequal energy sharing at one or more of the other Sr resonances, as was possible for Ca. Unfortunately there are major intensity problems involved in making coincidence measurements at any resonance other than the main resonance at 25.24 eV; the Sr^+ $5s$ CIS spectra of figures 7.14 and 7.15 show that the other resonances are weaker by almost an order of magnitude.

7.5 Conclusions

The TDCS of Ca and Sr were measured at selected photon energies resonant with excitations in the $3d \leftarrow 3p$ and $4d \leftarrow 4p$ excitation regions. In the case of Ca the results show that the TDCS depend on the selected resonance.

The TDCS of Sr shows dramatic changes when moving from equal to unequal energy sharing. The measured TDCS of Ca is less dependent on the energy sharing than the TDCS of Sr.

The TDCS of Ca was also measured at an excess energy of approximately 25 eV at a non-resonant photon energy. The result is very different from both the TDCS of Ca at resonant photon energies and the TDCS of He measured in similar conditions.

Bibliography

[1] KJ Ross, JB West, H-J Beyer and A De Fanis, *Journal of Physics B: Atomic, Molecular and Optical Physics*, **32** 2927-2934 (1999).

[2] DMP Holland and K Codling, *Journal of Physics B: Atomic, Molecular and Optical Physics*, **14** 2345-2351 (1981).
Y Sato, T Hayaishi, Y Itikawa, Y Itoh, J Murakami, T Nagata, T Sasaki, B Sonntag, A Yagishita and M Yoshino, *Journal of Physics B: Atomic, Molecular and Optical Physics*, **18** 225-231 (1985).

[3] KJ Ross, H-J Beyer and JB West, *Journal of Physics B: Atomic, Molecular and Optical Physics*, **30** L735-L740 (1997).

[4] AK Kazansky and VN Ostrovsky, *Journal of Physics B: Atomic, Molecular and Optical Physics*, **30** L835-L841 (1997).

[5] L Malegat, F Citrini, P Selles and P Archirel, submitted.

[6] B Kämmerling and V Shmidt, *Journal of Physics B: Atomic, Molecular and Optical Physics*, **26** 1141-1161 (1993).

[7] J Berakdar and H Klar, *Physical Review Letters*, **69** 1175-1177 (1992).

[8] JB West, personal communication (2000).

[9] F Maulbetsch and JS Briggs, *Journal of Physics B: Atomic, Molecular and Optical Physics*, **28** 551-564 (1995).

[10] F Maulbetsch, M Pont, JS Briggs and R Shakeshaft, *Journal of Physics B: Atomic, Molecular and Optical Physics*, **28** L341-L347 (1995).

[11] Vibrationally Resolved Photoelectron Angular Distribution and Branching Ratios. JB West, in *Vacuum Ultraviolet Photoionization and Photodissociation of Molecules and Clusters*, edited by CY Ng, World Scientific, London (1991).

[12] SJ Schaphorst, B Krässig, O Schwarzkopf, N Scherer and V Schmidt, *Journal of Physics B: Atomic, Molecular and Optical Physics*, **28** L233-L238 (1995).
SJ Schaphorst, B Krässig, O Schwarzkopf, N Scherer, V Schmidt, P Lablanquie, L Andric, J Mazeau and A Huetz, *Journal of Electron Spectroscopy and Related Phenomena*, **76** 229-235 (1995).

[13] F Maulbetsch, IL Cooper and AS Dickinson, *Journal of Physics B: Atomic, Molecular and Optical Physics*, **33** L119-L125 (2000).

[14] O Schwarzkopf, B Krässig, V Schmidt, F Maulbetsch and JS Briggs, *Journal of Physics B: Atomic, Molecular and Optical Physics*, **27** L347-L350 (1994).

[15] A Huetz, P Selles, D Waymel and J Mazeau, *Journal of Physics B: Atomic, Molecular and Optical Physics*, **24** 1917-1933 (1991).

[16] G Dawber, L Avaldi, AG McConkey, H Rojas, MA MacDonald and GC King, *Journal of Physics B: Atomic, Molecular and Optical Physics*, **28** L271-L277 (1995).

[17] R Dörner, H Braüning, JM Feagin, V Mergel, O Jagutzki, L Spielberger, T Vogt, H Khemliche, MH Prior, J Ullrich, CL Cocke and H Schmidt-Böcking, *Physical Review A*, **57** 1074-1090 (1998).

[18] JS Briggs and V Schmidt, *Journal of Physics B: Atomic, Molecular and Optical Physics*, **33** R1-R48 (2000).

[19] O Schwarzkopf and V Schmidt, *Journal of Physics B: Atomic, Molecular and Optical Physics*, **28** 2847-2862 (1995).

[20] BWD Mansfield and TW Ottley, *Proceedings of the Royal Society of London*, **377** 431-448 (1981).

[21] H Bräuning, R Dörner, CL Cocke, MH Prior, B Krässig, AS Kheifets, I Bray, A Bräuning-Demian, K Carnes, S Dreuil, V Mergel, P Richard, J Ulrich and H Schmidt-Böcking, *Journal of Physics B: Atomic, Molecular and Optical Physics*, **31** 5149-5160 (1998).

Chapter 8

Two-step double photoionization of atomic Ca and Sr. Complete photoionization experiments

8.1 Introduction

This chapter presents the results of measurements of two-step DPI of atomic Ca and Sr, with particular emphasis being put on the analysis of the data from the point of view of complete photoionization experiments.

Complete photoionization experiments on Ca and Sr have been reported at photon energies in the region of the $3d \leftarrow 3p$ and $4d \leftarrow 4p$ *giant* resonances respectively [1]. The amplitudes and the phase differences of the dipole matrix elements extracted by complete experiments are expected to evolve rapidly with energy in the region near threshold (within $0 - 10\,eV$), and also near Cooper minima, reaching asymptotic values far from threshold ($\geq 10eV$). This makes the threshold region, and the vicinity of Cooper minima, the most interesting regions in the context of complete experiments.

The processes that have been studied in this thesis are the $3p$ and $4p$ photoionizations of Ca and Sr respectively, followed by their corresponding Auger decays:

$$\begin{aligned} Ca^{+}\,3p^{5}4s^{2}\;{}^{2}P_{3/2} + e_{e}^{-} \leftarrow Ca\,3p^{6}4s^{2}\;{}^{1}S_{0} + h\nu \qquad & Ie = 34.34\,eV \\ Ca^{+}\,3p^{5}4s^{2}\;{}^{2}P_{3/2} \rightarrow Ca^{++}\,3p^{6}\;{}^{1}S_{0} + e_{A}^{-} \qquad & KE = 16.33\,eV \end{aligned} \tag{8.1}$$

and

$$\begin{aligned} Sr^{+}\,4p^{5}5s^{2}\ {}^{2}P_{3/2} + e_{e}^{-} &\leftarrow Sr\,4p^{6}5s^{2}\ {}^{1}S_{0} + h\nu & Ie &= 28.160\,eV \\ Sr^{+}\,4p^{5}5s^{2}\ {}^{2}P_{3/2} &\rightarrow Sr^{++}\,4p^{6}\ {}^{1}S_{0} + e_{A}^{-} & KE &= 11.46\,eV, \end{aligned} \tag{8.2}$$

where Ie and KE are ionization and kinetic energies respectively. The results for the study of the two-step DPI of Ca (8.1) have been published in reference [2]. The word "complete" refers to the first step of the DPI processes (8.1) and (8.2), where within the dipole approximation the photoelectron e_e^- is a superposition of $s_{1/2}$, $d_{3/2}$ and $d_{5/2}$ waves, as explained in section (3.2); in the second step only a $p_{3/2}$ wave is present.

As discussed in section (3.6) lack of absolute cross sections data means that the amplitudes reported here are on relative scales.

8.2 Analysis of the data

The anisotropy parameters for the photoelectron and Auger electron, β_e and β_A, can be extracted from the relative intensity of the photoelectron spectra at two different angles. In order to obtain the anisotropy parameters, the counts from one analyser must be rescaled relative to the other, in order to correct for the different efficiency of the two analysers. This relative efficiency can also depend on the electron kinetic energies. The signal for the Auger lines, both in the case of Ca and Sr, is scaled in such a way that the isotropic 1/2 component has the same intensity at the two angles of observation. The separation of the Auger doublet is $346\,meV$ and $976\,meV$ for Ca and Sr respectively, and for such a small energy difference the relative efficiency of the analysers does not change.

The kinetic energy of the photoelectron differs from that of the isotropic Auger component by up to $15\,eV$, so this procedure for correcting the relative efficiency of the analysers cannot be used for the photoelectron. The correction for the photoelectron is made by using the measured angular distribution of the $1s$ photoline of He, which has $\beta = 2$, at photon energies such that these electrons have the kinetic energies as the photolines of interest.

This correction for different efficiency propagates additional contributions to the uncertainties of the extracted β parameters. The estimate of these uncertainties is very difficult, and they play an important part in the following analysis. The errors reported here derive mainly from the reproducibility of the results. The uncertainties for β_A are considerably smaller than those for β_e as the Auger calibration is more precise than the He calibration.

This is mainly because the He angular distribution measurements were recorded up to three days after recording the Ca or Sr spectra, and the relative efficiency of the analysers could change slightly over this time interval.

The intensities of the signals are obtained by taking the sum of a few points in the peak region. Because of the asymmetric nature of the peaks, a least squares fit procedure using spectroscopic functions was not used.

From the corrected intensity of each peak in the PE spectra at the two angles of observation θ_R and θ_F, the beta parameters are calculated using the following expression:

$$\beta = 4\frac{I(\theta_F)/I(\theta_R) - 1}{3S_1 + 1 - [3S_1\cos(2\theta_R) + 1]\, I(\theta_F)/I(\theta_R)}, \tag{8.3}$$

where S_1 is the degree of linear polarization. Equation (8.3) comes from solving equations (3.9) and (3.17) specified to the two angles θ_R and θ_F.

As outlined in section 3.6 the values of the asymmetry parameters, together with the assumed validity of the lsj approximation, are sufficient for a complete characterization of the $3p$ and $4p$ photoionization of Ca and Sr respectively. The equations

$$\beta_e = \frac{|D_d|^2 - 2\sqrt{2}|D_s D_d|\cos\Delta_{sd}}{|D_s|^2 + |D_d|^2}, \qquad \beta_A = \frac{|D_s|^2 + 0.1|D_d|^2}{|D_s|^2 + |D_d|^2}, \tag{8.4}$$

derived in chapter 3, can be solved for $|D_s/D_d|$ and $\cos\Delta_{sd}$ as follows:

$$\left|\frac{D_s}{D_d}\right| = \sqrt{\frac{0.1 - \beta_A}{\beta_A - 1}}, \qquad \cos\Delta_{sd} = \frac{1 - \beta_e(1 + |D_s/D_d|^2)}{2\sqrt{2}|D_s/D_d|}. \tag{8.5}$$

The extraction of $|D_s/D_d|$ from these equations will be referred to in the following as the non-coincidence analysis.

The coincidence measurements between the photoelectron and the Auger electron were recorded with the Auger electron analysed by the fixed analyser set in the same direction of the **E** field of the radiation, at $\theta_F = 0^o$; the photoelectron was analysed by the rotatable analyser in the angular range $93^o \leq \theta_R \leq 267^o$ in steps of 10^o. Each individual data point is the result of a single measurement taken by counting over a period of time between 1 and 10 minutes. The counts could be affected if the overlap between the region of space "seen" by the two analysers, the light beam and the metal beam changes when one analyser is rotated; this could happen if the axis of rotation is not exactly aligned with the light beam. No exact correction is possible for this effect, which can be minimized by accurate alignment of the system. The He calibration correction procedure for relative

efficiency of the two analysers at different angles described above can only partly correct this effect.

The angular correlation between the directions of emission of the photoelectron and the Auger electron, discussed theoretically in section 3.5, was parametrized by the following expression:

$$A_0 + A_2 \cos(2\theta_{12}) + A_4 \cos(4\theta_{12}), \tag{8.6}$$

where θ_{12} is the relative angle of emission, $\theta_{12} = \theta_R - \theta_F$. Equation (8.6) was least chi square fitted to the coincidence data points. Errors in the data points include only the statistical contributions from *true* and *false* counts, assuming poissonian distributions for both.

A FORTRAN computer program was written to least chi square fit the relative dipole amplitudes and phase differences from the quantities β_e, β_A, A_0, A_2 and A_4 extracted from the measurements. The program reads the values of these quantities, their estimated uncertainties, and the degree of linear polarization of the radiation S_1 from a file, as well as the initial values of the parameters to be fitted: $|D_{1/2}|$, $|D_{1/2}|/\sqrt{|D_{3/2}|^2 + D_{5/2}|^2}$, $|D_{3/2}/D_{5/2}|$, $|\Delta_{1/2} - \Delta_{3/2}|$ and $|\Delta_{3/2} - \Delta_{5/2}|$. Each of these parameters can be fixed to its initial value; $|\Delta_{3/2} - \Delta_{5/2}|$ is always fixed to 0; fixing $|D_{3/2}/D_{5/2}|$ to 1/3 corresponds to assuming the *lsj* approximation and will be referred to in the following as the fix fit, while keeping $|D_{3/2}/D_{5/2}|$ as a free parameter will be called free fit.

8.3 3p photoionization of Ca

8.3.1 Previous work

A non-coincidence angle resolved study of $3p$ photoionization of Ca was performed by Lörch *et al.* in 1999 [3] in the range $h\nu$ = 45-95 eV. From the measured values of β_e and β_A, together with the absolute value for the $3p$ photoionization cross section and with the assumption of the *lsj* approximation, values of $|D_s|$, $|D_d|$ and Δ_{sd} were extracted. The absolute photoionization cross section was obtained by using a normalization procedure in which the relative intensities of all the main photolines and their satellites at a certain photon energy was compared with the known cross section for photoabsorption. The absolute photoionization cross section was extended over the whole photon energy range by a comparison between the photon energy dependence of the intensities of the $3p$ and of the $1s$ photolines of Ca and He respectively, the latter has a known photoionization cross section at all energies of interest. Comparison of the extracted elements with

$h\nu/eV$	KE/eV	$\beta_e(1/2)$	$\beta_e(3/2)$	β_A
36	1.66	0.60(25)	0.55(25)	0.126(16)
38	3.66	0.66(25)	0.74(25)	0.164(28)
40	5.66	0.77(25)	0.82(25)	0.156(10)
42	7.66	1.06(25)	1.03(25)	0.184(33)
45.1[a]	10.76	-	1.87(03)	0.230(30)

Table 8.1: Asymmetry parameters for the $3p^5 5s^2$ photoelectron and the $M_3N_1N_1$ Auger electron in Ca. [a] values from Lörch *et al.* The values within brackets are uncertainties on the last digits (one standard deviation).

the results from the *ls*-coupling limit of the relativistic random phase approximations (RRPA) demonstrated both the validity of the *lsj* approximation, and also the validity of a simplified intensity-borrowing model with the same strength for both the s and d partial waves at all energies. The photon energy range was chosen to include the Cooper minimum (see later and also reference [4]) which is at $h\nu = 59\,eV$.

8.3.2 This work

Photoelectron spectra have been recorded at $h\nu$ = 36, 38, 40 and $42\,eV$, and they are shown in figures 8.1 and 8.2 for the $3p^{-1}$ photolines and MNN Auger lines respectively; the monochromator bandwidth, the pass energies of the analysers and the degree of linear polarization were $50\,meV$, $10\,eV$ and 0.75 respectively. The spectra in figure 8.1 contain the photolines corresponding to the $Ca^+\,3p^5 4s^2\,{}^2P_{1/2,3/2}$ doublet; the stronger and weaker signals are the $J = 3/2$ and $J = 1/2$ components at $Ie = 34.34$ and $34.69\,eV$ respectively. The vertical scales are such that a direct comparison of intensities is possible: the decrease in count rates with higher photon energies can be noticed, which results from a reduction in photon flux, lower cross sections at higher photon energy, and a change in the efficiencies of the analysers at different kinetic energies. It was not possible to record spectra closer to threshold because of a rising background towards low kinetic energy. Figure 8.2 shows the photoelectron spectra in the energy region of the MNN Auger lines; the stronger and weaker signals correspond to the $M_3N_1N_1$ and $M_2N_1N_1$ Auger lines ($Ca^{++}\,3p^6\,{}^1S_0 + e_A^- \leftarrow Ca^+\,3p^5 4s^2\,{}^2P_{3/2,1/2}$) at kinetic energies of 16.33 and $16.68\,eV$ respectively.

Both the Auger and the photoelectron doublets show the 3/2 component approximately twice as intense as the 1/2 component at both angles of observation and at all photon energies; this is additional support to the validity of the LSJ coupling scheme for the intermediate ionic state.

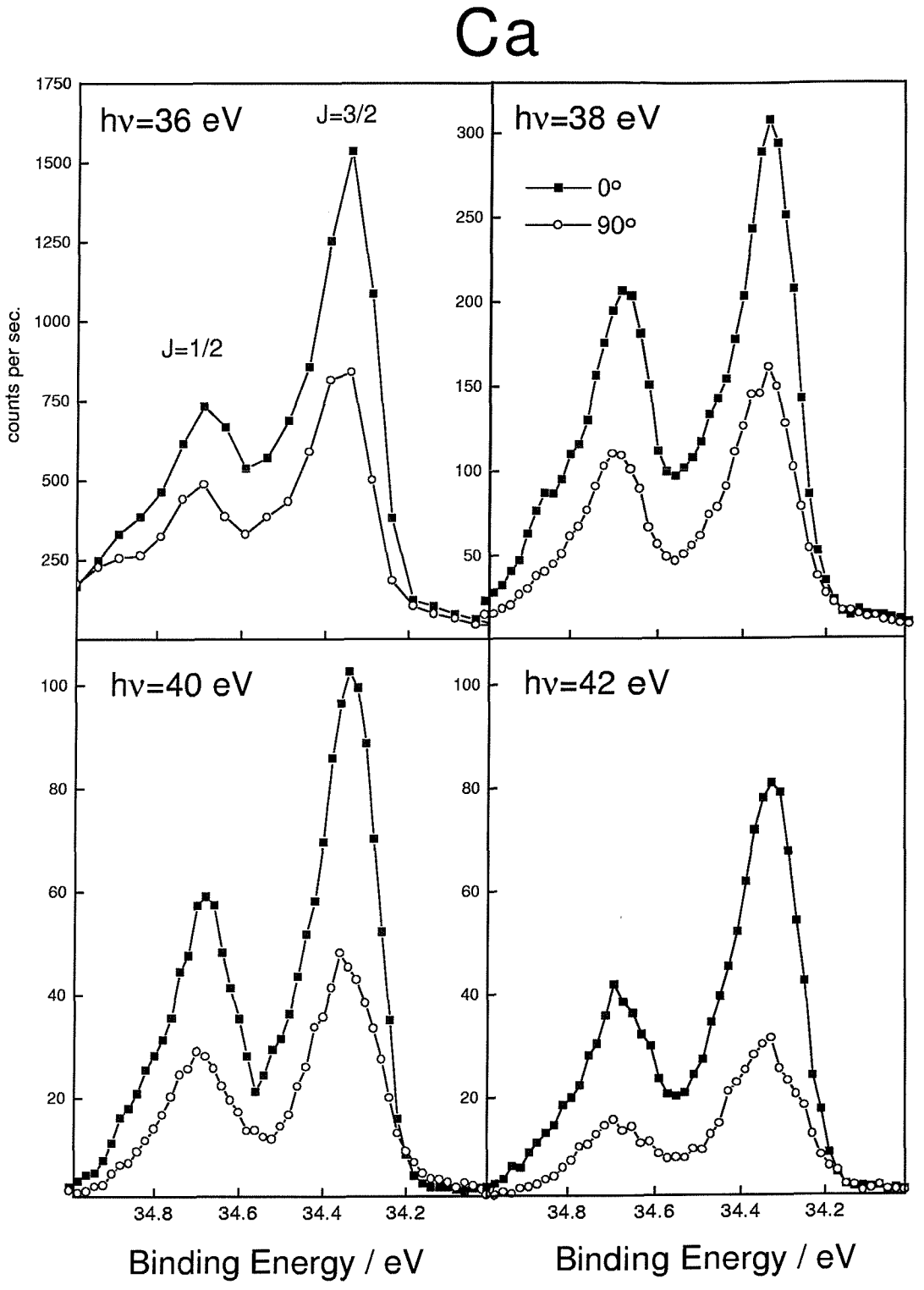

Figure 8.1: Photoelectron spectra of Ca in the region of the $3p^5 4s^2$ photolines recorded at $\theta = 0^o$ and $\theta = 90^o$.

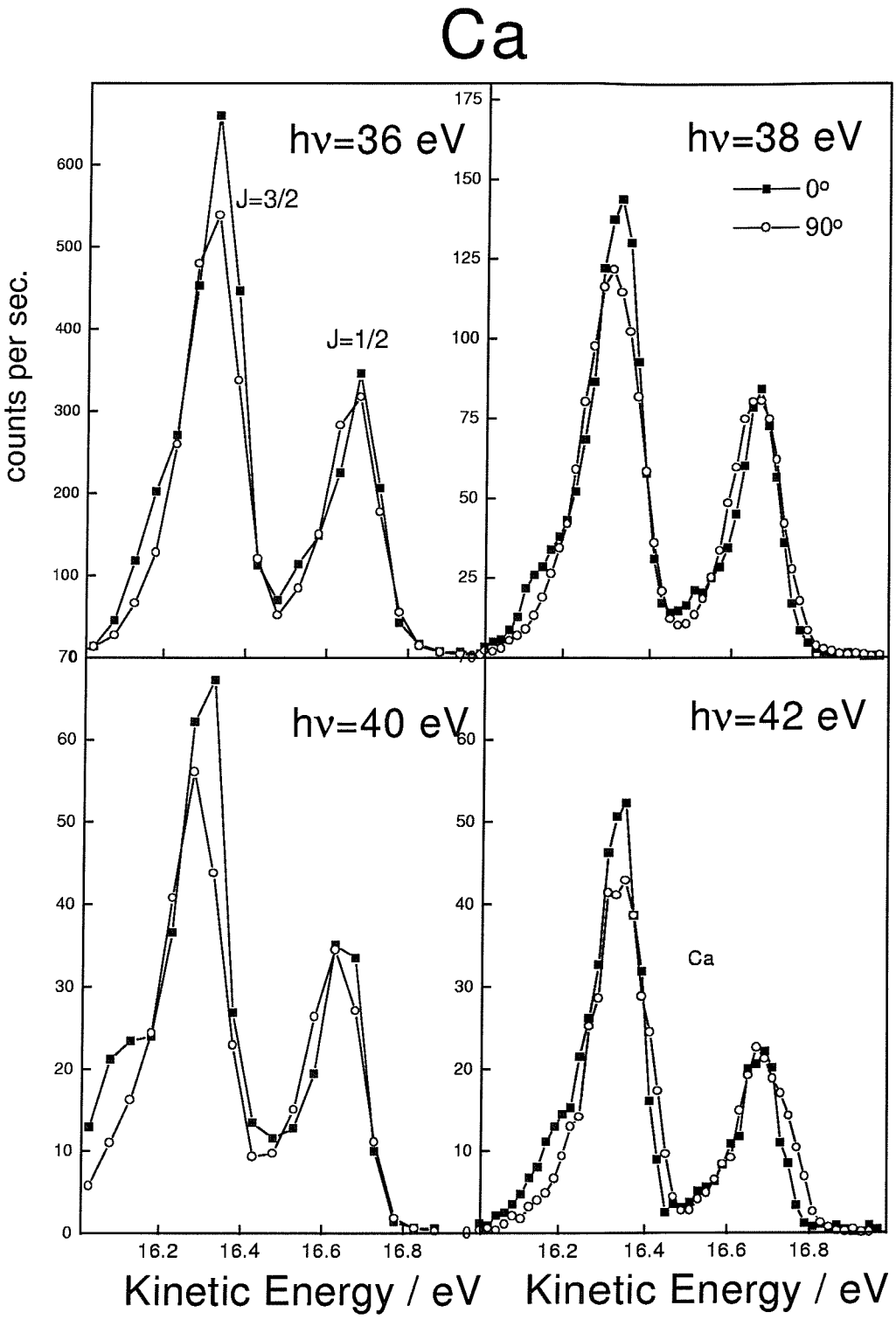

Figure 8.2: Photoelectron spectra of Ca in the region of the MNN Auger lines recorded at $\theta = 0^o$ and $\theta = 90^o$.

		non-coincidence		coincidence	
$h\nu/eV$	KE/eV	$\|D_s/D_d\|$	Δ_{sd}/π	$\|D_s/D_d\|$	Δ_{sd}/π
36	1.66	0.17(04)	0.15(15)	0.18(04)	0.24(04)
38	3.66	0.28(04)	0.42(21)	0.24(07)	0.30(07)
40	5.66	0.26(03)	0.44(21)	0.26(04)	0.34(07)
42	7.66	0.32(04)	0.55(20)	0.29(07)	0.41(09)

Table 8.2: Values of $|D_s/D_d|$ and Δ_{sd} for $3p$ photoionization of Ca. Third and fourth columns: non-coincidence analysis, fifth and sixth columns: fix fit. The values within brackets are the uncertainties on the last digits (one standard deviation).

The β_e and β_A parameters extracted from these spectra are given in table 8.1 together with the values at the lowest energy reported by Lörch *et al.* [3], these data are also plotted in figure 8.3. It is reassuring to see that at all energies the two components of the photoline have practically the same value of β_e, as it is expected from LSJ coupling; this is consistent with the 1/2 to 3/2 intensity ratios being 1/2 at both angles of observation.

The coincidence measurements between the $3p_{3/2}$ photoelectron and the corresponding Auger electron are plotted in figure 8.4. The solid curves are the functions of equation (8.6) least chi square fitted to the data points. An angle shift of 6° has been introduced to compensate for the angular asymmetry of the data. A possible cause of this asymmetry is a tilt of the **E** radiation field of the photon beam with respect to the fixed analyser. It can be observed in figure 8.4 that at different photon energies the width of the central peak remains constant, and the relative intensities of the side peaks at the extremes of the angular range vary, and they result in different sets of Ai values.

The results from both the non-coincidence analysis and from the fix fit are given in table 8.2; these data are also plotted in graph 8.5. It is not possible to extract the sign of Δ_{sd} from these measurements because Δ_{sd} enters the equations (3.25)-(3.31) for the parameters Ai only through its cosine; the sign of Δ_{sd} is then chosen to give the best agreement with the calculated values.

The agreement between the non-coincidence values and those from the fix fit is remarkable; this means that the non-coincidence data agree with the coincidence data. However, the agreement between the extracted values of $|D_s/D_d|$ and Δ_{sd} may also be caused by the large errors in the Ai parameters; the large errors on Ai reduce their importance in the fit procedure, which is driven by the most accurate data. Note that the errors in $|D_s/D_d|$ increase only slightly when moving from the non-coincidence analysis to the free fit, but they decrease considerably in Δ_{sd}; this means that the coincidence data provide valuable

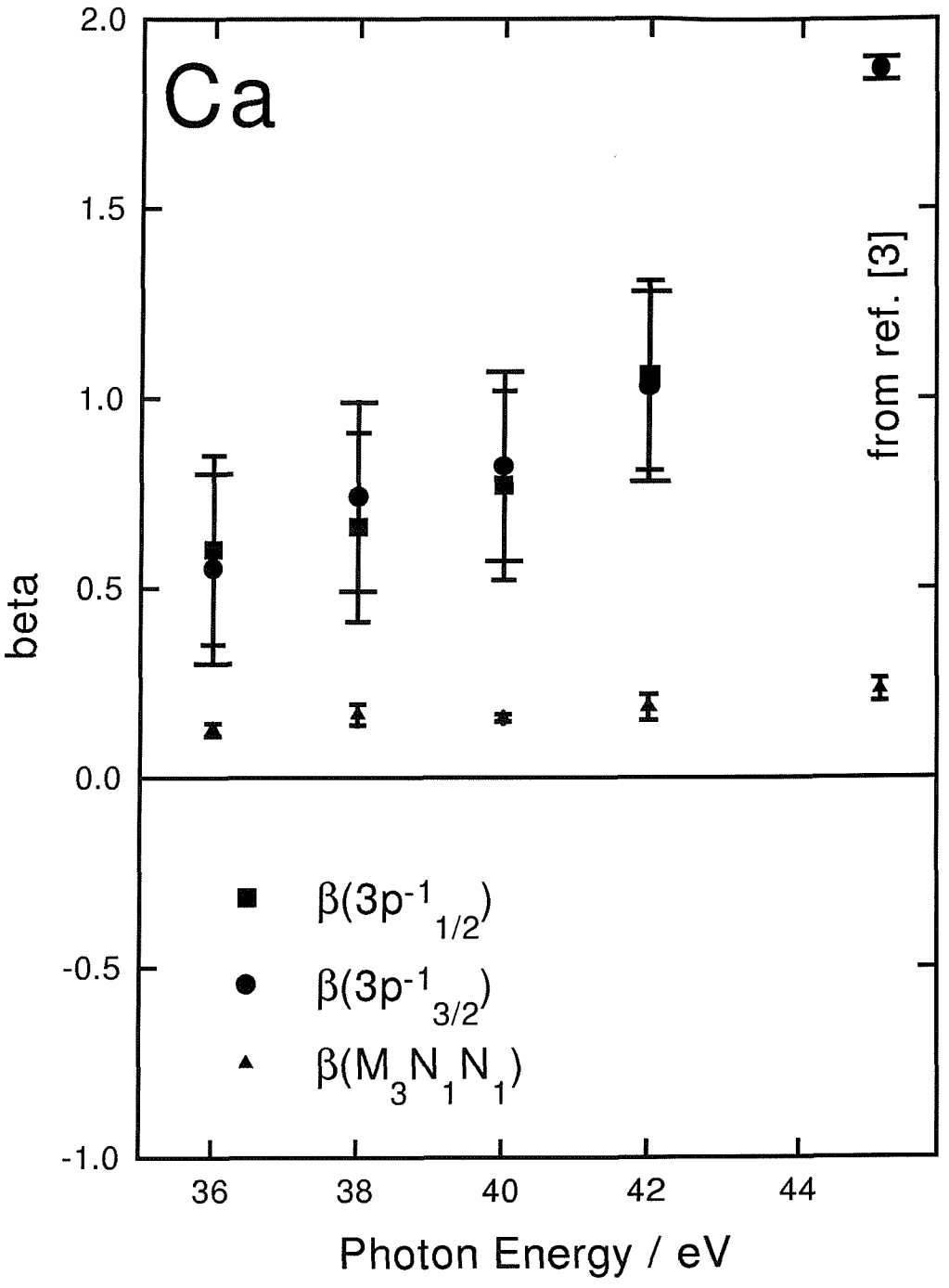

Figure 8.3: Asymmetry parameters for the $3p_{1/2,3/2}$ photolines and $M_3N_1N_1$ Auger lines of Ca.

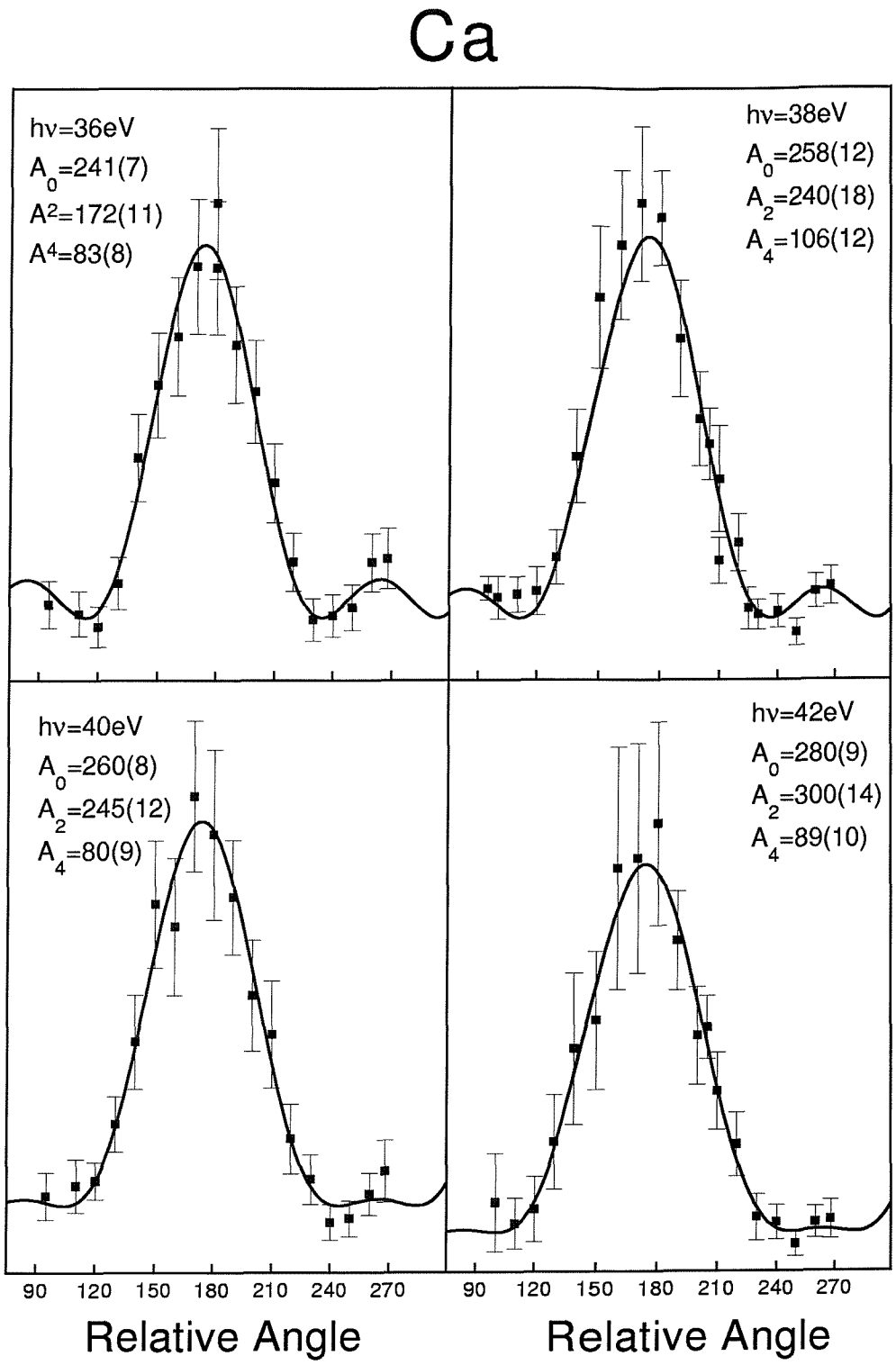

Figure 8.4: Coincidence measurements between the $3p_{3/2}$ photoelectron and the $M_3N_1N_1$ Auger electron in Ca. The solid curves are the least chi-square fits of equation (8.6) to the data points, the values obtained for the parameters in equation (8.6) are given for each data set.

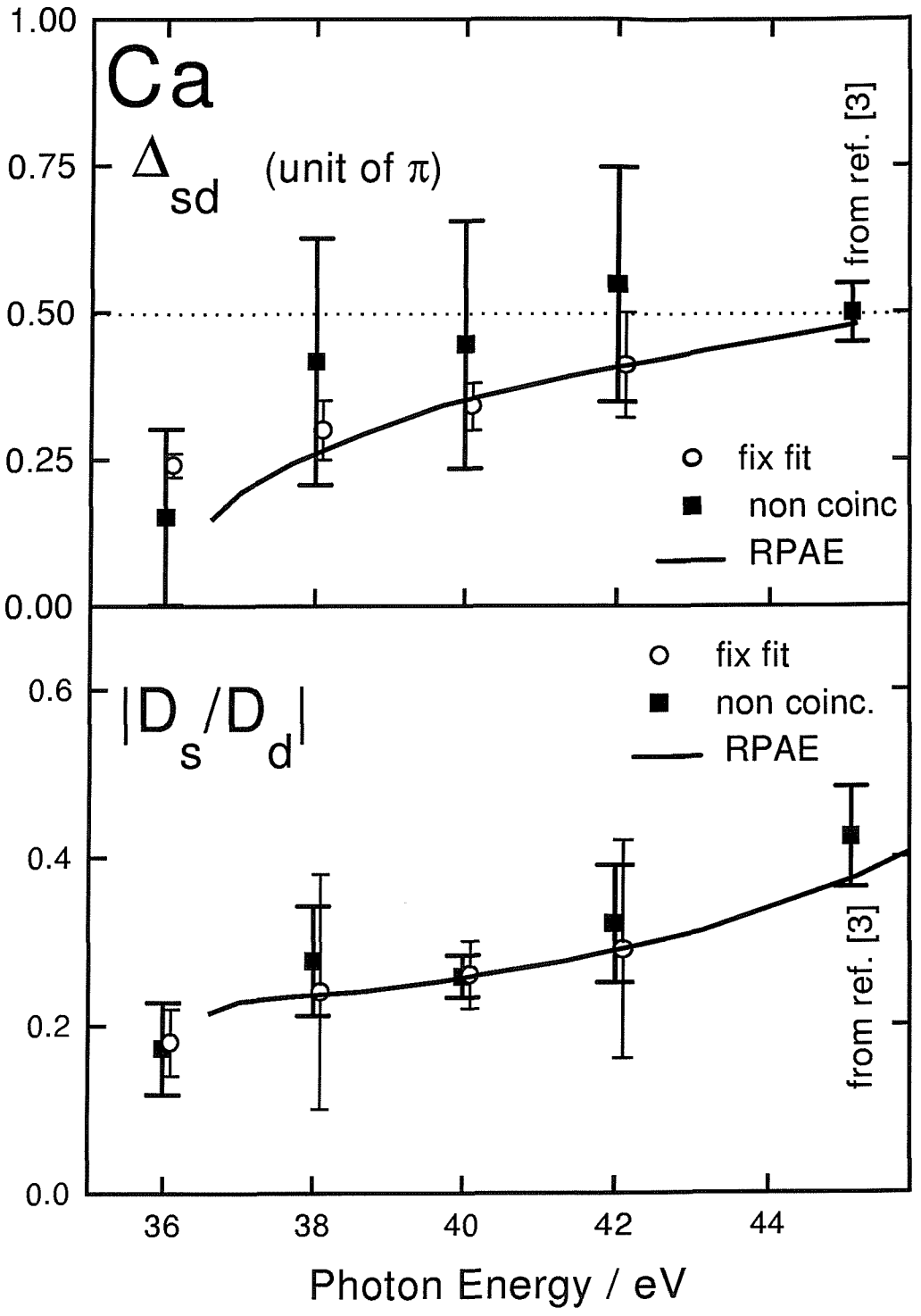

Figure 8.5: Values of $|D_s/D_d|$ and Δ_{sd} derived from the non-coincidence analysis (full dots) and from the fix fit (open circle), and calculated with RPAE procedure (continuous line). The dotted line divides the regions of constructive and destructive interference.

$h\nu/eV$	$\lvert D_s/D_d\rvert$ HF, r	$\lvert D_s/D_d\rvert$ HF, v	$\lvert D_s/D_d\rvert$ RPAE	Δ_{sd}/π	β_e	β_A
36.60	0.180	0.218	0.214	0.293	0.606	0.139
37.01	0.180	0.218	0.228	0.389	0.741	0.144
37.69	0.181	0.220	0.234	0.487	0.922	0.147
38.64	0.184	0.225	0.240	0.587	1.118	0.149
39.87	0.190	0.236	0.252	0.684	1.307	0.154
41.36	0.207	0.256	0.276	0.780	1.488	0.164
43.13	0.225	0.290	0.312	0.872	1.652	0.180
45.17	0.259	0.343	0.375	0.961	1.800	0.211
47.48	0.310	0.430	0.471	1.043	1.899	0.263

Table 8.3: Calculated values of $|D_s/D_d|$, Δ_{sd}, β_e and β_A for $3p$ photoionization in Ca.

information for the analysis undertaken.

The stability of the results from the fix fit was checked against changes in the initial values of the estimated values and it is good.

Running the fix fit with increased errors on Ai was also attempted. The result is that Δ_{sd} is not so well determined; the larger the errors in A_i the closer the values of Δ_{sd} become to those from the non-coincidence analysis; this shows that the coincidence data provide useful information for the determination of the parameters.

The free fit does not reach convergence if it is run with the errors as in table 8.1. However, it is possible to make the free fit converge by reducing the errors in β_e to 0.1, but this is not justifiable.

The RPAE calculations described in section 3.7 and aimed to calculate the quantities D_s, D_d and Δ_{sd} were performed for $3p$ photoionization of Ca by M Ya Amusia and LV Cherny-sheva and are presented in table 8.3 and in figure 8.5. The excellent agreement between the values extracted from the analysis of the experimental data and those calculated with RPAE confirms the validity of lsj coupling in this case.

The trend in both calculated and extracted values of $|D_s/D_d|$ was initially surprising. A simplistic picture would suggest that at low kinetic energy the d wave is much weaker than the s wave because of the centrifugal repulsive term $-l(l+1)r^{-2}$ in the Hamiltonian, while at higher energy this effect is weakened. This would make the $|D_s/D_d|$ ratio near threshold increase to its asymptotic value, but it is clear from both the experimental and theoretical results that this is not what happens. The discrepancy between the trend of both the experimental and theoretical values of $|D_s/D_d|$ and what would be expected from this

simple picture can be explained as follows: the d radial distribution for the photoelectron contains nodes, and by changing the energy of the photoelectron the positions of these nodes are also changed. The integral

$$\int_0^{+\infty} R_{3p}(r) r R_{\epsilon d}(r) r^2 dr \tag{8.7}$$

can then change sign at certain energies, resulting in zero values of D_d, that are defined Cooper minima [4]. This effect modifies the expected trend for $|D_s/D_d|$. This idea is in fact supported by Lörch *at al.* [3], where the presence of a Cooper minimum was found at $h\nu = 59\,eV$.

From the comparison between the extracted parameters and those calculated with RPAE, it can be concluded that the lsj coupling scheme seems entirely appropriate; this is also in agreement with both the independent results of Lörch *et al.* [3].

8.4 4p photoionization of Sr

Both the experimental procedure and the analysis of the measurements for $4p$ photoionization of Sr are very similar to those of $3p$ photoionization of Ca.

Photoelectron spectra were recorded at photon energies of 34, 36, 38, 40 and $42\,eV$. The low energy background in the electron spectra did not allow spectra to be recorded as close to threshold as in the case of Ca; the lowest kinetic energy possible was $4.87\,eV$ from threshold, while in the case of Ca it was $1.66\,eV$. This is a serious restriction because, as pointed out in section 8.1, it would normally be expected that the most interesting region for this investigation, apart from near Cooper minima, would be close to threshold.

The binding energy of the $4p_{3/2}$ orbital in Sr is lower than the binding energy of the $3p_{3/2}$ orbital in Ca: they are 29.13 and $34.34\,eV$ respectively, this made it possible to have reasonable count rates up to photon energies of $42\,eV$, this allowing measurements to be recorded over a broader photon energy range for Sr than in the case of Ca.

The Sr electron spectra are displayed in figures 8.6-8.10. Each figure contain the spectra recorded at both angles of observation, 0^o and 90^o, and shows both the $4p^5 5s^2$ photolines and the complementary NOO Auger lines as well as additional structure. The experimental conditions for these spectra were similar to the spectra of Ca: the pass energies of both analysers was $10\,eV$, the monochromator bandwidth was set to approximately $50\,meV$ and the degree of linear polarization S_1 was approximately 0.73. The count rate of each photo- and Auger line decrease when moving to higher photon energy, for the same reasons as in the case of Ca and explained in section 8.3.

In the spectra at $h\nu = 34\,eV$ the background has been removed in the energy region of the photolines; this subtraction propagates an additional contribution to the estimated uncertainties for the β_e parameters. The spectra recorded at higher photon energy presented lower backgrounds and their subtraction was considered not necessary.

A major difference between the spectra of Sr and of Ca is that more structure is present in the former spectra. Assignments to the spectra have been made with the help of the energies tabulated in table 5.4, which are from the photoabsorption work of Mansfield and Newsom [5], and from the ejected electron spectrum of White *et al.* [6]. The main photolines of the $4p^5 5s^2\,{}^2P_{3/2,1/2}$ doublet are labeled 2 and 3 and have ionization energies of $28.16\,eV$ and $29.13\,eV$ respectively. The peaks labeled 2' and 3' correspond to their complementary Auger lines, $N_3O_1O_1$ and $N_2O_1O_1$, with kinetic energies of $12.43\,eV$ and $11.46\,eV$ respectively. The $4p^5 4d(^3P)5s\,{}^2P_{3/2}$ photoline and its corresponding Auger line have ionization energy and kinetic energy of $27.37\,eV$ and $10.89\,eV$ respectively and are

observable for every photon energy at both angles and are labeled 1 and 1'.

An Auger line labeled 4' is present in the spectra at $h\nu = 36$, 38 and $42\,eV$ and it corresponds to the decay of the $4p^5 4d5s\,^4D_{1/2}$ state at a kinetic energy of $12.70\,eV$. Another Auger line, labeled 5' is present in the spectra at $h\nu = 40$ and $42\,eV$ and it corresponds to the decay of the $4p^5(4d^2\,^1D)^2P_{1/2}$ state with kinetic energy of $12.97\,eV$.

A further weak peak, at a kinetic energy of $10.20\,eV$, in the spectrum at $h\nu = 34\,eV$ of the fixed analyser, may correspond to unresolved Auger decays from the $4p^5 4d5s\,^4P$ states. These Auger lines could be responsible for the tailoring of peak 1' towards lower kinetic energies in the spectrum at $h\nu = 36\,eV$, even though peaks 2' and 3' have similar shapes and are more isolated.

In the spectra at $h\nu = 36\,eV$, at both angles of observation, peaks 3 look broader than peaks 1 and 2; this may be caused by partial overlap with the $4p^5 4d5s\,^4D_{1/2}$ photoline, that has an ionization energy of $29.401\,eV$, only $170\,meV$ higher than the binding energy of peak 3, and is the complementary photoline of the Auger line labeled 4'. If this is the case, this effect should be observable at every photon energy, it is in fact observable also at $h\nu = 38\,eV$, in particular in the rotatable analyser, and even more clearly at $h\nu = 40$ and $42\,eV$ (see below). The Auger lines corresponding to these photolines are labeled 3' and 4' and due their narrower profiles are well resolved; from the 3':4' intensity ratio it can be concluded that the $4p^5 4d5s\,^4D_{1/2}$ photoline gives only a very small contribution to peak 3.

The spectra taken at $h\nu = 40$ and $42\,eV$ show narrower peaks than those taken at lower photon energies, even though they were recorded with the same exit slit settings of the monochromator and with the same pass energies of the electron analysers. They were recorded one and two days after the spectra at $h\nu = 36$ and $38\,eV$ and four and five days after the spectrum at $h\nu = 34\,eV$; a possible explanation for the improved resolution in the spectra at higher photon energy may be the coating of the entrance slits of the analysers and theirs surroundings by metal vapour. This creates contact voltages that can slowly change with time, and at a certain point can improve the resolution of the electron optics. In these spectra the Auger lines are clearly narrower than the photolines, the reason for this is that there is no contribution from the light bandwidth.

In the spectra at $h\nu = 40\,eV$, at both angles of observation, the peaks labeled 3+1' are the result of the unresolved photoline 3 and Auger line 1', they are not resolved as their kinetic energies differ by less than $250\,meV$, comparable to the width of the photoline.

In the spectra at $h\nu = 40\,eV$ it can also be seen that, although peaks 1 and 3' have

$h\nu/eV$	KE/eV	$\beta_e(1/2)$	$\beta_e(3/2)$	β_A
34	4.87	1.46(25)	1.39(25)	0.18(10)
36	6.87	1.25(20)	1.36(20)	0.20(05)
38	8.87	1.33(20)	1.36(20)	0.25(05)
40	10.87	0.56(20)	1.44(20)	-0.03(10)
42	12.87	1.50(20)	1.39(20)	0.20(05)

Table 8.4: Asymmetry parameters for the $4p^5 5s^2$ photoelectron and $N_3O_1O_1$ Auger electron in Sr. The values between brackets are the uncertainties on the last digits (one standard deviation).

the same separation as peaks 3 and 1' because they are their complementary photo- and Auger lines, they appear better resolved. The overlap between peaks 1' and 3 makes what would otherwise be peak 3 more intense than peak 2 at both angles; this occurs for both spectrometers and is unique for this photon energy, and is also against what would be expected from the degeneracy ratio of the 3/2 and 1/2 components of the $4p^5 5s^2\,{}^2P$ doublet.

In the spectra at $h\nu = 40\,eV$ some overlap seems present on the left side of peak 3+1'; a possible candidate could be the Auger line from the $4p^5(4d^2\,{}^3F)({}^3P)\,{}^3D_{1/2}$ state, that has a kinetic energy of $11.03\,eV$, $140\,meV$ higher than peak 1', but strangely this Auger line seems absent in the spectra at $h\nu = 42\,eV$. In the Auger spectra following electron impact of White *et al.* of reference [6] the intensity ratio between this Auger line and the one from the $4p^5 4d5s\,{}^2P_{3/2}$ state (1') is less than 0.25. Since the energy of the electron impact in the work of reference [6] was $500\,eV$, from the Born approximation it would be reasonable to expect similar intensity ratios to those in this work. If this is the case, the problem of overlap between these photolines and Auger lines at $h\nu = 40\,eV$ may not be severe.

The $4p^5(4d^2\,{}^3F)({}^3P)\,{}^3D_{1/2}$ photoline in the spectra at $h\nu = 40\,eV$, at an ionization energy of $27.73\,eV$, can probably also be assumed to be very small. Otherwise it would be observable in the spectra at $h\nu = 42\,eV$ as a shoulder on the $4p^5 4d({}^3P)5s^2\,{}^2P_{3/2}$ photoline, or at the very least it would make this photoline appear broader.

The conclusion concerning the peaks 3+1' must be that it is not possible, from the spectra in figure 8.9, to extract the values β for lines 3 and 1'. This is not a serious restriction in the present work, because the following analysis does not require the asymmetry parameters of these lines.

With the better resolution in the spectra at $h\nu = 40$ and $42\,eV$ a shoulder is seen on the

		non-coincidence		coincidence	
$h\nu/eV$	KE/eV	$\lvert D_s/D_d\rvert$	Δ_{sd}/π	$\lvert D_s/D_d\rvert$	Δ_{sd}/π
34	4.87	0.31(10)	0.70(05)	0.31(02)	0.70(04)
36	6.87	0.35(05)	0.68(05)	0.34(10)	0.73(07)
38	8.87	0.45(05)	0.67(05)	0.44(07)	0.71(07)
40	10.87	-	-	-	-
42	12.87	0.35(05)	0.69(05)	0.37(09)	0.71(09)

Table 8.5: Values of $|D_s/D_d|$ and Δ_{sd} for $4p$ photoionization of Sr. Third and fourth columns: non-coincidence analysis, fifth and sixth columns: fix fit. The values within brackets are the errors on the last digits (one standard deviation).

right side of peak 3+1', in particular for the fixed analyser; this is probably due to the $4p^5 4d5s\,^4D_{1/2}$ photoline as tentatively mentioned before for the spectra at $h\nu = 36$ and $38\,eV$. The overlap with this photoline should not change with photon energy in this non resonant region and is probably not very important.

The asymmetry parameters extracted from the spectra of figures 8.6-8.10 are listed in table 8.4 and plotted in figure 8.11. As in the case of Ca, it is reassuring to see that the 1/2 and 3/2 photolines have very similar values of β_e at almost every energy, providing additional support to the LSJ coupling scheme for the $4p^5 5s^2$ configuration and also confirming consistency and reliability of the analysis. The reported value of $\beta_e(1/2)$ at $h\nu = 40\,eV$ is seriously affected by overlap, as pointed out above, and it cannot be used.

The measured values of β_e and β_A are constant within the reported uncertainties, apart from β_A at $h\nu = 40\,eV$. From the lsj approximation the minimum possible value for β_A is 0.1, while the measured value of β_A at $h\nu = 40\,eV$ is $-0.03(10)$ which seems to suggest a breakdown of the lsj coupling scheme. However, the measurements at this energy should be rejected on the basis of inconsistency with the data at other photon energy.

Most interesting is that within these uncertainties, the value of β_e is constant, and in β_A there is only a very small tendency to increase with photon energy. From this results it must be concluded that the extracted values of both $|D_s/D_d|$ and Δ_{sd} will be nearly constant with energy, in particular those extracted with the non-coincidence analysis.

The coincidence measurements between the $N_3O_1O_1$ Auger electron, detected by the fixed analyser at $\theta_F = 0^o$, and the $4p_{3/2}$ photoelectron, detected by the rotatable analyser at a varying θ_R, are shown in the graphs of figure 8.12. The solid curves are the least chi square fits of equation (8.6) to the data points; the resulting A_i parameters are written on the graphs.

$h\nu/eV$	KE/eV	$\lvert D_s/D_d \rvert$	$\lvert D_{3/2}/D_{5/2} \rvert$	Δ_{sd}/π
34	4.87	0.27(15)	0.29(12)	0.73(11)
36	6.87	0.49(31)	0.51(40)	0.71(06)
38	8.87	0.68(22)	0.57(25)	0.73(09)
40	10.87	-	-	-
42	12.87	-	-	-

Table 8.6: Results of the free fit for $4p$ photoionization of Sr. The values within brackets are the uncertainties on the last digits one standard deviation).

The values of $|D_s/D_d|$ and Δ_{sd} extracted with both the non-coincidence analysis and with the fix fit are listed in table 8.5. For the same reason as in the case of Ca, explained in section 8.3, the sign of Δ_{sd} cannot be extracted from these analysis, and is chosen to be the same as that of Ca. The values within brackets are the errors on the last digits (one standard deviation). The stability of the results from the fix fit with changes in the initial values of the parameters was tested and is good. As in the case of Ca, it is reassuring to see that the non-coincidence analysis agrees well with the fix fit of the data. It is clear from the data of table 8.5 that the d wave is dominant as the ratio $|D_s/D_d|$ is always lower than 1.

In order to understand how important the contribution of the coincidence data to this analysis is, the fix fit was also executed with the errors in Ai increased by a factor of 10. The result was that the fit converges to the same values and also with the same uncertainties. This means that, unlike the case of Ca where increasing the errors on Ai makes the results from the fix fit progressively closer to the results of the non-coincidence analysis, the coincidence data for Sr contain very little information.

As expected, both the parameters from the fix fit and from the non-coincidence analysis show very little change with photon energy; in particular, Δ_{sd} is constant at approximately 0.7π. $|D_s/D_d|$ is within the range 0.31 to 0.45. In the non-coincidence analysis this parameter depends only on β_A, which, because of its very low value, is easily affected by systematic errors introduced by the efficiency calibration of the analyser.

A possible interpretation for the fact that these parameters are rather constant is that the energy range investigated is too far from threshold to observe a negative slope of $|D_s/D_d|$, and is also far from the expected Cooper minimum.

It is very interesting to compare the values of Δ_{sd} for Sr, constant at approximately 0.7, with those for Ca, that rise from 0.24 to 1.03. No explanation for this marked difference is known at the present time.

Table 8.6 contains the results from the free fit. The free fit does not converge at $h\nu = 40$ and $42\,eV$. The reason is probably that, because the coincidence data are more scattered and less well determined than at other energies and also than the coincidence measurements in Ca, the A_i parameters are less accurate and therefore do not provide enough statistical information. The increased number of parameters in the free fit with respect to the tix fit makes their determination less accurate than in the fix fit. With the resulting uncertainties, the values of $|D_s/D_d|$ and Δ_{sd} of the free fit in table 8.6 are the same as those of the fix fit in table 8.5. Most interesting, the values of $|D_{3/2}/D_{5/2}|$ is 1:3. The conclusion is that there is no evidence for breakdown of the lsj coupling scheme.

8.5 Conclusions

Measurements of the asymmetry parameters for $3p$ and $4p$ photoelectrons of Ca and Sr respectively, and of the complementary Auger electrons, allowed the relative amplitudes and phases of the dipole matrix elements for the $3p$ and $4p$ photoionization processes in Ca and Sr to be extracted. Measurements of angular correlation between photoelectrons and Auger electrons have proved to be useful in testing the validity of the lsj approximation. Comparison between the results of the analysis of the non-coincidence data and the coincidence data, and also results of $RPAE$ calculations in the case of Ca, supported the validity of the lsj approximation for $3p$ and $4p$ photoionization of Ca and Sr.

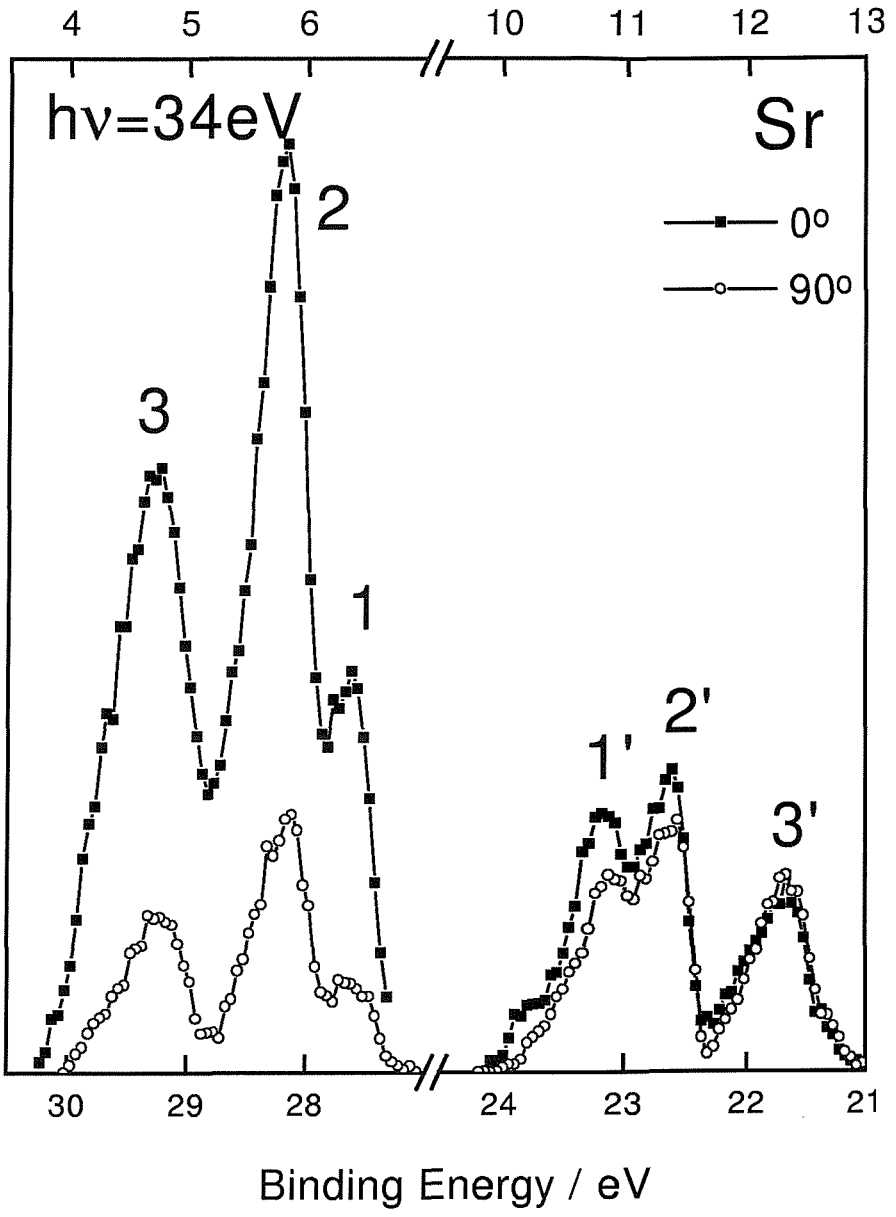

Figure 8.6: Photoelectron spectra of Sr at $h\nu = 34\,eV$ at two angles of observation: 0^o and 90^o. The kinetic energy is on the top scale.

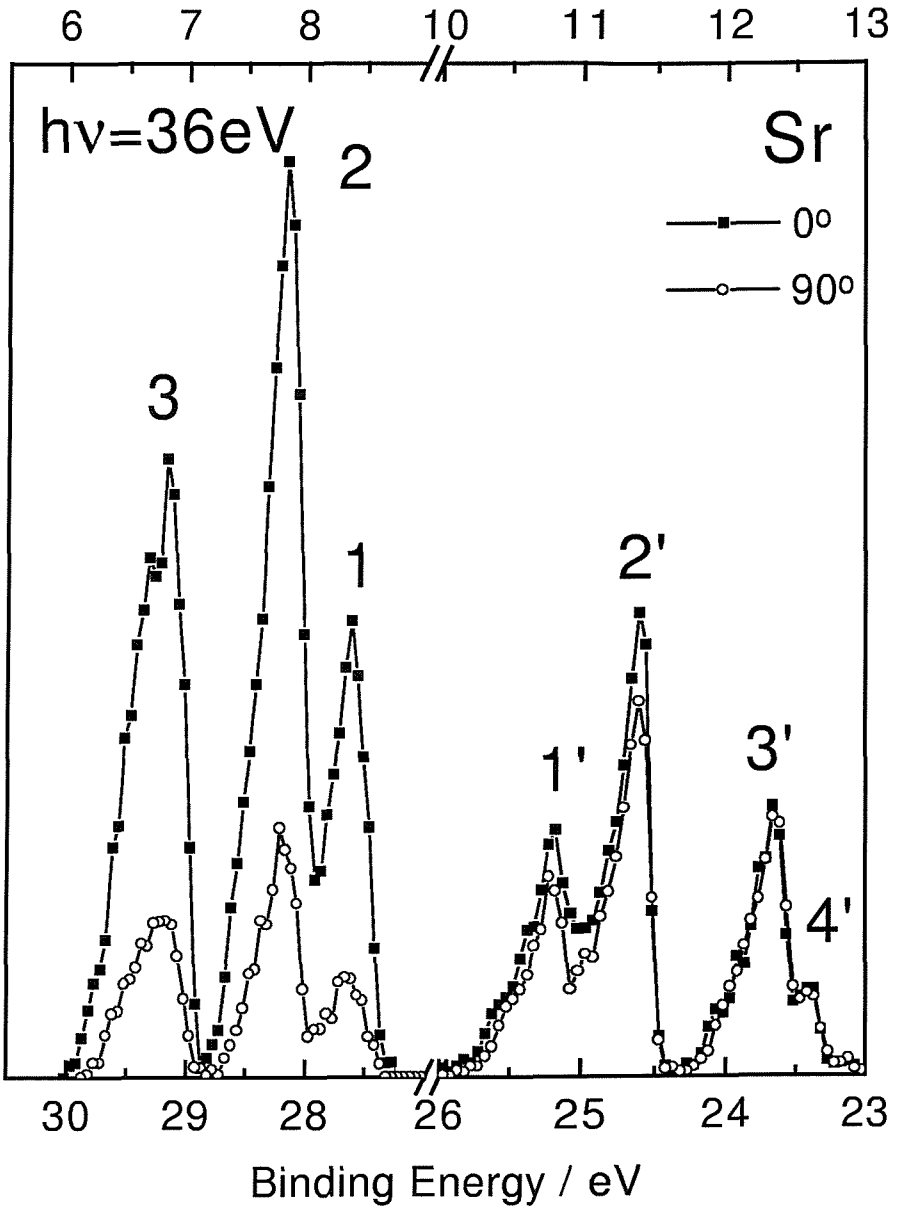

Figure 8.7: Photoelectron spectra of Sr at $h\nu = 36\,eV$ at two angles of observation: 0^o and 90^o. The kinetic energy is on the top scale.

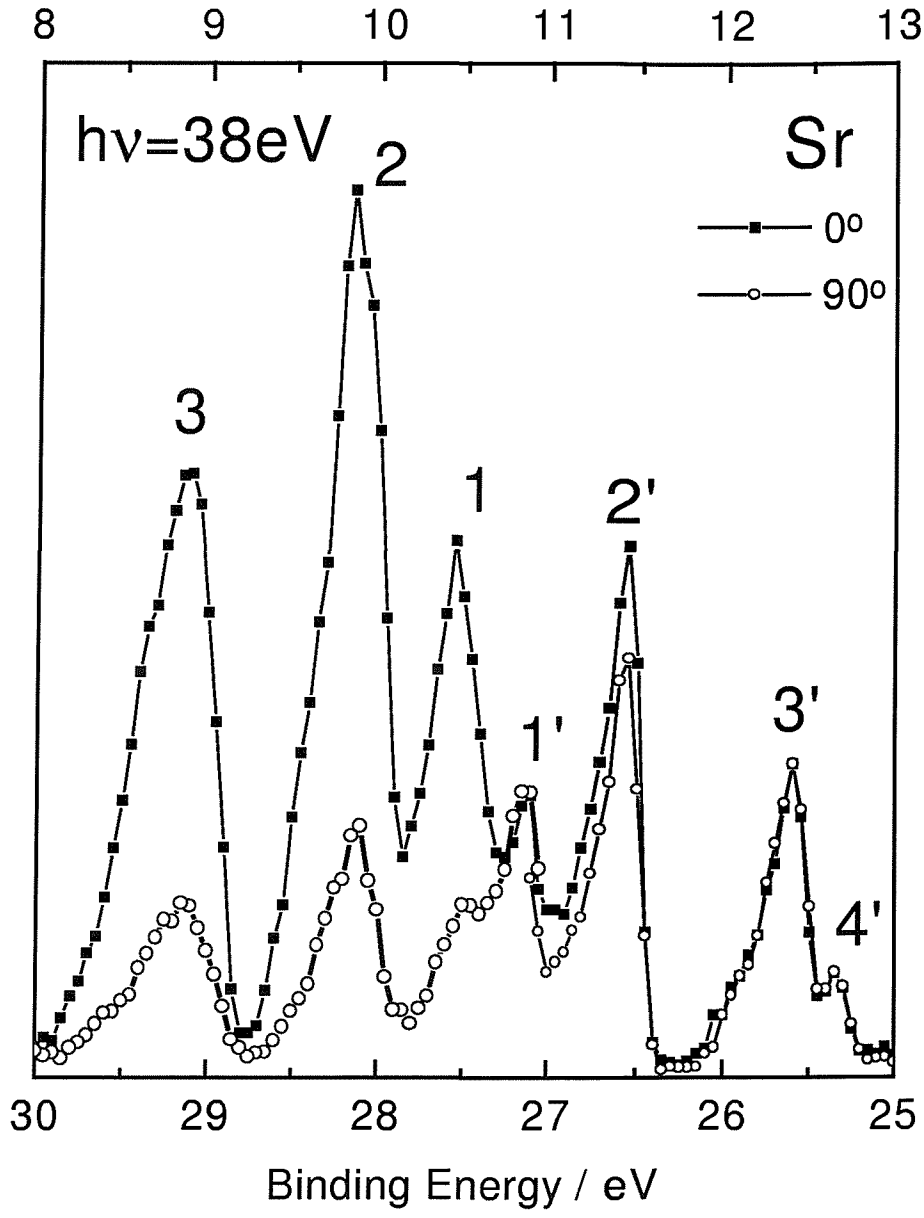

Figure 8.8: Photoelectron spectra of Sr at $h\nu = 38\,eV$ at two angles of observation: 0^o and 90^o. The kinetic energy is on the top scale.

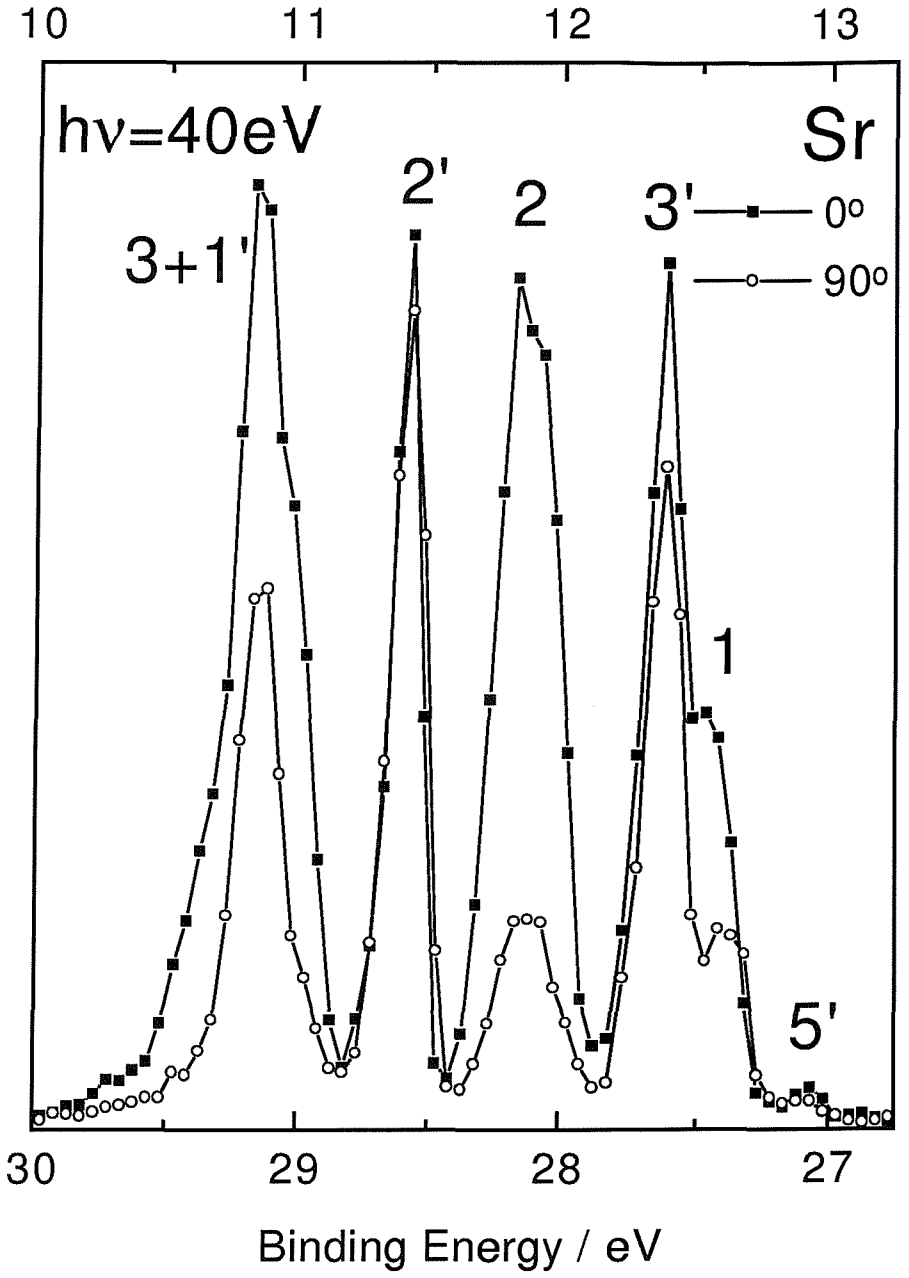

Figure 8.9: Photoelectron spectra of Sr at $h\nu = 40\,eV$ at two angles of observation: 0^o and 90^o. The kinetic energy is on the top scale.

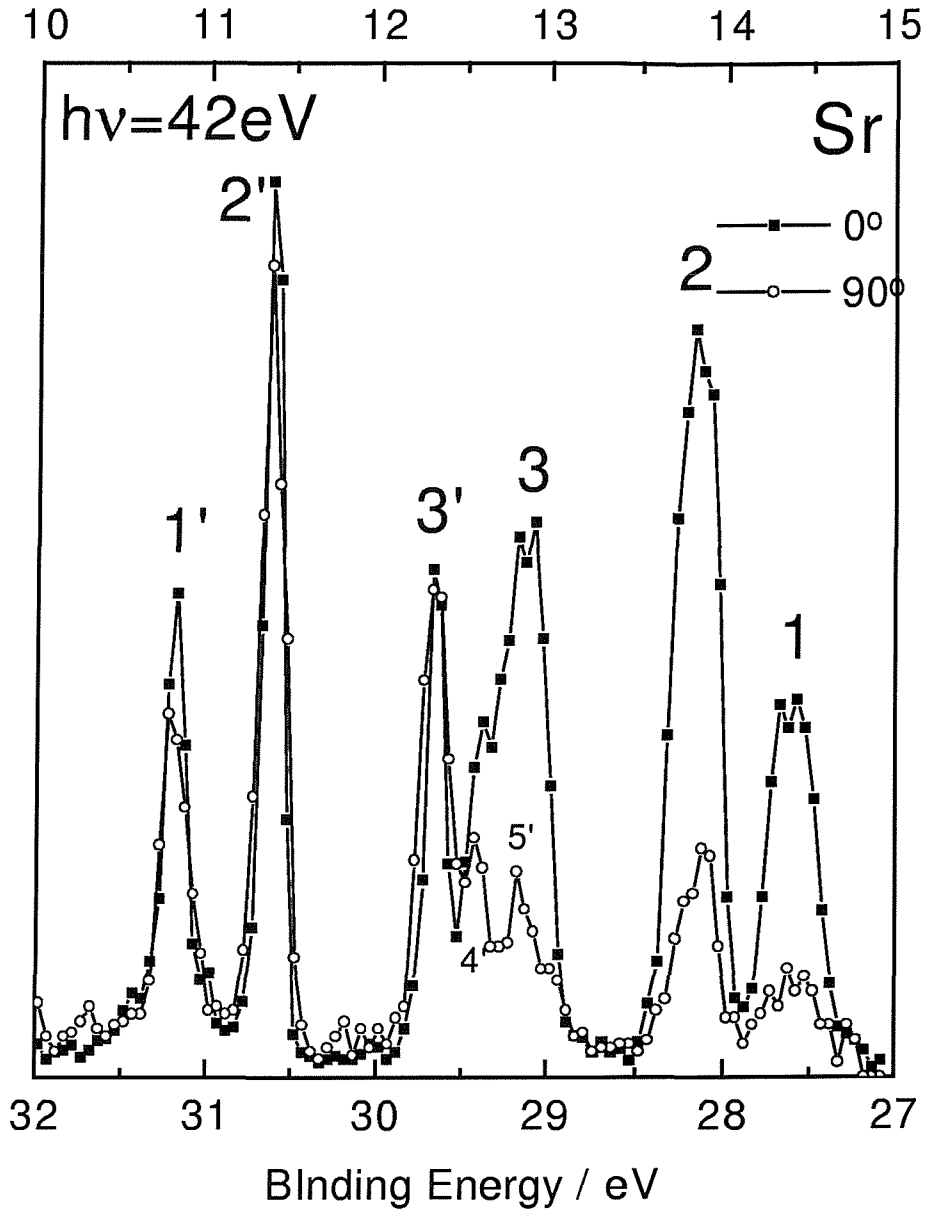

Figure 8.10: Photoelectron spectra of Sr at $h\nu = 42\,eV$ at two angles of observation: 0^o and 90^o. The kinetic energy is on the top scale.

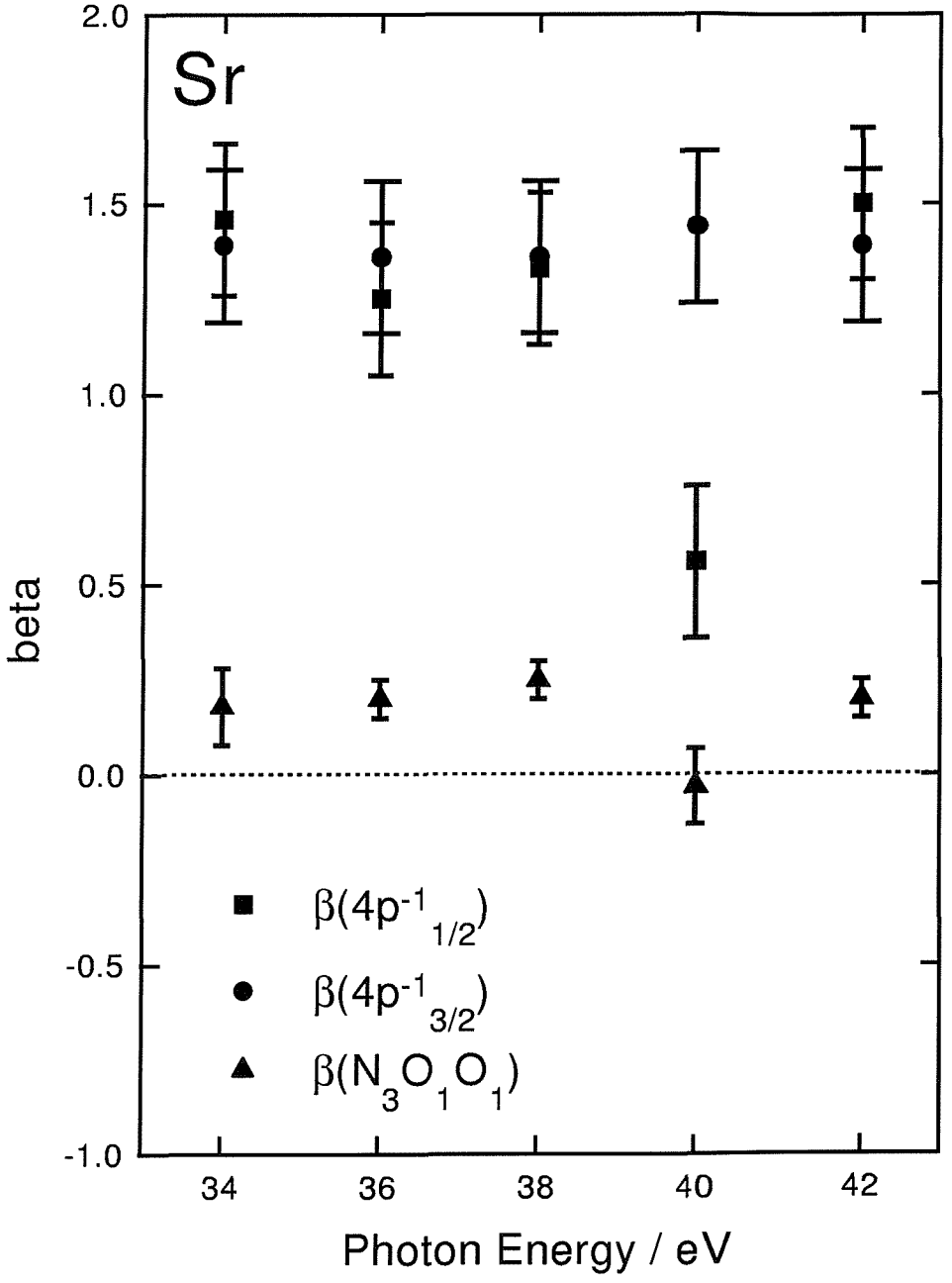

Figure 8.11: Asymmetry parameters for the $4p^5 5s^2\, ^2P_{1/2,3/2}$ photolines and the $N_3O_1O_1$ Auger lines of Sr.

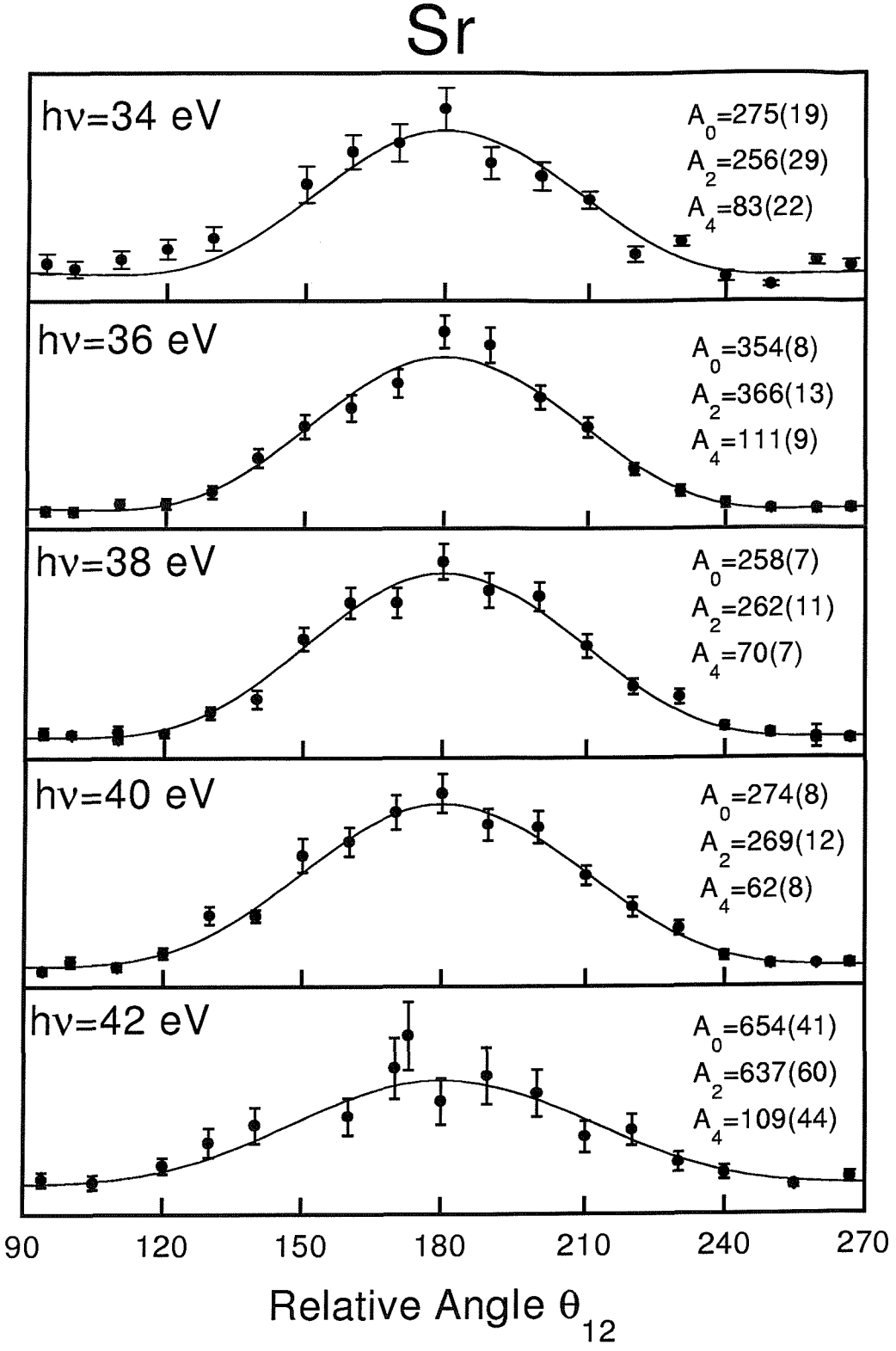

Figure 8.12: Coincidence measurements between the $4p_{3/2}$ photoelectron and the $N_3O_1O_1$ Auger electron in Sr at $h\nu$ = 34-42 eV. The solid curves are the least chi square fits of equation (6.6) to the data points and the resulting A_i parameters are displayed on the graphs.

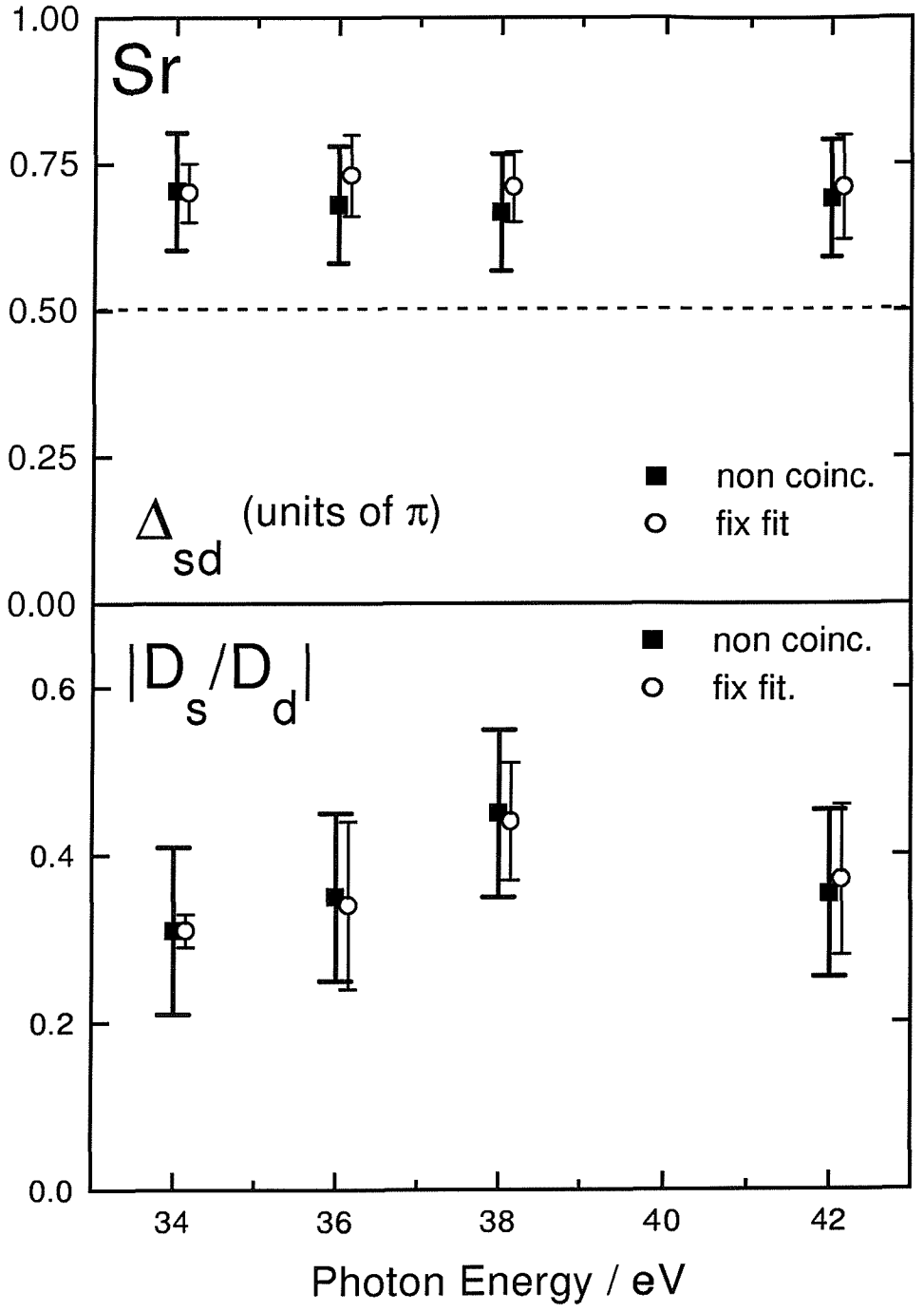

Figure 8.13: Values of $D_s/D_d|$ and Δ_{sd} from the non-coincidence analysis and from the fix fit for $4p$ photoionization of Sr; the latter have been plotted at slightly different energies to make the comparison easier.

Bibliography

[1] H-J Beyer, JB West, KJ Ross, K Ueda, NM Kabachnik, H Hamdy and H Kleinpoppen, *Journal of Physics B: Atomic, Molecular and Optical Physics*, **28** L47-L52 (1995).
JB West, K Ueda, NM Kabachnik, KJ Ross, H-J Beyer and H Kleinpoppen, *Physical Review A*, **53** R9-R11 (1996).
H-J Beyer, JB West, KJ Ross, K Ueda, NM Kabachnik, H Hamdy and H Kleinpoppen, *Journal of Electron Spectroscopy and Related Phenomena*, **79** 339-342 (1996).
JB West, KJ Ross, K Ueda and HJ Beyer, *Journal of Physics B: Atomic, Molecular and Optical Physics*, **31** L647-L654 (1998).

[2] A De Fanis, JB West, KJ Ross, K Ueda, H-J Beyer, M Ya Amusia and LV Chernysheva, *Journal of Physics B: Atomic, Molecular and Optical Physics*, **32** 5739-5749 (1999).

[3] H Lörch, JM Bizeau, N Scherer, S Diehl, D Cubaynes, O Zerouni, FJ Wuilleumier, V Schmidt and RW Johnson, *Journal of Physics B: Atomic, Molecular and Optical Physics*, **32** 2215-2226 (1999).

[4] J Cooper, *Physical Review A*, 128 681 (1962).
U Fano and J Cooper, *Review of Modern Physics*, **40** 441-507 (1968).

[5] BWD Mansfield and TW Ottley, *Proceedings of the Royal Society of London*, **377** 431-448 (1981).

[6] MD White, D Rassi and KJ Ross, *Journal of Physics B: Atomic, Molecular and Optical Physics*, **12** 315-322 (1979).

Chapter 9

Experimental apparatus for the study of photoelectron spectroscopy of reactive intermediates

9.1 Introduction

This chapter describes the experimental apparatus used for the study of PES of reactive intermediates [1]; a different spectrometer is used from that used for the work on metal vapours. This instrument enables reactive intermediates to be produced by microwave discharge of a flowing gas mixture or by rapid atom-molecule reactions. Angle resolved PES studies are also possible. Two kinds of spectra are normally recorded, they are described in section 9.2. The spectrometer is maintained under vacuum by the system described in section 9.3. Electrons produced by interaction between the sample and the vacuum ultraviolet radiation are analysed in energy and direction as described in section 9.4. Section 9.5 outlines the electronics used to control the voltages and acquire the signals. Sample production is presented in section 9.6, section 9.7 explains the rotation facility for angle resolved measurements, and section 9.8 describes the radiation sources used.

9.2 Types of spectra

The spectrometer has been designed to allow two different kinds of spectra to be recorded: photoelectron (PE) spectra and constant ionic state (CIS) spectra.

In a photoelectron spectrum the yield of electrons is measured as a function of their kinetic energy, with the wavelength of the incident radiation fixed at a particular value. This kind

of spectrum is recorded by scanning the voltage on the last element of an electron lens, V_3, that either accelerates or retards the electrons. The voltages on the two electrodes of the analyser are also scanned synchronously with V_3, in such a way to maintain the region of space in the middle of them at the same potential as the third lens element, but their potential difference is maintained at a constant value, in order to keep a constant pass energy through the analyser. The voltage on the second lens element is also scanned together with V_3, to focus electrons with different kinetic energies from the entrance to the exit slits of the lens. An electron energy spectrum of this type provides a map of the ionic states that are accessed, and allows ionization energies to be measured. The overall resolution, that is the combination of the resolution of the analyser and the bandwidth of the radiation, as well as any other contributions from, for example, contact potentials, is normally of the order of $45\,meV$. This allows vibrational progressions to be resolved in photoelectron spectra of most light molecules.

The spectrometer is routinely transported to the Daresbury SRS, where CIS spectra are also recorded. In a CIS spectrum the yield of electrons corresponding to a selected ionization process, normally a given vibrational component of a photoelectron band, is measured as a function of the wavelength of the incident radiation. In this kind of spectrum the kinetic energy of the electrons to be detected is scanned simultaneously with the wavelength of the radiation, while maintaining their difference equal to the ionization energy of the process under investigation; this is why these spectra are called "constant ionic state", or CIS. A CIS spectrum can show discrete structure when the radiation is resonant with a neutral state that autoionizes to the ionic state under investigation. The resolution in a CIS spectrum, that depends only on the radiation bandwidth and not on the analyser resolution, normally allows vibrational progressions in neutral excited states to be resolved.

9.3 The vacuum system

The spectrometer must be evacuated to high vacuum, $P < 10^{-5}\,mbar$, to let the radiation pass through, to allow the electrons to travel through the electron optics, and to allow the electron detector to operate properly.

In contrast to the work on metal vapours, where no gas is deliberately let into the chamber, a high gas throughput is desired here, and this can be obtained with a high pumping speed.

The present spectrometer has been designed with the objective of studying reactive intermediates, some of which are produced *in situ* by fast atom-molecule reactions with

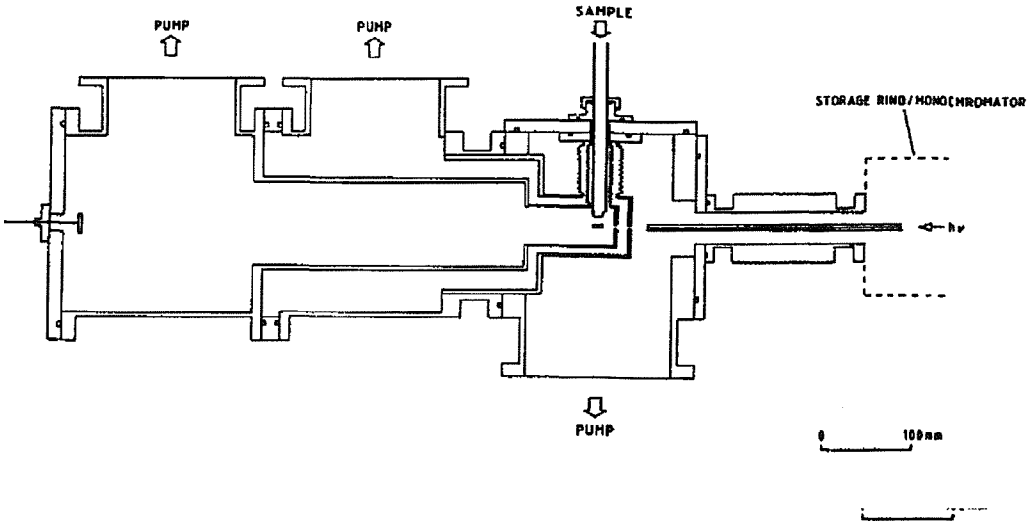

Figure 9.1: Cross section of the spectrometer in the vertical plane containing the photon beam.

precursors that can be chemically aggressive. This adds additional constraints to the spectrometer design. The performance of the spectrometer when using such gases is inhibited by contamination of electron optics components, as such contamination can coat surfaces and cause charging effects, or even damage or destroy the detector. Therefore, it is important to maintain low pressure in sensitive regions, and for this reason the spectrometer is differentially pumped.

PE spectrometers that are used by the Southampton PES group to study reactive species have the ionization and the analyser chambers isolated by the small slit at the entrance of the hemispheres [2]. One diffusion pump is fitted to each chamber, with the pump on the ionization region that receives most of the gas-load, reducing contamination of the analyser. This system was the basis of the spectrometer described here, but some modifications had to be introduced. Diffusion pumps must be avoided in a synchrotron environment because of the risk of backstreaming of oil towards the beam-line; as a result the present spectrometer is evacuated by turbomolecular pumps backed by oil-sealed rotary pumps. In addition, diffusion pumps must always operate vertically and this would not have been possible with the present rotation facility (see section 9.7).

Figures 9.1 and ?? show schematically the pumping system of the spectrometer. The ionization region, labelled D, is enclosed within two boxes (C). The boxes are closed, apart from a $2\,mm$ circular aperture at the front to collimate the photon beam, the slits ($10\,mm \times 2\,mm$) which point towards the electron analyser, and a $12\,mm$ diameter hole at the top for the introduction of the sample. The rear of each box is open to allow pumping.

The inner box is part of the region evacuated by pump 1 (Leybold Turbovac 361C, $400\,l/s$), and the bulk of the gas is pumped away through this region. Most of the gas that escapes through the slits on the inner box is pumped away by pump 2 (Leybold Turbovac 361C, $400\,l/s$).

A minimum amount of gas escapes from the boxes and enters the ionization chamber, connected to pump 3 (Leybold Turbovac 1000, $1000\,l/s$). Under working conditions an ionization gauge measures the pressure outside the boxes, whose base value is $2\times10^{-7}\,mbar$ and it rises up to between 5×10^{-6} and $5\times10^{-5}\,mbar$ when gas is admitted. A pressure higher by at least one order of magnitude than this is expected in the inner box. No appreciable change in the beam-line pressure is observed when gas is admitted. Pressures in the spectrometer are measured by ionization gauges and read by an Edwards AGC controller.

Because pumps 1 and 2 receive a heavy load of reactive gases, both have corrosion resistant coatings, and are also fitted with purge valves to reduce bearing contamination and extend the operational lifetime when pumping corrosive gases.

It is of paramount importance to avoid gases travelling towards the ultra high vacuum (UHV) environment of the beam-line, as they could severely damage optical components; this is even more critical when working with aggressive species. A glass capillary with low conductance ($300\,mm$ long $\times\,2\,mm$ bore), labelled G in figure 9.1, helps to maintain differential pumping between the spectrometer and the beam-line.

The analyser is separated from the ionization region by an electron lens, labelled B in figure 9.2 (see section 9.4). One of the reasons for using the lens is that it helps to maintain differential pumping between the ionization region and the analyser. As can be seen from figure 9.2 the region around the boxes and the chamber containing the analyser are pumped separately by pump 3 and pump 4 (Leybold Turbovac 600 and 1000, 600 and $1000\,l/s$ respectively). The base pressure in the analyser region is $10^{-6}\,mbar$, and it rises only slightly when gas is admitted.

9.4 The electron optics

Figure 9.2 is a view of the cross section through the analyser, perpendicular to the photon beam; it shows the ionization region (C), surrounded by two boxes (D), separated from the analyser (A) by an electron lens (B), all surrounded by a layer of μ-metal (F).

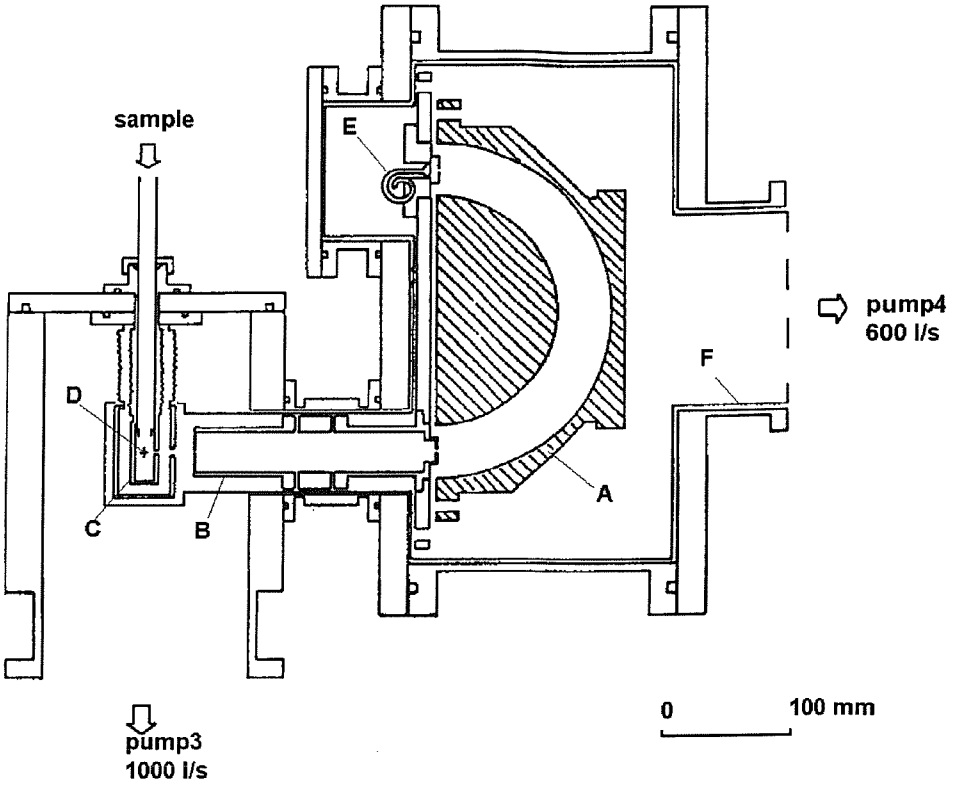

Figure 9.2: Cross section of the analyser system in the vertical plane perpendicular to the photon beam.

9.4.1 The analyser

The electron energy analysers consists of two 180^o hemispherical sectors. The inner and outer sectors are constructed from aluminium, and have radii R_i and R_o of 80 and 120 mm respectively. In order to select electrons with mean pass energy E_{pass}, the sectors have to be at potentials V_i and V_o given by:

$$V_i = E_{pass}\frac{R_o}{R_i}, \tag{9.1}$$

and

$$V_0 = E_{pass}\frac{R_i}{R_o}. \tag{9.2}$$

In the present geometry at $E_{pass} = 5$ and $10\,eV$ these equations make $V_i = 7.50$ and $15.0\,V$, and $V_o = 3.32$ and $6.64\,V$.

The contribution of the finite width of the slits of the analyser (ΔS) to the full width at half maximum (FWHM) of a photoelectron band is approximately [3]

$$\Delta E_{FWHM} = \frac{\Delta S}{R_i + R_o}E_{pass}. \tag{9.3}$$

In equation (9.3) ΔS is the common width of the entrance and exit slits, $\Delta S = \Delta S_{entrance} = \Delta S_{exit}$. For this analyser $\Delta S = 1\,mm$, at $E_{pass} = 5$ and $10\,eV$ equation (9.3) makes ΔE_{FWHM} equal to 25 and $50\,meV$. Narrower slits and lower pass energy would produce higher resolution but at the expense of the number of electrons transmitted; the values chosen are always the result of a compromise between count rate and resolution. Another important contribution to the FWHM comes from contact potentials that may cause the electron beam to spread, accelerate or decelerate. To minimise these potentials all the inner surfaces "seen" by the electrons are coated with a conductive layer of graphite, called "dag". Contamination of the electron optics from the reactive gases used, usually leads to the resolution and transmission deteriorating with time; cleaning and replacement of the dag coating is a simple way to regain suitable conditions.

9.4.2 The electron lens

In other spectrometers used in Southampton, PE spectra are recorded by sweeping the voltages on the hemispheres, so that the energy of the transmitted electrons varies. As mentioned in section 6.4, this procedure has the disadvantage of giving different resolution and transmission for electrons with different energies. In the present apparatus the analyser operates at a constant pass energy, typically 5 or $10\,eV$, and the electrons are accelerated (or retarded) by a lens to a fixed energy before they enter the analyser.

The lens is constructed from three electrically isolated, coaxial, cylindrical aluminum elements. The first element is earthed, so that the electrons in this segment have their initial kinetic energy from ionization. The third element is at a voltage $V_3 = E_{pass} - E_1$, with E_1 the original energy of the electrons, so that when moving from the first to the third element these electrons are accelerated or decelerated to the pass energy E_{pass}. The plate on which the lens and the analyser are mounted is also at the potential V_3, in order to have no change in energy when the electrons leave the lens and enter the analyser.

The focus curve

The second element of the lens is at a potential V_2, and acts as a focusing element. The value of V_2 must be such that it makes the exit slit of the lens the optical image of the entrance slit. The values of V_2 as a function of electron kinetic energy is called focus curve. Focus curves for various lens geometries have been calculated by Harting and Read [4], but are determined empirically in this work. This is done by optimising V_2 so that the intensity of a particular electron signal is maximised at a selected kinetic energy and for a selected pass energy. This operation is then repeated for a selection of kinetic energies;

a fourth order polynomial is fitted to the data so obtained, $(E_1 + V_2)/E_1$ vs E_{pass}/E_1, and the coefficients are passed to the controlling software that uses them to calculate the focusing voltage V_2 for each point in the spectrum.

At the Daresbury SRS, the data for the focus curve are obtained by observing the $Ar^+(3p^5\,{}^2P_{3/2}) \leftarrow Ar(3p^6\,{}^1S_0)$ photoline at different wavelengths. In Southampton only the HeI discrete line source is available, and different kinetic energies are obtained by observing at the Ar and O_2 PE bands.

9.4.3 The shielding

External electric and magnetic fields can affect the paths of electrons to be analysed and for this reason they must be suppressed. The spectrometer is made almost entirely of metal, so electrostatic fields do not penetrate. Screening of magnetic fields is more challenging. The laboratory based PE spectrometers in Southampton are enclosed in three orthogonal pairs of Helmoltz coils, in which currents are adjusted to minimise the magnetic field inside them. This is not suitable for experiments at a synchrotron radiation source because of space constraints, and also because Helmoltz coils would complicate the rotation of the apparatus. In the apparatus used here, critical regions of the spectrometer: the ionization region, the lens, the analyser and the detector, are surrounded by a $2\,mm$-thick layer of μ-metal, an alloy with high magnetic permeability that tends to constrain the magnetic field to pass within it rather than through it.

9.5 Electron detection and control system

Electrons that travel through the analyser and pass through the exit slit are detected by a single channel electron multiplier, or channeltron, labelled E in figure 9.2. This detector is of the same type as that described for the work on metal vapours in section 6.5. The electron pulses produced by the channeltron are preamplified and passed to an Ortec 590A amplifier, whose output goes to a CAMAC counter (Hytec 350A) and then to a computer. The output from the amplifier also goes to a ratemeter for visual display of the signal.

Voltages applied to the spectrometer, and signals from it, are controlled by a computer via a modular CAMAC system, with supporting NIM units and power supplies.

The voltages to the analyser should be controlled by an isolation amplifier; however, this was not used here due to the high level of noise. A simple battery is employed to float the voltages to the hemispherical sectors upon the accelerating potential applied to the third

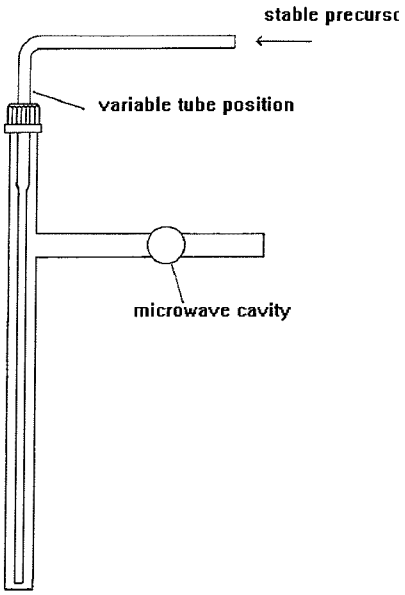

Figure 9.3: Schematic inlet system used for producing reactive intermediates by a rapid atom-molecule reaction.

element of the lens and also to the mounting plate of the two sectors. The potentials for the focusing and retarding elements of the lens are set by Kepco APH500M and BOP100-1M power supplies respectively, controlled by analog voltages from two digital to analog converters (DACs): Hytec 650 and 620, in the CAMAC crate, that are scanned by the computer.

The control software allows the collection of photoelectron (PE) and constant ionic state (CIS) spectra at the Daresbury SRS on beam-line 3.2 and 3.3, as well as their graphical display. Modified software will have to be written for future experiments at the Elettra SRS.

9.6 Production of the sample and inlet system

The species studied in this work are reactive molecules with short lifetimes, of the order of $\simeq 0.1\, msec.$ For this reason they must be produced *in situ*, for spectroscopic investigation, and then rapidly pumped away [5].

Methods that are commonly used to produce reactive intermediates are fast atom-molecule reactions, pyrolysis, photolysis, and gas-solid reactions. The first of these methods was

used to produce OH. OH was produced via the rapid reaction

$$H + NO_2 \rightarrow OH + NO. \tag{9.4}$$

The rate constant of this reaction is $1.1 \times 10^{-10}\, cm^3 molecule^{-1} sec^{-1}$ at room temperature [6]. Hydrogen atoms were produced by microwave discharging ($\simeq 2.45\, GHz$, $P \simeq 50 - 60\, W$) molecular hydrogen flowing through a $12\, mm$ bore glass inlet system. A schematic drawing of the inlet system used is shown in figure 9.3. In order to prevent low energy electrons produced in the discharge from entering the ionization region, the side inlet tube has three 90^o bends before it enters the central inlet tube. Helium is added to help to sustain the discharge, and the inner surface of the glass tube is coated with phosphoric acid to reduce hydrogen atom recombination. NO_2 is added to the $H/H_2/He$ mixture through a $1\, mm$ bore inner tube which passes down the centre of the vertical tube shown in figure 9.3. This inlet system has the facility of adjusting the position of the $H + NO_2$ mixing point above the photon beam by moving the central tube up or down.

The OH radicals produced by the reaction (9.4) undergo rapid secondary reactions:

$$OH + OH \rightarrow H_2O + O, \tag{9.5}$$

$$O + O + M \rightarrow O_2 + M, \tag{9.6}$$

that reduce the yield of radicals and also give H_2O bands in the spectra that can overlap with those from OH. This is a common problem when studying PES of reactive intermediates. In order to reduce the concentration of secondary products in the ionization region, the precursors must be mixed close to the photon beam, but too short a "mixing distance" would not allow the first reaction (9.4) to proceed. In fact, the yield of reactive intermediates as a function of the mixing distance starts from zero, rises up to a maximum and then decreases. This dependence can be useful to help to identify bands belonging to reactive intermediates in PE spectra. In the present case the optimum mixing distance was found to be $30\, mm$. The method to produce OD was the same as for OH, with D_2 being used instead of H_2.

$O_2(a^1\Delta_g)$ was produced by flowing molecular oxygen through a microwave discharge under similar condition as for H atoms. It is known that $O_2(a^1\Delta_g)$ is the dominant excited molecular product from such a discharge, but also atomic oxygen in the ^3P ground state and a negligible amount of $O_2(b^1\Sigma_g^+)$ are present [7]. From the published HeI photoionization cross sections of the $a^1\Delta_g$ and $X^3\Sigma_g^-$ states of O_2 [8], and with the relative intensities observed in HeI PE spectra recorded for a typical discharge, the yield of $O_2(a^1\Delta_g)$ is

estimated to be approximately 15%.

A modification to the present inlet system is being considered. The outer glass tube shown in figure 9.3 will be elongated through the boxes and then joined to a funnel shaped adaptor that goes straight to pump 3. Three small holes will be in the tube to let the radiation through and the electrons out. The longer tube with the funnel will have a lower conductance than in the original design, but pump 3 has a higher pumping speed than pump 1, and the gas will not have to go through two 90^o bends from the mixing point to the pumps as it does now. A higher gas throughput should be achievable, and this should result in a higher sample density. Before this can be done pump 3 must be treated for handling chemically aggressive species.

9.7 The rotation mechanism

Angle resolved PE spectra are conventionally recorded by rotating one analyser inside the vacuum chamber, in the plane perpendicular to the linearly polarized photon beam. However, the need for differential pumping for the different parts of the spectrometer, and the size of the analyser, preclude this possibility, so instead the entire vacuum system, including the pumps, is rotated.

Figure 9.4 shows the two cases in which the lens axis, that defines the direction of collection of electrons, is positioned at the two extremes: 0^o and 75^o with respect to the horizontal direction, the direction of polarization of the photon beam.

A fixed vertical screw-drive is mounted in bearings located at the top and bottom of the fitting. When rotated, this moves the threaded block, and the attached arm, up or down. A computer controlled electrical motor is connected to the screw-drive, placed on the base frame.

The angles of rotation were initially measured with a device composed of a spirit level fitted to a goniometer, that was placed on a part of the frame parallel to the axis of the lens. Marks on the vertical bar in figure 9.4 were made corresponding to angles between $\theta = 0^o$ and 75^o, in steps of 15^o.

The spectrometer was constructed with bearings and supports positioned at the left and right ends of the spectrometer axis shown in figure 9.1. A differentially pumped rotary feed-through is used to connect the fixed light guide mounting to the spectrometer so that vacuum integrity is preserved during the rotation procedure. The pumps 1, 2, and 3 are mounted as shown in figure 9.1, so that the torque occurring for rotation is minimised; the use of diffusion pumps would not permit such an arrangement.

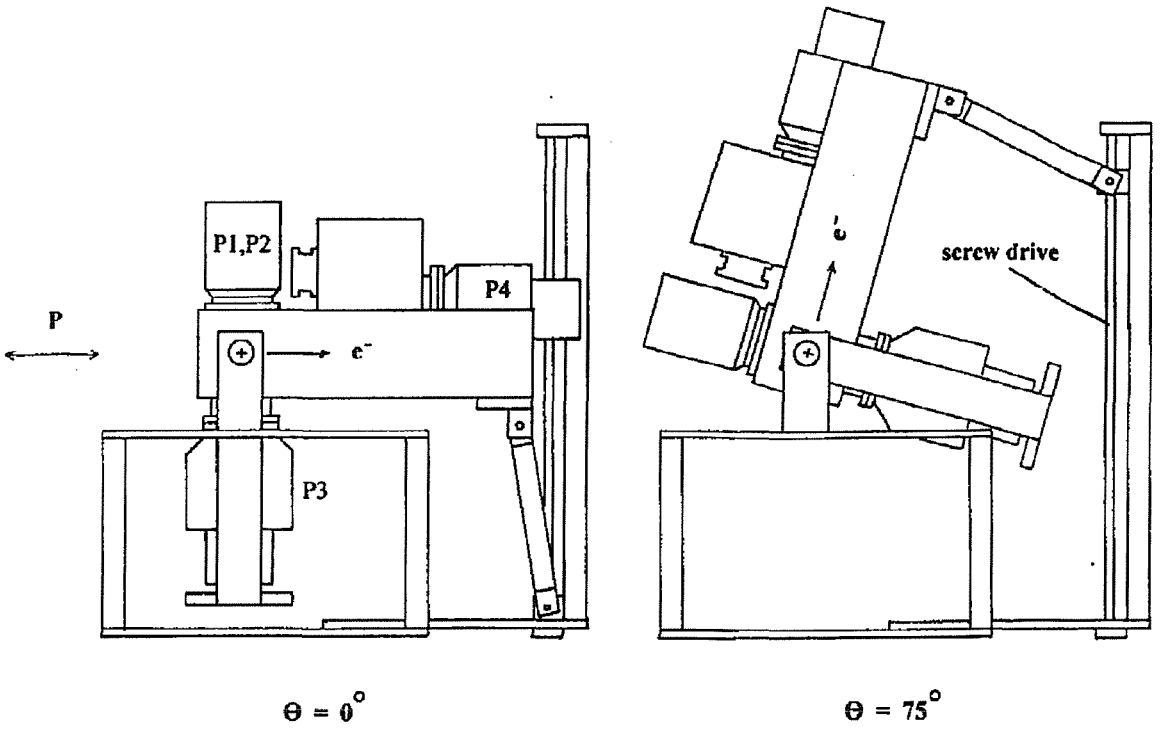

Figure 9.4: A view in the photon beam direction showing the mechanism for rotating the spectrometer.

9.8 Radiation sources and alignment

All the spectra presented in this thesis were recorded either on beam-line 3.2 or 3.3 at the Daresbury SRS. The angle resolved spectra of $O_2(a^1\Delta_g)$ have all been obtained on beam-line 3.3, where the degree of linear polarization is $S_1 \simeq 0.9$ at the wavelength used. Attempts were also made to record them on beam-line 3.2, but a lower degree of linear polarization, $S_1 = 0.3 - 0.4$, did not allow angular distributions to be measured. Beam-lines 3.2 and 3.3 are described in section 2.4.2 and 2.4.3 respectively.

The radiation bandwidth was normally set to 1 $\mathring{A}$, which at the photon energy of 21.22 eV corresponds to 36 meV.

During each beam-time, CIS spectra are recorded with the intent of measuring excitation energies to autoionizing states. It is therefore important for the wavelength scale of the monochromator to be accurately calibrated. The wavelength scale is corrected by comparing the measured energies of the resonances in the CIS spectra of $O^+(2p^3\,{}^4S) \leftarrow O(2p^4\,{}^3P)$, $Xe^+(5p^5\,{}^2P_{3/2}) \leftarrow Xe(5p^6\,{}^1S_0)$ and $Ar^+(3p^5\,{}^2P_{3/2}) \leftarrow Ar(3p^6\,{}^1S_0)$ in the photon energy regions $13.5 - 18.5\,eV$, $20.0 - 23.5\,eV$ and $26.0 - 30.0\,eV$ with their nominal values from references [9] and [10]. The changes in the photon energy scale after calibration are smaller than 50 meV.

Synchrotron radiation is channeled into the ionization chamber by a 2 mm bore 300 mm

long glass tube, labelled G in figure 9.1.

At the start of each beam-time the spectrometer is connected to the beam-line and it must be aligned. The base frame has wheels for mobility, but during experiments it stands on feet that can be raised or lowered for vertical adjustment. A plate mounted upon the base frame can slide in the direction of the photon beam for horizontal adjustment so that the spectrometer can be moved into position before connection to the beam-line. A second frame is on this plate, and it can be translated horizontally, in the direction perpendicular to the photon beam.

A He discharge lamp (Fisons/VG 232) is fitted to the spectrometer in Southampton, to record test PE spectra when beam-time is not available. The radiation emitted is mainly HeIα ($He(1s2p\,^1P) \rightarrow He(1s^2\,^1S) + h\nu(21.218\,eV)$, $> 95\%$), although a minor contribution from HeIβ radiation ($He(1s3p\,^1P) \rightarrow He(1s^2\,^1S) + h\nu(23.087\,eV)$, $< 5\%$) is present. The unwanted HeIβ component can be useful as "shadow" bands in PE spectra can help calibration of the electron kinetic energy scale.

The radiation from the He lamp is unpolarized and, as a result, no angle resolved experiments can be performed in Southampton. However, it allows the change in collection efficiency of the spectrometer when the analyser is rotated to be tested.

The plate at the rear of the spectrometer, labelled H in figure 9.1, is a photodiode used to measure the relative photon flux. The current that passes through it is measured by a Keithley nanoammeter, whose output goes to a CAMAC counter for automatic reading and then to a computer.

9.8.1 Measurements of polarization

In order to extract the asymmetry parameter β (see section 10.2.1 from the measured angle resolved spectra, the degree of linear polarization S_1 of the ionizing radiation must be known. The value of S_1 on beam-line 3.3 at the Daresbury SRS was not previously known at the wavelengths of interest in the present work, and was measured during the course of this work.

Measurements of S_1 are normally executed by measuring the angular distribution of photolines of rare gases with well known values of asymmetry parameters β. Helium is normally chosen for this purpose, the value of β for the main He photoline is always 2 at non resonant energies. Unfortunately, the ionization energy of He is $24.59\,eV$, higher than the photon energies used in this work: $13.8 - 15.2$, $18 - 19.2$ and $21.22\,eV$, and therefore He could not be used.

The value of S_1 was extracted from the measured angular distribution of the $Xe^+(5p^5\ ^2P_{3/2}) \leftarrow Xe(5p^6\ ^1S_0)$ and $Ar^+(3p^6\ ^2P_{3/2}) \leftarrow Ar(3p^6\ ^1S_0)$ photolines, whose ionization energies are 12.13 and 15.76 eV respectively, and whose β parameters are listed in reference [11]. The possibility of using two different gases in the photon energy region above 18.0 eV allowed consistency cross checks to be made.

The direction of polarization of the radiation from the beam-line is expected to be horizontal, parallel to the plane where the spectrometer stands. Nevertheless, checks were made for small angular tilt between the direction of polarization and the horizontal direction, by measuring angular distribution of rare gases at photon energies where they have well known values of asymmetry parameters. With the present accuracy ($\pm 5^o$) the direction of polarization was found to be horizontal.

9.8.2 Change in efficiency of the analyser

For the measurements of angular distribution it is also important to make sure that the efficiency of the analyser does not change when the spectrometer is rotated. The biggest contribution to the change in the efficiency of the analyser is likely to come from small misalignments between the axis of rotation, the direction of the photon beam, and the apertures in the boxes around the ionization region. This contribution is minimised with the following procedure. For each angular position of the spectrometer, the direction of the capillary that channels the synchrotron radiation from the exit slit of the monochromator into the spectrometer and is pivoted at the exit slit, is adjusted with a set of X-Y micromanipulators in such a way that the current reading from the photodiode at the back of the spectrometer is maximum. Checks for change in efficiency of the analyser were executed by measuring the angular distribution of gases with known asymmetry parameters: Ar, He, Xe and O_2. Within a level of accuracy of $\pm 5\%$ the efficiency of the analyser did not change when moving from $\theta = 0^o$ to $\theta = 75^o$.

9.9 Conclusions

The spectrometer that was used for the study of the reactive intermediates $O_2(a^1\Delta_g)$, OH and OD with PES with synchrotron radiation, described in chapters 10 and 11 respectively, has been described in this chapter. Particular emphasis is placed on the need for differential pumping system. This is a unique property of this spectrometer, and is essential for studying reactive intermediates with synchrotron radiation.

Bibliography

[1] JM Dyke, SD Gamblin, A Morris, TG Wright, AE Wrigth and JB West, *Journal of Electron Spectroscopy and Related Phenomena*, **97** 5-14 (1998).
A Morris and JM Dyke, *Vacuum*, **5** 339-345 (1999).

[2] Electron Spectroscopy: Theory, Techniques and Applications.
JM Dyke, N Jonathan and A Morris, edited by CR Brundle and AD Baker, Academic Press, London (1977).

[3] A Poulin and D Roy, *Journal of Physics E: Scientific Instruments*, **11** 35-42 (1978).

[4] Electrostatic Lenses.
E Harting and FH Read, Elsevier, Amsterdam (1976).

[5] Photoelectron Spectroscopy of Short-Lived Molecules.
MCR Cockett, JM Dyke and H Zamanpour, in *Vacuum Ultraviolet Photionization and Photodissociation of Molecules and Clusters*, edited by CY Ng, World Scientific, London (1991).

[6] PP Benard and MAA Clyne, *Journal of The Chemical Society, Faraday Transaction II*, **73** 394-397 (1977).

[7] N Jonathan, M Okuda, KJ Ross and DJ Smith, *Journal of The Chemical Society, Faraday Transaction II*, **70** 1810-1816 (1974).

[8] WJ van der Meer, P van der Meulen, M Volmer and CA de Lange, *Chemical Physics*, **126** 385-391 (1988).

[9] Atomic Energy Levels.
C Moore, circular 467, United States National Bureau of Standards (1949).

[10] RP Madden, DL Ederer and K Codling, *Physical Review Letters*, **117** 136-138 (1969).

[11] DMP Holland, AC Parr, DL Ederer, JL Dehmer and JB West, *Nuclear Instruments and Methods in Physics Research*, **195** 331-337 (1982).

Chapter 10

Angle resolved photoelectron spectroscopy of $O_2(a^1\Delta_g)$ with synchrotron radiation

10.1 Introduction

Due to its importance in the photochemistry and photoionization in the upper atmosphere, photoionization of O_2 with VUV radiation has been extensively studied in the past. Most of the spectroscopic investigations on O_2 focused on its ground state, $X^3\Sigma_g^-$; less is known about photoionization of O_2 from its metastable state $a^1\Delta_g$.

This chapter presents work on angle resolved PES of $O_2(a^1\Delta_g)$. The work presented here is the continuation of an investigation with PES using photoelectron spectroscopy with synchrotron radiation on $O_2(a^1\Delta_g)$ [1], that was carried on by the author of this thesis together with the Southampton PES group.

The chapter is organized as follows. Sections 10.2 reviews briefly previous spectroscopic investigations on $O_2(X^3\Sigma_g^-)$ that are relevant to the present work. Section 10.3 introduces the importance of $O_2(a^1\Delta_g)$ as an atmospheric constituent. Section 10.4 reviews briefly previous research on electron spectroscopy of $O_2(a^1\Delta_g)$ that is considered relevant for the present work. The results of the present work on angle resolved PES of $O_2(a^1\Delta_g)$, together with their interpretation, are presented and discussed in section 10.5.

ionization	state	AIE from $X^3\Sigma_g^-$	AIE from $a^1\Delta_g$
$1\pi_g$	$X^2\Pi_g$	12.08	11.10
$1\pi_u$	$a^4\Pi_u$	16.10	-
$1\pi_u$	$A^2\Pi_u$	17.04	16.06
$3\sigma_g$	$b^4\Sigma_g^-$	18.17	-
$1\pi_u$	$C^2\Phi_u$	-	17.51
$3\sigma_g$	$D^2\Delta_g$	-	18.81
$3\sigma_g$	$B^2\Sigma_g^-$	20.30	-

Table 10.1: Adiabatic ionization energies (AIEs) and symmetries of the states of O_2^+ accessible from dipole photoionization of $O_2(X^3\Sigma_g^-)$ and $O_2(a^1\Delta_g)$ with a photon energy of $21.22eV$. Energies are in eV.

10.2 Previous electron spectroscopy work on $O_2(X^3\Sigma_g^-)$

The ground state of molecular oxygen has the following electronic configuration:

$$1\sigma_g^2\,1\sigma_u^2\,2\sigma_g^2\,2\sigma_u^2\,3\sigma_g^2\,1\pi_u^4\,1\pi_g^2, \tag{10.1}$$

and a $^3\Sigma_g^-$ symmetry. Photoionization of $O_2(X^3\Sigma_g^-)$ with HeI radiation ($h\nu = 21.22\,eV$) can give rise to doublet and quartet states, and is very well characterized since the early PES work of Turner and May in 1966 [2], Turner in 1968 [3], and Edqvist in 1970 [4]. The ground state of O_2^+, $X^2\Pi_g$, arises from removal of an electron from the antibonding $1\pi_g$ orbital, with an adiabatic ionization energy (AIE) of $12.08\,eV$. Ionization from the $1\pi_u$ orbital gives rise to the $a^4\Pi_u$ and $A^2\Pi_u$ states, with AIEs of 16.10 and $17.04\,eV$ respectively. HeI photoelectron bands of these states show long overlapping vibrational progressions, characteristic of ionization from bonding orbitals. Photoionization from the bonding $3\sigma_g$ orbital gives rise to the $b^4\Sigma_g^-$ and $B^2\Sigma_g^-$ states at AIEs of $18.17\,eV$ and $20.30\,eV$ respectively.

Table 10.1 summarizes the symmetries and AIEs of the states of O_2^+ that can be accessed by photoionization of O_2 with radiation of $21.22\,eV$ of energy.

In a more recent high resolution HeI PES work on $O_2(X^3\Sigma_g^-)$, Baltzer *et al.* [5] discovered a sixth band of unknown symmetry at an AIE of $20.35\,eV$, interspaced between the vibrational progression of the $B^2\Sigma_g^-$ band. This band is much weaker than the other five bands and it probably corresponds to a formally forbidden ionization that becomes allowed by configuration interaction.

Early studies on Rydberg series in O_2 were made with photoabsorption by using con-

tinuous VUV radiation produced by rare gases discharge lamps [6], or by observing the dispersed emission spectrum of discharged O_2. These studies were started in 1935 by Price and Collins [7], who observed the $(a^4\Pi_u,\, nd\sigma_g)\,^3\Pi_u$ and $(a^4\Pi_u,\, nd\delta_g)\,^3\Pi_u$ series. The work of Lindholm in 1968 [8] summarised known Rydberg series converging to the $X^2\Pi_g$, $a^4\Pi_u$, $A^2\Pi_u$, $b^4\Sigma_g^-$, $D^2\Delta_g$, $B^2\Sigma_g^-$ and $c^4\Sigma_u^-$ states of O_2^+. Yoshino and Tanaka in 1968 [9] added information on the Rydberg bands of O_2 converging to the $b^4\Sigma_g^-$ and $B^2\Sigma_g^-$ states of O_2^+. The work of Dehmer and Chupka of 1975 [10] reported Rydberg series converging to the $a^4\Pi_u$, $b^4\Sigma_g^-$, $B^2\Sigma_g^-$ and $c^4\Sigma_u^-$ states studied by high resolution photoionization mass spectrometry. Nishitani *et al.* in 1984 [11] studied Rydberg series of O_2 converging to the $a^4\Pi_u$, $b^4\Sigma_g^-$ and $B^2\Sigma_g^-$ ionic states.

In more recent years, when the use of synchrotron radiation became more common, the differential nature of PES was exploited by measuring CIS spectra for selected vibronic components of the ion. This allowed the study of the different autoionization channels leading to different vibrational components of the ion. Cafolla *et al.* in 1989 [12] measured CIS spectra for the $X^2\Pi_g$, $b^4\Sigma_g^-$ and $B\,^2\Sigma_g^-$ states of O_2^+ in the photon energy region $18.5 - 25.0\,eV$, where Rydberg states converging to the $B\,^2\Sigma_g^-$ and $c^4\Sigma_u^-$ ionic states exist, and also found as a shape resonance centered at the energy of $21.5\,eV$. A number of studies with threshold photoelectron spectroscopy (TPES) were also reported; they allowed the determination of ionization energies with higher accuracy than conventional PES [13], and in some cases the resolution allowed rotational structure to be resolved [14].

The usefulness of Franck-Condon factors (FCF) calculations to both assign Rydberg resonances and test the validity of the Born-Oppenheimer (BO) approximation for photoionization of O_2 was proved by Eland in 1980 [15] and by Čubrić *et al.* in 1996 [16], who measured the first PE band of O_2 in the $14.75 - 15.05\,eV$ resonant region, where autoionizing Rydberg states of a $^3\Pi_u$ series converging to the second ionic limit are present.

10.2.1 Angle resolved PES of O_2

The use of synchrotron radiation, which is naturally linearly polarized, allows angle resolved PE measurements to be recorded.

It has been known since 1948 [17] that the angular distribution of photoelectrons, in the plane perpendicular to the photon beam, for non polarized and randomly oriented atoms and molecules follows the following expression:

$$\frac{d\sigma}{d\theta} = \frac{\sigma}{4\pi}\left\{1 + \frac{\beta}{4}\left[3S_1\cos(2\theta) + 1\right]\right\}. \tag{10.2}$$

In equation (10.2), θ is the angle between the direction of linear polarization of the radiation and the direction of emission of the photoelectron, σ is the integrated cross section of the process under investigation, and β is called asymmetry parameter. Equation (10.2) is the same as equation (3.9) in chapter 3.

According to Cooper and Zare [18], for dipole photoemission from the nl subshell of a closed shell atom, the β parameter has the following expression:

$$\beta = \frac{l(l-1)D_{l-1}^2 + (l+1)(l+2)D_{l+1}^2 - 6l(l+1)D_{l+1}D_{l-1}\cos(\delta_{l+1} - \delta_{l-1})}{3(2l+1)\left[lD_{l-1}^2 + (l+1)D_{l+1}^2\right]}, \qquad (10.3)$$

where $D_{l\pm1}$ are the amplitudes of the reduced transition matrix elements between the radial part of the initial bound orbital, $R_{np}(r)$, and of the degenerate channels of the photoelectron, $R_{\epsilon l\pm1}(r)$, with angular momenta $l \pm 1$:

$$D_{l\pm1} \equiv \int_o^\infty R_{nl}(r) r R_{\epsilon l\pm1}(r) r^2 dr, \qquad (10.4)$$

and $\delta_{l\pm1}$ are their phases. In photoionization of molecules it is not possible to write an equation corresponding to (10.3) in terms of a finite set of molecular orbitals. An expansion in atomic orbitals would also contain infinite terms, such an expansion is given in reference [19] and is not reported here.

It is clear from equation (10.3) that the asymmetry parameter β depends on the relative strengths and phase difference of the degenerate channels of the photoelectron with different angular momenta. Photoelectron channels with different angular momenta gain strength differently when the photoionization process proceeds via a resonance: this makes the β parameter resonance dependent. Higher values of the angular momentum of the photoelectron become stronger at resonant energies, where the angular momentum of the electron trapped in a Rydberg orbital couples with the angular momentum of the ionic core during the lifetime of the autoionizing state, so that when the electron is emitted, channels with higher value of l are increased in strength.

It often happens that the β parameter is vibrationally dependent. The dependence of β on the ionic vibrational quantum number, v^+, can be interpreted as a manifestation of the breakdown of the BO approximation. Another reason for β to be dependent on v^+ can be the presence of *shape* resonances. A *shape* resonance appears when a sub-valence shell electron is excited to a *quasi* bound orbital. A centrifugal barrier temporarily traps the excited electron in certain directions, before the electron eventually tunnels and escapes [20]. Both the breakdown of the BO approximation and the presence of *shape* resonances

are normally very difficult to observe with most of the other spectroscopic techniques, this underlines the importance of angle resolved PES in molecules.

Angle resolved PES measurements on $O_2(X^3\Sigma_g^-)$ have been reported by numerous authors. McCoy *et al.* in 1978 [21] measured the asymmetry parameter for the $O_2^+(X^2\Pi_g\, v^+) \leftarrow O_2(X^3\Sigma_g^-\, v''=0)$ band in the photon energy range $20-45\,eV$. Such measurements extended the work of Hancock and Samson in 1976 [22], who measured the β parameter for the same band at the fixed wavelengths of the HeI, HeII and NeI discharge lamps.

The more recent work of Codling *et al.* in 1981 [23] studied vibrational branching ratios and asymmetry parameters for the $O_2^+(X^2\Pi_g\, v^+) \leftarrow O_2(X^3\Sigma_g^-\, v''=0)$ band in the photon energy region $20.65-21.60\,eV$, where states of Rydberg series converging to the $c^4\Sigma_g^-$ state of O_2^+ can be accessed. A strong v^+ dependence of β was found, as well as strong variations of β at resonant energies.

Parr *et al.* in 1998 [24] investigated the behaviour of β for the $O_2^+(X^2\Pi\, v^+) \leftarrow O_2(X^3\Sigma^-\, v''=0)$ band in the photon energy range $16.75-18.50\,eV$, where Rydberg states belonging to series converging to the $B^2\Sigma_g^-$ ionic limit are present, at the Daresbury SRS.

At the present time the only work on angle resolved PES from O_2 in the $a^1\Delta_g$ state is that obtained during the course of the work of reference [25], that is the subject of this chapter.

10.3 Atmospheric importance of $O_2(a^1\Delta_g)$

Oxygen in its first excited state is an atmospherically important species. $O_2(a^1\Delta_g)$ is produced together with $O(^1D)$ from photodissociation of ozone in the troposphere. Photoionization of $O_2(a^1\Delta_g)$ has been suggested as an important source of ions in the D region of the atmosphere to explain both the relatively high O_2^+ partial pressure and the total ion densities at these altitudes ($< 70\,km$). This would provide a source of O_2^+ ions which can be involved with NO, NO^+ and H_2O, in a sequence of reactions leading to the formation of protonated water clusters [26].

10.4 Previous work on the electron spectroscopy of $O_2(a^1\Delta_g)$

The first excited state that arises from the lowest energy electronic configuration (10.1) of O_2 is $a^1\Delta_g$. This state lies $0.98\,eV$ above the $X^3\Sigma_g^-$ ground state and is very well

characterized [3].

There are fewer studies of $O_2(a^1\Delta_g)$ than of $O_2(X^3\Sigma_g^-)$. One reason is that $O_2(a^1\Delta_g)$ cannot be obtained in laboratory in a pure form. Although $O_2(a^1\Delta_g)$ can be produced with simple experimental methods, it can be prepared only in small concentration, and signals from spectroscopic investigations tend to be overwhelmed by the stronger signals from $O_2(X^3\Sigma_g^-)$.

Because its symmetry is different from that of the ground state, one-photon selection rules allow different neutral and ionic states to be accessed from $O_2(a^1\Delta_g)$ than from $O_2(X^3\Sigma_g^-)$. Only states with $^1\Pi_u$, $^1\Delta_u$ and $^1\Phi_u$ symmetry can be accessed by photoabsorption from $O_2(a^1\Delta_g)$. In photoelectron spectra of $O_2(a^1\Delta_g)$ only ionic states with a doublet spin character can be reached, in contrast to photoelectron spectra of $O_2(X^3\Sigma_g^-)$ where both doublet and quartet states can be observed.

The HeI photoelectron spectrum of $O_2(a^1\Delta_g)$ has been known since the work of Jonathan *et al.* in 1974 [28] and of van Lonkhuyzen and de Lange in 1982 [29]. Photoionization from a $1\pi_g$ orbital gives rise to the $X^2\Pi_g$ ionic state with an AIE of $11.10\,eV$, while loss of an electron from a $1\pi_u$ orbital gives the $A^2\Pi_u$ and $C^2\Phi_u$ ionic states at AIEs of 16.07 and $17.51\,eV$ respectively, and ionization from the $3\sigma_g$ shell produces the $D^2\Delta_g$ ionic state at an AIE of $18.81\,eV$.

Table 10.1 lists the symmetries and adiabatic ionization energies of the states of O_2^+ that can be accessed by photoionization of $O_2(a^1\Delta_g)$ with radiation of $21.22\,eV$ of energy.

Rydberg states of $O_2(a^1\Delta_g)$ which are members of series converging to the first ionic limit have been studied by several authors with laser multiphoton ionization spectroscopy [30].

Huffman *et al.* in 1971 [31] measured the photoionization cross section of $O_2(a^1\Delta_g)$ in the photon energy range $11.09 - 12.07\,eV$, between the ionization threshold of the a and the X neutral states.

Collins *et al.* in 1973 [32] measured the absorption spectrum of $O_2(a^1\Delta_g)$ in the photon energy region $7.5 - 11.1\,eV$ and observed resonances corresponding to states which are parts of Rydberg series converging to the $X^2\Pi_g$ state of O_2^+.

The most important investigations on photoabsorption of $O_2(a^1\Delta_g)$ for the work of this thesis are the work of Katayama *et al.* in 1975 [33] and in 1977 [34] in the photon energy regions $7.6 - 9.6\,eV$ and $13.7 - 14.8\,eV$. A vibrationally resolved band at an excitation energy of approximately $14.0\,eV$ was assigned to a $O_2^*((C^2\Phi_u\,3s\sigma_g)p^1\Phi_u) \leftarrow O_2(a^1\Delta_g)$ transition. Some of the vibrational components were rotationally resolved and an unusual alternating pattern of narrow and broad lines was observed in the vibrational members of

this band, which was attributed to a combination of autoionization and predissociation in the excited state.

The only previous investigation of $O_2(a^1\Delta_g)$ with photoelectron spectroscopy using synchrotron radiation is the work of Barr *et al.* in 1998 [1], that was caried out as a part of this project by the Southampton PES group. In the CIS spectra for the $v^+ = 0-3$ components of the $O_2^+(X^2\Pi_g\, v^+) \leftarrow O_2(a^1\Delta_g\, v'' = 0)$ band in the $14.0 - 15.0\, eV$ photon energy region, resonances were found at energies corresponding to the $O_2^*(p^1\Phi_u\, v') \leftarrow O_2(a^1\Delta_g\, v'' = 0)$ transitions observed in photoabsorption by Katayama *et al.* [33], [34]. The vibrational branching ratios in this region were very different from those expected from FCF calculations. This poor agreement was interpreted as a consequence of competition between autoionization and predissociation in the $p^1\Phi_u$ state. The conclusion in the work of Barr *et al.* [1] was that predissociation of the $v' = 3$ and $v' = 5$ components in $O_2^*(p^1\Phi_u)$ is slow relatively to autoionization, while for the other components it is much faster as very little or no signals were seen in the CIS spectra for these levels.

In the PES work of Barr *et al.* [1], resonances were also found in the photon energy range $18.0 - 19.0\, eV$ in the CIS spectra for the $v^+ = 0 - 3$ components of the $O_2^+(X^2\Pi_g\, v^+) \leftarrow O_2(a^1\Delta_g\, v'' = 0)$ band. Two overlapping vibrational progressions were observed, with the first member of the lower energy progression at an energy of $18.46\, eV$. The only well characterized state of O_2^+ accessible from $O_2(a^1\Delta_g)$ above $18.0\, eV$ is the $D^2\Delta_g$ state, with an AIE of $18.81\, eV$, and in the previous work [1] the resonant Rydberg state associated with the $18.46\, eV$ series was tentatively assigned as $(D^2\Delta_g\, 7p\pi)$.

10.5 Results and discussion

Angle resolved photoelectron spectra of discharged O_2 were recorded at the non-resonant photon energy of $21.22\, eV$, and at the photon energies of 14.11 and $14.37\, eV$, that correspond to the $O_2^*(p^1\Phi_u\, v' = 3,\, 5) \leftarrow O_2(a^1\Delta_g\, v'' = 0)$ resonances.

The asymmetry parameters for the $v^+ = 0 - 3$ components of the $O_2^+(X^2\Pi_g\, v^+) \leftarrow O_2(a^1\Delta_g\, v'' = 0)$ band were also measured in the photon energy ranges $13.8 - 15.2\, eV$ and $18.0 - 19.2\, eV$, where from the work of reference [1] autoionizing resonances are known to exist.

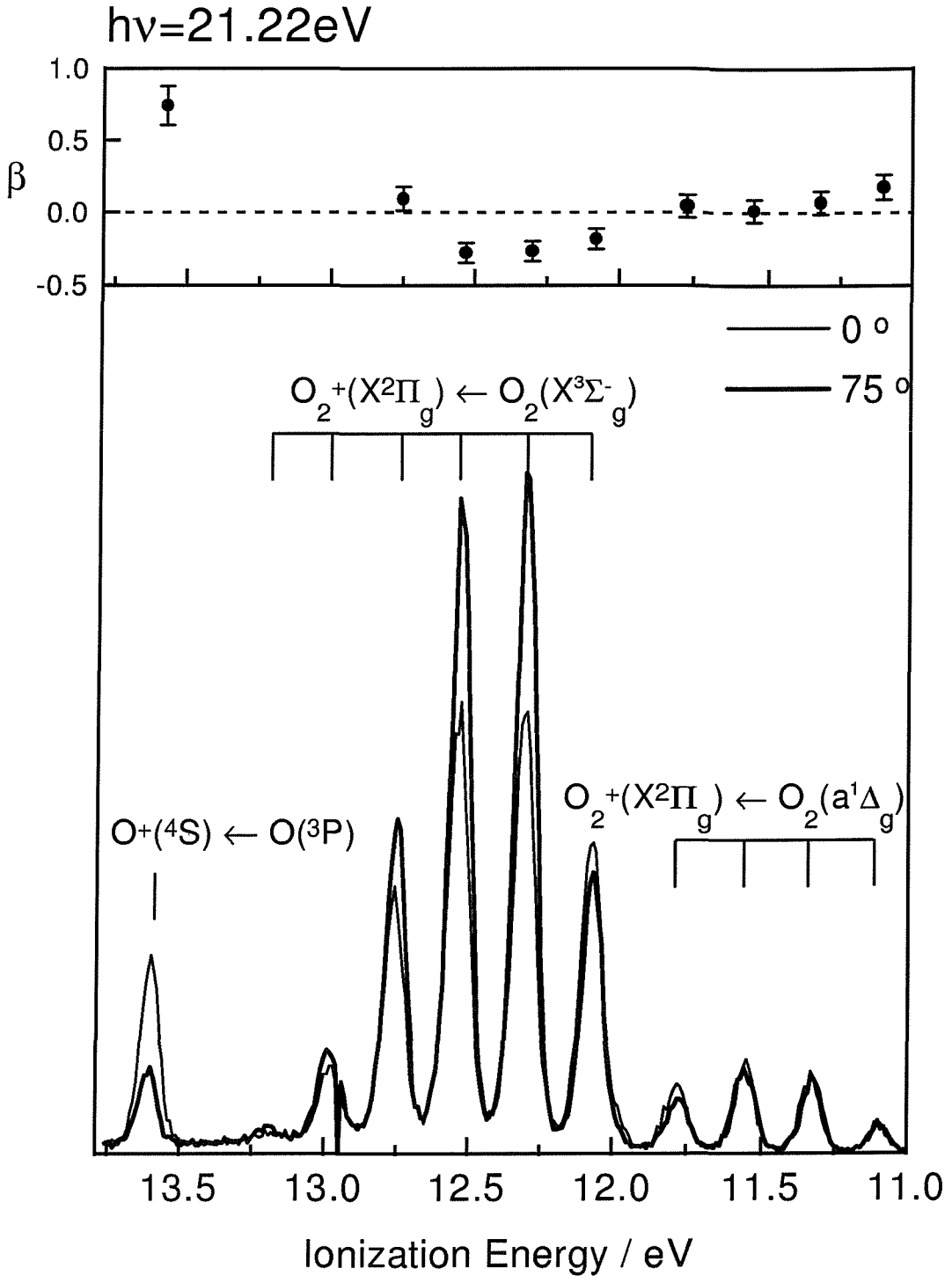

Figure 10.1: Upper: β parameters for the photoelectron bands of discharged O_2 shown below. Lower: photoelectron spectra of discharged O_2 at the photon energy of $21.22\,eV$ at two angles of observation: $\theta = 0^o$ and 75^o.

10.5.1 Photoelectron spectra at the photon energy of $21.22\,eV$

Photoelectron spectra of discharged O_2 recorded at the photon energy of $21.22\,eV$ are shown in the lower part of figure 10.1, at the two angles of observation: $\theta = 0^o$ and $\theta = 75^o$. The two spectra are plotted on the same vertical scale by correcting them for the relative efficiencies of the analyser at the two angles, as described in chapter 9, and by dividing the electron counts by the relative photon flux; this is the case also for all the other spectra in this chapter. In this way a direct comparison of the intensities at the two angles of emission is possible.

The four lowest v^+ components of the $O_2^+(X^2\Pi_g\, v^+) \leftarrow O_2(a^1\Delta_g\, v'' = 0)$ band are observable in figure 10.1, with the $v^+ = 0$ component at an ionization energy of $11.10\,eV$. The $O_2^+(X^2\Pi_g\, v^+) \leftarrow O_2(X^3\Sigma_g^-\, v'' = 0)$ band shows six v^+ components starting at an AIE of $12.08\,eV$.

Each of the v^+ components of the $O_2^+(X^2\Pi_g\, v^+) \leftarrow O_2(a^1\Delta_g\, v'' = 0)$ band in figure 10.1 have very similar intensities at the two angles of observation. The results are quite different for the $O_2^+(X^2\Pi_g\, v^+) \leftarrow O_2(X^3\Sigma_g^-\, v'' = 0)$ band, as when moving from $\theta = 0^o$ to $\theta = 75^o$ a different vibrational pattern is observed. In both these spectra the $O^+(^4S) \leftarrow O(^3P)$ band at an ionization energy of $13.61\,eV$ is also present, and this also shows a big change in intensity when changing the angle of observation.

The asymmetry parameters extracted from the photoelectron spectra in the lower part of figure 10.1 are plotted in the upper part of the figure, and are also listed in table 10.2. Also in this work, as in the work on metal vapours discussed in chapter 8, is very difficult to estimate the uncertainties in these results; they are estimated of the order of ± 0.10. These errors come mainly from the reproducibility of the efficiency of the analyser at the different angles of observation, that is described in chapter 9, as well as from the measurements of the degree of linear polarization S_1.

The β parameters for the $v^+ = 0-3$ components of the $O_2^+(X^2\Pi_g\, v^+) \leftarrow O_2(a^1\Delta_g\, v'' = 0)$ band are very similar to each other, and are all very close to 0. The fact that the β parameters for all the v^+ components are very similar to each other is in agreement with what is expected from the BO approximation, that should work in non-threshold ionization and away from resonances. These values of β were measured in this work for the first time, and no comparison with previous results is possible.

An indication of the reliability of the present result comes from a comparison of the β parameters for the $O_2^+(X^2\Pi_g\, v^+) \leftarrow O_2(X^3\Sigma_g^-\, v'' = 0)$ band with previously published values: the values obtained here are in reasonable agreement with those of Codling *et*

Band	v^+	This work	Previous work
$O_2^+(X^2\Pi_g\, v^+) \leftarrow O_2(a^1\Delta_g\, v''=0)$	0	0.05	
	1	0.01	-
	2	0.07	-
	3	0.18	-
$O_2^+(X^2\Pi_g\, v^+) \leftarrow O_2(X^3\Sigma_g^-\, v''=0)$	0	0.09	-0.18(05) [23]
	1	-0.28	-0.28(05) [23]
	2	-0.27	-0.30(05) [23]
	3	-0.18	-
$O^+(^4S) \leftarrow O(^3P)$		0.74	0.60(05) [23]

Table 10.2: Asymmetry parameters of bands of $O_2(a^1\Delta_g)$, $O_2(X^3\Sigma_g^-)$ and $O(^3P)$ at the non resonant photon energy of $21.22\,eV$. Errors in the values of β from this work are estimated to be of the order of ± 0.10.

al. [23], which are also shown in table 10.2. It is interesting to observe in figure 10.1 the constant intensities at different angles for the $v^+ = 0$, 3, 4 and 5 components of the $O_2^+(X^2\Pi_g\, v^+) \leftarrow O_2(X^3\Sigma_g^-\, v''=0)$ band in contrast to the marked change in intensities of the $v^+ = 1$ and 2 components of the same band when changing angles of observation. Two tentative interpretations why the β parameters show vibrational dependence presented are given in section 10.5.2.

The value of β for the $O^+(^4S) \leftarrow O(^3P)$ process measured here is 0.74 (10), and is close to that of van der Meulen *et al.* [35], who obtained 0.60(05).

10.5.2 Photoelectron spectra at the resonant photon energies of 14.11 and 14.37 eV

Photoelectron spectra of discharged oxygen at the photon energies of 14.11 and 14.37 eV, that correspond to the $O_2^*(p^1\Phi_u\, v' = 3,\, 5) \leftarrow O_2(a^1\Delta_g\, v'=0)$ resonances, are displayed in the lower parts of figures 10.2 and 10.3 respectively. At these wavelengths only the $O_2^+(X^2\Pi_g\, v^+) \leftarrow O_2(a^1\Delta_g\, v''=0)$ band is resonantly enhanced; the $O_2^+(X^2\Pi_g\, v^+) \leftarrow O_2(X^3\Sigma_g^-\, v''=0)$ band is not enhanced because the $O_2^*(p^1\Phi\, v' = 3,\, 5) \leftarrow O_2(X^3\Sigma_g^-\, v''=0)$ transitions: 1) would appear at different energies and 2) are formally spin and Λ forbidden.

The values of β at these photon energies are plotted in the upper parts of figures 10.2 and 10.3 respectively, and are also listed in table 10.3. Previous work on angular distribution measurements for the $O_2^+(X^2\Pi_g\, v^+) \leftarrow O_2(X^3\Sigma_g^-\, v''=0)$ band have been reported in the

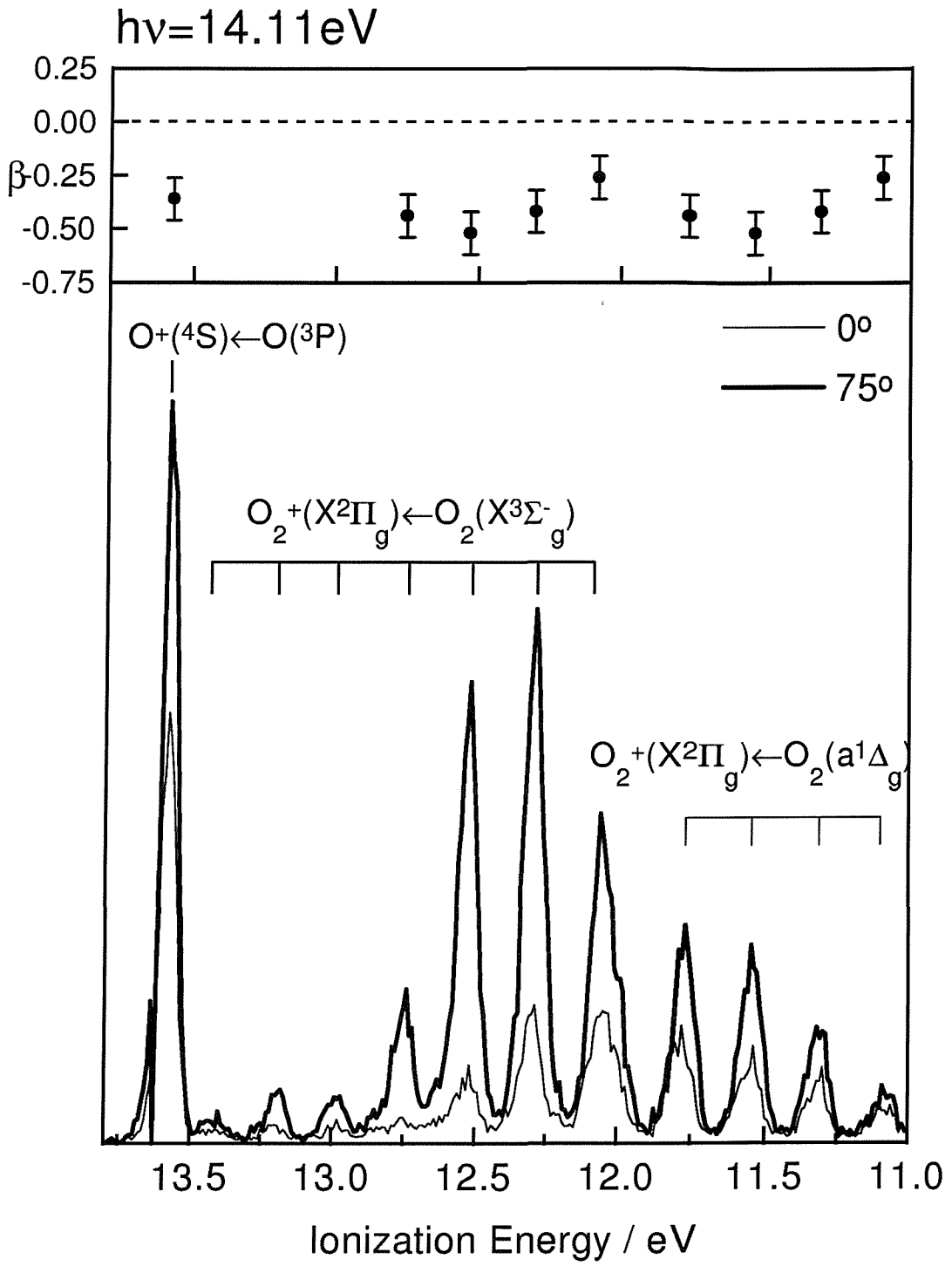

Figure 10.2: Upper: β parameters for the photoelectron bands of discharged O_2 shown below. Lower: photoelectron spectra of discharged O_2 at the photon energy of 14.11 eV, resonant with the $O_2^*(p^1\Phi_u\, v' = 3) \leftarrow O_2(a^1\Delta_g\, v'' = 0)$ excitation, at two angles of observation: $\theta = 0^o$ and 75^o.

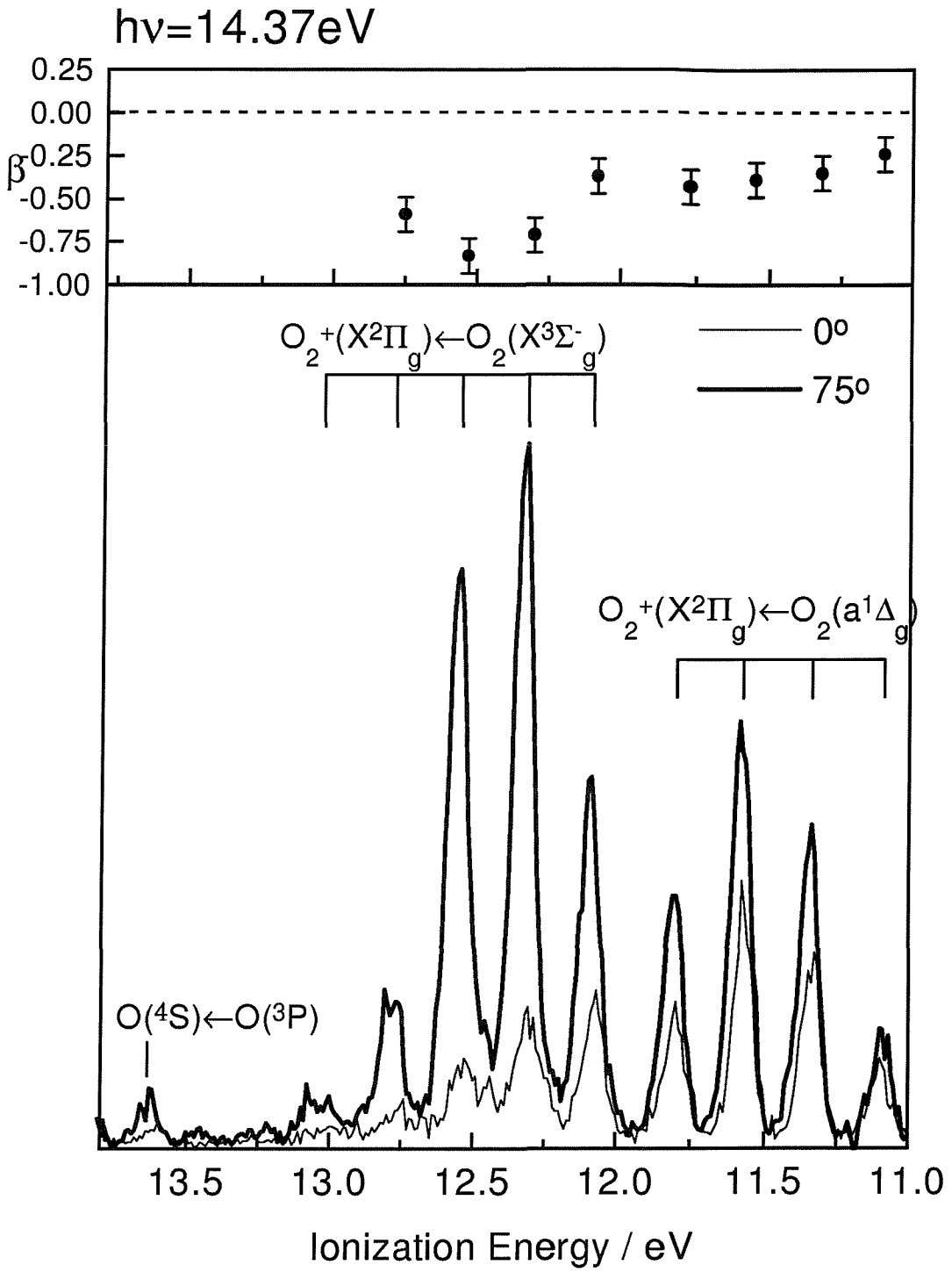

Figure 10.3: Top: β parameter for the photoelectron bands of discharged oxygen shown below. Bottom: photoelectron spectra of discharged O_2 at photon energy of $14.37\,eV$, resonant with the $O_2^*(p^1\Phi_u\, v' = 5) \leftarrow O_2(a^1\Delta_g\, v'' = 0)$ excitation, at two angles of observation: $\theta = 0^o$ and 75^o.

Band	v^+	$\beta(h\nu = 14.11\,eV)$	$\beta(h\nu = 14.37\,eV)$
$O_2^+(X^2\Pi_g\, v^+) \leftarrow O_2(a^1\Delta_g\, v'' = 0)$	0	-0.26	-0.24
	1	-0.42	-0.35
	2	-0.52	-0.39
	3	-0.44	-0.43
$O_2^+(X^2\Pi_g\, v^+) \leftarrow O_2(X^3\Sigma_g^-\, v'' = 0)$	0	-0.23	-0.37
	1	-0.50	-0.71
	2	-0.65	-0.83
	3	-0.64	-0.59
	4	-0.15	-0.11
	5	-0.17	-
	6	-0.08	-
$O^+(^4S) \leftarrow O(^3P)$		-0.36	-

Table 10.3: Asymmetry parameters of $O_2(a^1\Delta_g)$, $O_2(X^3\Sigma_g^-)$ and $O(^3P)$ at the resonant photon energies of 14.11 and $14.37\,eV$. Errors in the values of β from this work are estimated to be of the order of ± 0.1.

photon energy regions $16.8 - 18.5\,eV$ [24] and $20.65 - 21.60\,eV$ [23], but measurements of β for the $O_2^+(X^2\Pi_g\, v^+) \leftarrow O_2(X^3\Sigma_g^-\, v'' = 0)$ band in the energy range investigated here have not been reported before the present, work and so no comparison of the results reported here with other values is possible.

In both resonant photoelectron spectra of figures 10.2 and 10.3, the relative change in intensity of the $v^+ = 0$ component of the $O_2^+(X^2\Pi_g\, v^+) \leftarrow O_2(a^1\Delta_g\, v'' = 0)$ band is small, and is very similar for all the $v^+ = 1 - 3$ components. The asymmetry parameter for each of the v^+ components of the $O_2^+(X^2\Pi_g\, v^+) \leftarrow O_2(a^1\Delta_g\, v'' = 0)$ band is negative, as the signals for all these components are stronger at $\theta = 75^o$ than at $\theta = 0^o$. Within the estimated errors (± 0.1), the values of β for the different v^+ components of the $O_2^+(X^2\Pi_g\, v^+) \leftarrow O_2(a^1\Delta_g\, v'' = 0)$ band are not very different. The values of β for each v^+ component does not change much when changing photon energies between 14.11 and $14.37\,eV$.

In the spectra of discharged O_2 at $h\nu = 14.11\,eV$ shown in figure 10.2, the $O^+(^4S) \leftarrow O(^3P)$ signal is enhanced by a $O^*(^3P) \leftarrow O(^3P)$ resonance at this photon energy [36], and it overlaps with the $v^+ = 7$ component of the $O_2^+(X^2\Pi_g\, v^+) \leftarrow O_2(X^3\Sigma_g^-\, v'' = 0)$ band. However, from the photoelectron spectra recorded at the same photon energy with the discharge turned off and shown in figure 10.4 (see later), it is found that this O_2 component has very little intensity; if its small contribution to the overall intensity of the band at $13.61\,eV$ is neglected, the β value for this O atom band is obtained as $-0.36(10)$.

In the spectra of discharged O_2 recorded at $h\nu = 14.37\,eV$ shown in figure 10.3, the angular distribution results are very similar to those obtained from the spectra recorded at $h\nu = 14.11\,eV$. The relative change in intensity in the $O_2^+(X^2\Pi_g\, v^+) \leftarrow O_2(a^1\Delta_g\, v'' = 0)$ band is very small for the $v^+ = 0$ component, and for the $v^+ = 1 - 3$ members is very similar to that observed at $h\nu = 14.11\,eV$.

In these resonant photoelectron spectra, the $O_2^+(X^2\Pi_g\, v^+) \leftarrow O_2(a^1\Delta_g\, v'' = 0)$ band shows an extended vibrational progression [1], and for the higher vibrational components strong overlap with the $O_2^+(X^2\Pi_g\, v^+) \leftarrow O_2(X^3\Sigma_g^-\, v'' = 0)$ band occurs. As a result, it was not possible to obtain from these spectra the β parameters for any of the components of the $O_2^+(X^2\Pi_g\, v^+) \leftarrow O_2(X^3\Sigma_g^-\, v'' = 0)$ band, and for the $v^+ \geq 5$ components of the $O_2^+(X^2\Pi_g\, v^+) \leftarrow O_2(a^1\Delta_g\, v'' = 0)$ band. To help with this problem, angle resolved photoelectron spectra were also recorded under similar conditions with the microwave discharge turned off, such that only the contribution from $O_2(X^3\Sigma_g^-)$ is present. These spectra are shown in figure 10.4 and show seven vibrational components in the $O_2^+(X^2\Pi_g\, v^+) \leftarrow O_2(X^3\Sigma_g^-\, v'' = 0)$ band. The β parameters for the $O_2^+(X^2\Pi_g\, v^+) \leftarrow O_2(X^3\Sigma_g^-\, v'' = 0)$ band plotted in figures 10.2 and 10.3 were obtained from the spectra recorded with the discharge turned off. A subtraction of the photoelectron spectra recorded with the discharge turned off from the spectra of discharged O_2 was attempted, in order to isolate the contribution of $O_2(a^1\Delta_g)$, but this did not prove successful.

As shown in figure 10.4, the change in intensity for the $v^+ = 0 - 3$ components of the $O_2^+(X^2\Pi_g\, v^+) \leftarrow O_2(X^3\Sigma_g^-\, v'' = 0)$ band when moving from $\theta = 0^o$ to $\theta = 75^o$, is quite dramatic in both spectra at $h\nu = 14.11$ and $14.37\,eV$, and shows negative values of β. The values of β for the $O_2^+(X^2\Pi_g\, v^+) \leftarrow O_2(X^3\Sigma_g^-\, v'' = 0)$ band at these energies are listed in table 10.3. The values of β for the $v^+ = 0 - 3$ components are on average more negative than for the $v^+ = 4$, 5 and 6 members; this would suggest different dynamics between the low and the high v^+ components for the photoionization process.

It is extremely interesting to observe that for the $O_2^+(X^2\Pi_g\, v^+) \leftarrow O_2(X^3\Sigma_g^-\, v'' = 0)$ band, at the two photon energies of interest, the change in intensity is different for different vibrational components, and consequently different v^+ components have different values of β. A similar result was also found in section 10.5.1 for the spectra recorded at the photon energy of $21.22\,eV$. This is partly true also for the $O_2^+(X^2\Pi_g\, v^+) \leftarrow O_2(a^1\Delta_g\, v'' = 0)$ band, but for the $O_2^+(X^2\Pi_g\, v^+) \leftarrow O_2(X^3\Sigma_g^-\, v'' = 0)$ band this effect is much stronger, and is particularly strong at the photon energy of $14.37\,eV$.

A v^+ dependence of β for the $O_2^+(X^2\Pi_g\, v^+) \leftarrow O_2(X^3\Sigma_g^-\, v'' = 0)$ band was also found by Codling *et al.* [23] in the photon energy range $20.65 - 21.60\,eV$, where Rydberg states

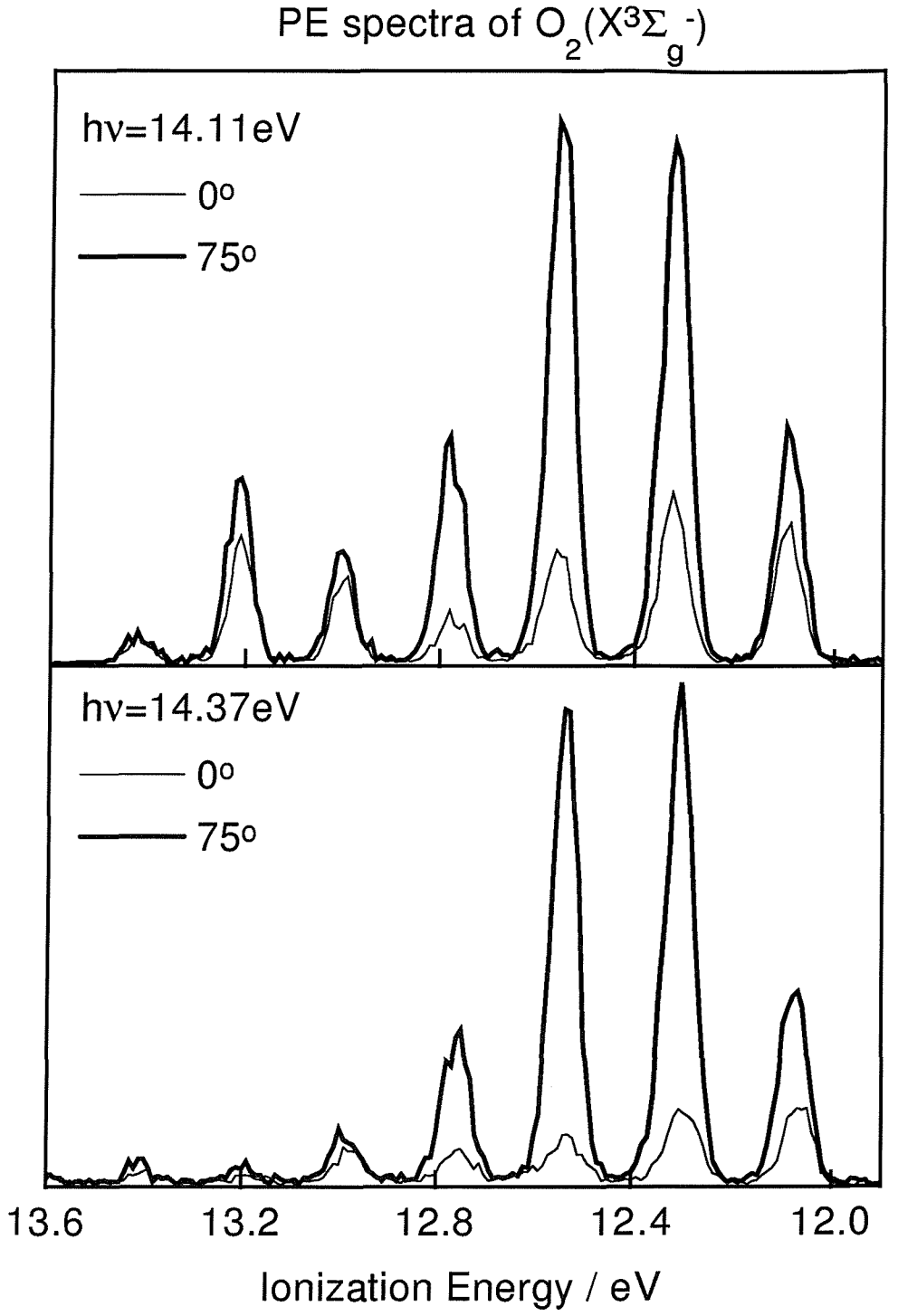

Figure 10.4: Photoelectron spectra of O_2 with the microwave discharge turned off at photon energies of $14.11\,eV$ (upper) and $14.37\,eV$ (lower) at two angles of observation: $\theta = 0^o$ and 75^o.

converging to the $O_2^+(c^4\Sigma_g^-)$ limit are present. In the work of Codling *et al.* [23], the v^+ dependence of β was interpreted as a manifestation of different coupling between the Rydberg states with the continuum channels. Their interpretation cannot be extended to the present work as there are no known Rydberg states accessible from $O_2(X^3\Sigma_g^-)$ at the energies considered here.

It is surprising to notice that the v^+ dependence of β is more pronounced in the $O_2^+(X^2\Pi_g\, v^+)$ $\leftarrow O_2(X^3\Sigma_g^-\, v''=0)$ band than in the $O_2^+(X^2\Pi_g\, v^+) \leftarrow O_2(a^1\Delta_g\, v''=0)$ band. According to the interpretation of reference [23], the presence of Rydberg states accessible from the $a^1\Delta_g$ state, but not from the $X^3\Sigma_g^-$ state, would lead to the reverse trend to be expected.

The v^+ dependence of β at non-resonant energies is normally a manifestation of either the breakdown of the Born-Oppenheimer approximation or the presence of a shape resonance [20]. Both the breakdown of the Born-Oppenheimer approximation and the presence of shape resonances are very difficult to find with conventional (non angle resolved) PES, and present results underline the importance of angle resolved PES on molecules.

10.5.3 Asymmetry parameters for the $O_2^+(X^2\Pi_g\, v^+) \leftarrow O_2(a^1\Delta_g\, v''=0)$ band in the photon energy range $13.8-15.2\,eV$

The behaviour of β as a continuous function of photon energy can be even more interesting than its value at selected resonant energies. It has been shown theoretically [37] and also experimentally in numerous cases [23], [24], [38], that measurements of β as a function of the incident photon energy can show structure corresponding to autoionizing resonances. The asymmetry parameter depends not only on the square amplitudes of the degenerate photoelectron channels as the cross section σ does, but it also depends on the relative phases between these amplitudes, as is clear from equation (10.3). Therefore, a plot of β as a function of photon energy can reveal the presence of resonances that are barely visible, or in some cases not resolvable, in CIS spectra. For the same reason, lineshapes in β plots can be different from those in CIS spectra.

The CIS spectra for the $v^+=0-3$ components of the $O_2^+(X^2\Pi_g\, v^+) \leftarrow O_2(a^1\Delta_g\, v''=0)$ band, recorded over the photon energy range $13.8-15.2\,eV$, are shown in figure 10.5. These spectra were measured during the course of this work on beam-line 3.3 at the Daresbury SRS, and are slightly different than those recorded by Barr *et al.* [1] on beam-line 3.2; the reason for their slight difference is probably due to a different degree of linear polarization: $S_1 \simeq 0.9$ here, and $S_1 \simeq 0.3$ in the work of reference [1]. Nevertheless, from both sets of CIS spectra it is clear that strong resonances are present for the $v'=3$ and

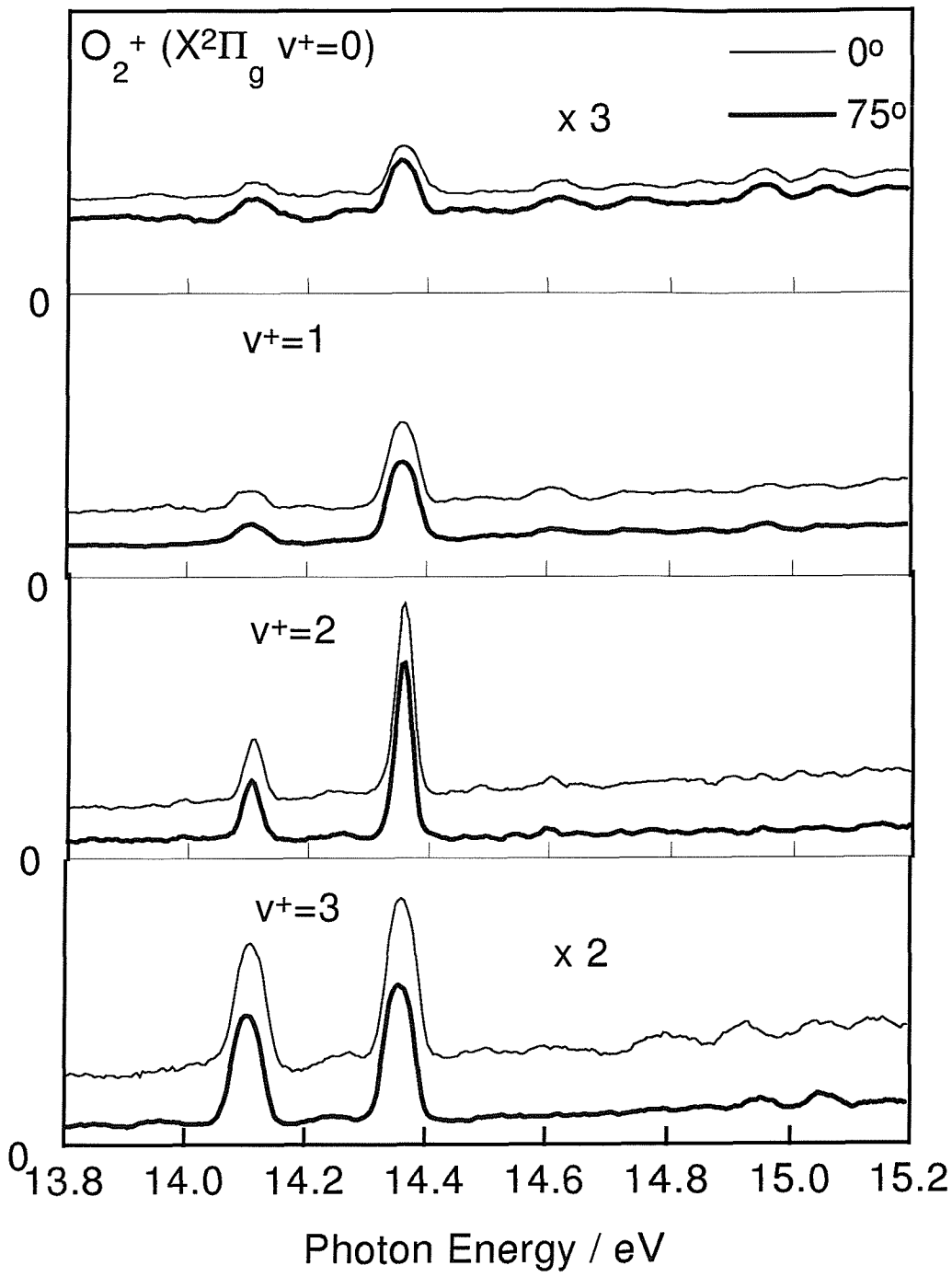

Figure 10.5: CIS spectra for the $O_2^+(X^2\Pi_g\, v^+) \leftarrow O_2(a^1\Delta_g\, v'' = 0)$ band in the region of the $O_2^*(p^1\Phi_u\, v') \leftarrow O_2(a^1\Delta_g\, v'' = 0)$ resonances at two angles of observation: $\theta = 0^o$ and 75^o.

5 components of $O_2^*(p^1\Phi_u\, v')$ at excitation energies of 14.11 and $14.37\,eV$ respectively, whilst no band is present in the position of the $v' = 4$ resonance at an energy of $14.24\,eV$. The reason for this effect is that, as explained in reference [1], the $v' = 4$ level undergoes more rapid predissociation than the $v' = 3$ and 5 levels, that instead decay preferably by autoionization giving rise to strong signals in the CIS spectra.

The β parameters extracted from the CIS spectra of figure 10.5 are displayed as continuous lines in figure 10.6. The most interesting feature in these β plots is that they all show positive peaks at energies corresponding to the autoionizing resonances $O_2^*(p^1\Phi_u\, v') \leftarrow O_2(a^1\Delta_g\, v'' = 0)$. The lack of a strong peak at $h\nu = 14.24\,eV$ confirms the interpretation of reference [1] of predissociation of the $O_2^*(p^1\Phi_u\, v' = 4)$ state. However, a small band is seen at $h\nu = 14.24\,eV$ in the $v^+ = 0$-3 β plots of figure 10.6, supporting the presence of the $O_2^*(p^1\Phi_u v' = 4) \leftarrow O_2(a^1\Delta_g)$ resonance, reduced in size by predissociation in the excited state.

In the β plots of figure 10.6, the β parameters extracted from the photoelectron spectra at resonant wavelengths of figure 10.2 and 10.3 are also displayed, together with their estimated errors. Although in principle these points must exactly fit the continuous lines because they are measurements of the same quantities, they could slightly differ for many experimental reasons, as they were obtained from different spectra recorded at different time. The points in figure 10.6 fit very well the continuous lines, and this is a manifestation of consistency between the angle resolved PE spectra and CIS spectra.

At this point it is strongly desirable to find a simple explanation why the β plots show less negative values at energies corresponding to the $O_2^*(p^1\Phi_u\, v') \leftarrow O_2(a^1\Delta_g\, v'' = 0)$ excitations than the β values recorded off-resonance. According to electric dipole selection rules, in the $O_2^+(X^2\Pi_g) + e^- \leftarrow O_2(a^1\Delta_g) + h\nu$ photoionization process, the photoelectron is in a superposition of degenerate σ_u, π_u and δ_u channels. For the analysis of the behaviour of β in terms of the symmetry of the channels of the photoelectron it is of advantage to switch to atomic symmetry. Each of these channels can be described as an infinite combination of components with different atomic orbital angular momentum l; only odd values of l are present because of the *ungerade* character of the photoelectron channels. The $1\pi_g$ orbital from which the electron is removed becomes a d orbital ($l = 2$) in a united atom picture. According to this very simplified model, the strongest components in the photoelectron wave are $l = 1$ (p wave) and $l = 3$ (f wave); from equation (10.3) $\epsilon p \leftarrow nd$ and $\epsilon f \leftarrow nd$ have values of β of 0.2 and 0.8 respectively. This approach can be tentatively extended to autoionization from an O_2 state of $^1\Phi_u$ symmetry. The ion has a $^2\Pi_g$ symmetry, and the autoionization process must proceed such that the overall symmetry of the final contin-

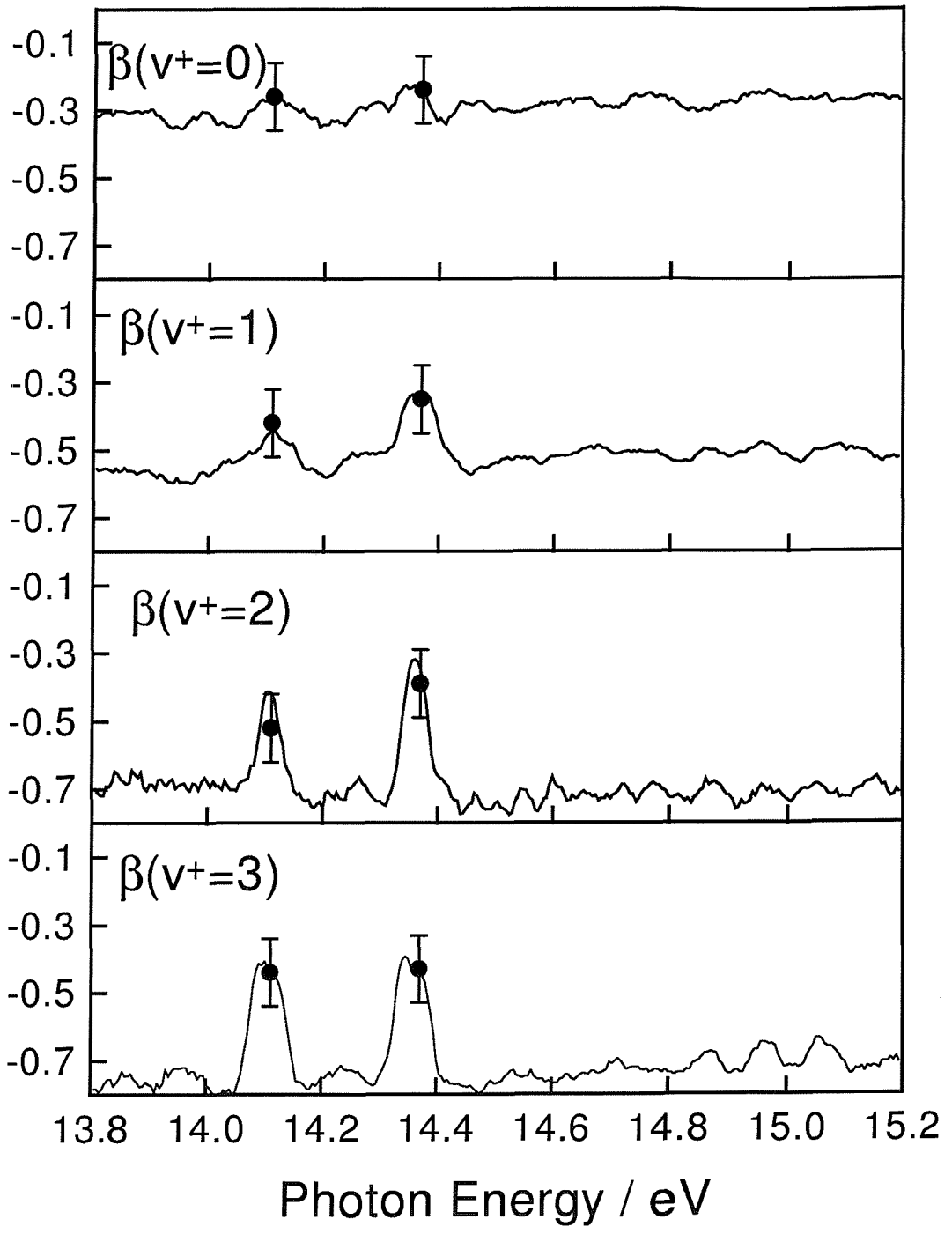

Figure 10.6: Asymmetry parameters for the $O_2^+(X^2\Pi_g\, v^+) \leftarrow O_2(a^1\Delta_g\, v'' = 0)$ band in the region of the $O_2^*(p^1\Phi_u\, v') \leftarrow O_2(a^1\Delta_g\, v'' = 0)$ resonances. The continuous lines come from the CIS spectra, the circles with error bars come from the PE spectra.

uum state remains $^1\Phi_u$. Therefore the photoelectron wave is constrained to be composed by only δ_u and γ_u components. Each of these components contain the $l = 3$ (f wave) but not the $l = 1$ (p wave) term in an expansion in atomic angular momenta. Therefore it is expected that the relative f contribution to the photoelectron wave increases at the resonant energies, as the p contribution arises only from direct ionization and is not resonantly enhanced. This partly explains why at the $O_2^*(p^1\Phi_u\, v') \leftarrow O_2(a^1\Delta_g\, v'' = 0)$ resonances β increases, driven by the enhanced presence of the f wave. However, this may only be a fortuitous coincidence as in equation (10.3), β depends also on the relative phase between these two waves, $\delta_f - \delta_p$. This phase difference can also change between resonant and non-resonant conditions, and symmetry considerations are not helpful in predicting this behaviour. Unfortunately, neither the relative amplitudes of the p and f channels nor their phase difference can be quantified from the present measurements.

10.5.4 Asymmetry parameters for the $O_2^+(X^2\Pi_g\, v^+) \leftarrow O_2(a^1\Delta_g\, v'' = 0)$ band in the photon energy range $18.0 - 19.2\, eV$

CIS spectra for the $v^+ = 1 - 3$ components of the $O_2^+(X^2\Pi_g\, v^+) \leftarrow O_2(a^1\Delta_g\, v'' = 0)$ band were recorded at the two angles $\theta = 0^o$ and $\theta = 75^o$ in the photon energy range $18.0 - 19.2\, eV$. These spectra are shown in figure 10.7. As in the work of reference [1], the $v^+ = 0$ component proved to be too weak to record reliable spectra.

As mentioned in section 10.4, the CIS spectra of reference [1] in the photon energy region $18.0 - 19.2\, eV$ were analyzed in terms of two overlapping vibrational progressions, starting at the energy of $18.46\, eV$. The vibrational series in this photon energy region could not be definitely assigned. The spectra in figure 10.7 cannot be assigned in terms of only two vibrational progressions, but three overlapping series must be considered. The need for three series in this region can be seen most clearly in the components labeled M, M' and N" at approximately $18.75\, eV$ of energy in the $v^+ = 3$ spectra of figure 10.7. When moving from 0^o to 75^o the maximum of the main component, composed of M and M', moves to lower energy and the component N" is still present but decreases in intensity.

The three vibrational progressions start at energies of 18.06, 18.08 and $18.12\, eV$, well before the component observed in the work of reference [1] at $18.46\, eV$ and labeled K in figure 10.7. The average vibrational separations of these components are estimated to be of 1065, 1105 and $900\, cm^{-1}$, although with the present resolution it is very difficult to obtain accurate values and uncertainties for these vibrational spacings. These vibrational spacings compare favourably with the value of the vibrational constant $\omega_e = 995\, cm^{-1}$ of the $D^2\Delta_g$ state of O_2^+.

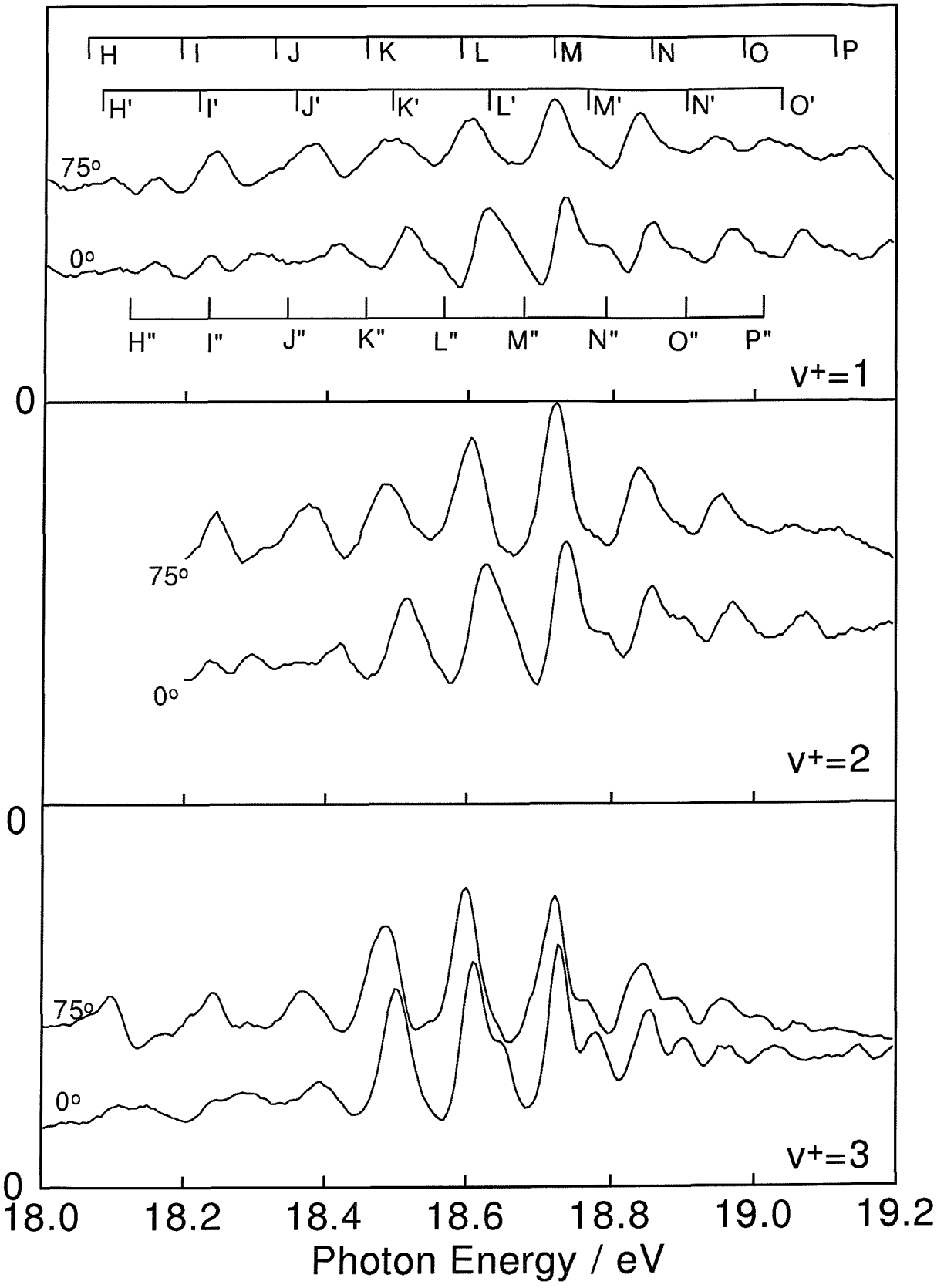

Figure 10.7: CIS spectra for the $O_2^+(X^2\Pi_g\, v^+) \leftarrow O_2(a^1\Delta_g\, v'' = 0)$ band in the photon energy range $18.0 - 19.2\, eV$. The vertical scales represent counts normalized by photon flux and is the same for all the spectra.

In view of an additional vibrational progression, and components observed at lower energies than $18.46\,eV$, the previous interpretation can now be revisited. Assuming features H, H' and H" at 18.06, 18.08, and $18.12\,eV$ to be the $v' = 0$ members of the three progressions, the effective quantum numbers $(n - \delta)$ of the associated Rydberg states would be 4.26, 4.44 and 4.32, suggesting a $(D^2\Delta_g,\, 5p\pi)^1\Phi_u$ or $(D^2\Delta_g,\, 5p\pi)^1\Pi_u$ excited state assignment for the series beginning at H and H" and a $(D^2\Delta_g,\, 5p\sigma)^1\Delta_u$ assignment for the series beginning at H' [39].

Asymmetry parameters were obtained from the CIS spectra of figure 10.7 and are plotted in figure 10.8. In the top graph in figure 10.8 the positions of the components of the three vibrational progressions identified from the CIS spectra in figure 10.7 are marked and labelled. The β parameter plots show similar structure to the CIS spectra. The presence of at least two vibrational progressions can be seen in all the graphs; the maxima and minima in the β plots are in different positions than in the CIS spectra of figure 10.7.

10.6 Conclusions

Angle resolved PE and CIS spectra of the $O_2^+(X^2\Pi_g\, v^+) \leftarrow O_2(a^1\Delta_g\, v'' = 0)$ band were recorded in the photon energy ranges $13.8 - 15.2\,eV$ and $18.0 - 19.2\,eV$.

Autoionizing resonances were observed in the CIS spectra, and in the asymmetry parameter plots, for the $O_2^+(X^2\Pi_g\, v^+) \leftarrow O_2(a^1\Delta_g\, v'' = 0)$ band at energies corresponding to the $O_2^*(p^1\Phi_u\, v') \leftarrow O_2(a^1\Delta_g\, v'' = 0)$ excitations in the photon energy region $13.8 - 15.2\,eV$. Angle resolved measurements allowed new information on the photoionization dynamics in this photon energy region to be obtained.

New autoionizing resonances were observed in the photon energy region $18.0 - 19.2\,eV$, where three vibrational progressions belonging to singlet Rydberg states based on a $D^2\Delta_g$ core have been discovered.

Other short lived molecules have been studied with PES using synchrotron radiation in the past, notably SO [40], CS [41], and OH and OD [42]. The present work proves that angle resolved PES can be successfully extended to these molecules and new insight into their photoionization dynamics can be obtained.

A third generation synchrotron radiation source will be used in the near future. This will allow CIS measurements to be recorded at higher optical resolution, a higher photon flux will make possible the study of weaker transitions, and a more collimated photon beam will allow asymmetry parameters to be recorded with a improved accuracy.

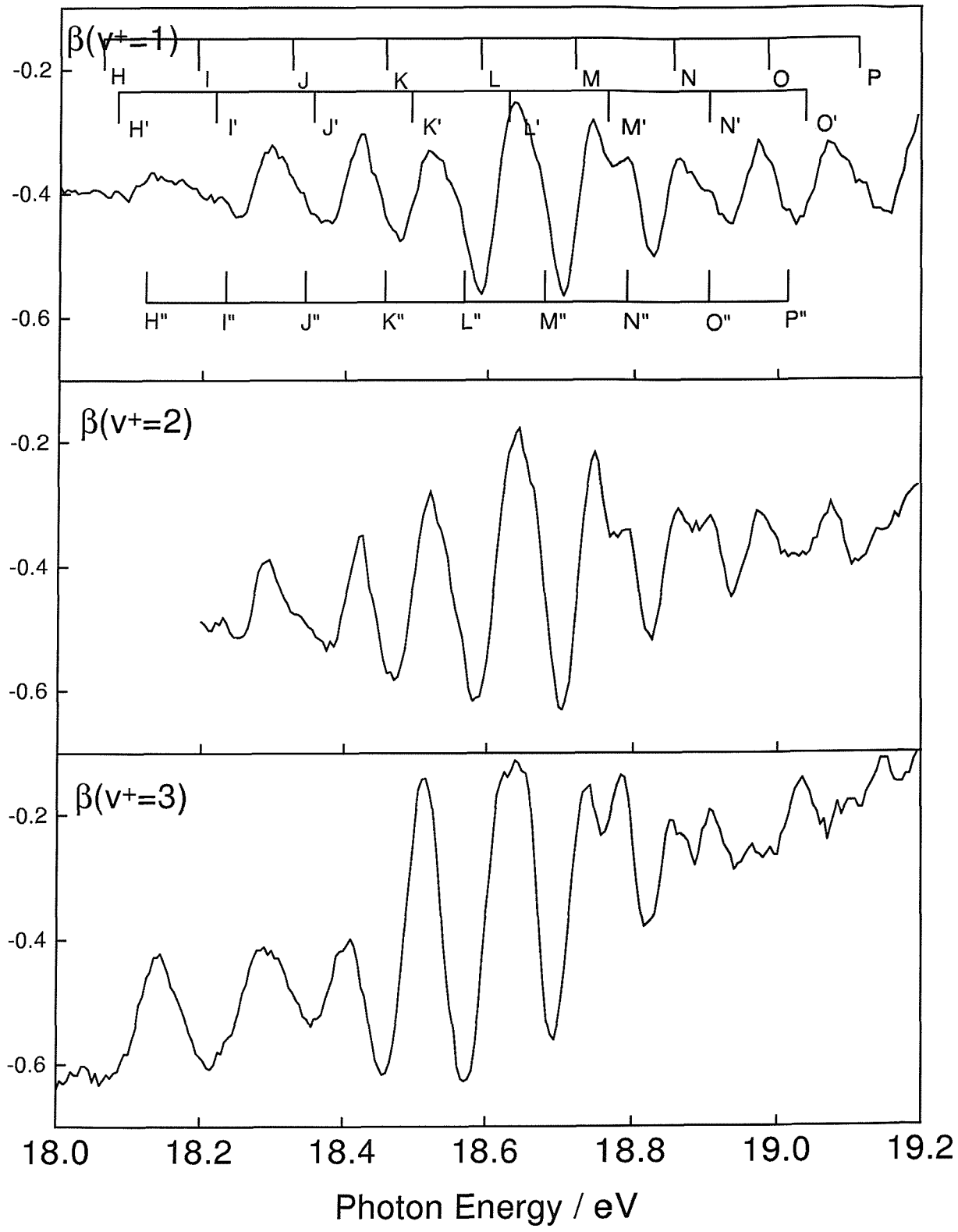

Figure 10.8: Asymmetry parameters for the $O_2^+(X^2\Pi_g\, v^+) \leftarrow O_2(a^1\Delta_g\, v'' = 0)$ band in the photon energy range $18.0 - 19.2\, eV$.

Bibliography

[1] JD Barr, A De Fanis, JM Dyke, SD Gamblin, A Morris, S Stranges, JB West, TG Wright and AE Wright, *Journal of Chemical Physics*, **7** 2737-2747 (1998).

[2] DW Turner and DP May, *Journal of Chemical Physics*, **45** 471-478 (1966).

[3] DW Turner, *Proceedings of the Royal Society of London*, **307** 15-22 (1968).

[4] O Edqvist, E Lindholm, LE Selin and Åsbrink, *Physica Scripta*, **1** 25-30 (1970).

[5] P Baltzer, B Wannberg, L Karlsson, M Karlsson Göthe and M Larsson, *Physical Review A*, **45** 4374-4384 (1992).

[6] Techniques of Vacuum Ultraviolet Spectroscopy.
JAR Samson, John Wiley & Sons Inc., London (1967).

[7] WC Price and G Collins, *Physical Review*, **48** 714-719 (1935).

[8] E Lindholm, *Arkiv för Physik*, **40** 117-124 (1968).

[9] K Yoshino and Y Tanaka, *Journal of Chemical Physics*, **48** 4859-4867 (1968).

[10] PM Dehmer and WA Chupka, *Journal of Chemical Physics*, **62** 4525-4534 (1975).

[11] E Nishitani and I Tanaka, *Journal of Chemical Physics*, **81** 3429-3437 (1984).

[12] AA Cafolla, T Reddish, AA Wills and J Comer, *Journal of Physics B: Atomic, Molecular and Optical Physics*, **23** 1433-1445 (1989).

[13] K Ellis, RJ Hall, L Avaldi, G Dawber, A McConkey, L Andric and GC King, *Journal of Physics B: Atomic, Molecular and Optical Physics*, **27** 3415-3426 (1994)

[14] T Akahori, Y Morioka, T Tanaka, H Yoshii, T Hayashi and K Ito, *Journal of Chemical Physics*, **197** 4875-4880 (1997).

[15] JHD Eland, *Journal of Chemical Physics*, **72** 6015-6019 (1980).

[16] D Čubrić, A Willis, J Comer and P Hammond, *Journal of Physics B: Atomic, Molecular and Optical Physics*, **29** 4151-4160 (1996).

[17] CN Yang, *Physical Review Letters*, **74** 764-767 (1948).

[18] J Cooper and RN Zare, *Journal of Chemical Physics*, **48** 942-943 (1968).

[19] JC Tully, RS Berry and BJ Dalton, *Physical Review Letters*, **176** 95-105 (1968).
AD Buckingham, BJ Orr and JM Sichel, *Phylosophical Transactions of the Royal Society of London*, **268** 147-157 (1970).

[20] JL Dehmer, D Dill and S Wallace, *Physical Review Letters*, **43** 1005-1008 (1979).

[21] DG McCoy, JM Morton and GV Marr, *Journal of Physics B: Atomic, Molecular and Optical Physics*, **11** L547-L549 (1978).

[22] WH Hancock and JAR Samson, *Journal of Electron Spectroscopy and Related Phenomena*, **9** 211-216 (1976).

[23] K Codling, AC Parr, DL Ederer, R Stockbauer, JB West, BE Cole and JL Dehmer, *Journal of Physics B: Atomic, Molecular and Optical Physics*, **14** 657-666 (1981).

[24] AC Parr, JB West, GV Marr and JL Dehmer, *Journal of Physics B: Atomic, Molecular and Optical Physics*, **31** 5161-5173 (1998).

[25] L Beeching, A De Fanis, JM Dyke, SD Gamblin, N Hooper, A Morris and JB West, *Journal of Chemical Physics*, **7** 1707-1712 (2000).

[26] Chemistry of Atmosphere.
RP Wayne, Clarendon Press, Oxford (1969).

[27] Molecular Spectra and Molecular Structure *IV*. Constants of Diatomic Molecules.
KP Huber and G Herzberg, van Nostrand Reinhold Company, New York (1979).

[28] N Jonathan, A Morris, M Okuda, KJ Ross and DJ Smith, *Journal of The Chemical Society, Faraday Transaction II*, **70** 1810-1816 (1974).

[29] H van Lonkhuyzen and CA de Lange, *Journal of Electron Spectroscopy and Related Phenomena*, **27** 255-260 (1982).

[30] RD Johnson, GR Long and JW Hudgens, *Journal of Chemical Physics*, **87** 1977-1981 (1987).
H Park, LP Li, WA Chupka, *Chemical Physics Letters*, **162** 317-320 (1989).

L Ogorzalek Loo, WJ Marinelli, PL Houston, S Arepelli, JR Wisenfeld and RW Field, *Journal of Chemical Physics*, **91** 5185-5200 (1989).
H Park, LP Li, WA Chupka, *Journal of Chemical Physics*, **92** 61-64 (1990).
A Sur, SR Friedman and PJ Miller, *Journal of Chemical Physics*, **94** 1704-1711 (1991).
RJ Yokelson, RJ Lipert and WA Chupka, *Journal of Chemical Physics*, **97** 6144-6152 (1992).
RJ Yokelson, RJ Lipert and WA Chupka, *Journal of Chemical Physics*, **97** 6153-6167 (1992).
PJ Miller, WA Chupka, J Winniczek and MG White, *Journal of Chemical Physics*, **89** 4059-4061 (1988).

[31] RE Huffman, DE Paulsen, JC Larrabee and RB Cairns, *Journal of Geophysical Research*, **76** 1028-1038 (1971).

[32] RJ Collins, D Husain and RJ Donovan, *Journal of The Chemical Society, Faraday Transaction II*, **69** 145-151 (1971).

[33] DH Katayama, RE Huffman and Y Tanaka, *Journal of Chemical Physics*, **62** 2939-2948 (1975).

[34] DH Katayama, S Ogawa, M Ogawa and Y Tanaka, *Journal of Chemical Physics*, **67** 2132-2142 (1977).

[35] P van der Meulen, CA de Lange, MO Krause and DC Mancini, *Physica Scripta*, **41** 837-840 (1990).

[36] Atomic Energy Levels.
C Moore, circular 467 United States National Bureau of Standards, Washington (1949).

[37] D Dill, *Physical Review A*, **7** 1976-1987 (1973).

[38] GV Marr, JM Morton, RM Holmes and DG McCoy, *Journal of Physics B: Atomic, Molecular and Optical Physics*, **12** 43-52 (1979)

[39] CYR Wu, *Journal of Quantum Spectroscopy and Radiation Transfer*, **37** 1-15 (1987).

[40] JM Dyke, D Haggerston, A Morris, S Stranges, JB West, TG Wright and AE Wright, *Journal of Chemical Physics*, **76** 165-170 (1995).

[41] JM Dyke, SD Gamblin, D Haggerston, A Morris, S Stranges, JB West, TG Wright and AE Wright, *Journal of Chemical Physics*, **108** 6258-6255 (1998).

[42] JD Barr, A De Fanis, JM Dyke, SD Gamblin, N Hooper, A Morris, S Stranges, JB West and TG Wright, *Journal of Chemical Physics*, **110** 345-354 (1998).

Chapter 11

Photoelectron spectroscopy of OH and OD with synchrotron radiation

11.1 Introduction

This chapter reports studies of photoelectron spectroscopy using synchrotron radiation on the OH and OD radicals. The results obtained during this work have recently been published in reference [1].

The chapter is organized as follows. In section 11.2 previous spectroscopic investigations on OH, OD, and their cations, that are considered important for the present work are briefly reviewed. Section 11.3 presents the results of the measured CIS spectra, and resonant photoelectron spectra, together with their interpretations. Section 11.4 summarizes the results obtained and suggests possible extensions of the present work.

11.2 Previous investigations on OH and OD with electron spectroscopy

The hydroxyl radical, OH, is one of the most studied reactive intermediates in the gas phase, because it plays important roles in the chemistry of the Earth's atmosphere, combustion processes and interstellar media [2].

The ground state of the OH and OD radicals has the following electronic configuration:

$$1\sigma^2 2\sigma^2 3\sigma^2 1\pi^3 \tag{11.1}$$

and a ^{2}H symmetry. Several bound and dissociative states of OH and OD below the first

ionization energy are well characterized [3].

Experimental and theoretical spectroscopic investigations on OH have progressed simultaneously with those on OD. One reason for this is that, as expected from the Born-Oppenheimer approximation, they have identical electronic structures. Also, due to the isotopic shifts of vibrational and rotational frequencies, studies where vibrational or even rotational resolution are achieved can be easily compared and interpreted.

Photoabsorption measurements have been carried out by Douglas in 1974 [4], by Viney in 1980 [5] and by Nee and Lee in 1984 [6]. Observed absorption bands were assigned to states belonging to Rydberg series with the help of the ab-initio calculations of Easson and Price in 1973 [7], and of van Dishoek *at al.* in 1983 [8].

De Beer *et al.* [9] and Collard *et al.* [10], in 1991, studied OH and OD with rotationally resolved (2+1) laser photoelectron spectroscopy, via the $D^2\Sigma^-$ resonant Rydberg state. Their interpretation was in agreement with the prediction of Stephens and McKoy in 1988 [11] of the presence of a Cooper minimum for ionization to the ground ionic state via the $D^2\Sigma^-$ Rydberg state. Zero electron kinetic energy (ZEKE) spectroscopy was reported by Wiedmann *et al.* in 1992 [12] for the first band of OH and OD.

Less information is available for the neutral states of OH and OD above their first ionization energies, and for the states of their singly charged positive ions.

Photoelectron spectra of OH and OD have been recorded with HeI α radiation by Katsumata and Lloyd in 1977 [13], and more recently by van Lonkhuyzen and de Lange in 1984 [14]. In the first study, where the $H + NO_2$ and $D + NO_2$ reactions described in section 9.6 were used to produce OH and OD, the first and second PE bands were observed. Bands at higher ionization energies could not be observed because of overlap with bands from secondary products. In the second investigation, where OH and OD were produced with the $F + H_2O$ and $F + D_2O$ abstraction reactions, combined with a phase sensitive detection method, four of the five expected OH and OD bands could be observed.

Photoionization from the valence 1π molecular orbital produces the $X^3\Sigma^-$, $a^1\Delta$ and $b^1\Sigma^+$ ionic states at adiabatic ionization energies (AIEs) of 13.01, 15.17 and 16.61 eV. The 1π orbital is composed mainly of an $O\,2p$ atomic orbital and is non bonding in character; this makes the potential energy curves of the $X^3\Sigma^-$, $a^1\Delta$ and $b^1\Sigma^+$ states very similar to that of the ground state of the neutral. As a result, the corresponding PE bands show quasi diagonal vibrational branching ratios. Removal of one electron from the 3σ subvalence shell gives rise to the $A^3\Pi$ and $c^1\Pi$ ionic states at AIEs of 16.48 and 18.00 eV respectively. The $A^3\mathrm{H}\,v^+ \leftarrow X^2\Pi\,v'' = 0$ band shows a broad vibrational progression

Final state	Ionization	AIE	Reference
$X^3\Sigma^-$	$1\pi^{-1}$	13.01	[13, 14]
$a^1\Delta$	$1\pi^{-1}$	15.17	[13, 14]
$b^1\Sigma^+$	$1\pi^{-1}$	16.61	[14]
$A^3\Pi$	$3\sigma^{-1}$	16.48	[14]
$c^1\Pi$	$3\sigma^{-1}$	18.30	[15, 16]

Table 11.1: Symmetries and adiabatic ionization energies (AIEs), in eV, of the states of OH^+ and OD^+ accessible from photoionization of the neutral ground state with one photon of $21.22\,eV$ of energy.

typical of ionization from bonding orbital. The $c^1\Pi\, v^+ \leftarrow X^2\Pi\, v'' = 0$ band has never been observed with photoelectron spectroscopy because of 1) overlap with bands arising from the precursors and secondary products used for the production of the radical [13], and 2) poor transmission of the electron energy analyser at low kinetic energies [14]. The ionization energy to the $c^1\Pi$ state of OH^+ is known only because of the laser photofragmentation spectroscopy measurements of Rodgers and Sarre in 1988 [15], who measured the $OH^+(c^1\Pi\, v' = 3) \leftarrow OH^+(b^1\Sigma^+\, v'' = 0)$ transition energy.

Table 11.1 lists symmetries and ionization energies to ionic states accessible by one photon ionization from the ground state of OH and OD with radiation of $21.22\,eV$ of energy.

The study of Merer *et al.* in 1975 [18] is the most detailed spectroscopic investigation of OH^+ and OD^+. They observed the $A^3\Pi \rightarrow X^3\Sigma^-$ emission band with resolution that allowed rotational structure to be resolved. The spectra were analysed in terms of perturbations of the A^3H state caused by the nearby $b^1\Sigma^+$ state.

Hirst and Guest in 1983 [16] and Saxon and Liu in 1986 [17] performed ab-initio calculations on the low lying states of OH^+. They calculated potential energy curves, spectroscopic constants, transition moments and photodissociation cross sections.

Little information is available concerning autoionization in OH and OD. The only previous spectroscopic investigations on autoionizing states are the photoionization mass spectroscopy (PIMS) studies of Dehmer in 1984 [19] and of Cutler *et al.* in 1995 [20]. In the first work, performed with a He continuum light source over the photon energy region $12.91 - 16.52\,eV$, several resonances thought to belong to Rydberg series converging to the $a^1\Delta$, $A^3\Pi$ and $b^1\Sigma^+$ ionic states at AIEs of 15.17, 16.48, and $16.61\,eV$ were observed. No resonance was assigned to a vibrationally excited state (i.e. $v' > 0$). In the second PIMS study [20], performed with higher resolution at the Aladdin SRS in Wisconsin, over the photon energy range $13.00 - 18.20\,eV$, resonances were assigned to states belonging to

the Rydberg series $a^1\Delta\, nd$, $A^3\Pi\, nd$ and $b^1\Sigma^+\, ns$. The l character of the Rydberg orbitals was derived from analysis of the quantum defects. No vibrationally excited resonances were found for the $a^1\Delta\, nd$ and $b^1\Sigma^+\, ns$ series, that have almost diagonal FCFs from the neutral ground state, but up to three vibrational components were observed for members of the $A^3\Pi\, nd$ series.

11.3 Results and discussion

A fundamental limitation of PIMS is that it has no vibrational specificity: it cannot measure the branching ratios of autoionizing resonances to the different vibrational components of the ion. It was anticipated in references [19] and [20] that photoelectron spectroscopy with synchrotron radiation would provide additional information on the nature of resonances unassigned in PIMS investigations. Comparison between resonance enhanced PE spectra and the FCFs for the autoionization processes can help the assignment of the resonant states.

The aims of this work were to record CIS spectra for the ionic states of OH and OD that could be observed free from overlap from bands belonging to other species in the PE spectra, namely the $X^3\Sigma^-\, v^+ = 0, 1$ and $a^1\Delta\, v^+ = 0$ states of OH^+ and OD^+; and to record PE spectra at resonant wavelengths identified in the CIS spectra.

11.3.1 Photoelectron spectra at the photon energy of $21.22\,eV$

Figure 11.1 shows two photoelectron spectra of the reaction mixture $H_2/He + NO_2$ recorded at the photon energy of $21.22\,eV$. This reaction mixture, together with a microwave discharge of H_2/He, is used to produce the OH radical, as explained in section 9.6.

The upper part of figure 11.1 contains the spectrum recorded with the microwave discharge turned on, the lower part of the figure contains the spectrum recorded with the discharge turned off. Bands due to the products from the secondary reactions

$$OH + OH \rightarrow H_2O + O, \tag{11.2}$$

and

$$O + O + M \rightarrow O_2 + M, \tag{11.3}$$

can be clearly seen and are labeled in the spectrum. Virtually no NO_2 is present in the spectrum, only a very small NO_2 contribution is present as a tiny hump in the

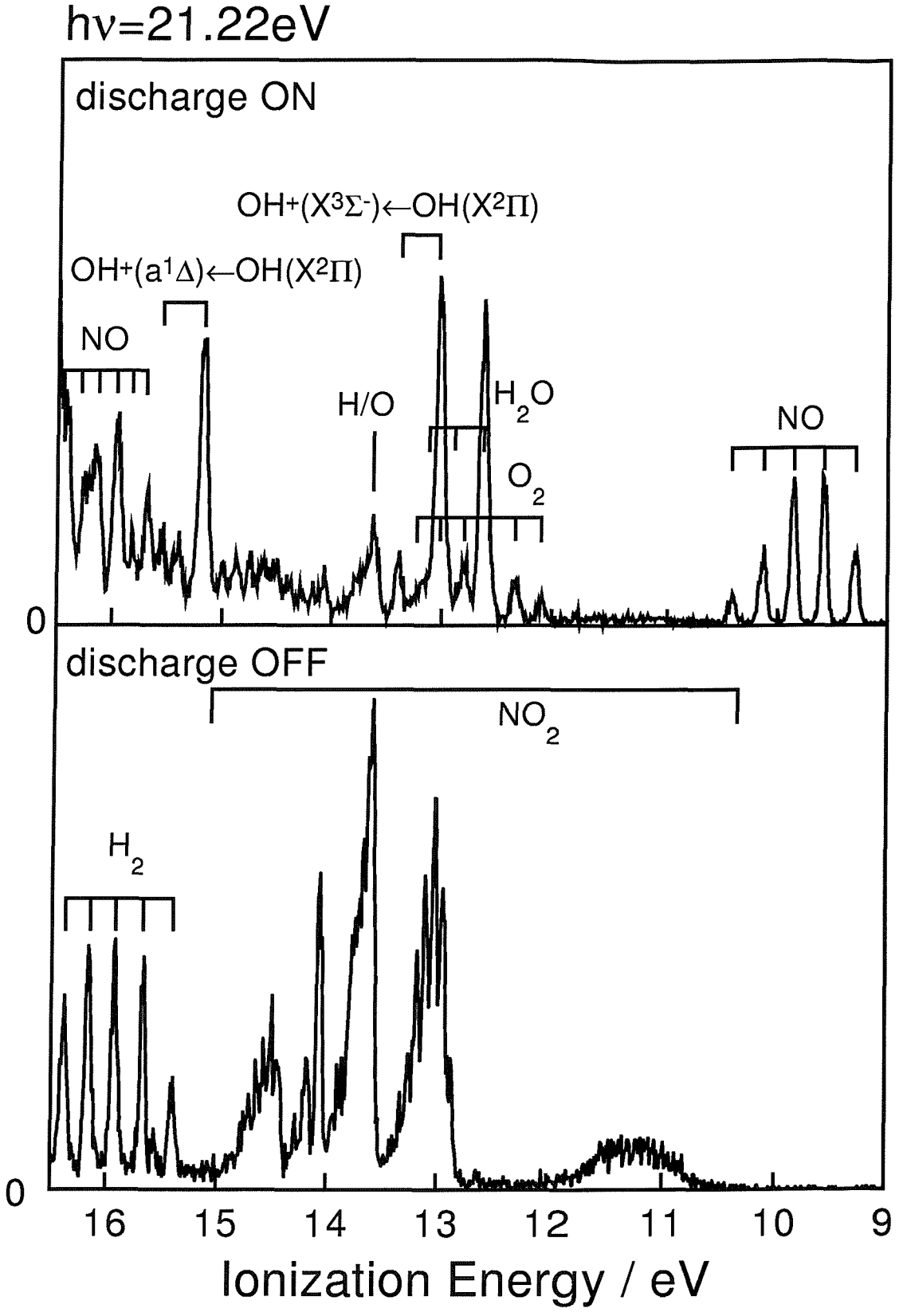

Figure 11.1: Photoelectron spectra of the reaction mixture $H_2/He + NO_2$ with the microwave discharge on and off, recorded at the photon energy of $21.22\,eV$.

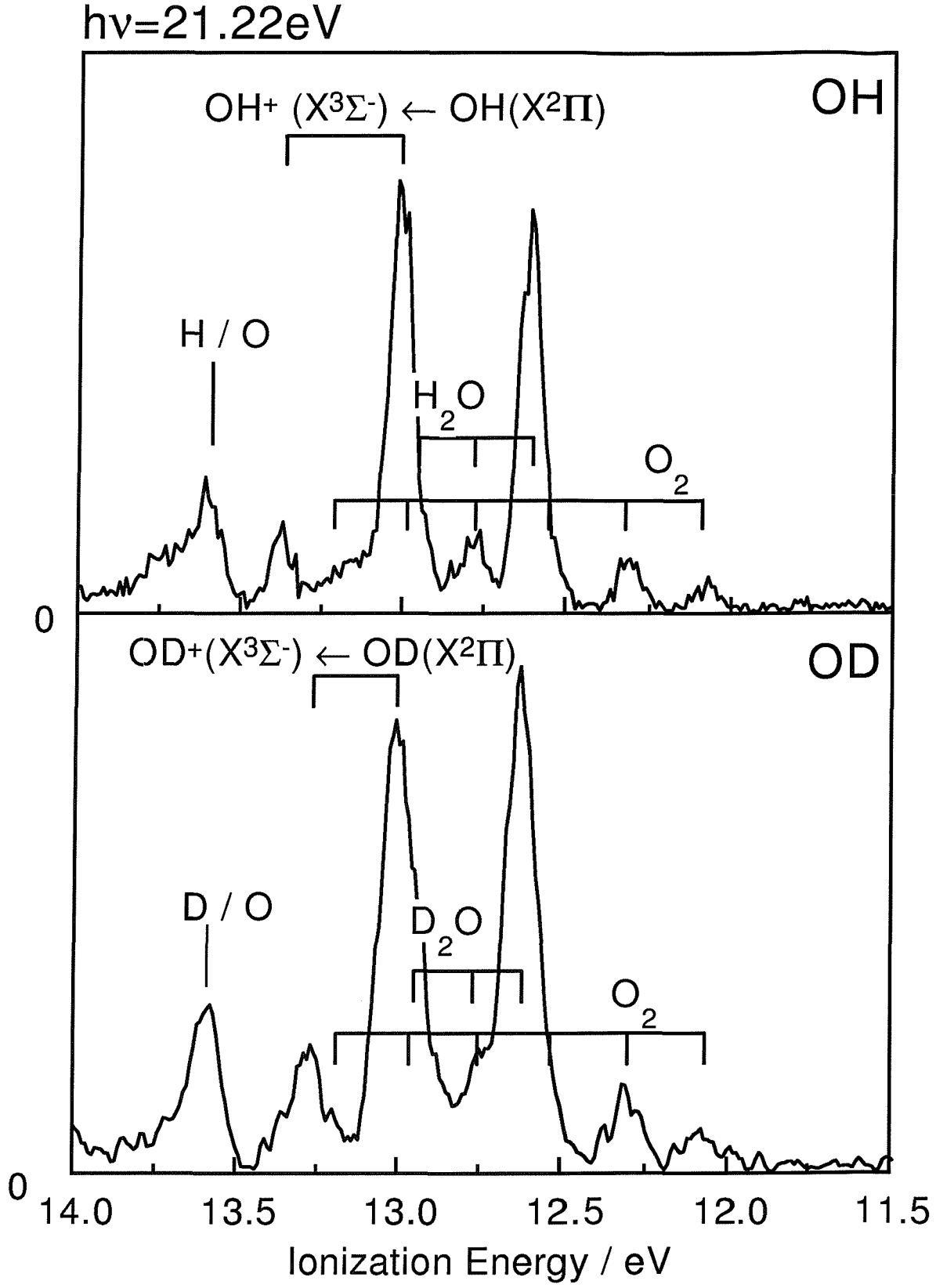

Figure 11.2: The $11.5 - 14.0\,eV$ ionization energy region of the photoelectron spectra of the discharged reaction mixtures $H_2/He + NO_2$ (upper) and $D_2/He + NO_2$ (lower), recorded at the photon energy of $21.22\,eV$.

region of energy between 11 and 12 eV. The $OH^+(X^3\Sigma^-\, v^+) \leftarrow OH(X^2\Pi\, v'' = 0)$ and $OH^+(a^1\Delta\, v^+) \leftarrow OH(X^2\Pi\, v'' = 0)$ bands are also present in this spectrum at AIEs of 13.01 and 15.17 eV respectively. The spectrum is in good agreement with that recorded by Katsumata and Lloyd [13]. Both the $OH^+(X^3\Sigma^-\, v^+) \leftarrow OH(X^2\Pi\, v'' = 0)$ band and the $OH^+(a^1\Delta\, v^+) \leftarrow OH(X^2\Pi\, v'' = 0)$ band show the $v^+ = 0$ component much stronger than the $v^+ = 1$, higher vibrational components cannot be observed, as expected from the similar potential energy curves of the $X^2\Pi$ neutral and $X^3\Sigma^-$ and $a^1\Delta$ ionic states of OH. PE bands at higher ionization energies cannot be observed due to overlap with strong bands of NO above 16 eV.

The lower part of figure 11.1 contains the spectrum recorded under the same condition as in the upper part of the figure, but with the microwave discharge turned off. Only bands from H_2 and NO_2 are present in the spectrum.

Recorded photoelectron spectra of the $D_2/He + NO_2$ mixture are very similar to the spectra in figure 11.1, and they are not presented here. The only difference is that the vibrational separations in the D_2, D_2O and OD bands are smaller than in the corresponding bands of H_2, H_2O and OH, as expected. Figure 11.2 contains the part of the PE spectra of the discharged $H_2/He + NO_2$ and $D_2/He + NO_2$ mixtures in the region of energy $11.5 - 14.0\, eV$. The first two vibrational components of the first band of OH and OD are clearly visible.

The measured vibrational separations for the first photoelectron bands of OH and OD are 0.37 and 0.26 meV respectively (2984 and 2100 cm^{-1}). They match the values known from other spectroscopic investigations [3], and their ratio matches the ratio expected from isotopic substitution.

The measured ionization energies to the $X^3\Sigma^-\, v^+ = 0$, 1 and $a^1\Delta\, v^+ = 0$ states are 13.01, 13.38 and 15.17 eV for OH and 13.01, 13.27 and 15.17 eV for OD, in agreement with the values reported in references [13] and [14].

11.3.2 CIS spectra for the $X^3\Sigma^-\, v^+ = 0$, 1 and $a^1\Delta\, v^+ = 0$ states

CIS spectra have been recorded for the $X^3\Sigma^-\, v^+ = 0, 1$ and $a^1\Delta\, v^+ = 0$ states of both OH^+ and OD^+, from threshold up to 17 eV, where Rydberg states belonging to series converging to the $b^1\Sigma^+$, $A^3\Pi$ and $c^1\Pi$ ionic states are expected.

The CIS technique cannot distinguish between different photoionization processes with the same ionization energy; therefore it is possible that bands with similar ionization energies to that investigated give rise to contamination features in the CIS spectra. From

the photoelectron spectra in figure 11.1, it is evident that the $v^+ = 0$ component of the first band of OH and OD ($13.01\,eV$) overlaps with the $v^+ = 2$ component of the third band of unreacted NO_2 ($13.02\,eV$) and is close to the $v^+ = 2$ component of the first band of H_2O ($13.07\,eV$) and to the $v^+ = 4$ component of the first band of O_2 ($12.97\,eV$). Separate CIS spectra were recorded for each of these potential contaminants over the photon energy range $13.0 - 17.0\,eV$. The CIS spectra of NO_2 and H_2O did not show any significant resolved structure. The CIS spectrum of O_2 did exhibit many sharp resonances but the most intense of these occur in the region of flat baseline in the CIS spectra of OH, therefore, the contribution of O_2 features to the CIS spectra of OH, was concluded to be negligible.

A more significant contaminant is NO, which despite displaying only six vibrational components in the first band of the $21.22\,eV$ PE spectrum, with ionization energies between 9 and $11\,eV$ [21], is known to have many sharp resonances in the $13.0 - 17.0\,eV$ photon energy region [22]. Photoelectron spectra of NO at resonant energies can extend the vibrational profile of the first band up to the onset of the second band at an AIE of $15.65\,eV$. NO was also studied by recording CIS spectra at the ionization energies used to record CIS spectra of OH and OD (13.01, 13.27, 13.38 and $15.17\,eV$). The conclusion was that NO contributes to peaks at a total of four energies in the CIS spectra of OH and OD. The peaks due to NO are marked with asterisks (*) in the CIS spectra. Apart from these features, the positions of all other peaks in the CIS spectra are in good agreement with those previously observed in PIMS spectra and so can be confidently assigned to autoionizing resonances of OH and OD.

The CIS spectra recorded for both OH and OD in the photon energy region $13.0 - 16.8\,eV$ are displayed in figures 11.3 and 11.5. The upper parts of the figures contain the spectra of OH and the lower parts those of OD; figures 11.3 and 11.5 contain portions of the spectra in the $13.00 - 15.25\,eV$ and $14.80 - 16.80\,eV$ photon energy intervals respectively. For each peak in figures 11.3 and 11.5, the effective principal quantum number n^* and quantum defect δ of the corresponding Rydberg state were calculated assuming the resonant state to be the $v' = 0$ component of a Rydberg state based on a $a^1\Delta$, $b^1\Sigma^+$, $A^3\Pi$ or c^1H ionic core. From these preliminary values of n^* and δ, two Rydberg series could be identified: one in the $13.00 - 15.25\,eV$ photon energy region, assigned as $a^1\Delta\,nd$, and the other in the $14.80 - 16.80\,eV$ photon energy region, assigned as $A^3\Pi\,nd$. The first series was identified in the PIMS work of Dehmer [19], and both series were observed and assigned in the work of Cutler *et al.* [20].

The $a^1\Delta\, nd \leftarrow X^2\Pi$ series

CIS spectra for the $X^3\Sigma^-\, v^+ = 0$ and 1 states of OH^+ and OD^+ recorded in the photon energy range $13.00 - 15.25\, eV$ are plotted in the upper and lower parts of figure 11.3 respectively.

At least five of the most intense peaks in the CIS spectra of figure 11.3 can be assigned to $v' = 0$ components of states belonging to Rydberg series converging to the $a^1\Delta$ ionic limit at $15.17\, eV$. The combs in the figure mark the positions of all the resonances assigned to this series. Peaks are assigned to vibrationally excited states on the basis of the positions expected from the known vibrational separations of the $a^1\Delta$ ionic state. All the resonances assigned to $v' = 0$ components in the OH spectra are also present at approximately the same energy in the OD spectra, and peaks assigned to $v' = 1$ components in the OH spectra are present in the OD spectra at reduced excitation energies consistent with the expected isotopic change of vibrational frequencies.

The energies of the peaks assigned to $v' = 0$ resonances and their quantum defects are listed in the upper part of table 11.2. The quantum defects are all approximately 0.05 or 1.05, suggesting excitations to either nd or $(n+1)s$ Rydberg orbitals. Both the nd and $(n+1)s$ assignments are reasonable considering that the 1π molecular orbital from which the electron is promoted is predominantly $O\,2p$ in character. The nd assignment could have been rejected if it was possible to observe a resonance with a value of n^* of approximately 1.90; this would necessarily correspond to a $3s$ orbital as a $2d$ orbital does not exist. Unfortunately, such a member would appear at an energy of approximately $11.39\, eV$, well below the AIE of the $X^3\Sigma^-\, v^+ \leftarrow X^2\Pi\, v'' = 0$ band at $13.01\, eV$, and so it is not possible to distinguish with confidence between these two assignments. Nevertheless, the nd assignment is preferred for the following reasons.

Two Rydberg states exist in OH and OD below the first ionization limit, that have been experimentally characterized by resonance enhance multiphoton ionization (REMPI) spectroscopy [9] and [10]. These states are labeled $D^2\Sigma^-$ and $3^2\Sigma^-$, and lie at energies of 10.14 and $10.46\, eV$ respectively. Ab-initio calculations of de Beer *et al.* in 1991 [9] show that, in the Franck-Condon region of the $D^2\Sigma^-$ state, the outermost orbital is of mixed $3s - 3p$ character. The quantum defect of this state is 0.82; this value is in between the quantum defects normally expected for s and p atomic orbitals, 1.0 and 0.6 respectively, and is consistent with $s - p$ mixing. The quantum defect of the $3^2\Sigma^-$ state is 0.48, which is also different from the values of δ of pure s or p orbitals. Therefore, it seems that in low lying Rydberg states strong $s - p$ mixing tends to be present in the outermost orbitals. If this conclusion is extended to the present series, values of δ noticeably different from

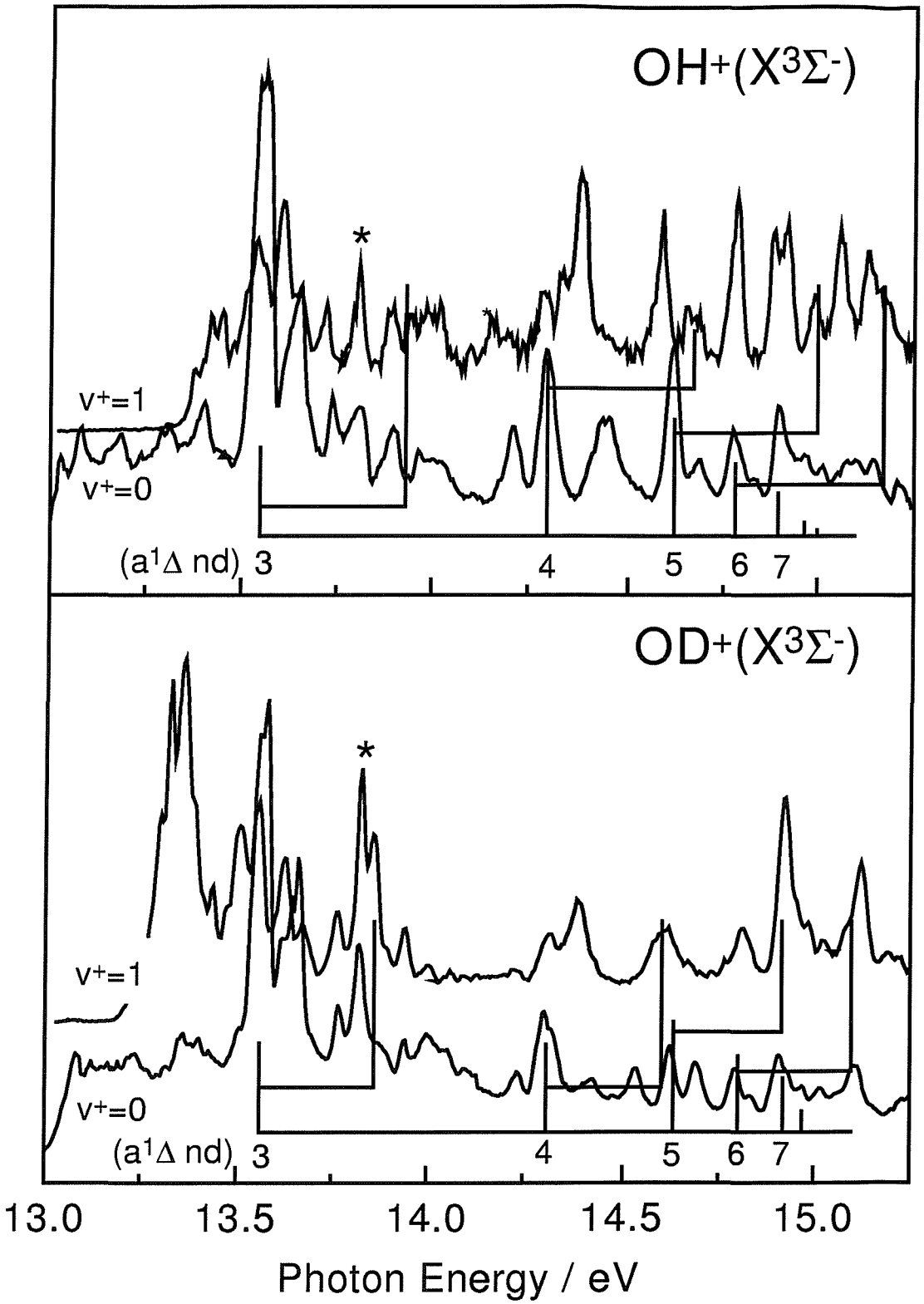

Figure 11.3: CIS spectra for the $X^3\Sigma^-$ v^+0 = and 1 states of OH^+ and OD^+. Peaks which may due to NO resonances are marked with an asterisk (*). The positions and assignments of OH^* and OD^* $v' = 0$ and 1 resonances are indicated for each Rydberg state.

Ionic core	Rydberg orbital	Energy	n^*	Quantum defect δ
$a^1\Delta$	3d	13.550	2.90	0.10
	4d	14.300	3.95	0.07
	5d	14.620	4.97	0.03
	6d	14.785	5.94	0.06
	7d	14.895	6.97	0.03
$A^3\Pi$	3d	14.88	2.92	0.08
	4d	15.61	3.95	0.05
	5d	15.93	4.97	0.03
	6d	16.10	5.98	0.02
	7d	16.20	6.97	0.02

Table 11.2: Resonances in the CIS spectra of OH and OD assigned to $v' = 0$ components of states belonging to Rydberg series.

1 should be expected for the $(n+1)s$ orbitals. As the extracted quantum defects are approximately 1.05, or 0.05, the nd assignment is preferred.

It is interesting to study the vibrational envelopes in the CIS spectra in figure 11.3. Vibrational envelopes in the CIS spectra were simulated by performing calculations of FCFs for the photoexcitation

$$OH^*(a^1\Delta\, nl\, v') \leftarrow OH(X^2\Pi\, v'' = 0) + h\nu, \tag{11.4}$$

and for the autoionization processes

$$OH^*(a^1\Delta\, nl\, v') \rightarrow OH^+(X^2\Sigma^-\, v^+ = 0\, or\, 1) + e^-. \tag{11.5}$$

FCFs were calculated for both OH and OD. Morse potentials were assumed for all the states, using the spectroscopic parameters from references [3]. The computed profiles were obtained by multiplying together the FCFs for the two steps (11.4) and (11.5) and are shown in figure 11.4. From these calculations, it seems that the $v^+ = 0$ ($v^+ = 1$) CIS spectra of both OH and OD should contain only the $v' = 0$ ($v' = 1$) component. This is a consequence of the fact that the potential energy curves of both the $X^3\Sigma^-$ and $a^1\Delta$ ionic states are very similar to that of the $X^2\Pi$ state of the neutral, as they result from ionization from a non bonding orbital.

Unfortunately, due to the presence of overlapping resonances and high background, it is not possible to reach definitive conclusions regarding the experimental vibrational profiles. Nevertheless, it seems that the $v' = 0$ and 1 components appear strong and weak

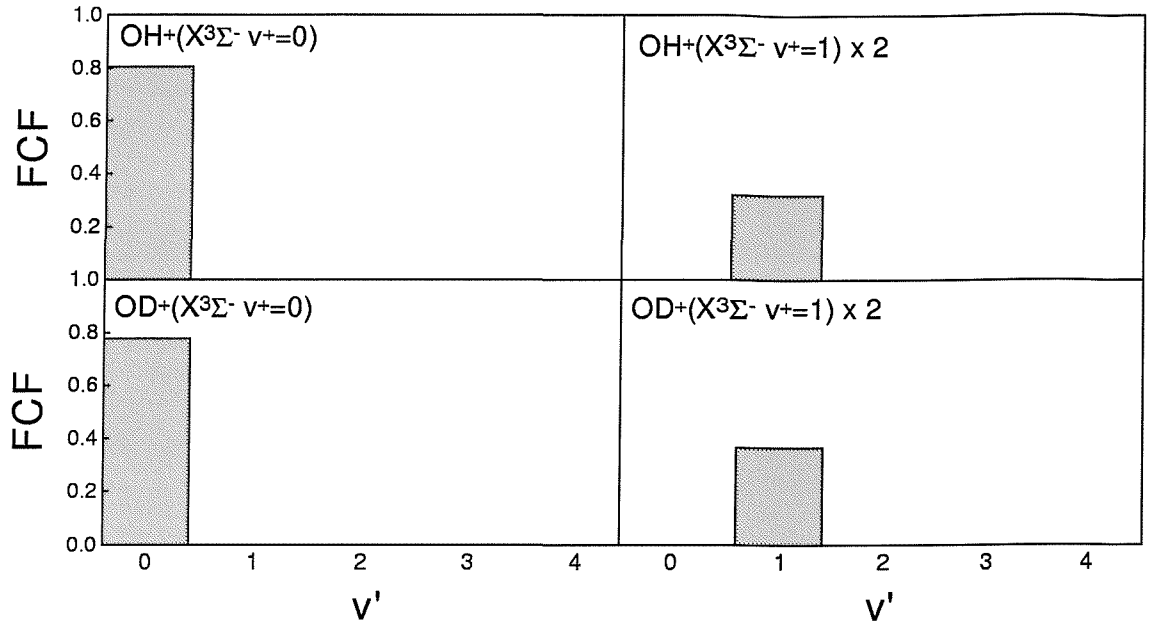

Figure 11.4: Simulation of vibrational profiles in the CIS spectra of the $X^3\Sigma^-$ $v^+ = 0$ and 1 states for autoionization via the $a^1\Delta\, nlv'$ states.

respectively in the $v^+ = 0$ CIS spectra, and the opposite is true in the $v^+ = 1$ CIS spectra. This is true for the $n = 4$, 5 and 6 members of the series, for both OH and OD. However, despite the presence of a strong signal at $14.55\,eV$, assigned to the $A^3\Pi\, 3d\, v' = 0$ state, no strong signal is present at the corresponding $v' = 1$ position in the $v^+ = 1$ CIS spectra. Even more difficult to explain is that in the $v^+ = 1$ CIS spectra of OD, the $A^3\Pi\, 3d\, v' = 0$ resonance is stronger than the $A^3\Pi\, 3d\, v' = 1$ peak. These facts are not consistent with what is expected from the calculated FCFs.

The series assigned as $a^1\Delta\, nd$ results in $(a^1\Delta\, nd\sigma)^2\Delta$, $(a^1\Delta\, nd\pi)^2\Pi$ and $(a^1\Delta\, nd\delta)^2\Sigma^\pm$ states, which are all accessible from the $X^2\Pi$ state. However, in the present investigation the photon energy resolution was of the order of $10\,meV$, and the components at different energies resulting from different angular momentum coupling could not be resolved.

The $A^3\Pi\, nd \leftarrow X^2\Pi$ series

CIS spectra for the $X^3\Sigma^-$ $v^+ = 0, 1$ and $a^1\Delta\, v^+ = 0$ states of OH and OD in the photon energy range $14.8 - 16.8\,eV$ are plotted in the upper and lower parts of figure 11.5 respectively. From the energy of each peak, the value of n^* has been extracted assuming an $A^3\Pi$ ionic core at an AIE of $16.48\,eV$, and from a selection of these values a Rydberg series converging to the $A^3\Pi$ ionic limit has been identified. The energies of these resonances, together with their assignments, are listed in the lower part of table 11.2. As was made for the $a^1\Delta\, nd$ series, from their effective principal quantum numbers these resonances could be assigned either to an $A^3\Pi\, nd$ or to an $A^3\Pi\,(n+1)s$ series, with quantum defects δ of

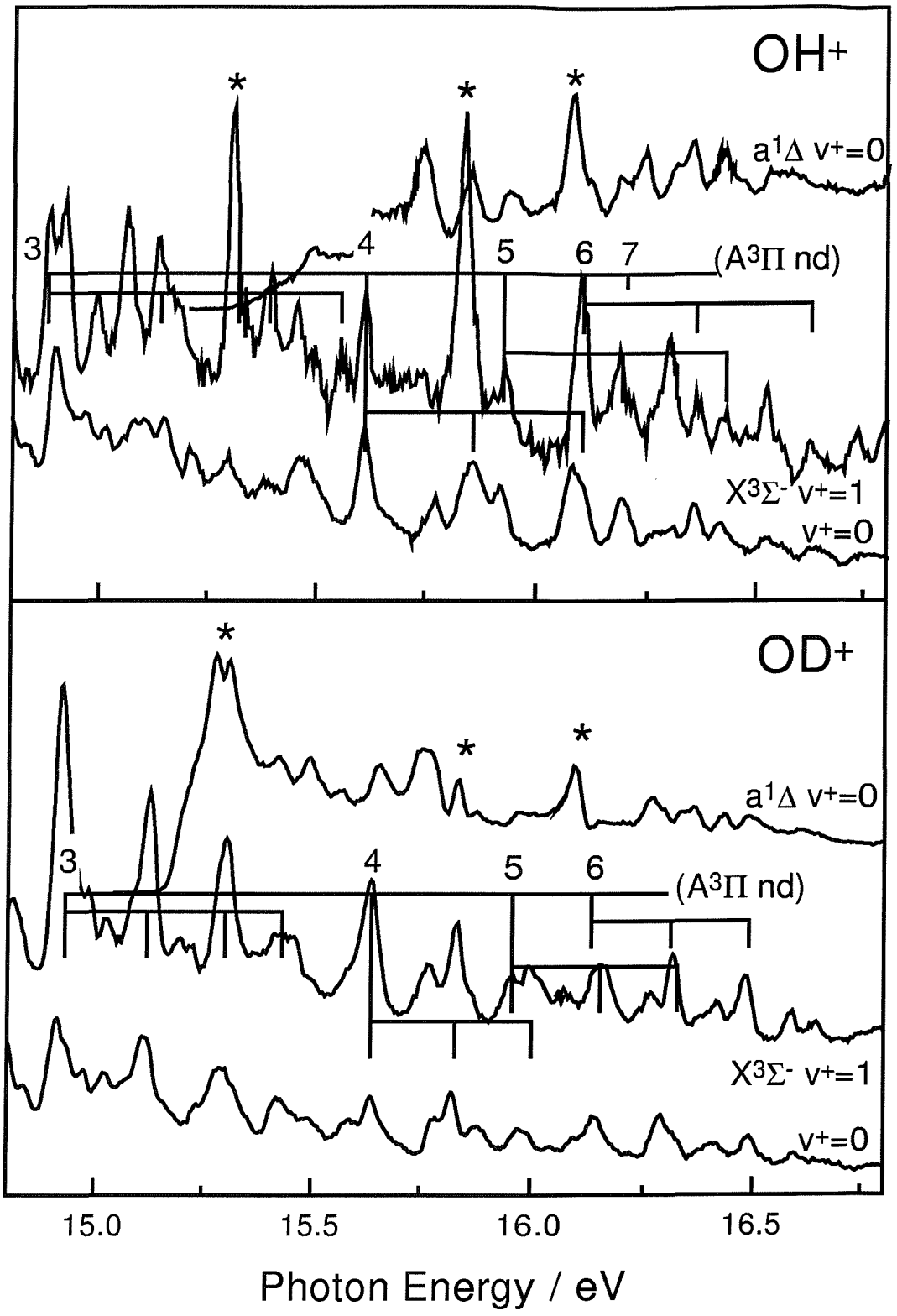

Figure 11.5: CIS spectra for the $X^3\Sigma^-$ $v^+ = 0$, 1 and $a^1\Delta$ $v^+ = 0$ states of OH^+ and OD^+. Peaks which may due to NO resonances are marked with an asterisk (*). The positions and assignments of OH^* and OD^* $v' = 0$, 1, 2 and 3 resonances are indicated for each Rydberg state.

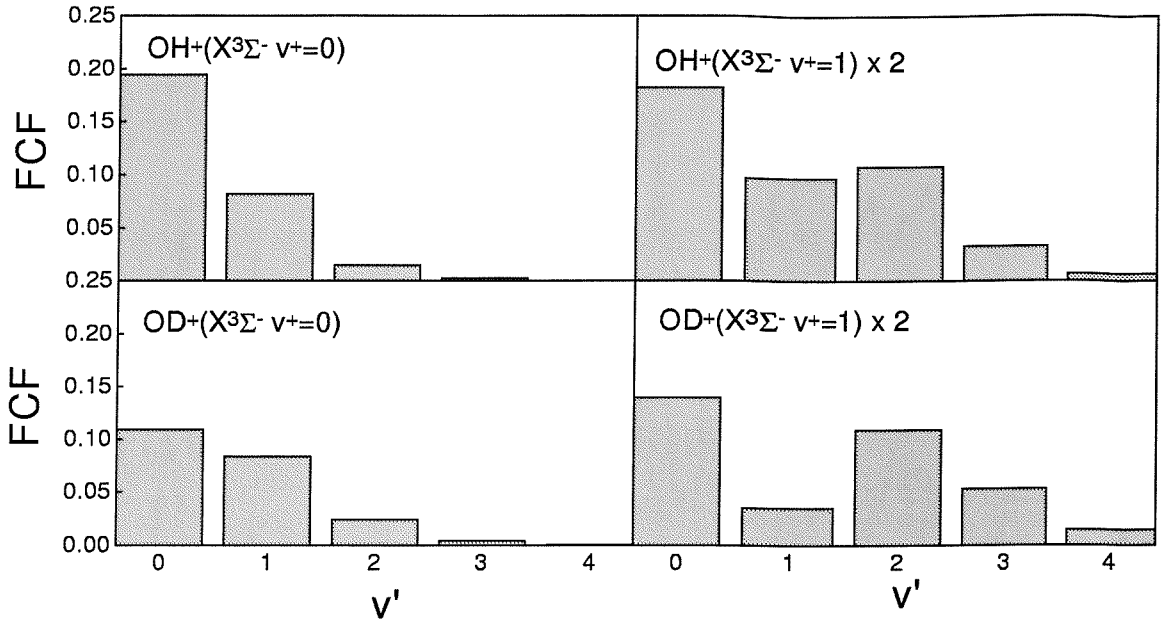

Figure 11.6: Simulation of vibrational profiles in the CIS spectra for the $X^3\Sigma^-$ $v^+ = 0$, 1 band for autoionization via the $A^3\Pi\, nlv'$ states.

approximately 0.03 or 1.03 respectively. The energies of these resonances (14.88, 15.61, 15.93, 16.10 and 16.20 eV) are very close to those calculated by adding the $A^3\Pi$-$a^1\Delta$ separation (1.31 eV) to the main components of the $a^1\Delta\, nd$ series in the upper part of table 11.2 (14.86, 15.61, 15.93, 16.09 and 16.20 eV), and therefore the nd assignment is preferred.

It must be mentioned that in this photon energy region, Rydberg states built on a $b^1\Sigma^+$ ionic core are also expected. However, the resonances present in the spectra of figure 11.5 are assigned to $A^3\Pi\, nl$ states because Rydberg states built on a $b^1\Sigma^+$ ionic core would result in diagonal vibrational profiles in the CIS spectra, while here several vibrational components are present for each member of the $A^3\Pi\, nd$ series (see later).

It is useful to compare the CIS spectra of OH and OD in figure 11.5. All the main $A^3\Pi\, nd$ excited state features present in the OH spectra are also present in the OD spectra. Peaks assigned to $v' = 0$ resonances in the OH spectra are observed at approximately the same energies in the OD spectra, and peaks assigned to $v' = 1$, 2 and 3 resonances in the OH spectra are present in the OD spectra at reduced energies consistent with the expected isotopic changes of vibrational frequencies. This supports the assignments in both the OH and OD CIS spectra.

The vibrational profiles in the CIS spectra of figure 11.5 have been simulated with FCF calculations, assuming autoionization from Rydberg states with an $A^3\Pi$ ionic core, and are shown in figures 11.6. Morse potentials were assumed for all the states, with the r_e, ω_e and $\omega_e x_e$ parameters being taken from reference [3].

In the emission study of the $A^3\Pi \rightarrow X^3\Sigma^-$ band of reference [18], vibrationally excited components of $A^3\Pi\, nd$ states, with n from 3 to 6, were observed, and they have frequencies very close to that of the $A^3\Pi$ ionic state ($245\, meV = 1974\, cm^{-1}$). Many of these vibrational features overlap with other members of the $A^3\Pi\, nd$ series, with members of the earlier $a^1\Delta\, nd$ series, and in this work also with NO contaminating bands. As a result, it is difficult to estimate the vibrational envelope of a single member of the Rydberg series. Nevertheless, it is clear that in the $X^3\Sigma^-\, v^+ = 0$ CIS spectrum of OH, three vibrational components are present for the $A^3\Pi\, 3d$ member, that are free from overlap; they show a steady decrease in intensity and the first component is much stronger than the other.

Also the $A^3\Pi\, 4d$ and $A^3\Pi\, 5d$ members are relatively free from overlap, and three vibrational components are present for each of them with intensity ratios close to the simulated FCFs. In the $X^3\Sigma^-\, v^+ = 0$ spectrum of OD four vibrational components are present for the $A^3\Pi\, 3d$ member, with the $v' = 2$ and 3 stronger than expected from the FCF simulation. For the $A^3\Pi\, 4d$ member the relative intensities of the three components are in good agreement with the FCF simulation.

The $A^3\Pi\, 3d\, v'$ are the only members of this series, in the $X^3\Sigma^-\, v^+ = 1$ CIS spectrum of OH, that are clearly free from overlap. They show a steady drop in intensity over the $v' = 0 - 3$ vibrational components, in reasonable but not good agreement with the FCF simulation.

In the $X^3\Sigma^-\, v^+ = 1$ CIS spectrum of OD four and three vibrational components are clearly seen for the $A^3\Pi\, 3d$ and $A^3\Pi\, 4d$ members, all reasonably free from overlap. For both members the relative intensities of the $v' = 1$ and 2 components are respectively stronger and weaker than expected.

The potential energy curves of the $X^3\Sigma^-$ and $a^1\Delta$ ionic states are similar to each other, and as a consequence, bands in the CIS spectra for these two states should exhibit similar vibrational profiles, at least for those levels that autoionize to both states. Calculations of FCFs for ionization to the $a^1\Delta$ state have not been executed, as very little new information is expected to be gained from them. The $a^1\Delta\, v^+ = 0$ CIS spectra of both OH and OD are also displayed in figure 11.5 and show significant structure. The positions of most resonances coincide with those already assigned in the $X^3\Sigma\, v^+ = 0$ CIS spectra as members of the $A^3\Pi\, nd$ series. Despite this general agreement, the $a^1\Delta\, v^+ = 0$ and $X^3\Sigma^-\, v^+ = 0$ CIS spectra do differ in detail, and the exact reason for these differences is not clear at the present time.

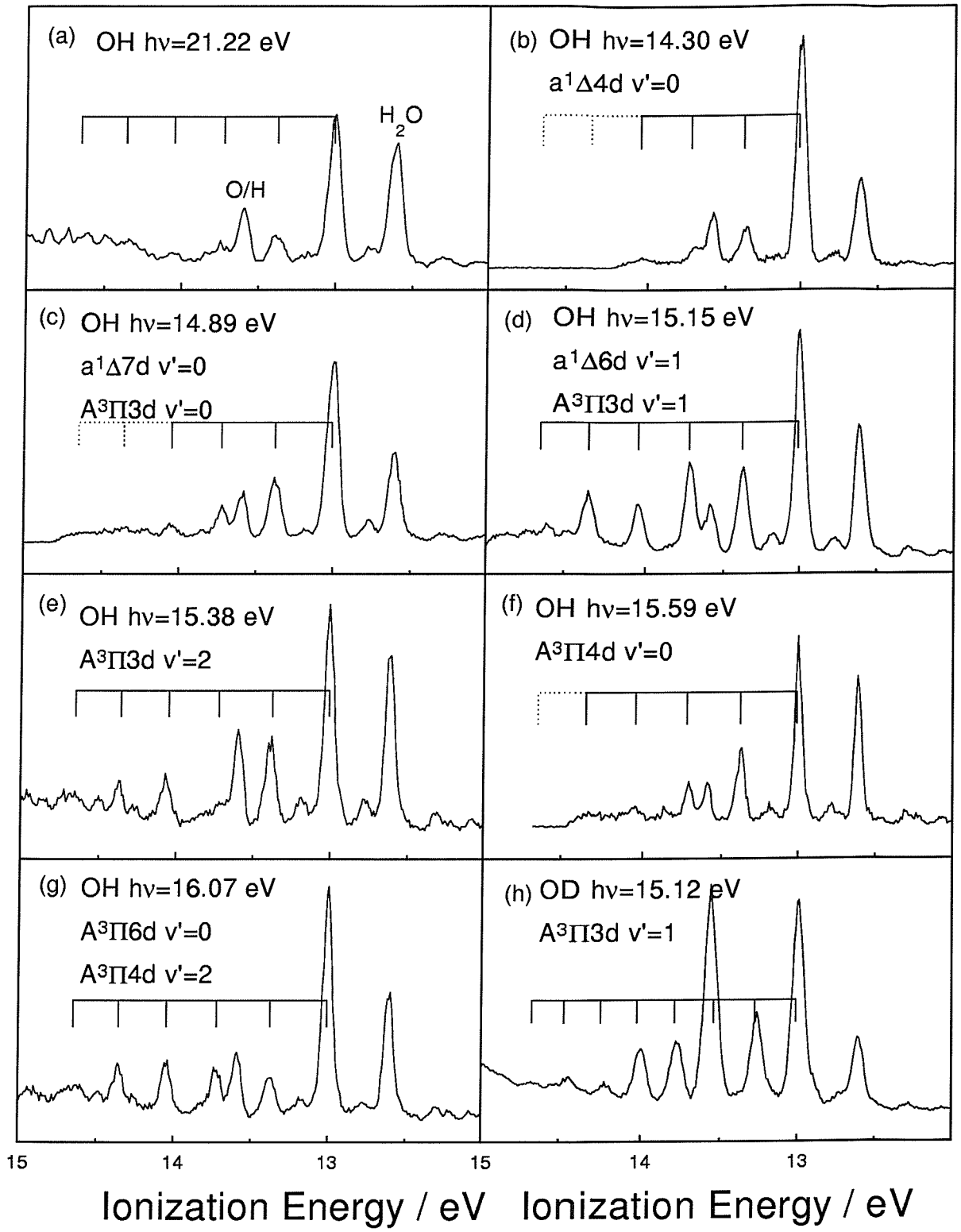

Figure 11.7: Photoelectron spectra showing the $X^3\Sigma^- v^+ \leftarrow X^2\Pi\, v'' = 0$ band of OH (a)-(g) and OD (h). The positions of expected vibrational components, as calculated from known vibrational frequencies, are indicated by the combs.

11.3.3 Resonant photoelectron spectra

Photoelectron spectra were recorded at wavelengths corresponding to resonances observed in the CIS spectra. The spectra showing the $X^3\Sigma^- v^+ \leftarrow X^2\Pi\, v'' = 0$ band of OH and OD that are considered most interesting are shown in figure 11.7. The spectrum 11.7(a) is a typical photoelectron spectrum of OH recorded at the non resonant photon energy of $21.22\,eV$. Spectra 11.7(b) to 11.7(h) contain photoelectron spectra of OH or OD recorded at resonant photon energies. In all these spectra, the combs mark the positions of the vibrational components of the $X^3\Sigma^-$ state, up to $v^+ = 5$ for OH and $v^+ = 7$ for OD, known from other spectroscopic investigations [3]. In all these spectra the first band of H_2O at an AIE of $12.62\,eV$ is also present, its $v^+ = 0$ component was always approximately constant in intensity and the change in intensity of the OH and OD bands can be estimated relatively to this band.

To help the understanding of the resonant contribution to the photoelectron spectra shown in figure 11.7, these spectra were simulated with the calculations of FCFs for autoionization of Rydberg states based on the $a^1\Delta$ and $A^3\Pi$ ionic cores, shown in figures 11.8 and 11.9 respectively. The FCF simulations for OH and OD are virtually identical for autoionization from the $a^1\Delta\, nl\, v'$ resonances, and are very similar for autoionization from the $A^3\Pi\, nl\, v'$ states. The $a^1\Delta\, nd$ states give diagonal vibrational branching ratios: the autoionization proceeds without change in vibrational components. This was expected because both the $a^1\Delta$ and the $X^3\Sigma^-$ states arise from ionization of a non bonding 1π orbital and have very similar potential energy curves. In contrast, in the autoionization from the $A^3\Pi$ state several vibrational components have appreciable intensities. This was also expected, because the $A^3\Pi$ state arises from ionization of a 3σ bonding orbital and thus its potential energy curve is very different from that of the $X^3\Sigma^-$ state.

In comparing the FCFs in figure 11.8 and 11.9 with the resonant photoelectron spectra in figure 11.7, it must be remembered that the FCF simulations do not include the direct photoionization contribution. The direct contribution is expected to make the vibrational profiles to appear less diagonal for $a^1\Delta\, nl$ resonances, and this effect is not negligible as the intensities of most resonances in the CIS spectra are comparable to that of the non resonant process.

The spectrum 11.7(b) shows the PE spectrum of OH via the $a^1\Delta\, 4d\, v' = 0$ resonant state, that in the CIS spectra seems to be free from overlap. As expected, the $v^+ = 0$ component is considerably enhanced; however, in contrast to the FCF simulation, also the $v^+ = 1$ component is increased.

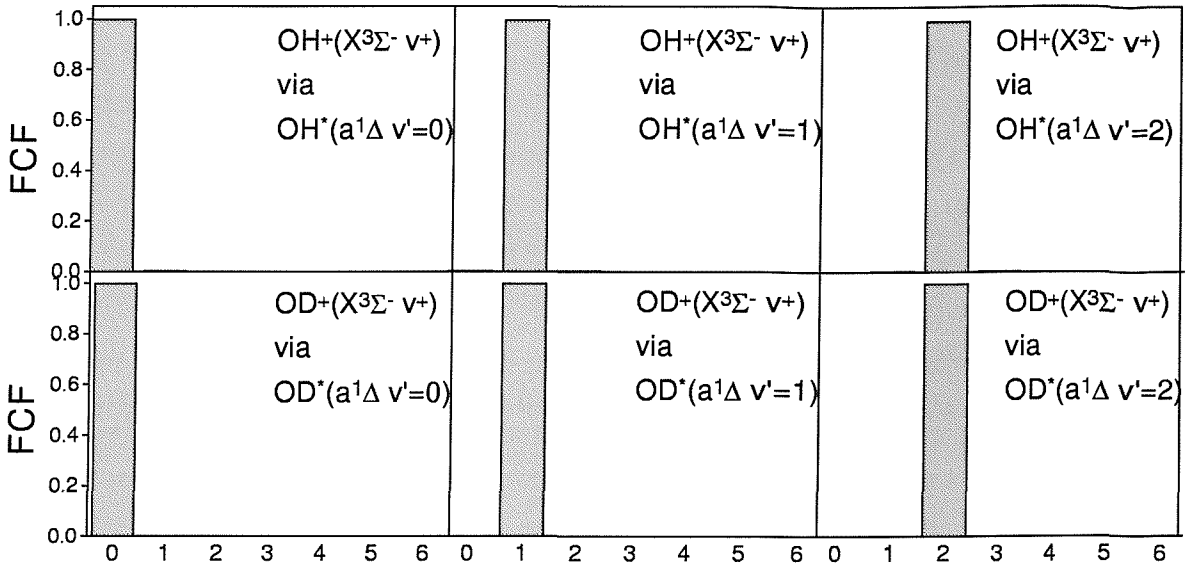

Figure 11.8: Computed FCFs for the $X^3\Sigma^- v^+ \leftarrow X^2\Pi\, v'' = 0$ photoionization process via $a^1\Delta\, nlv'$ resonances.

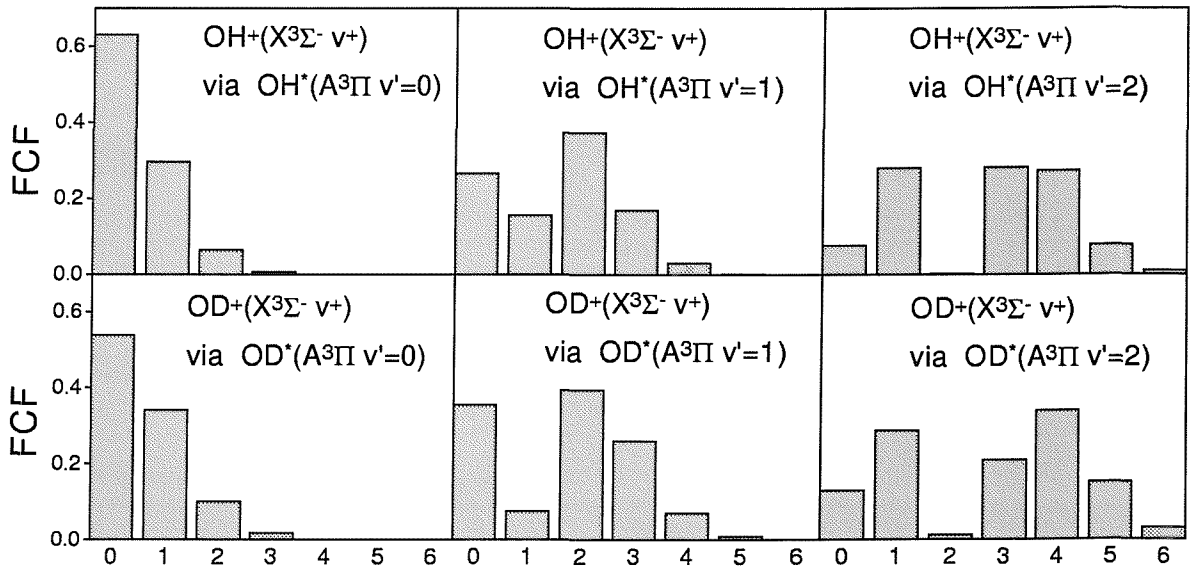

Figure 11.9: Computed FCFs for the $X^3\Sigma^- v^+ \leftarrow X^2\Pi\, v'' = 0$ photoionization process via $A^3\Pi\, nlv'$ resonances.

The spectrum 11.7(c) proceeds via the unresolved resonances assigned as $a^1\Delta\, 7d\, v' = 0$ and $A^3\Pi\, 3d\, v' = 0$. The vibrational envelope in the PE spectra shows the $v^+ = 0 - 3$ components decreasing in intensity, with the $v^+ = 0$ component much stronger than the others, in good agreement with the FCF simulation of autoionization of a $A^3\Pi\, nl\, v' = 0$ state. Therefore, of the two unresolved resonances at this photon energy, the $A^3\Pi\, 3d\, v' = 0$ contribution is probably stronger.

The spectrum 11.7(d) was recorded at a wavelength resonant with the unresolved $a^1\Delta\, 6d\, v' = 1$ and $A^3\Pi\, 3d\, v' = 1$ states. The $v^+ = 2$, 3 and 4 components are increased more than the $v^+ = 1$ component, in closer agreement with the simulation for autoionization of the $A^3\Pi\, nl\, v' = 1$ state rather than of the $a^1\Delta\, 6d\, v' = 1$ state. Therefore, the contribution from the $A^3\Pi\, nl\, v' = 1$ state is probably stronger.

The spectra 11.7(e) and 11.7(f) proceed via isolated resonances, assigned as $A^3\Pi\, 3d\, v' = 2$ and $A^3\Pi\, 4d\, v' = 0$ respectively. The spectrum 11.7(e) shows components up to $v^+ = 5$, with the $v^+ = 2$ component much weaker than all the others. The $v^+ = 0$ component is the most intense and the $v^+ = 4$ and 5 components are weak and of comparable intensity. The spectrum 11.7(f) shows five vibrational components, decreasing in intensity from $v^+ = 0$ to 4, with the $v^+ = 2$ and 3 components very weak. These relative intensities are in good agreement with the results of FCF calculations shown in figure 11.9.

In the spectrum 11.7(g), recorded at a wavelength resonant with the unresolved $A^3\Pi\, 6d\, v' = 0$ and $A^3\Pi\, 4d\, v' = 2$ states, all the vibrational components up to the $v^+ = 5$ are present. The $v^+ = 2$ component is stronger than $v^+ = 1$ and of similar intensity to the $v^+ = 3$ component, in disagreement with the calculations for autoionization from both the $A^3\Pi\, 6d\, v' = 0$ and $A^3\Pi\, 4d\, v' = 2$ resonances. The intensity of the $v^+ = 0$ component is increased more than the intensity of the $v^+ = 1$ component, in closer agreement with the simulation of autoionization from the $A^3\Pi\, 6d\, v' = 0$ state, that therefore is likely to provide the stronger contribution.

The spectrum 11.7(h) shows the first band of OD recorded at the photon energy resonant with the $A^3\Pi\, 3d\, v' = 1$ state. All the vibrational components up to $v^+ = 7$ are present. The $v^+ = 0$ and 2 components are particularly enhanced, much more than the $v^+ = 1$ component, in agreement with the corresponding FCF simulation. However, the enhancement of the $v^+ = 2$ and $v^+ = 4 - 7$ components are respectively less and more than predicted.

11.3.4 Other resonances in the CIS spectra

There are resonances in the CIS spectra of OH and OD that cannot be assigned to members of the $a^1\Delta\, nd$ or $A^3\Pi\, nd$ series. These features were also observed in both the PIMS investigations [19] and [20], but were not assigned. The most intense unassigned resonances are at 14.785 and 15.06 eV in the $OH^+(X^3\Sigma^-\, v^+ = 1)$ CIS spectrum, and are also observed less strongly in the corresponding $v^+ = 0$ spectrum; at 14.21 and 14.44 eV in the $OH^+(X^3\Sigma^-\, v^+ = 1)$ CIS spectrum at 14.39 and 14.59 eV in the $OH^+(X^3\Sigma^-\, v^+ = 1)$ CIS spectrum. These six resonances are marked in figure 11.10.

The separation between the resonances at 14.785 and 15.06 eV is close to the vibrational frequency of the $A^3\Pi$ state of OH^+, and assuming the resonance at lower energy to be a $v^+ = 0$ component, n^* for this state would be 2.83, consistent with $3d$ ($\delta = 0.17$) or $4s$ ($\delta = 1.17$) Rydberg orbital assignments. The FCF simulation suggests that the $v^+ = 2$ component should be observable in the $OH^+(X^3\Sigma^-\, v^+ = 1)$ CIS spectrum, but in the measured spectrum it is probably masked by the strong NO feature at 15.30 eV. The photoelectron spectra recorded at 14.785 and 15.06 eV, that are not included here, show extended vibrational profiles, in support of the assignments of these two features as $A^3\Pi\, nl\, v' = 0$ and 1. The CIS spectra of OD exhibit corresponding peaks at the appropriately reduced energies.

It is difficult to identify the character of the Rydberg orbital of these resonances. If the resonance at 14.785 eV was a $A^3\mathrm{H}\, 4s$ state, then the $s-p$ mixing discussed before would be expected to make the value of δ significantly different from 1, and for this reason the $A^3\Pi\, n\tilde{d}$ assignment is preferred. The most favoured interpretation is that this resonance corresponds to a state that arises because the $3d$ orbitals in the $C_{\infty v}$ group split in $3d\sigma$, $3d\pi$ and $3d\delta$ components and each configuration $A^3\Pi\, 3d\lambda$ gives rise to more than one state. For this reason this orbital is labeled $\tilde{d}$.

The spacings between the peaks at 14.21 and 14.39 eV, and those at 14.44 and 14.59 eV, are less than the vibrational frequencies in any known state of OH^+. The peaks in the $v^+ = 0$ CIS spectra at 14.21 and 14.44 eV are appropriately positioned to be $v' = 0$ components associated with the $v' = 1$ components present in the $v^+ = 1$ CIS spectrum at 14.59 and 14.785 eV. The only ionic core that would give diagonal FCFs in this energy region is the $b^1\Sigma^+$, and this assignment gives values of n^* of 2.38 and 2.50, which could indicate $b^1\Sigma^+\, 3p\sigma$ and $b^1\Sigma^+\, 3p\pi$ Rydberg states. However, this assignment is inconsistent with the CIS spectra of OD where the 14.21, 14.39 and 14.59 resonances remain approximately at the same energies, suggesting that they are all $v' = 0$ components. If this is the case, the absence of strong peaks in the $v^+ = 0$ CIS spectrum at energies corresponding

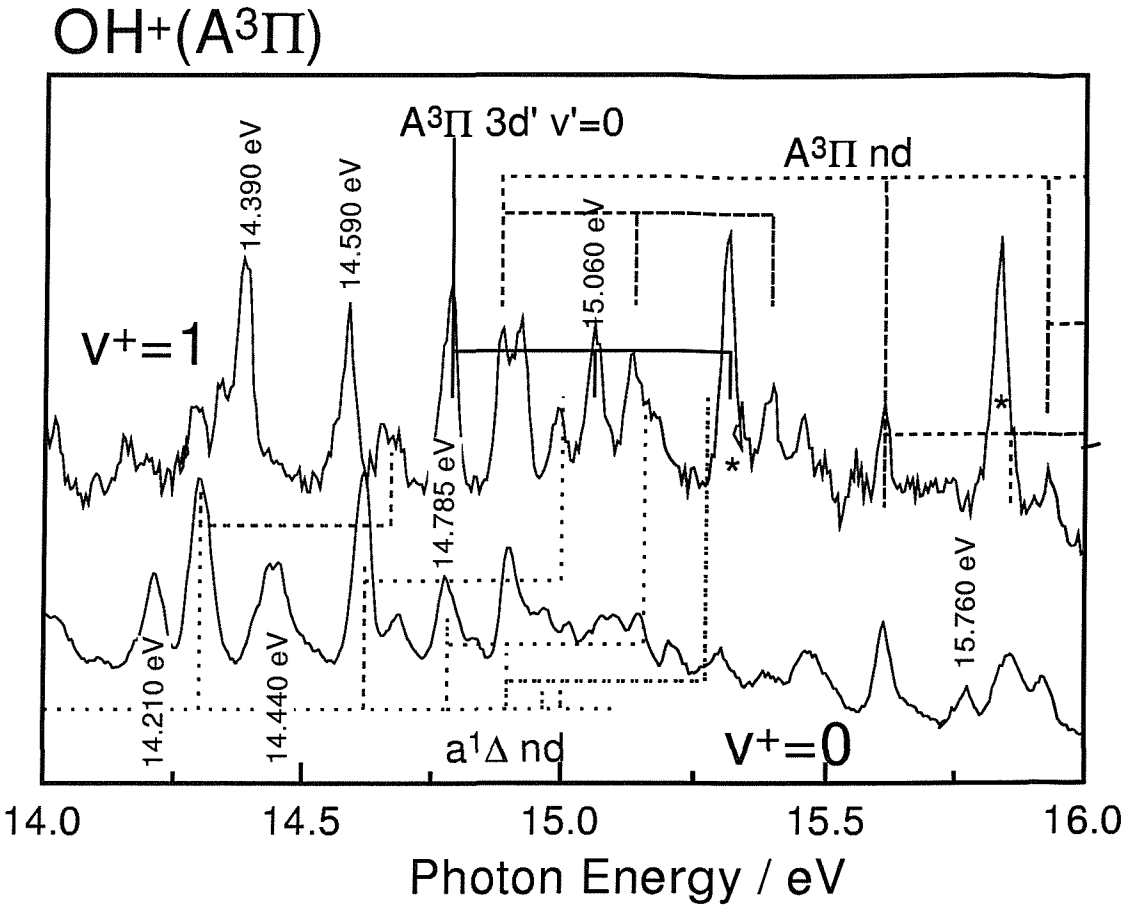

Figure 11.10: CIS spectra of the $X^3\Sigma^-$ $v^+ = 0$ and 1 states of OH^+. The solid combs mark resonances assigned to the $A^3\Pi\, n\tilde{d}$ series.

to the 14.39 and 14.59 eV peaks in the $v^+ = 1$ CIS spectrum is difficult to rationalise, because for Rydberg states built on any known ionic core of OH^+, the $v' = 0$ component should autoionize to the $v^+ = 0$ level at least as strongly as to the $v^+ = 1$ level.

Photoelectron spectra of OH were recorded at the energies of each unassigned resonances, and the vibrational envelopes were found to be significantly differently from each other. The conclusion is that there is no Rydberg state assignments for the 14.21, 14.39, 14.44 and 14.59 eV resonances that is consistent with the experimental evidence. This is not unrealistic as the presence of several valence states of OH was suggested in this energy region by the ab-initio calculations [7], and [8].

In the PIMS work of Cutler *et al.* [20], resonances at 13.18, 15.07, 15.57 and 16.07 eV were assigned to $v' = 0$ components of a $b^1\Sigma^+\, ns$ series. All these resonances are present also in the CIS spectra of this work, but this assignment cannot be confirmed in the present work. However, the peak at 13.18 eV is very weak. The peak at 15.07 eV is present in the $v^+ = 1$ CIS spectrum, which is inconsistent with the $b^1\Sigma^+\, nl\, v' = 0$ assignment. The peak at 15.75 eV is present in the $v^+ = 0$ CIS spectrum but not in the $v^+ = 1$ spectrum, and this would be consistent with a $b^1\Sigma^+\, nl\, v' = 0$ assignment. The peak at 16.07 eV is

coincident with the peaks assigned as $A^3\Pi\, 4d\, v' = 2$ and $A^3\Pi\, 6d\, v' = 0$. Consequently, the only resonance that could be assigned to a $b^1\Sigma^+\, nl$ Rydberg state is the peak at $15.75\, eV$, that would correspond to the $v' = 0$ component of either a $b^1\Sigma^+\, 5s$ ($\delta \simeq 1.00$), or a $b^1\Sigma^+\, 4d$ ($\delta \simeq 0.00$) state.

11.4 Conclusions

Photoelectron spectroscopy of OH and OD with synchrotron radiation has been performed in the region of the 1π and 3σ ionizations. Vibrationally resolved CIS spectra for the $X^3\Sigma^-\, v^+ = 0$, 1 and $a^1\Delta\, v^+ = 0$ states have been recorded in the $13.0 - 17.0\, eV$ photon energy region at a fixed angle of observation. Most of the resonances in these spectra have been assigned in terms of Rydberg states belonging to series converging to the $a^1\Delta$ and $A^3\Pi$ ionic states. The vibrational specificity of the CIS technique allowed the vibrationally excited components of autoionizing states to be identified. The vibrational profiles in CIS spectra are in reasonable but not good agreement with their simulations via calculations of FCFs.

Photoelectron spectra of OH and OD, in the region of the first photoelectron band, have been recorded at resonant wavelengths. The measured vibrational branching ratios partly agree with the vibrational profiles obtained from the FCF calculations. Up to the $v^+ = 5$ and 7 vibrational components are observed in resonant photoelectron spectra of OH and OD respectively.

Four resonances present in the CIS spectra cannot be assigned as members of Rydberg series, and probably correspond to excitations to valence states.

A natural extension of this work would be to investigate the angular momentum composition of the photoelectrons from the first bands of OH and OD by measuring angle resolved PE and CIS spectra. Although evidence for different states that arise from the different coupling of the angular momentum of the Rydberg orbital with the ionic core has been found, this is an issue that would be interesting to investigate more in depth. This may be achievable using high resolution radiation available from a third generation synchrotron radiation source.

Bibliography

[1] JD Barr, A De Fanis, JM Dyke, SD Gamblin, N Hooper, A Morris, S Stranges, JB West and TG Wright, *Journal of Chemical Physics*, **110** 345-354 (1998).

[2] Chemistry of Atmosphere.
RP Wayne, Clarendon Press, Oxford (1969).

[3] Molecular Spectra and Molecular Structure *IV*. Constants of Diatomic Molecules.
KP Huber and G Herzberg, Van Nostrand Reinhold Company, New York (1979).

[4] AE Douglas, *Canadian Journal of Physics*, **52** 318-323 (1974).

[5] JC Viney, *Journal of Molecular Spectroscopy*, **83** 465-468 (1980).

[6] JB Nee and LC Lee, *Journal of Chemical Physics*, **81**, 31-36 (1984).

[7] I Easson and MHL Price, *Canadian Journal of Physics*, **51** 518-529 (1973).

[8] E van Dishoek and A Dalgarno, *Journal of Chemical Physics*, **79** 873-888 (1983).
E van Dishoek, SR Langhoff and A Dalgarno, *Journal of Chemical Physics*, **78** 4552-4561 (1983).

[9] E de Beer, CA de Lange, JA Stephens, Kwanghsi Wang and V McKoy, *Journal of Chemical Physics*, **95** 714-716 (1991).

[10] M Collard, P Kerwin and A Hodgson, *Chemical Physics Letters*, **179** 422-428 (1991).

[11] JA Stephens and V McKoy, *Physical Review Letters*, **62** 889-892 (1989).

[12] RT Wiedmann, RG Tonkyn and MG White, *Journal of Chemical Physics*, **97** 768-772 (1992).

[13] S Katsumata and DR Lloyd, *Chemical Physics Letters*, **45** 519-522 (1977).

[14] H van Lonkhuyzen and CA de Lange, *Molecular Physics*, **51** 551-568 (1984).

[15] DJ Rodgers and PJ Sarre, *Chemical Physics Letters*, **143** 235-239 (1988).

[16] DM Hirst and MF Guest, *Molecular Physics*, **49** 1461-1469 (1983).

[17] RP Saxon and B Liu, *Journal of Chemical Physics*, **85** 2099-2104 (1986).

[18] AJ Merer, DN Malm, RW Martin, M Horani and J Rostas, *Canadian Journal of Physics*, **53** 251-283 (1975).

[19] PM Dehmer, *Chemical Physics Letters*, **110** 79-84 (1984).

[20] JN Cutler, ZX He and JAR Samson, *Journal of Physics B: Atomic, Molecular and Optical Physics*, **28** 4577-4591 (1995).

[21] Handbook of HeI Photoelectron Spectra of Fundamental organic molecules. K Kimura, S Katsumata, Y Achiba, T Yamazaki and S Iwata, Japan Scientific Societies Press, Tokyo (1981).

[22] P Erman, A Karawajczyk, E Rachlew-Källne and C Strömholm, *Journal of Chemical Physics*, **102** 3064-3076 (1995).

Chapter 12

Summary and future work

12.1 Summary

In the introduction of this thesis it was stated that the original plan of this work was to make progress in two areas of photoelectron spectroscopy with synchrotron radiation: DPI of alkaline earth atoms in the vapour phase and photoelectron spectroscopy of reactive intermediates.

Measurements of TDCS for double photoionization of the outermost s^2 electrons in atomic Ca and Sr have been collected. Most of the measurements of TDCS for direct DPI have been recorded at the Daresbury SRS using resonant photon energies, in order to enhance the otherwise extremely low cross sections of these processes. The sets of data show strong dependence of TDCS on the selected resonance and on the kinetic energy sharing in the case of Ca and Sr respectively. In the case of Ca, the results are in good agreement with those collected previously with a different geometry [1]. Comparison of the present experimental results with the limited existing ab-initio calculations [2] show rather poor agreement.

Direct double photoionization of Ca has also been investigated at a non-resonant photon energy at the Elettra SRS. The results show major differences compared to the similar process in He [3], and also compared to the resonant DPI of Ca.

Measurements of angular distributions and angular correlations of the photoelectron and the associated Auger electron in two-step DPI of Ca and Sr have been recorded. Analysis of these data allowed relative amplitudes of the dipole matrix elements and their relative phase to be extracted. The theory necessary to undertake this analysis was partially existing, and has been completed in the course of this work. In the case of $3p$ photoionization of Ca the results obtained are in good agreement with ab-initio calculations; the results

obtained for $4p$ photoionization of Sr show similarity to the case of Ca, but calculations are not available at the present time on Sr against which the results can be compared.

For the first time, angle resolved photoelectron spectroscopy of a short lived species, $O_2(a^1\Delta_g)$, has been performed. Resonances assigned to states of Rydberg series are observed not only in CIS spectra, but also in the plots of anisotropy parameters as functions of photon energy. Full analysis of the physical meaning of such measurements could not be performed; nevertheless, these results provide further insight on the selected photoionization processes.

Photoelectron spectroscopy of OH and OD with synchrotron radiation, at a fixed angle of observation, has also been performed. Most of the resonances in the CIS spectra have been assigned to series of Rydberg states converging to higher ionic limits. The vibrational specificity of the CIS technique, combined with FCF simulations and photoelectron spectra recorded at selected resonant photon energies, allowed vibrational structure of resonant autoionizing states to be studied in detail. Also, photoelectron spectra recorded at resonant wavelengths gives extra vibrational structure compared with those recorded at off-resonant wavelengths.

12.2 Further work

Several results have been obtained in the areas investigated, and further progress can still be made.

Measurements of resonant DPI in Sr, with a different geometric arrangement from that used in this work, can be collected with the existing apparatus. This has been planned for the next weeks at the Daresbury SRS. Such measurements will provide a stringent test for both the existing theory and the measurements collected during the course of the present work.

Resonant DPI could also be studied at the Daresbury SRS with the existing apparatus on other alkaline earth-atoms, such as Mg and Ba.

Measurements of non-resonant DPI of alkaline earth atoms are possible on a third generation SRS. However, such experiments are extremely difficult due to the low cross sections and the low collection efficiency. This could be improved by constructing a system that collects electrons simultaneously at several angles of emission, or at several kinetic energies; such a system could be made with several deflection type electron energy analysers, or with time-of-flight (TOF) analysers respectively [4]. Also, complete photoionization experiments, by studies of two-step DPI, could be extended to other alkaline earth atoms.

Photoelectron spectroscopy of reactive intermediates with synchrotron radiation can be extended by a range of experiments with the existing apparatus. The photoelectron spectrometer used in this work will be transported to the third generation Elettra SRS [5], in Trieste, in November 2000. Higher resolution, greater photon flux, a higher degree of linear polarization and a more collimated radiation beam than at the second generation Daresbury SRS will be available at Elettra. This should make studies of angle resolved photoelectron spectroscopy feasible, that are not possible on a second generation SRS. A candidate for the next investigation is the $O_2^+(X^2\Pi\, v^+) \leftarrow O_2(a^1\Delta_g\, v'' = 0)$ PE band in the region of energy $18.0 - 19.0\, eV$, where the presence of more than two overlapping vibrational progressions could be studied in more detail than was possible in this work. Another candidate is the $SO^+(X^2\Pi\, v^+) \leftarrow SO(X^3\Sigma^-\, v'' = 0)$ PE band in the region of energy $15.0 - 16.5\, eV$, where CIS spectra recorded with high resolution would allow the Fano profiles of known window resonances to be accurately measured [6]. The angular distribution of the first and second PE bands of OH and OD could be measured even at a second generation SRS. Other species produced by fast atom-molecule reactions, like CH_3, produced by $F + CH_4$ [7], could also be studied on a second generation SRS.

Several PE bands of reactive intermediates cannot be studied with the spectrometer used in this work, because of overlap with bands arising from their precursors or from secondary reaction products. This problem could be solved by up-grading the present spectrometer in such a way to make photoelectron-photoion coincidence (PEPICO) possible [8]. The spectrometer could be modified by including an ion TOF analyser with a multichannel plate detector and a coincidence detection system. The electron signal would provide the start to the coincidence circuit and also the trigger for the ion extracting field, the stop to the coincidence signal would be provided by the ion signal.

Such a system would allow several PE bands of reactive intermediates to be studied. Examples are the third and fourth bands of OH and OD at AIEs of $\sim 16.5\, eV$, that in the present work could not be resolved from bands due to NO. Other examples are the second band of CS, that overlaps with the second band of CS_2 at an AIE of $\sim 13.0\, eV$ [9], and the fourth band of SO, that overlaps with the third band of SO_2 at an AIE of $\sim 16.5\, eV$ [10].

In the long term plan the construction of an analyser that allows zero electron kinetic energy (ZEKE) pulsed field ionization (PFI) PES, with an electron TOF analyser in tandem with an hemispherical analyser, should be considered. This would allow ZEKE to be analysed, resulting in a higher resolution than is possible to obtain with conventional PES [11]. A major problem that will have to be solved is that a nozzle injection system, neces-

sary to obtain a rotationally cold sample, which is needed to resolve rotational structure, is not suitable for producing short-lived molecules.

A further modification to be made for these improvements would be to the pumping system. The present spectrometer has been designed in such a way as to give primary importance to differential pumping, in order to minimize contamination of the electron optics components and of the beam-line. This requirements will have to be maintained in every spectrometer designed with the aim to study reactive intermediates with synchrotron radiation, but enhancements of the sample pumping speed would be a big improvements.

12.3 Conclusions

In conclusion, the initial objectives of this project on resonant and non-resonant DPI and complete photoionization of Ca and Sr have been achieved. Photoelectron spectroscopy of selected reactive intermediates, $O_2(a^1\Delta_g)$ and OH and OD, has been successfully performed, and measurements of angular distribution asymmetry parameters have also been obtained on $O_2(a^1\Delta_g)$.

The two existing experimental apparatuses can allow further measurements on both DPI of alkaline earth atoms and photoelectron spectroscopy of reactive intermediates to be obtained. A selection of these are planned for the near future, and others have been indicated.

Bibliography

[1] KJ Ross, H-J Beyer and JB West, *Journal of Physics B: Atomic, Molecular and Optical Physics*, **30** L735-L740 (1997).
F Maulbetsch, IL Cooper and AS Dickinson, *Journal of Physics B: Atomic, Molecular and Optical Physics*, **33** L119-L125 (2000).

[2] AK Kazansky and VN Ostrovsky, *Journal of Physics B: Atomic, Molecular and Optical Physics*, **30** L835-L841 (1997).
L Malegat, F Citrini, P Selles and P Archirel, submitted.

[3] O Schwarzkopf and V schmidt, *Journal of Physics B: Atomic, Molecular and Optical Physics*, **28** 2847-2862 (1995).

[4] J Viefhaus, L Avaldi, F Heiser, R Hentges, O Gessner, A, Rüdel, M Viedenhöft, K Wieliczek and U Becker, *Journal of Physics B: Atomic, Molecular and Optical Physics*, **29** L729-L736 (1996).
J Viefhaus, L Avaldi, G Snell, M Wiedenhöft, R Hentges, A Rüdel, F Schäfers, D Menke, U Heinzmann, A Engelns, J Berakdar, H Klar and U Becker, *Physical Review Letters*, **77** 3975-3978 (1996).

[5] A Derossi, F Lama, M Piacentini, T Prosperi and N Zema, *Review of Scientific Instruments*, **66** 1718-1720 (1995).

[6] JM Dyke, D Haggerston, A Morris, S Stranges, JB West, TG Wright and AE Wright, *Journal of Electron Spectroscopy and Related Phenomena*, **76** 165-170 (1995).

[7] JM Dyke, AR Ellis, N Keddar and A Morris, *Journal of Chemical Physics*, **88** 2565-2569 (1983).

[8] Vacuum Ultraviolet Photoionization and Photodissociation of Molecules and Clusters.
CY Ng, World Scientific, London (1991).

[9] JM Dyke, SD Gamblin, D Haggerston, A Morris, S Stranges, JB West, TG Wright and AE Wright, *Journal of Chemical Physics*, **108** 6258-6265 (1998).

[10] JM Dyke, D Haggerston, A Morris, S Stranges, JB West, TG Wright and AE Wright, *Journal of Chemical Physics*, **106** 821-830 (1997).

[11] GK Jarvis, RC Shiell, JW Hepburn, Y Song and CY Ng, *Review of Scientific Instruments*, **71** 1325-1331 (2000).

GK Jarvis, K-M Weitzel, M Malow, T Baer, Y Song and CY Ng, *Review of Scientific Instruments*, **70** 3892-3906 (1999).

GK Jarvis, Y Song and CY Ng, *Review of Scientific Instruments*, **70** 2615-2621 (1999).

M Evans, S Stimson, CY Ng, C-W Hsu and GK Jarvis, *Journal of Chemical Physics*, **110** 315-327 (1999).

Appendix

Parts of the results presented in this thesis have been published in the following papers:

[1] A study of $O_2(a^1\Delta_g)$ with photoelectron spectroscopy using synchrotron radiation.
JD Barr, A De Fanis, JM Dyke, SD Gamblin, A Morris, S Stranges, JB West, TG Wright and AE Wright, *Journal of Chemical Physics*, **109** 2737-2747 (1998).

[2] Study of the OH and OD radicals with photoelectron spectroscopy using synchrotron radiation.
JD Barr, A De Fanis, JM Dyke, SD Gamblin, N Hooper, A Morris, S Stranges, JB West and TG Wright, *Journal of Chemical Physics*, **110** 345-354 (1998).

[3] A triple differential cross section study of calcium atoms for equal and unequal energy sharing of the photoionized electrons.
KJ Ross, JB West, H-J Beyer and A De Fanis, *Journal of Physics B: Atomic, Molecular and Optical Physics*, **32** 2927-2934 (1999).

[4] An experimental and theoretical study of the $3p$ photoionization of Ca based on a measurement of the angular correlation between the photoelectrons and Auger electrons.
A De Fanis, JB West, KJ Ross, K Ueda, H-J Beyer, M Ya Amusia and LV Chernisheva, *Journal of Physics B: Atomic, Molecular and Optical Physics*, **32** 5739-5749 (1999).

[5] Angle resolved photoelectron spectroscopy of $O_2(a^1\Delta_g)$ with synchrotron radiation.
L Beeching, A De Fanis, JM Dyke, SD Gamblin, N Hooper, A Morris and JB West, *Journal of Chemical Physics*, **112** 1707-1712 (2000).

Further manuscripts, containing the results on complete $4p$ photoionization of Sr, resonant DPI of Sr, and non resonant DPI of Ca are in preparation.